University of York

Edge Turbulence Studies during Inter-ELM Periods in the Mega-Amp Spherical Tokamak

Nizar Ben Ayed

A thesis submitted to the University of York in accordance with the requirements for the Degree of Doctor of Philosophy.

Plasma Physics & Fusion Group
Department of Physics
University of York
Heslington York, Y10 5DD
August 2009

Parts of this thesis were published in

N. Ben Ayed, A. Kirk, B. Dudson, S. Tallents, R. G. L. Vann, H. R. Wilson and the MAST Team. *"Inter-ELM filaments and turbulent transport in the Mega-Amp Spherical Tokamak"*. Plasma Physics and Controlled Fusion, **51**,2008.

N. Ben Ayed, A. Kirk, B. Dudson, R. G. L. Vann, S. Tallents, H. Wilson and the MAST team. "Structure and motion of inter-ELM filaments in MAST". In 35th EPS Conference on plasma physics, Herssonissos, Greece, ECA Vol.32D, P1.007, 2007.
This contribution received a high commendation for the Itoh Prize 2008.

N. Ben Ayed, A. Kirk, B. Dudson, R. G. L. Vann, S. Tallents, H. Wilson and the MAST team. "Structure and motion of inter-ELM filaments in MAST". In 34th EPS Conference on plasma physics, Warsaw, ECA Vol.31 F, P1.057, 2007.

B. Dudson, N. Ben Ayed, A. Kirk, H. R. Wilson, G. Counsell, X. Xu, M. Umansky, P. B. Snyder, B. Lloyd and the MAST team. *"Experiments and simulation of edge turbulence in MAST"*. Plasma Physics and Controlled Fusion, **50**, 124012, 2008.

R. Scannell, A. Kirk, N. Ben Ayed, J. McCone, P. G. Carolan, G. Cunningham, S. L. Prunty and M. J Walsh, *"Experimental investigation into ELM filament formation in MAST"*. Plasma Physics and Controlled Fusion, **49**, 1431–446, 2007.

A. Kirk, N. Ben Ayed, G. Counsell, B. Dudson, T. Eich, A. Herrmann, B. Koch, R. Martin, A. Meakins, S. Saarelma, R. Scannell, S. Tallents, M. Walsh, H. R. Wilson and the MAST team. *"Filament structures at the plasma edge in MAST "*. Plasma Physics and Controlled Fusion, **48**, B433–B441, 2006.

A. Kirk, A. Herrmann, N. Ben Ayed , T. Eich, H. W. Muller, G. F. Counsell, S. Lisgo, M. Price M, A. Schmid, S. Tallents, H. R. Wilson, *"Comparison of the spatial structure of type-I ELMs in ASDEX-Upgrade and MAST"*. In 11th IAEA Technical Meeting on H-mode Physics and Transport Barriers, Japan, *123*, 012012, 2008.

S. Lisgo, N. Ben Ayed, P. Boerner, G. F. Counsell, B. Dudson, A. Kirk, D. Reiter, S. Tallents and MAST Team "The influence of filaments in scrape-off-layer transport". In 22nd IAEA Fusion Energy Conference, Geneva, Switzerland, March 2008.

G. F. Counsell, N. Ben Ayed, R. Dendy, B. Dudson, B. Hnat, A. Kirk, S. Lisgo, T. D. Rognlien, R. Scannell, S. Tallents, M. V. Umansky, X. Q. Xu. *"Analysis of L-mode Turbulence in MAST"*. Proceedings of the 21st IAEA Conference, EX/P4-6 IAEA Conference Proceedings, Chengdu, China, 2006.

Measurements have been carried out for

S. Zoletnik, D. Dunai, A.R. Field, , A. Kirk, A. Bencze, S. Saarelma, N. Ben Ayed, G. Veres, B. Tl, R. A. Pitts and the MAST Team *"Observations of ELM precursor structures using Beam Emission Spectroscopy in MAST"*, In 35th EPS Conference on Plasma Phys, ECA Vol.32D, O-4.031, Hersonissos, 9 – 13 June 2008.

Other work during this thesis

N. Ben Ayed, A. Thyagaraja, K. G. McClements. *"Alfvén eigenmodes in magnetic X-point configurations with strong longitudinal field"*. Journal of Plasma Physics, **75**, part 2, 203215, 2009.

N. Ben Ayed, A. Thyagaraja, K. G. McClements. *"Alfvén eigenmodes in magnetic X-point configurations with strong longitudinal field"*. In 35th EPS Conference on plasma physics, Hersonissos, Greece, 2007, ECA Vol.32D, P1.007

N. Ben Ayed, A. Thyagaraja, K. G. McClements. *"Alfvén eigenmodes in magnetic X-point configurations with strong longitudinal field"*. In 35th IoP Conference on plasma physics, London 2008.

Edge Turbulence Studies during Inter-ELM Periods in the Mega-Amp Spherical Tokamak

Nizar Ben Ayed

Submitted for the degree of Doctor of Philosophy
August 2009

Abstract

An improved confinement regime such as the H-mode is critically important for the realisation of a fusion power plant based on a magnetically confined plasma. The performance of the plasma core, stability and confinement are strongly influenced by the interaction of many diverse physics processes. Among such processes is transport at the plasma edge, and particularly the physics of field-aligned filamentary structures which have been observed using high resolution cameras to leave the edge and hit the confining wall. A thorough characterisation of this transport in H-mode is therefore paramount since the filaments are directly responsible for power deposition onto material surfaces.

This thesis presents experimental analysis of filamentary structures at the plasma edge in the Mega Amp Spherical Tokamak (MAST) during H-mode inter-ELM periods. Using a background subtraction technique, camera images recorded at a rate of 100 kHz during these periods reveal that similarly to L-mode and ELM events, field-aligned filamentary structures also exist in inter-ELM periods. Analysis of their corresponding D_α light emission shows that inter-ELM filaments are the lowest amplitude fluctuations in the MAST scrape-off layer (SOL) relative to L-mode and ELM filaments.

Using magnetic equilibrium reconstructions of field-lines, filaments in the camera images are tracked in radial and toroidal directions both manually and using semi-automated techniques. Analysis of their spatio-temporal evolution confirms that despite the reduction in turbulence levels seen in the H-mode, inter-ELM filaments exist on timescales $\sim$ 50–120 μs, and during this time contribute directly to transport: they are found to rotate in the vicinity of the last closed flux surface (LCFS) with a mean toroidal velocity of 9 km s^{-1} in the co-current direction, and propagate radially outwards with a constant velocity in the range 1–2 km s^{-1}. Motion of these filaments is found to depend strongly on plasma density such that with increasing density, there is decrease in toroidal motion and an enhancement of the radial transport manifested by an increased number of filaments which leave the edge and travel faster into the SOL.

Semi-Automated methods are also applied to the inter-ELM camera images in order to determine physical properties of these filaments. A wide range of mode numbers is found (6–48) with a mean of 24. Analysis of toroidal and radial widths indicate that inter-ELM filaments are elliptical in size with an average toroidal width of 16 cm and a radial width of 4 cm. Camera images recorded at a rate of 100 kHz have been compared to data recorded simultaneously by the mid-plane reciprocating probe. This cross-comparison shows that intermittent fluctuations in ion saturation current (I_{SAT}) signals correspond to inter-ELM filaments passing the probe, appearing immediately before and after the ELM.

Peak detection algorithms have been applied to I_{SAT} signals in order to isolate the peaks corresponding to filamentary structures. Based on these I_{SAT} values, a density estimate for inter-ELM filaments is found to be in the range 6.5 $\times 10^{16}$ – 6.7 $\times$ 10^{17} m^{-3}. This result has been compared to L-mode and ELM filaments.

The I_{SAT} signals from single and neighbouring probe tips have been used to verify the properties of filaments at the edge, finding toroidal widths, mode number and toroidal velocity - in good agreement with camera estimates.

The radial motion of inter-ELM filaments is also captured in Langmuir probe data through measurements of the radial fall-off of I_{SAT}, denoted λ_{SAT}. Fits of the I_{SAT} values as a function of distance from the LCFS yield particle e-folding lengths of $\lambda_{\mathrm{SAT}}^{\mathrm{high}} \sim 41$ mm at high density discharges ($0.55 \leq n_e/n_{\mathrm{GW}} \leq 0.75$ where n_e is the line-averaged electron density and n_{GW} is the Greenwald density), and $\lambda_{\mathrm{SAT}}^{\mathrm{low}} \sim 28$ mm at low density ($0.3 \leq n_e/n_{\mathrm{GW}} \leq 0.45$). Similar trends are also obtained in simulations of a filament propagating radially with a velocity V_r and losing particles on ion parallel loss timescales $\tau_{\|}$, such that $\lambda \sim V_r\tau_{\|}$ where $\tau_{\|} \equiv L_{\|}/C_s$ ($L_{\|}$ is the connection length and C_s is the ion sound speed). Crucially, it is shown through simulation that this simple model is only valid when the radial dependence of C_s and $L_{\|}$ parameters is included.

Radial velocity and I_{SAT} measurements reported in this thesis have been used in order to test predictions made by the different models, namely the interchange and sheath-dissipative models. The observed data are at least a factor of 2 smaller than both model predictions. In fact, the scaling observed has been found to vary as a function of distance in the SOL – a feature which is not captured in either

model.

Finally, physical properties of inter-ELM filaments are compared and contrasted with those of L-mode and ELM filaments. Observations would indicate a strong similarity between L-mode and inter-ELM filaments which leads one to speculate that these have a common driving mechanism which is different to the ELM instability.

Acknowledgments

The best analogy that springs to mind with the writing of this thesis is that's its a little like running a marathon, except harder, much harder. Similar to cheering crowds who push you along a 26.2 mile stretch, there are a number of people who pushed me along my 3.5 year thesis journey, and without whom this thesis would simply not be completed. First and foremost, I would like to express profound gratitude to both my supervisors Drs Andrew Kirk and Roddy Vann for their unwavering guidance, continuous support and good advice from start to finish. Andrew has always been generous with his time, enthusiastic and full of great research ideas, while Roddy, acting as my York supervisor, was constantly encouraging and did wonders to bridge the gap between Culham and York. I also thank Ben Dudson with whom many research ideas were conceived while walking the corridors of Culham with a coffee cup, and Prof. Howard Wilson for his help in placing the PhD at the outset. I also thank Dave Taylor, Rory Scannell for their help with some coding questions and Sarah Newton for answering general physics questions.

I would also like to thank Dr Richard Martin and the Culham management for their patience whilst this thesis was being written.

And last but not least, I would like to thank my family for their unconditional love and support over many years of me being a student.

This work was funded jointly by the United Kingdom Engineering and Physical Sciences Research Council and by the European Communities under the contract of Association between EURATOM and UKAEA. The views and opinions expressed herein do not necessarily reflect those of the European Commission.

Declaration

I declare that the work in this thesis was carried out in accordance with the Regulations of the University of York. The work is original, except where indicated by special reference in the text, and no part of the thesis has been submitted for any other academic award. Any views expressed in the thesis are those of the author.

SIGNED: ....

DATE: ....

Contents

List of Figures

List of Tables

Chapter 1

INTRODUCTION

Since the beginning of industrialisation, mankind has become increasingly dependent on cheap and abundant energy. Energy consumption has grown steadily in the past, and it is now widely accepted that this energy demand, which is currently at 5×10^{20} J/yr [1], can no longer be sustained through the burning of fossil fuels. Growing global industrialisation, emerging economies in China and India, increasing world population, demands for higher standards of living, the strong dependence of economies on ever decreasing amounts of fossil fuels and their environmental impact on climate change [2] all make for a certain energy crisis. Without a reliable supply of constant energy, the industrialised infrastructure of the 21st century world would collapse: agriculture, transportation, waste collection, information technology, communications and many of the pre-requisites that a developed nation takes for granted would vanish.

The renewables (biomass, hydro, solar, wind, geothermal and biofuels) show potential as clean and abundant sources of energy. While small now, $\sim$ 9% of the global power usage in 2005, it is possible that they will provide a significant share of the energy in the future. However, it is unlikely that these sources will provide a baseline electricity generation capacity due to fluctuations in the outputs.

Conventional nuclear energy that is based on the fission of heavy elements, like Uranium, can contribute to energy production and does not produce any greenhouse gases. However, the fission power industry suffers from poor political acceptance due to the risk of a serious accident, long term radioactive waste and its connections to nuclear weapons. Furthermore, without breeder reactors, uranium reserves are questionable.

1.1 Nuclear fusion

A promising alternative energy source is fusion. Fusion reactions are brought about by heating a hydrogenic fuel to a sufficiently high temperature that the thermal velocities of nuclei are high enough to fuse into a heavier nucleus. The mass defect δm in the reaction is turned into energy ϵ according to Einstein's $\epsilon = \delta m c^2$ law. Fusion brought about in this way is called thermonuclear fusion. Energy production in the Sun occurs through nuclear fusion which proceeds predominantly via the proton cycle [3]. Despite the low cross section for this reaction, reaction rates are sufficient to produce most of the energy output of the Sun ($E \sim 3.86 \times 10^{21}$ J [3]) due to its large volume which is confined by gravity.

1.2 Plasma

Due to the increase in the binding energy per nucleon up to mass numbers of $A \propto 50$, fusion reactions between light nuclei are generally exothermic. For the short range nuclear forces to take effect, and hence fusion to occur, the nuclei involved must approach one another with high relative velocities in order to overcome the Coulomb repulsion due to their positive charges. In thermonuclear fusion, the energies required are supplied by heating the reactants to high temperatures with the resulting ensemble of electrons and fully stripped ions forming a quasi-neutral gas called a plasma.

1.3 Controlled thermonuclear fusion

In practice, only the reactions involving the hydrogenic isotopes (H, D, T) and the lightest elements (e.g. He) are of interest. Fusion reactions involving these elements include:

$$\begin{aligned}
\mathrm{D+T} &\longrightarrow {}^4\mathrm{He} + \mathrm{n} + 17.6 \quad \mathrm{MeV} \\
\mathrm{T+T} &\longrightarrow {}^4\mathrm{He} + 2\mathrm{n} + 11.3 \quad \mathrm{MeV} \\
\mathrm{D+D} &\longrightarrow {}^3\mathrm{He} + \mathrm{n} + 3.27 \quad \mathrm{MeV} \\
\mathrm{D+D} &\longrightarrow {}^3\mathrm{He} + \mathrm{p} + 4.03 \quad \mathrm{MeV} \\
\mathrm{D+{}^3He} &\longrightarrow {}^4\mathrm{He} + \mathrm{p} + 18.3 \quad \mathrm{MeV}
\end{aligned}$$

Of these, the reaction between deuterium and tritium is the most favoured for use in a fusion power plant. This is because the fusion cross section, σ, for this reaction is much larger than other reactions within achievable temperature ranges. Figure 1.1 shows that σ reaches a maximum ($\sigma \sim 7 \times 10^{-28} \mathrm{m}^{-2}$) for a deuteron energy of 100 keV (1keV $\approx 10^7$ K) on a stationary tritium nucleus - considerably higher at this impact energy than the cross section for alternative combinations (D–D, D–$H_e{}^3$) [4].

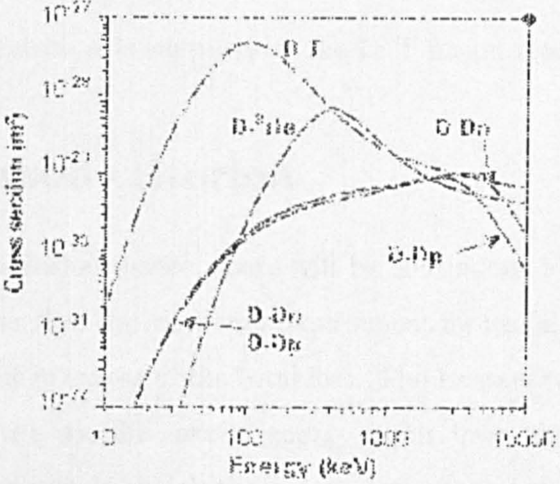

Figure 1.1: *Fusion cross-sections for the most important fusion reactions as a function of the centre-of-mass energy of the reacting particles.*

More specifically, the plasma ions will be characterised by Maxwellian velocity distributions at temperature T_i, and a more relevant parameter is the reaction rate $\langle \sigma v \rangle$ averaged over all velocities. Due to the contribution of energetic ions in the tail of the distribution, $\langle \sigma v \rangle$ is found to reach half of the maximum value for ion temperatures as low as 20 keV [4] .

In these reactions, the charged 3.5 MeV helium atoms remain confined by the plasma serving to heat it through collisions, while the majority of the energy ~ 14.1 MeV is carried by the neutrons. These escape the plasma and interact with a surrounding "blanket" transferring their energy into heat which is then carried away by a suitable coolant (either water or He). This coolant is then used to drive a conventional turbine to generate electricity.

While deuterium is readily obtained from water with an isotopic abundance in normal hydrogen is 0.015% , tritium, which is an unstable isotope of Hydrogen, occurs naturally only in negligible amounts due to it being radioactive with a half-life of 12 years. For this reason, the blanket capturing the neutrons is also engineered so as to allow the breeding of tritium from lithium, in order to fuel the D – T fuel cycle through one of the following reactions:

$$\begin{aligned} \mathrm{n} + {}^{6}\mathrm{Li} &\longrightarrow \mathrm{T} + {}^{4}\mathrm{He} \\ \mathrm{n} + {}^{7}\mathrm{Li} &\longrightarrow \mathrm{T} + {}^{4}\mathrm{He} + \mathrm{n} \end{aligned}$$

where the reactant neutron n is supplied by the D–T fusion reaction.

1.4 The Lawson criterion

Since in any future fusion device, there will be continuous loss of energy from the fusion plasma, it is clear that the minimum requirement for useful power production is a minimum power output in excess of the total loss. The Lawson criterion is a statement of this condition for the specific case of energy input from an external source. An idealised process is assumed in which the power output can be converted to electrical energy and regained later as useful heat.

Denoting P_H the heating power, P_L the total power loss, and P_T as the total useful power leaving the plasma which can be converted to electrical energy with an efficiency η, then for this simple model it is at least necessary that:

$$\eta P_T \geq P_L, \tag{1.1}$$

be satisfied for power balance within the plasma, $P_H = P_L$.

The thermonuclear power per unit volume per unit time from a fusion plasma with deuterium and tritium species of density n_{D} and n_{T} is given by:

$$P_{Tn} = n_{\mathrm{D}} n_{\mathrm{T}} \langle \sigma v \rangle_{\mathrm{DT}} E = \frac{1}{4} n_i^2 \langle \sigma v \rangle_{\mathrm{DT}} E, \tag{1.2}$$

where E is the energy released per reaction (17.6 MeV).

Taking into account losses due to Bremsstrahlung radiation, and writing the remaining power loss which result from other processes as a ratio of the total plasma energy density W and the characteristic time over which it is confined τ_E:

$$P_L = \frac{W}{\tau_E} = \frac{3}{2}\frac{n_e T_e + n_i T_i}{\tau_E}, \tag{1.3}$$

the total power loss can be written as:

$$P_L = \beta n_e n_i T_e^{1/2} + \frac{3}{2}\frac{n_e T_e + n_i T_i}{\tau_E}, \tag{1.4}$$

where β is a constant (3.8×10^{-29} $\mathrm{J^{\frac{1}{2}}m^3s^{-1}}$ [5]). The total power leaving the plasma is thus:

$$P_L = n_i^2 \left(\frac{\langle \sigma v \rangle_{\mathrm{DT}} E}{4} + \beta T^{1/2} \right) + \frac{3 n_i T}{\tau_E} \tag{1.5}$$

Substituting equations (1.5) and (1.2) into the requirement of equation (1.1), the criterion for a system with net power gain is:

$$n\tau_E(T) \geq \frac{3T}{\frac{\eta}{1-\eta}\frac{1}{4}\langle \sigma v \rangle_{\mathrm{DT}} E - \beta T^{1/2}}. \tag{1.6}$$

For $\eta = 1/3$, the curve of $n\tau_E$ versus T has a minimum of 6×10^{19} $\mathrm{m^{-3}s}$ for temperatures in the range 20–30 keV. Since for a future power plant, $n\tau_E$ must exceed this minimum value, the condition for net power gain, formally known as the Lawson criterion becomes:

$$n\tau_E \geq 6 \times 10^{19} \mathrm{m^{-3}s}. \tag{1.7}$$

1.5 Ignition

The continuous source of external heating power assumed in deriving the Lawson criterion would not be required if the energy released from the fusion reactions within the plasma volume could be used to balance the losses. When adequate confinement conditions are achieved, a point is reached where the plasma temperature can be maintained against the energy losses solely by ^{4}He (α-particle) heating. In a D-T fusion plasma this is possible through the retention of charged α-particle reaction products by the confining magnetic field. When the heat losses are balanced by the α heating, the plasma ignites and any external power input may be discontinued.

By analogy with equation (1.2) the α-particle heating power per unit volume may be written:

$$P_\alpha = \frac{1}{4} n_i^2 \langle \sigma v \rangle_{\mathrm{DT}} E_\alpha, \tag{1.8}$$

where $E_\alpha = 3.5$ MeV is the α-particle energy. Using the relation (1.4) for the total power loss, the condition for ignition $P_\alpha \geq P_L$ is:

$$n\tau_E \geq \frac{3T}{\frac{\eta}{1-\eta}\frac{1}{4}\langle\sigma v\rangle_{\mathrm{DT}} E_\alpha - \beta T^{1/2}}. \tag{1.9}$$

In common with equation (1.6), $n\tau_E(T)$ has a minimum value at $T \sim 30$ keV, giving for the ignition criterion at this temperature[4]:

$$n\tau_E \geq 1.5 \times 10^{20}\mathrm{m}^{-3}\mathrm{s}. \tag{1.10}$$

However, since τ_E is itself a function of temperature, it can be shown that the ignition criterion becomes:

$$nT\tau_E \geq 3 \times 10^{21}\mathrm{m}^{-3}\mathrm{keVs}. \tag{1.11}$$

Ideally, fusion devices would seek to maximise both n and τ_E parameters in order to achieve the conditions of equation (1.11). However in practice, two existing approaches have been followed. The first favours maximising n at the expense of τ_E, and is known as Inertial Confinement Fusion (ICF). The second method adopts the reciprocal relations where it is sought to maximise τ_E through magnetic confinement.

1.6 Inertial Confinement Fusion (ICF)

The ICF method attempts to produce high densities and temperatures for a short time to satisfy Lawson's criterion. Fusion reactions are initiated by heating and compressing a fusion capsule (typically D and T) situated within a gold-plated hohlraum cavity by the use of intense laser or ion beams. A process known as "indirect drive" is used during which the laser beams rapidly heat the surface of the hohlraum which absorbs the energy and re-radiates it as X-rays. The X-rays then uniformly heat the fusion target leading to (1) an explosive detonation of its outer layers, and (2) the acceleration of the remaining target layers inwards, thereby creating a shock wave into the centre. As a result, the fuel core in the target is compressed reaching a high enough density (typically $n \sim 10^{31}$ m^{-3}) and temperatures so as to ignite and cause fusion reactions on time scales $\tau_E \sim 10^{-11}$ s. For a multimedia animation, see [6]. First experiments are scheduled for 2010 at the National Ignition Facility (NIF) at the Lawrence Livermore National Laboratory (LLNL)[6].

1.7 Magnetic confinement

The second approach to fusion, which is the implementation considered in this thesis, is to use magnetic fields to confine D-T plasmas at temperatures of $T \sim 10$ keV at relatively low densities $n \sim 10^{20}\mathrm{m}^{-3}$ for long periods of time $\tau_E \sim 10s$. As previously mentioned, the plasma energy density must be maintained to ensure significant reaction probability and power output.

The basic principle of magnetic confinement may be understood by considering a charged plasma particle. In the presence of a magnetic field, the particle will gyrate in a plane perpendicular to the field direction, and thus it follows that the flow of particles across the field is restricted. With no other external influences, the particle will to first order simply follow the magnetic field direction. Thus, by controlling the direction of this guiding magnetic field, the plasma as a whole may be manipulated. The ionised fusion fuel and charged α particles will be affected, whereas the neutrons released from the fusion reactions will pass through freely to a surrounding absorbing blanket, where they will generate tritium and deposit their energy.

A variety of magnetic confinement devices have been proposed. The two basic confinement concepts which have been successful are the stellerator [7] and the tokamak [4]. Both confine a plasma in a toroidal configuration but differ mainly in the structure of the guiding magnetic field, and the way it is produced.

Stellerators generate all the confining fields externally using highly complicated field coils. Some important stellerator experiments include the Wendlestein stellerator (Germany) and the Large Helical Device (Japan). The main advantage of the stellerator concept is that they can be operated in steady state and do not require an internal current. The expenses and complexity therefore of current drive are avoided. However, the complexity of the field coils and asymmetry of the plasma complicates theoretical stability analysis and the implementation of experimental diagnostics becomes more difficult.

1.7.1 The tokamak

The tokamak has emerged as the leading concept for high temperature confinement of plasmas, with a simpler magnetic configuration in comparison to the stellerator. It was first developed in the Soviet Union in the early 1960s – the name, an acronym from the Russian words Toroidalnaya Kamera and MAgnitnaya Katuchka, meaning "toroidal chamber" and "magnetic coil". The progress of experimental work on tokamaks towards reactor conditions can be illustrated by the fusion triple product where most of this progress is based on building successively larger devices rather than through improvements of the thermal insulation. The largest and most powerful tokamak devices, JET and JT-60U, have reached plasma parameters equivalent to break even. There are now two categories of tokamaks: the conventional tokamak such as JET, and a more recently developed spherical tokamak. The two designs have similar fundamental properties which will be described briefly in subsection 1.7.4, while their differences are outlined in section 1.8.

1.7.2 Magnetic geometry

The principle of magnetic confinement in a tokamak is based on an equilibrium in which a force balance is achieved between the expansion effects of a hot pressure-driven plasma and the magnetic forces acting on it. The magnetic field arises from both induced and self-generated plasma currents, as well as externally applied magnetic fields. This section will describe the magnetic fields necessary for tokamak confinement.

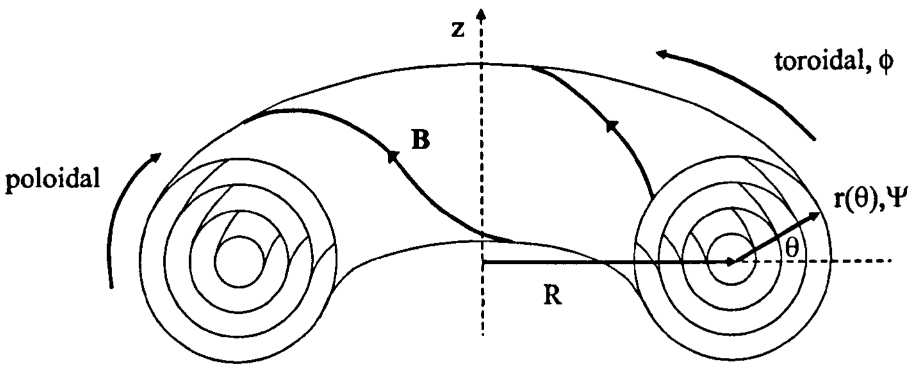

Figure 1.2: *Illustration of the magnetic field configuration with the topology of nested flux surfaces in a tokamak. The toroidal coordinate system* (R, ϕ, Z).

Toroidal field

Two basic components of the total field are necessary for confinement: a toroidal and poloidal component. First, the toroidal component which is responsible for the basic plasma shape is discussed.

As mentioned earlier, charged particles follow the direction of the guiding magnetic field line whilst gyrating around them. The idea of confinement is that all particles are charged and that their orbits in the magnetic field remain within the confined plasma. This implies that there can be no outward component of the magnetic field at the plasma boundary. It was shown through a conjecture made by Poincaré that in order to achieve this, the plasma confining surfaces are toroidal in shape, and that guiding magnetic field lines would densely cover these surfaces. The confinement region within a tokamak plasma is therefore described as a series of nested flux surfaces which ideally provide a barrier to radial motion of charged particles. The innermost magnetic surface is known as the magnetic axis, and is simply a toroidal line. The outermost surface which marks the boundary of the confinement region is referred to as the last closed flux surface (LCFS). A toroidal angle, ϕ, is introduced to define the toroidal location along the torus (See figure 1.2). In the tokamak, this component of the field is referred to as B_ϕ, it prevents end losses from the plasma and plays an important role for its general stability.

Poloidal field

The toroidal field alone does not allow confinement of the plasma since the field gradient would lead to a charge separation between top and bottom of the torus as the electron and ion guiding centre drifts are in opposite directions; the resulting electric field would then force a further $\mathbf{E} \times \mathbf{B}$ drift outwards in the direction of the major radius. To eliminate the charge imbalance, a field line connection between top and bottom of the torus is necessary. In the tokamak, this component of field, B_θ, is known as the poloidal field, and serves to maintain an equilibrium in which the plasma pressure is balanced by the magnetic forces. The poloidal angle θ is introduced to define the poloidal position around a flux surface. Toroidal and poloidal directions are thus shown in figure 1.2. The trajectory of charged particles can now be visualised through the total magnetic field line which is helical and spirals on a given magnetic flux surface. Note that r - the minor radius, is the distance between the magnetic axis to the plasma edge.

Axisymmetry

Axisymmetry is an important feature of the tokamak since this property greatly simplifies the engineering and mechanical challenges as well as introduces a tractable mathematical description of the system. It can be shown that an axisymmetric magnetic field in a quiescent plasma may be written as:

$$B = \nabla\psi \times \nabla\phi + f(\psi)\nabla\phi, \tag{1.12}$$

where ψ is called the poloidal flux function and represents the amount of poloidal flux lying within each magnetic surface (i.e., between the magnetic axis and the radial location R). The poloidal component of the magnetic field (which lies in the (R, Z) plane), is represented by $\mathbf{B}_\theta = \nabla\phi \times \nabla\psi$, whilst the toroidal component of the field is $\mathbf{B}_\phi = f(\psi)\nabla\phi$. As the system is axisymmetric, it follows that $\mathbf{B}.\nabla\psi = 0$ and magnetic field lines lie on surfaces of constant flux, referred to earlier as magnetic flux surfaces. Figure 1.2 shows a section through the nested toroidal flux surfaces. Details of the derivation for equation 1.12 can be found in [8].

Note that any deviation from axisymmetry for the magnetic field, for example due to a current perturbation, will result in magnetic field lines which travel through flux volumes (rather than magnetic field-lines being confined to a specific flux surface). The exact structure of this magnetic field depends on the currents inside both the magnetic field coils and the plasma.

Safety factor

The magnetic field lines are located at the magnetic surfaces winding on them as helical lines: under angle displacement $d\phi$ along the torus, the magnetic field line rotates by angle $d\theta$ in the poloidal direction. Since the arc length along ϕ is equal to $Rd\phi$, and along θ is equal to $rd\theta$, their ratio is equal to the ratio of the components of the corresponding fields, and thus measures the field line pitch. This is expressed as:

$$q = \frac{r}{R}\frac{B_\phi}{B_\theta}, \tag{1.13}$$

where q is the safety factor, R the major radius and r the distance from the axis of symmetry to a given flux surface.

The value of q is of significance in a tokamak. The field lines may either be closed, in which case they meet themselves after one or more transit of the torus, or open, in which case a single magnetic field line densely covers an entire flux surface. When the field lines close, the value of q may be interpreted geometrically: q will be a "rational" number and may be written as $q = m/n$ where n is the number of toroidal circuits a field line makes before completing m poloidal circuits. If q is irrational, the magnetic field line is never closed and the definition of q as the ratio of number of turns is understood asymptotically, i.e. as the limit when the number of rotations tends to infinity. The name derives from the requirement that $q \geq 1$ everywhere for gross stability against certain plasma instabilities.

1.7.3 Equilibrium force balance

The basic MHD equilibrium force balance which must hold in the plasma in order to contain the plasma energy density, or pressure, by the magnetic forces will now be outlined. The momentum balance equation for a plasma species, denoted by a subscript α, is expressed as [9]:

$$m_\alpha n_\alpha \left.\frac{d\mathbf{V}_\alpha}{dt}\right|_\alpha = -\nabla p_\alpha - \nabla \cdot \mathbf{\Pi}_\alpha + z_\alpha e n_\alpha (\mathbf{E} + \mathbf{V}_\alpha \times \mathbf{B}) + \mathbf{F}_\alpha. \tag{1.14}$$

This is similar to the Navier-Stokes equation for a fluid, with the addition of the Lorentz force and the friction, $\mathbf{F}_\alpha$, between the plasma species. Here, m_α and z_α are the mass and charge of the particle respectively, e is the unit electronic charge, n_α, T_α and $p_\alpha = n_\alpha T_\alpha$ are the species' density, temperature and pressure respectively, $\mathbf{\Pi}_\alpha$ is the viscosity tensor and $\mathbf{V}_\alpha$ is the flow velocity of the species. The convective derivative is taken in the frame moving at the velocity $\mathbf{V}_\alpha$. To determine the plasma force balance, the sum of the momentum equations for each species must be taken. The inter-species forces cancel, as do the terms dependent on the electric field, due to quasi-neutrality. To determine the equilibrium, the inertia and viscosity terms are neglected [9]. Defining the total current $\mathrm{j} = e\Sigma_\alpha n_\alpha z_\alpha \mathbf{V}_\alpha$ and the total plasma pressure $p = \Sigma_\alpha n_\alpha T_\alpha$, the force balance takes the form:

$$\mathrm{j} \times \mathbf{B} = \nabla p. \tag{1.15}$$

The dot product of this equation with $\mathbf{B}$ gives $\mathbf{B} \cdot \nabla p = 0$, so that, in equilibrium, the pressure is constant on a flux surface. The plasma may be understood to evolve slowly through a series of quasi-equilibrium states. The force balance equation holds at each flux surface, so that, at each radius, there is a balance between the pressure and the Lorentz force due to the current contained in the interior.

By using the explicit form of the magnetic field in an axisymmetric system (see equation (1.12)), the force balance equation (as shown in equation (1.15)), becomes the Grad-Shafranov equation [4]. This is solved to give the 2-D description of the magnetic flux surface cross-sections. Typically this is done numerically, using experimental measurements of the magnetic fields to reconstruct the equilibrium magnetic field distribution which is established in the plasma.

Plasma beta

The efficiency of confinement of plasma pressure by the magnetic field, as expressed in equation (1.15), is represented in a simple way by the ratio:

$$\beta = \frac{\langle p \rangle}{B^2/2\mu_0}, \qquad (1.16)$$

where $\langle p \rangle$ is kinetic energy density, and $B^2/2\mu_0$ is the magnetic energy density. For the most effective use of the generated magnetic field, it is preferable to have values of β as high as possible.

1.7.4 Principles of a tokamak

Typical plasma densities in a tokamak are of the order of 10^{19} particles/m^3, which is roughly five orders of magnitude lower than air density. Therefore in magnetic confinement devices such as the tokamak, the plasma is produced in a metal high vacuum chamber, and evacuated to low base pressures. The chamber is then filled with a gas mixture which has to be heated to temperatures in excess of 10 keV. Note the temperature T=1 keV corresponds to 1.16×10^7 K. The confinement of this plasma is achieved by the combination of magnetic fields generated by external current-carrying coils and by current flowing through the plasma to produce a closed magnetic field line system. Figure 1.3 is a schematic representation of a standard experimental machine configuration.

Figure 1.3: *Schematic view of a tokamak and the three magnetic fields: Toroidal field* B_ϕ*, poloidal field* B_θ *and vertical field* B_z*. The ratio of the three components is typically* B_ϕ*,* B_θ*:* $B_z \approx$ *100:10:1 for conventional machines.*

The main toroidal guiding field, B_ϕ is produced by a series of discrete toroidal coils which encircle the plasma in the poloidal direction - see blue coils in figure 1.3. The number of toroidal coils varies depending on the device but are equally spaced in all devices so as to minimise deviations from axisymmetry. Ampéres law applied to a toroidal circuit within the toroidal field coil gives:

$$2\pi R B_\phi = \mu_0 I_T, \tag{1.17}$$

where I_T is the total current in the toroidal coils. It is seen from equation (1.17) that the vacuum toroidal field varies as $B_\phi \propto 1/R$.

The poloidal field is produced by a toroidal current induced in the plasma by transformer action with the plasma as a single turn secondary. The primary winding, or primary solenoid, sits along the symmetry axis - see in green inner poloidal coils in figure 1.3.

In addition to toroidal and poloidal fields, a vertical magnetic field B_z is produced by external toroidal windings. This component is also required to counteract hoop forces which expand the plasma ring due to toroidal geometry.

In addition to providing the poloidal component of the magnetic field, the induced plasma current, denoted in this thesis as I_p, is also a source of plasma heating through the resistance to the current caused by electron-ion collisions; this is known as Ohmic heating. At low temperatures the Ohmic heating density is large but, because the resistance of the plasma, η, varies as $T_e^{-3/2}$, this heating power $P_\omega = \eta j^2$ is less efficient at high temperatures [4].

One limitation of the tokamak design is manifested in the short duration of the plasma discharge which is limited by the maximum current that can be driven through the transformer.

1.8 Spherical tokamaks

The shape of a torus is characterised using several parameters, the most important being the major and minor radii, denoted respectively as R and r. Initially, all tokamaks were of conventional aspect-ratio (A), that is with $A \equiv R/r \geq 2$. This evolved, and the concept of spherical tokamaks (STs), or small aspect-ratio tokamak, was introduced. This is primarily obtained from a conventional aspect-ratio tokamak by reducing its major radius while keeping the minor radius fixed. A further distinction is the natural vertical elongation which ensues from the compact design. These two distinguishing features are illustrated in figure 1.4. Shown in (a) is a conventional aspect ratio tokamak with its large distance between the machine axis and the plasma such that $A = 3$, which is in contrast with an $A = 1.3$ ST tokamak characterised by a distinctive D-shaped poloidal cross-section.

The main motivation for a smaller aspect ratio tokamak stems from the desire to extend the operational limits, particularly in terms of higher plasma current. This can be seen from the scaling of plasma current I_p in a tokamak which is expressed as:

$$I_p \sim \left(rB_\phi/q\right)/A, \tag{1.18}$$

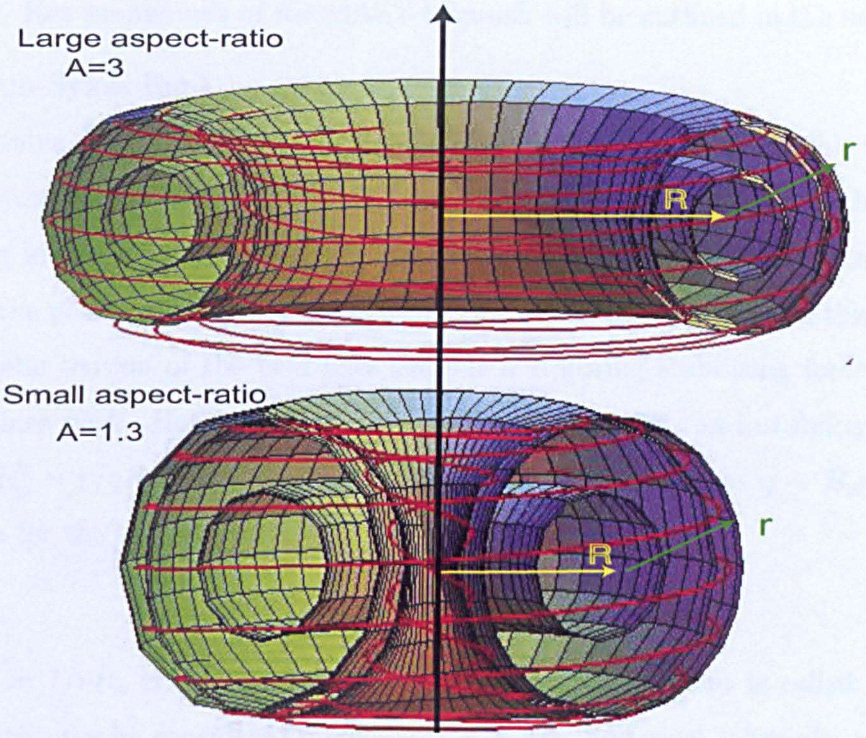

Figure 1.4: *Illustration showing difference between an (a) large aspect ratio tokamak with $A = 3$ and (b) small aspect ratio, $A = 1.3$. Major radius R shown as red arrow, and minor radius r as black arrow. Overlaid are also field lines on the outer most surface.*

where any advantages of high current are more readily obtained with a small aspect-ratio. Furthermore, the ST benefits from being able naturally to exploit the high field region near the central column. Indeed, as the plasma in the ST is closer to the central solenoid, the toroidal field which must be generated to ensure plasma stability is generally less than that required in a conventional tokamak for the same plasma current. Considering that the power required to generate the magnetic field is the most significant cost for tokamak operation, the ST design is an economically attractive option. The theoretical advantages of the ST design were introduced in a publication by Peng and Strickler[10], and predictions were subsequently verified experimentally on a range of small STs (e.g CDX-U, HIT, TS-3, MEDUSA, ROTMAK-ST), and in particular on the START device at Culham. Promising results have led to the design and construction of the current generation STs including PEGASUS (USA), GLOBUS-M (Russian Federation), ETE (Brazil), and TST-2 (Japan), and two larger Mega-Ampere devices, NSTX (USA) and MAST (UK). It is from the latter device that data for this thesis are presented. Key parameters of the MAST tokamak will be outlined in the next section.

The Tryon-Sykes limit

The β value, (as expressed in equation (1.16)) has a maximum achievable value given by the Tryon-Sykes limit [11]. This is a pressure limit, and is related to the so-called ballooning instability where magnetic field lines experience a "swelling" on the outer region of the plasma where they are convex with radius of curvature. In this situation, the magnetic tension of the field-lines provide a restoring stabilising force and draw the field-lines back. However, if a critical value is exceeded, an instability occurs at $\beta = \langle p \rangle / B_\phi^2 \sim r/qR$. Since the safety factor can be expressed as $q \sim B_\phi r^2/IR$, the expression for the limiting value of β is given by:

$$\beta_n = g\frac{I}{rB_\phi} \equiv gI_N \tag{1.19}$$

where $I_N = I/rB_\phi$ is the normalised current. The g coefficient is called the Tryon factor which may be considered a constant: $g \approx 3\%$. Spherical tokamaks are capable of achieving a higher β due to a higher normalised current. The START tokamak was the first ST to produce a hot ($\geq$ 100 eV) plasma, and was able to produce record β values of 40%, which was much higher than the previous maximum 12.6 % obtained in the larger aspect ratio DIII-D machine.

1.8.1 The MAST tokamak

The Mega Amp Spherical Tokamak (MAST) is a spherical tokamak which became operational in December 1999. It was designed to test the promising results obtained from its forerunner; the START device, which was operational at Culham from 1991 to 1999. The objectives of the MAST programme are to establish the physics basis for a Spherical Tokamak-based Component Test Facility (CTF) and to advance understanding of key tokamak physics issues for optimal exploitation of next step fusion machines ITER [12] and DEMO [13]. In support of these objectives, MAST is equipped with two neutral beam heating systems, a cryogenic pellet injector, digital plasma control systems, error field compensation coils, and internal coil arrays for (1) control of edge localised modes (ELMs) and (2) excitation of Toroidal and Compressional Alfvén Eigenmodes (TAEs & CAEs).

In addition there is a comprehensive array of advanced diagnostics including high spatial and temporal resolution kinetic diagnostics (Thomson Scattering, charge exchange recombination spectroscopy, etc.), a multi-chord Motional Stark Effect (MSE) system, extensive 2D imaging diagnostics (visible, infra-red, multi-wavelength narrow band systems), numerous spectroscopic systems including edge Doppler spectroscopy and new beam emission spectroscopy (BES), magnetic measurements (integrated and unintegrated) up to 5 MHz and an array of Langmuir probes.

1.8.2 MAST engineering parameters

Key MAST parameters are summarised in Table 1.1 below.

Table 1.1: MAST engineering parameters

	Design	Achieved
Major radius, R (m)	0.85	0.85
Minor radius, r (m)	0.65	0.65
Aspect ratio, ϵ	2.5	2.4
Elongation, δ	2.5	2.4
Triangularity, κ	0.5	0.5
Plasma current, I_p (MA)	2	1.35
Toroidal field (T)	0.51	0.51
NBI heating (MW)	5	3.8
Pulse length (s)	5	0.65
Plasma volume (m^3)	10	10

1.8.3 The vacuum vessel

The MAST vessel is a stainless steel shell. It provides the ultra-high vacuum enclosure, and supports vessel components such as external toroidal field coils and internal poloidal field coils (as will be described in section 1.8.5). As shown in Figure 1.5, the vacuum vessel is a large cylinder, 4.0 m diameter and 4.4 m in height. Access for heating and diagnostics into the vessel is provided by three rings of large ports in the outer wall with additional ports in the top and bottom end plates.

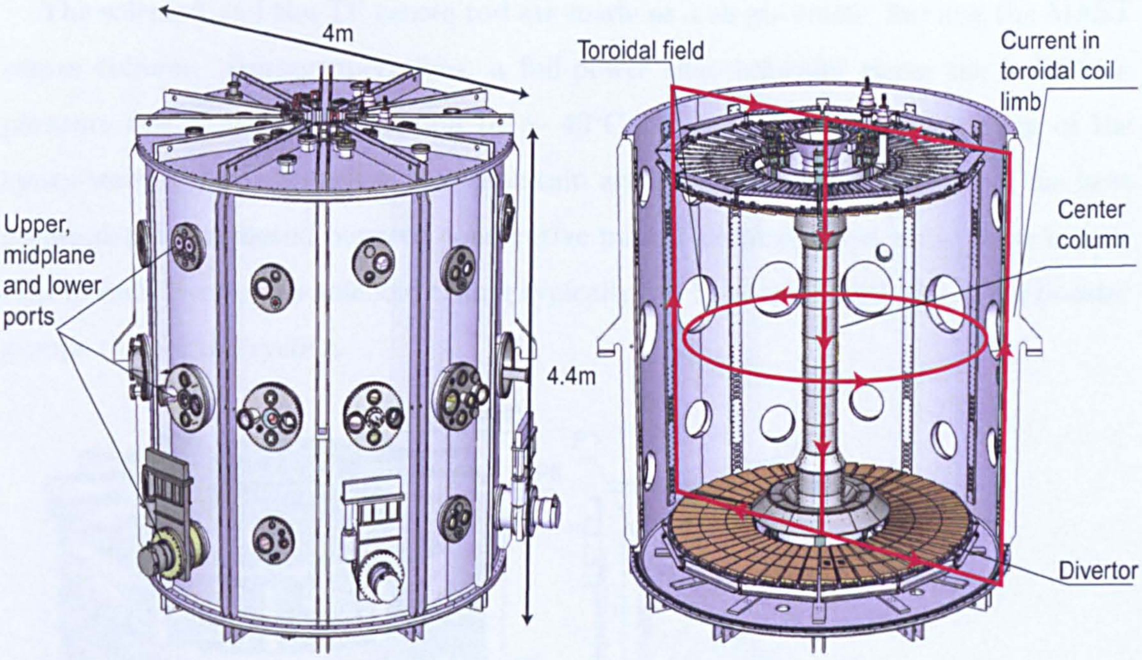

Figure 1.5: *The MAST vessel is cylindrical with access for heating and diagnostics provided by three rings of large ports in its outer wall. The internal view (right) also shows the open surface area, known as divertor, and the primary poloidal coil referred to as the central column.*

1.8.4 Toroidal and poloidal field systems

External to the vacuum vessel are 24 toroidal field coil limbs each capable of supporting a current of 92 kA (see red outline in figure 1.5(b)). The coils are water-cooled conductors connected in series giving a total current of 2.2 MA – this is known as the rod current and gives rise to the vacuum magnetic field in the toroidal direction B_ϕ.

In addition to the poloidal currents (from toroidal coils which link the plasma), a set of 6 poloidal coils, shown in figure 1.6, exist in-vessel and provide toroidal currents. Each coil pair is designed with a specific purpose and will be described briefly.

The main coil P1 consists of a solenoid wound around the central rod. The current is ramped between ± 50 kA in P1, and leads to a flux swing of 1Vs required to produce toroidal current in the plasma, and an associated poloidal magnetic field. This component of the field produces an inward force needed to balance outward force (along the minor radius) due to the plasma pressure. The remaining flux volt-seconds remaining after the ramp, in conjunction with that provided by the other poloidal coils (as will be described) will then sustain the flat-top current for typically 0.3 – 0.5 s.

The solenoid and the TF centre rod are made as a single entity, forming the MAST centre column. During operations, a full-power shot typically raises the bulk temperature rise of the centre-column by ∼ 40°C. In order to prevent softening of the epoxy-resin insulation system, and maintain acceptable electrical resistance, the heat accumulated is removed between consecutive pulses: demineralised water flows in parallel in each layer of the solenoid taking typically 10–15 minutes with the aid of booster pumps to cool the system.

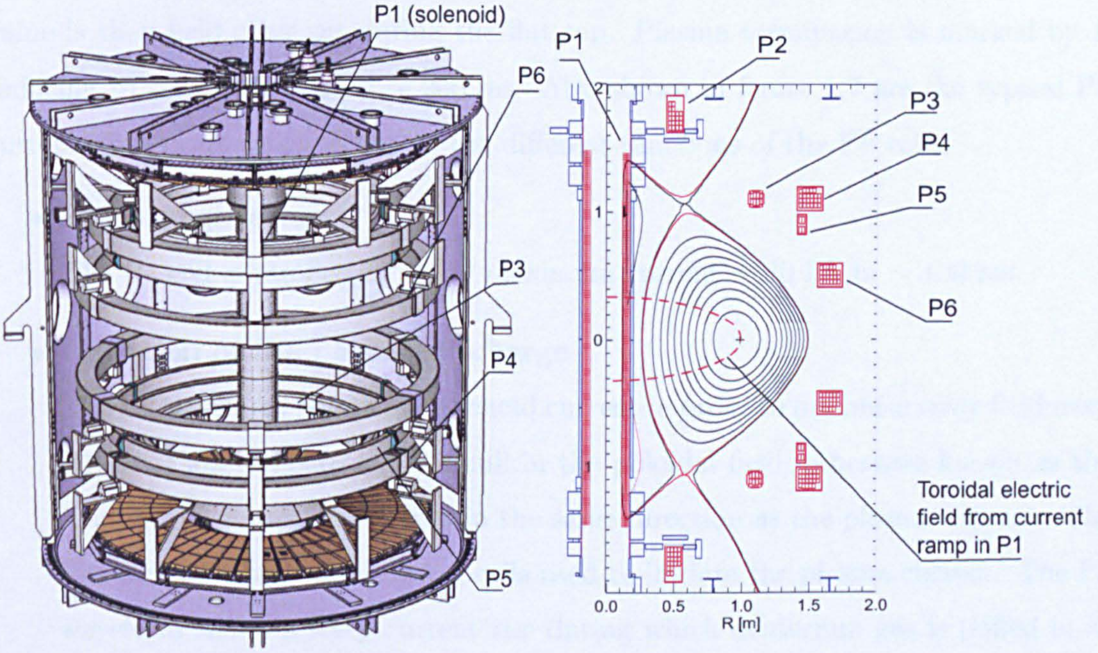

Figure 1.6: *Layout of the PF coils in the vacuum vessel. The internal support structure is designed to provide adjustable support to the internal components. The divertor coils and target plates are supported from the vessel end plates while other internal coils are supported from the vessel side walls.*

The five pairs of poloidal field coils P2, P3, P4, P5 and P6 (shown in figure 1.6) are used to produce the wide variety of plasma shapes in addition to providing plasma positional control and providing a vertical field to counteract the hoop force. These coils are inside the vacuum tank and consist of water-cooled conductors encased in stainless steel jackets.

1.8.5 Typical current waveforms

A typical plasma current waveform is shown in figure 1.7. The evolution of the plasma current is directly linked to specific PF current waveforms, each serving a different function. Prior to plasma initiation, the P1 waveform is marked initially by a pre-magnetisation phase lasting ~ 100 ms. This is closely followed in the plasma current waveform by an induction phase where I_p ascends to I_p ~ 200 kA in 5 ms. Subsequently, the current is ramped up to the desired level and at a desired rate. This value is then held constant during the flat top. Plasma termination is marked by I_p reducing to zero, typically on ~ 200 ms. Also shown in figure 1.7 are the typical PF current waveforms which illustrate the different functions of the PF coils.

- **Premagnetisation**

  The P1 coil is ramped up to its maximum current ~ 40 kA in ~ 100 ms.

- **Initiation of the plasma discharge**

  The P2 waveform tracks the solenoid current in order to minimise stray field from P1. It is also used to make a null in the poloidal field, otherwise known as the X-point, by running a current in the same direction as the plasma current. The P3 coils are a pair of induction coils used to initiate the plasma current. The P3 waveform shows a steep current rise during which deuterium gas is puffed in at various locations in the vessel. A fast P1 current decay dI_{P1}/dt then causes a flux variation which induces an electric field able to ionise the low pressure deuterium gas in the vacuum vessel. The gas breakdown is promoted by the toroidal field which channels the electrons thus amplifying the avalanche effect.

- **Plasma current rise and flat top**

  The P1 current (and therefore the flux variation) is controlled in order to achieve the desired rate of rise of the plasma current and, once the current has reached its nominal value, to maintain the current during the flat top duration. As the plasma current ramps up from its post breakdown value ~ 200 kA to its flat top value ~ 500 – 900 kA, so do the currents in P4 and P5. Negative currents (i.e, in opposite direction to direction of plasma current) in these coils provide the vertical field and the main plasma control. During the flat top phase, the flux rate of change is determined by the resistive voltage in the loop: P4 and P5 currents are held constant and the plasma loop voltage is typically in the range 0.7–1.7 V.

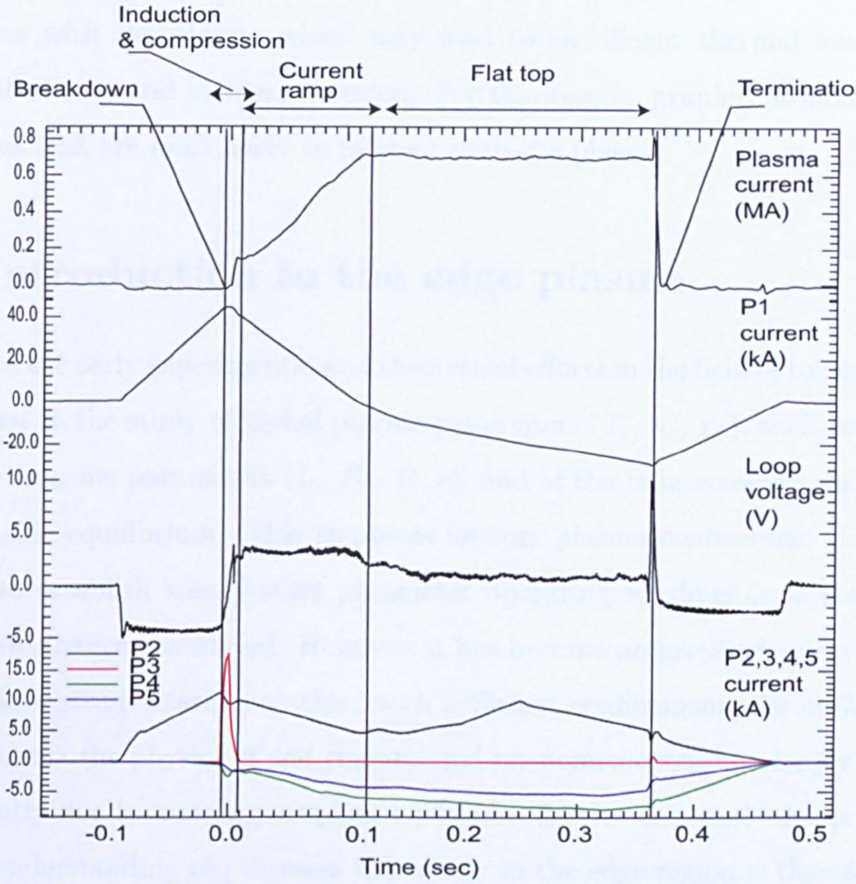

Figure 1.7: *Typical waveforms for P1,2,3,4,5 coils. P2 are used to produce a divertor coil to generate a double null X-point plasma. P3 are a pair of induction coils used to initiate the plasma current. Negative currents (in convention of positive current being that of the plasma) in P4 and P5 provide the vertical field and the main plasma control. P6 are connected in anti-series (upper and lower in opposite directions) so as to produce a radial field used to control the vertical position of the plasma.*

- **Plasma termination**

  When the current in the P1 coil reaches its second maximum value (this may also be in the opposite direction) imposed by the structural and thermal limits, the plasma discharge is terminated. At this point, the P1 current (and flux) is reduced so as to induce a reverse electric field and ramp down the plasma current.

P6 coils are connected in odd parity in order to produce a radial field used to control the vertical position of the plasma. The current waveforms are therefore dependent on feedback signals from pick-up coils which detect vertical instabilities in the plasma.

During MAST operations, both P2 and P3 coil packs are particularly prone to interactions with the plasma which may lead to significant thermal loading of the stainless steel case and increased erosion. For this reason, graphite armours are fixed to the faces that are most likely to interact with the plasma.

1.9 Introduction to the edge plasma

Much of the early experimental and theoretical efforts in the field of tokamak physics was devoted to the study of global plasma parameters (T_e, n_e, τ_E), their scalings with important machine parameters (I_p, B_ϕ, R, r), and of the numerous instabilities which prevent stable equilibrium. This emphasis on core plasma confinement derived from the need to establish steady-state parameter operating windows in which optimum plasma performance is achieved. However, it has become progressively clear that in order to achieve steady-state operations with sufficient confinement, the performance of the core plasma the physics of and edge-related phenomena could no longer be treated independently due to a strong coupling between collective core and edge pressures. A thorough understanding of processes that occur in the edge region is therefore vital.

A generalised picture of overall research programmes of present day tokamaks concerning both reactor design and plasma scenarios is presented in figure 1.9. Research topics from a reactor design include fuelling (gas, pellet, beam), heating, current drive, magnetic coils systems and exhaust systems (control systems, cooling circuits). Also, from a plasma scenario development, the exhaust of particles (He, impurity influx) and power (neutrons, photons, plasma), heat loads to plasma facing components and impurity influx all influence plasma edge conditions and are therefore pertinent issues which parallel research on confinement and core plasma condition studies.

While the power exhaust in both neutron and photon channels is spread over the whole vessel surface area, this is not the case for plasma exhaust which is found to be localised in narrow regions. A crucial problem of realising next step devices such as ITER is to handle the energy flux into the Scrape-Off-Layer (SOL) and control the energy flux onto the deposition areas. A requirement on the first wall is that it must withstand and exhaust the α particle heating power and helium-ash must be removed

Figure 1.8: *Current research topics concerning reactor design and plasma scenario development. Exhaust issues ranging from particle and power exhaust to plasma facing components and impurity influx are crucial to the realisation of future fusion reactors.*

(pumped). Furthermore, design materials for the first wall must take into account the combined effects of numerous processes (such as erosion, ablation and sputtering which will be described later) which not only lead to fuel dilution and energy loss due to radiation from the plasma centre (within a single pulse), but also seriously affect the lifetime of wall elements, reactor reliability and cost effectiveness of fusion as a whole.

1.9.1 The plasma edge

No unique definition exists for the "plasma edge", or "plasma boundary". The region immediately inside the separatrix (to a few cms) is generally called the edge, while the low density region between the separatrix and the wall is called the scrape-off-layer (SOL). The plasma region of interest in this thesis is the entire plasma boundary region comprising the SOL as well as part of the edge of the confined plasma.

As previously mentioned, the edge plasma is a complex region providing the interface between the core and vacuum. Not only do heat and particle losses from the centre pass through the edge, but numerous processes sweep particles in the reverse direction through the edge into the core. Among the processes which have been shown to have a significant impact on the properties of both the edge and core plasma, are the processes of recycling, sputtering, along with a host of atomic and molecular reactions.

Sputtering is the removal of atoms from the surface of a solid as a result of impact by plasma ions or atoms. It gives rise to impurities which cause power to be radiated from the plasma.

Plasma ions which are lost from the core plasma often reach the plasma again. This may occur either through backscattering of ions incident on a solid surface of the vessel wall, or diffusion to the surface of the solid after becoming trapped in the lattice. This process is called recycling, and is often associated with many atomic and molecular reactions which occur in the boundary layer as the incoming hydrogen isotopes meet the energetic ions and electrons of the plasma. Further reactions also occur when impurities created by sputtering and by other plasma surface interactions enter the plasma. In most cases the dominant atomic reactions are excitation and ionisation. These lead to emission of radiation and cooling of the edge plasma. For example, considering the recycling of hydrogen isotopes from the wall, the following reactions occur:

$$\begin{array}{ll} \text{Excitation:} & \mathrm{H} + e \longrightarrow \mathrm{H}^{\star} + e \\ \text{Ionisation:} & \mathrm{H} + e \longrightarrow \mathrm{H}^{+} + 2e \\ \text{Charge exchange:} & \mathrm{H}^{+} + \mathrm{H} \longrightarrow \mathrm{H} + \mathrm{H}^{+} \end{array}$$

1.9.2 Diverted plasmas

As described in section 1.5 the fusion plasma is sustained by maintaining a power balance between power input and power losses. The power loss which is not radiated away or carried by neutrons must be carried by electrons and ions across field-lines into the SOL ultimately reaching plasma facing components. To prevent the ensuing plasma-wall interactions, limiters or divertors are used to "scrape-off" or divert particles and energy in the peripheral zones of the plasma.

An illustration of the divertor configuration is shown in figure 1.9. It is produced using an external coil carrying a current in the same direction as the core plasma current, thus producing a null point in the poloidal field (an X-point). A sink action is achieved by introducing a solid target which cuts through the flux surfaces. The sink action is due to a sheath which forms just in front of any electrically-isolated object inserted to the plasma edge, namely in this case upper and lower solid targets. As such, particles and heat which leave the plasma through diffusion across the separatrix flow along a narrow region to the divertor tiles - see green arrows in figure 1.9.

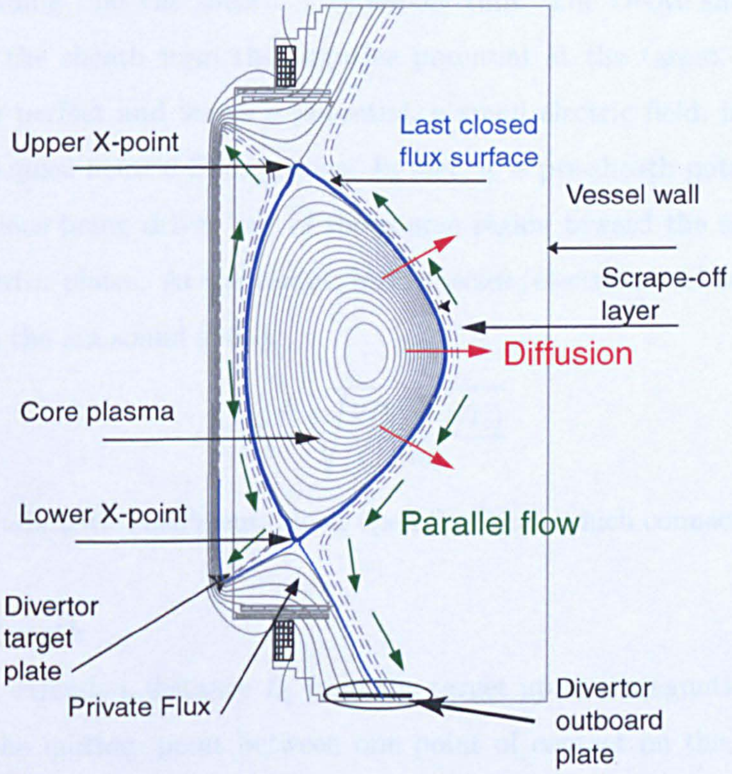

Figure 1.9: *Schematic of plasma flows in the SOL. Cross-field diffusion shown as red arrows. Parallel flow along open field lines to target is indicated by the green arrows.*

Sheath and presheaths

The formation of the sheath is a simple consequence of the large discrepancy between the random thermal velocities of ions and electrons in the plasma. The greater mobility of the electrons compared to the more massive ions:

$$\mu_e = \frac{e}{m_e v_e} >> \mu_i = \frac{Ze}{m_i v_i}, \tag{1.20}$$

means that electrons tend to leave a plasma surface ahead of the ions. This gives rise to a negative surface charge of sufficient magnitude to repel all but the highest energy electrons. A floating surface thus resides at a negative potential with respect to the plasma potential at the sheath edge. The layer of negative charge is followed by a region of positive space charge where n_i exceeds n_e and the potential drop occurs over a distance of the order of the Debye length, λ_D in the edge plasma, where

$$\lambda_D = \sqrt{\frac{\epsilon_0 k T_e}{n_e e^2}}. \tag{1.21}$$

The Debye length for typical SOL values (T_e = 20eV, n_e = 10^{19}m^{-3}) is of the order of 10 μm, meaning that the sheath is extremely thin. The Debye sheath shields the plasma inside the sheath from the negative potential at the target. This shielding is however not perfect and leaves a potential, a small electric field, in the presheath penetrates the quasi-neutral SOL plasma. In fact, it is pre-sheath potential fall which results in the ions being driven out of the source region toward the sink provided by the target divertor plates. At the target, both species (electrons and ions) have a fluid speed equal to the ion sound speed:

$$C_s = \sqrt{\frac{k\left(T_e + \gamma T_i\right)}{m_i}} \tag{1.22}$$

where γ is the adiabatic coefficient, along open field lines which connect directly to the solid surfaces.

Connection length

The presheath extends a distance $L_{\|}$ from the target up to a stagnation point, which is defined as the midway point between one point of contact on the target (say the lower divertor plate) and the next point of contact along the magnetic field line in the SOL (say the upper divertor plate). Electrons thus find themselves trapped in an electrostatic potential well between the two surfaces, and crucially, their drift velocity is much smaller compared with their parallel velocity along the field line. The safety factor q is often used in theoretical models as a proxy for the connection length since $L_{\|} \sim qR$.

1.10 The scrape-off layer

Under the assumption that there are no ionisation sources in the volume of the SOL, and that the sources are located inside the confined volume, the SOL is filled solely by a cross-field diffusion in the radial direction r, with a flux density $\Gamma_{\perp}$ such that:

$$\Gamma_\perp = -D_\perp \partial n/\partial r, \tag{1.23}$$

where $D_\perp$ is the cross-field diffusion coefficient. This is generally known as the simple SOL. In this picture, flux across the magnetic field is balanced by flows along the open field lines toward the plates. The width of the SOL is determined by the radial variation of particle density which can be derived from a simple 1D calculation based on the conservation of mass along the field line:

$$\partial_r D_\perp \partial_r n = \partial_\parallel (nc_s). \tag{1.24}$$

The outwards flux from the core is balanced by flows along the field lines. Assuming the latter to be constant, and that $\partial_\parallel(nc_s) = n/\tau_\parallel$ where $\tau_\parallel$ is the characteristic ion parallel transport time to the target, the particle density shows an exponential decay inside the SOL, such that:

$$n(r) = n(0)\exp\left(-r/\sqrt{D_\perp \tau_\parallel}\right). \tag{1.25}$$

The exponential decay length is given by the expression:

$$\lambda_n \sim \lambda \sim \sqrt{D_\perp \tau_\parallel}, \tag{1.26}$$

and is often used to first order as an approximation for the width of the SOL. Taking typical values of $D_\perp$ ~1 m^2 s^{-1}, and $\tau_\parallel$ ~ 1 ms gives a radial width for the SOL ~ 3 cm, which is much smaller than the plasma minor radius r. The high power density in the divertor, resulting from the narrowness of the SOL defines the heat load problem in the development of a fusion power plant, since there is a maximum tolerable heat flux for solid surfaces. The upper limit to what presently can be achieved in the best designs for steady-state heat transfer is 10 - 20 MW m^{-2} and, for high reliability, values of 2 - 5 MW m^{-2} are more typical. A proper understanding of the underlying mechanisms giving rise to the cross field transport, and ways of controlling the deposition of heat loads is a vital task on the route to a future fusion burning device.

1.11 Thesis outline

This thesis may be divided into two major sections. The first three chapters give an introduction to the edge plasma and various transport processes leading to important evidence for cross-field transport relevant to this study (chapter 2). A brief review of the various experimental diagnostic evidence of plasma edge turbulence during L-mode and ELM phases is also outlined and finally theoretical efforts of edge turbulence relevant to this study are presented in chapter 3. In the second section, a description of the experimental setup and introduction to the data are presented. Chapters 5 and 6 encompass all experimental results of inter-ELM filaments from both camera and Langmuir probes, with a detailed description of various analysis methods adopted for each diagnostic: chapter 5 reports on results specific to the camera, while chapter 6 those of Langmuir probes. Overall results of inter-ELM filaments are compared and contrasted with those for ELM and L-mode filaments leading to a global picture of filamentary structures during the inter-ELM period. Chapter 7 summarises the major findings of this research and outlines future work.

Chapter 2

Turbulence & Intermittency

Transport studies of heat and particles have shown that the plasma is a turbulent medium, with major fluctuations dominating a significant part of the observed transport. The turbulent transport is an issue which receives much attention in current fusion research. In this chapter, basic turbulence concepts are introduced leading to the topic which this thesis is based on, namely, the intermittent transport in terms of filamentary structures.

2.1 Transport

Transport occurs in a tokamak because there is a source of free energy in the system. When this occurs, the system relaxes toward a global equilibrium, removing the driving thermodynamic forces - the gradients - via transport. Understanding the transport properties of the plasma is therefore understanding the relation between the observed fluxes and the gradients. This is further complicated if the plasma is turbulent. Initial expectations of the level of transport which would occur in a tokamak were based on predictions for linear devices. Transport in a straight magnetic field is known as classical collisional transport.

2.1.1 Collisional transport

The most obvious source of heat/particle loss from a magnetically contained plasma is due to collisions between particles which are gyrating along adjacent field lines with frequency $\omega_c = eB/m_{i,e}$ where B is the magnetic field strength. Particles will suffer collisions with a characteristic collision time/frequency τ_{ie}/ν_{ie}, which allows them to step across the magnetic field in a random walk with a step length equal to the particle Larmor radius, $\rho \equiv v_\perp/\omega_c$ where $v_\perp$ is the perpendicular velocity. The resulting particle diffusion coefficient D^C is approximately the square of the step length:

$$D^C \sim \rho^2 \nu_{ie} \sim \rho^2/\tau_{ie}, \tag{2.1}$$

where ν_{ie} and τ_{ie} are the ion-electron collision frequency and times respectively. Note that collisions between like-particles do not produce net particle diffusion.

Since both collision time and Larmor radius of charged particles are proportional to the square root of the particle mass m, the ion particle diffusivity D_i^C should be a factor of $\sqrt{m_i/m_e}$ higher than the particle diffusivity for electrons, D_e^C. However, it is found that particle diffusivities are similar for both species, $D_i^C = D_e^C$, since any difference in the particle diffusivities generates a radial electric field which slows the diffusion of the ions.

While the classical picture may be sufficient to describe the diffusion processes which occur in a simplified homogeneous and stationary straight field-line configuration, it does not apply for toroidal tokamak geometry. This is because transport processes in the classical picture are by definition insensitive to the gross structure of the magnetic field: they are spatially localised, that is, the classical fluxes are driven by forces at approximately the same spatial location. This in turn arises because the plasma in this regime is collision-dominated to the extent that the mean free path is much shorter than the gradient length in the direction of the magnetic field.

It was shown in the early 1960s that global geometric characteristics of the confining machine have a strong influence on the transport. The predictions of classical theory could not be tested since end losses from early linear machines were so large that scalings could not be determined for a tokamak.

2.1.2 Neoclassical transport

In toroidal devices there are other, stronger, collisional transport mechanisms which are sensitive to the magnetic field structure and arise from the friction experienced by particles as they move in the direction of the magnetic field. Indeed, as particles travel along the parallel direction, particularly in a plasma with low collisionality, they may explore most of the flux surface before suffering a collision. The theoretical efforts which emerged from these considerations are what is now known as the neoclassical theory of collisional transport. Three distinct regimes have been identified, namely the Pfirsch-Schlüter, plateau and banana regimes. The relevant regime depends crucially on the collisionality of the plasma, ν_{ei}, expressed as:

$$\nu_{ei} = \frac{4\pi n_e^2 e^4 \ln\lambda}{(2T_e)^{3/2} m_e^{1/2}}, \tag{2.2}$$

where $\ln\lambda$ is the Coulomb logarithm, and n_e, T_e, m_e, e are the electron density, temperature, mass and charge, respectively. A heuristic consideration (as was presented for the classical transport) is used to identify the magnitude of the neoclassical transport in these regimes. The dependence of the estimated diffusion coefficient, and hence transport, on collisionality is shown in figure 2.1.

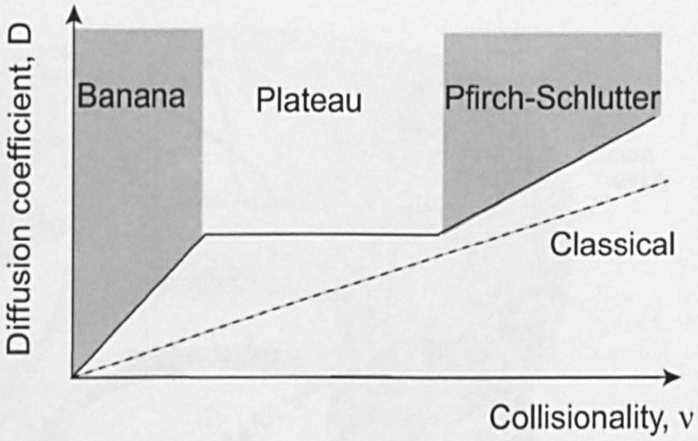

Figure 2.1: *Dependence of neoclassical diffusion coefficients on plasma collisionality.*

At low temperatures for which the plasma is collisional, a process known as Pfirsch-Schlüter diffusion occurs. This process is due to the gradient in the toroidal field which causes particles to drift vertically. Since the electrons and ions drift in opposite directions, an electric field is produced which causes an **E** × **B** particle drift, resulting in enhanced diffusion. This is only slightly enhanced over the classical diffusion coefficient. In this case, with the collision frequency given by equation (2.2), the diffusion coefficient is:

$$D_{ps}^{nc} = D^C(1 + q^2), \tag{2.3}$$

where D^C is given by equation (2.1). The additional factor of q^2 shows that the enhancement arises as a result of the toroidal geometry.

In the high temperatures of a fusion reactor, the collisionality will be lower, thus reducing the resistivity of the plasma $\mu_s \sim T_e^{-3/2}$, and hence restricting the validity of the Pfirsch-Schlüter diffusion regime. The requirement on collisionality in this new regime is that collisions are sufficiently infrequent that the trapping of particles in the region of lower magnetic field becomes important. This occurs when the collision frequency is less than the trapped particle bounce frequency.

Trapped particles (a fraction of the total number of particles $\sim \sqrt{2\epsilon}$), dominate the transport in this regime, and execute banana-like orbits as shown by the solid black lines in figure 2.2, whose half widths can be approximated as:

$$\rho_b = q\rho/\epsilon^{1/2}. \tag{2.4}$$

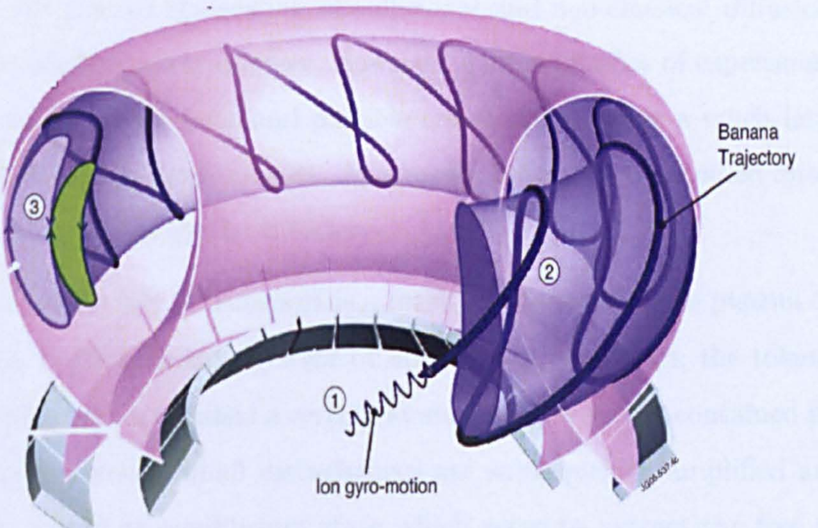

Figure 2.2: *In the banana regime of the neo-classical transport theory, trapped particles follow banana orbits. The constant detrapping and retrapping of these particles produces a random walk with a large step length which enhances particle and heat transport. The net flow between two adjacent banana orbits also gives rise to a current which dominates the edge transport and overall stability of the plasma.*

Since the factor $q/\epsilon^{1/2}$ is generally greater than unity, it follows that trapped particles have a larger step length than un-trapped particles. Consequently, the collisional detrapping and retrapping of these particles produces a random walk with a larger step length, which considerably enhances the particle and heat transport. Diffusion coefficient D^{nc}_{ban} is expressed as:

$$D^{nc}_{ban} = D^{C} q^{2} \epsilon^{-3/2}. \tag{2.5}$$

This results in typical values of 10^{-2} - 10^{-1} ms^{-1}. Typical ion heat diffusivities are expected close to 1 ms^{-1} .

Finally, the plasma is said to be in the *plateau* regime when the transport is observed to be independent of collisionality. The regime links the Pfirsch-Schlüter and *banana* regimes, and allows both transport descriptions to be applied to the plasma.

2.1.3 Anomalous Transport

With an established neoclassical theory, transport of heat and particles was long regarded in the tokamak community as an effective diffusion process, and the main focus was toward the scaling of collisional and neo-classical diffusion coefficients with respect to plasma parameters. However, a large number of experimental measurements soon revealed that heat and particle transport occur at a much larger rate than predicted by neoclassical theories. As a result, transport was coined *anomalous*, i.e. larger than values given by the theories.

The high levels of transport is a result of the state of the plasma equilibrium. Much like the Earth's climate system or an inverted pendulum, the tokamak equilibrium is unstable, and there exists a certain amount of free energy contained in plasma pressure, flow and current. Small disturbances are subsequently amplified and exist as fluctuations about the equilibrium state which serve to extract the free energy. Transport events are then often manifested through fluctuations in n, T, B and the electrostatic potential Φ which are much higher then the thermal levels.

Anomalous transport was attributed to microscopic turbulence as early as 1949 by Bohm [14] who suggested that oscillating electric and magnetic fields due to plasma instabilities can substantially increase diffusion. In the spirit of the previous subsections, a random-walk estimate of this anomalous diffusion is now estimated from electrostatic turbulence fluctuations alone. Indeed, electrostatic turbulence gives rise to fluctuating electric fields $\mathbf{E} = -\nabla\phi$ which affect the motion of electrons. The gyro-motion is not much affected but superimposed on it is a drift:

$$\mathbf{v}_E = \frac{\mathbf{E} \times \mathbf{B}}{B^2} \tag{2.6}$$

across the magnetic field. Thus, the turbulent electric field produces a random drift velocity of electron guiding centres. The random walk estimate for the electron particle diffusion coefficient perpendicular to **B** is:

$$D_e = (\Delta x)^2/\tau \tag{2.7}$$

where τ is the time per step in the random walk, and

$$\frac{\Delta x}{\tau} = v_E = -\frac{\nabla\phi}{B} \sim \frac{\phi}{\Delta x B} \tag{2.8}$$

is the velocity. Taking the step size $\Delta x \sim \lambda$ to be of the order of the perpendicular turbulent wavelength, it can be shown that transport coefficients are still about order of magnitude higher than neoclassical estimates.

2.2 Turbulence

The term turbulence first appeared in fluid mechanics and was later generalised for solids and plasmas. It occurs in many natural systems and remains an unsolved problem of classical mechanics. Generally, turbulence is the state of physical systems whose macroscopic description is characterised by large degrees of freedom deviated far from equilibrium. Crucially, turbulence is a state with a "similar physics" occurring on many spatial and temporal scales.

Studies of turbulence in magnetised plasmas has been driven by the need to understand the anomalously high loss of particles and energy across the confining magnetic field. Unfortunately, the task of diagnosing turbulence in plasmas is at a disadvantage since the many-body plasma has not only all the complications of the neutral fluid, but also has much richer behaviour because of the presence of electromagnetic forces.

Fortunately, the magnetically-confined plasma can exist in a quasi-stationary turbulent state with effective transport coefficients larger than neo-classical values, provided external driving sources are kept fixed. This is known as fully developed or saturated turbulence. Even more remarkable (as will be shown later in section 2.4) is the fact that plasma turbulence is suppressed with increasing external driving sources.

The Navier-Stokes equations governing fluid turbulence have been known since 1845 [15], and their extension to MHD turbulence has been achieved [16, 17]. Many different models have been proposed, some of which are capable of describing turbulence successfully under specific conditions. One such example is the work by Reynolds who showed that an obstacle (such as a pipe) of size L placed into a fluid moving with velocity V provides for a turbulent wake if the Reynolds number $R_e = VL/\nu$ is large, where ν is the kinematic viscosity of the fluid.

Turbulent eddies

Turbulence is usually visualised as consisting of a sea of eddies of different sizes: fluid structures of variable sizes continuously stretching, twisting and spinning under the influence of their associated velocity fields. The angular velocity characterising each vortex is what is better known as vorticity ω where $\omega = \nabla \times u$ and u is the velocity. A schematic of these fluid elements are shown in figure 2.3.

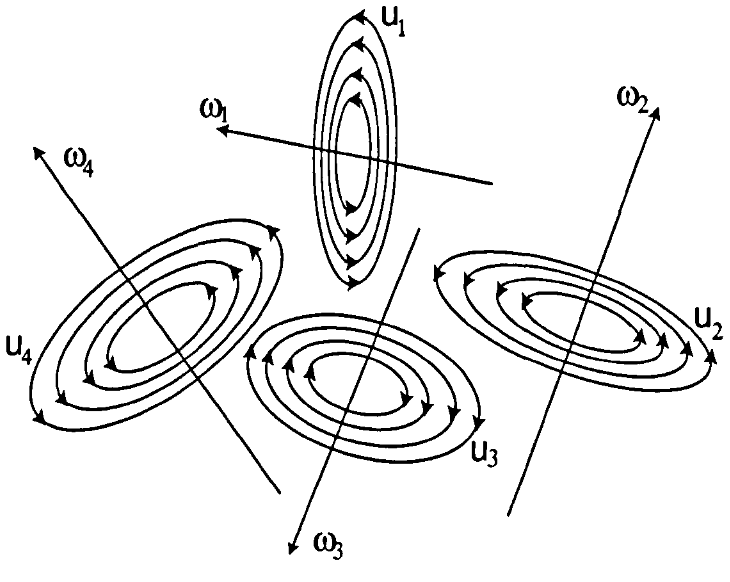

Figure 2.3: *Turbulence is often visualised as consisting of a sea of eddies: fluid-like structures of variable sizes spinning and twisting under the influence of their associated velocity fields.*

Spatial and temporal scales of plasma turbulence

The complexity in the study of tokamak electromagnetic turbulence arises due to the wide range of spatial and temporal scales of the turbulent spectra. Generally, the turbulent spectra can be classed into three categories depending on the wavelengths of the fluctuations. A schematic of this classification is shown in figure 2.4 where the largest are the macro-scales which are characterised by wavelengths of the order of the system size ~ 1 m, and time-scales approximating the energy confinement time ($\tau_E \sim 0.1$–10 s). The meso-scales are the intermediate fluctuations characterized by wavelengths between the ion Larmor radius ($\rho_i \sim 1$ mm) and the system size while time-scales between the Alfvén time $\tau_A \sim 1$–10 ns and the confinement time. Finally, the smallest scales, termed microscales, are characterised by $\rho_i \ll 1$ with frequencies $\omega \gg 500$ kHz.

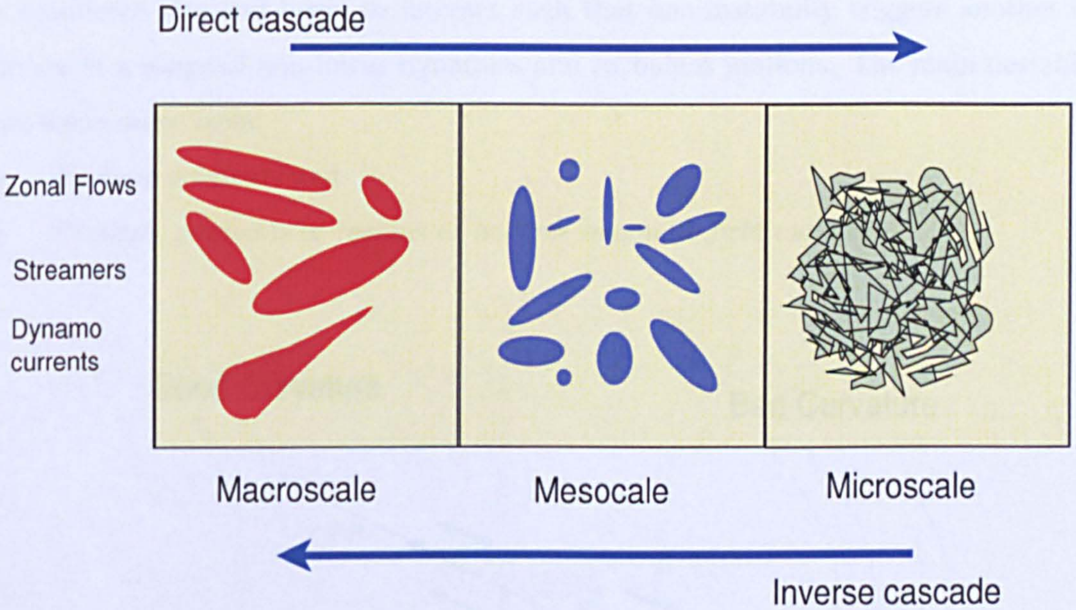

Figure 2.4: *Different turbulence scales in a plasma.*

Energy cascades

These dynamical processes are thought to be mediated by interactions involving direct (i.e., low to high wave number/frequency) and inverse (high to low wave number/frequency) spectral energy cascades – ideas first postulated by Richardson and Kolmogorov[15]. These are based on the idea that turbulence consists of large-scale eddies breaking up into smaller structures which in turn break up into even smaller structures in a cascade. Energy is injected into the system at the macro-scale range and cascades down the micro-scales, at which point it is dissipated as heat due to viscosity.

2.3 Plasma instabilities - turbulence starting point

The strong gradients in density and temperature contained in the tokamak plasma provide sources of free energy which drive a wide range of instabilities which in turn provide a starting point for turbulence. Here, an instability is a plasma motion (transport event) which decreases the free energy and brings the plasma closer to a quasi thermodynamic equilibrium. The strongest instabilities are those described by the MHD fluid model of the plasma, and can be classified according to the types of free energy available to drive them. Small linear perturbations to the equilibrium grow to a significant size and begin to interact such that one instability triggers another and produces a range of non-linear dynamics and turbulent motions. The main destabilising forces arise from:

- *Current gradients* and
- *Pressure gradients* in regions of *adverse magnetic field curvature.*

Figure 2.5: *Side view of a torus showing good (inboard) and bad (outboard) regions of curvature.*

The resulting instabilities are characterised by an infinite spectrum of possible modes, each being characterised by a typical range of mode numbers. In the case of a circular, large aspect ratio tokamak the mode variation is written as $\exp i(m\theta - n\phi - \omega t)$ where m and n are the poloidal and toroidal mode numbers.

In a tokamak the regions of good and bad curvature are on the inboard (near the centre) and outboard sides respectively. This can be seen in figure 2.5 which shows a side view of a torus where a field line is indicated by the solid black line. The pressure gradient ∇p is always directed towards the plasma core, whilst the curvature vector is always in the direction of major radius R. A perturbation to field-lines in a *good* curvature region results in compression of the magnetic field, an increase in field strength and hence a restoring force. On the other hand, in a region of *bad* curvature a perturbation results in a stretching of field-lines and a reduction in field strength. This reduces the restoring force on the plasma, resulting in further perturbation and an instability. Next, some plasma instabilities related to discussions later in this thesis are briefly presented.

2.3.1 Ballooning modes

Ballooning instabilities are a class of MHD instability (an interchange mode) which are driven by the combination of a pressure gradient and adverse magnetic field curvature [4, 18]. These macro-scale modes owe their name to their tendency to have large amplitudes in the outboard plasma where the destabilising pressure gradients originate. The eigenmode structure of a simulated n=32 ballooning mode is shown in figure 2.6.

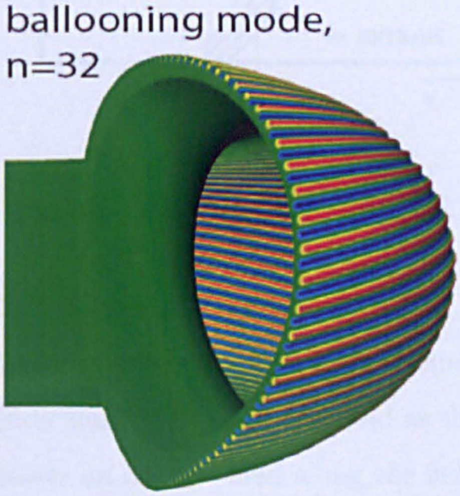

Figure 2.6: *Mode structure of a n=32 ballooning mode. Figure adapted from [19].*

2.3.2 Drift waves

Drift waves are a particularly important class of plasma instability which occur in the micro-scale range and have been invoked as the source of plasma turbulence responsible for anomalous transport. An overview can be found in [21, 22, 23] and references therein. Drift instabilities are a class of electrostatic waves in which the $\mathbf{E} \times \mathbf{B}$ drift moves plasma radially. They are the basic low-frequency oscillations of a magnetically confined plasma, and result from tapping the free energy of the density and/or temperature gradients. The drift instability is called "universal" because it is driven by the gradient of the background density profile, which is inevitably present in every confined plasma.

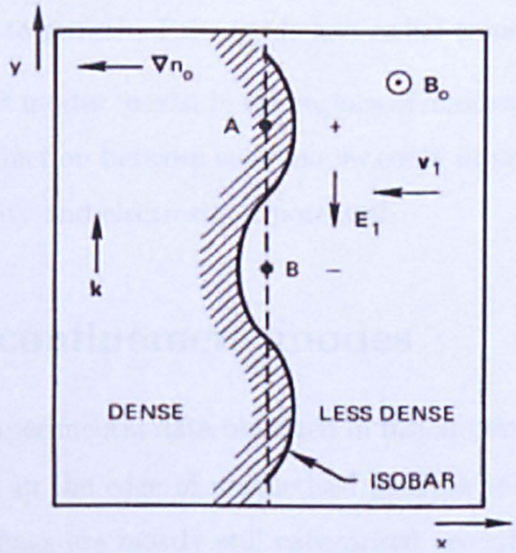

Figure 2.7: *Electron drift wave [21].*

The simplest type of drift wave is the electrostatic drift wave. This wave can be illustrated by considering a slab of plasma in a uniform magnetic field. In the presence of a density gradient perpendicular to the magnetic field as shown in figure 2.7, an ion density perturbation will create an electric field along the field lines. Because of their low inertia, electrons will then flow parallel to the magnetic field in order to establish a force balance in this direction such that:

$$mn\frac{\partial V_{\parallel}}{\partial t} = enE_{\parallel} - \nabla_{\parallel} P_e, \tag{2.9}$$

where P_e is the electron pressure, E is the electric field, and $||$ denotes the component in the direction of the magnetic field. Linearising equation (2.9) leads to a relation between the perturbed electron density $\tilde{n}_e$, and electrostatic potential ϕ:

$$\frac{\tilde{n}_e}{n_e} = \frac{e\phi}{T_e}, \tag{2.10}$$

where n_e and T_e are the equilibrium density and temperature respectively. The electrostatic potential, and associated $\mathbf{E} \times \mathbf{B}$ drift enhances the density in the less dense regions and reduces it in the more dense regions, causing the density and potential perturbations to oscillate in time. The resulting wave propagates perpendicular to B and ∇n, and no radial transport occurs when ϕ and n are out of phase. This situation is altered with some form of dissipation which could be in the form of resistivity. This would have an effect on the time response of the electrons and result in a phase shift between ϕ and n leading to growth of the mode and radial transport.

Both interchange and drift modes coexist in the regions of maximum density gradient in the low B-field side. Distinction between such modes could in principle be determined from phase shifts of density and electrostatic potential.

2.4 Tokamak confinement modes

Despite a wealth of experimental data obtained in fusion devices, understanding of turbulence and transport in the edge of magnetised plasmas is still limited. For this reason, experimental findings are mostly still categorised according to their empirical signatures into confinement "modes" - operating regimes which are characterised by sudden transitions in the overall turbulence level, and routinely observed across different machines. The simplest regime is called Ohmic because energy is injected into the plasma by driving a current, as described in section 1.7.4.

Fig. 2.8 illustrates qualitatively the characteristic pressure profiles of two other regimes in addition to the Ohmic regime. The L-mode ("low" confinement mode) is the most common mode of tokamak operation when auxiliary heating is applied. The inner part of the discharge is generally affected by periodic, crash-like turbulent rearrangements of the temperature, density and current profiles ("sawtooth" crashes). The H-mode ("high" confinement mode), which was first observed in the divertor of

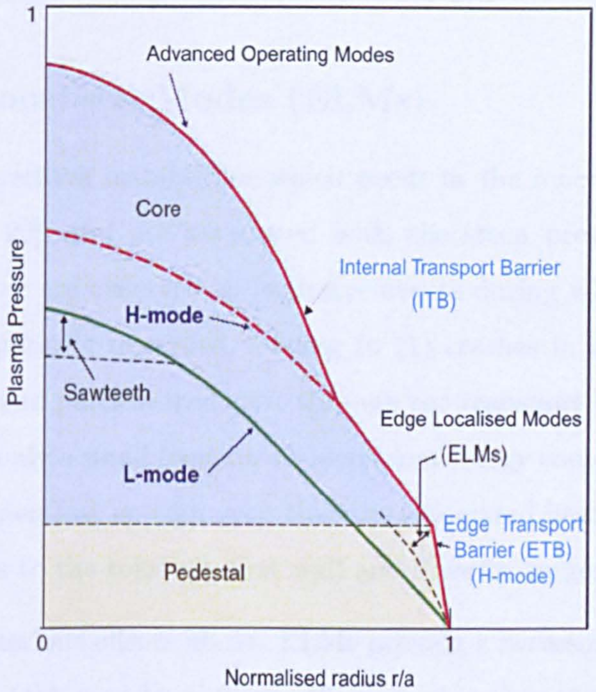

Figure 2.8: *Typical pressure profiles for different confinement modes in a tokamak.*

the ASDEX tokamak [24, 25] and later in other divertor and some limiter tokamaks, is characterised by an improvement of the energy confinement time by a factor of about 2 compared to the standard L-mode. Empirically it has been found that the transition to H-mode takes place above a certain threshold of the heating power.

The improved confinement of the H-mode regime is due to the build up of a transport barrier a short distance away from the LCFS. As shown in Fig. 2.8, this occurs over a narrow region in which the pressure profile is raised beyond the standard L-mode level to form a *pedestal*. The top of the sharp pressure rise is often referred to as the *height* of the pedestal. The width of the pedestal, known also as the *width* of the transport barrier, is an equally important parameter used in investigation of transport processes in the edge.

Crucially, transport coefficients of cross field diffusion during H-mode and advanced opertaing modes indicate a strong reduction in anomalous transport, particularly turbulence-driven radial transport. However, above a critical pressure gradient MHD plasma instabilities develop which lead to so-called *edge localised modes* (ELMs). A brief description of this instability is presented in the following subsection.

2.4.1 Edge Localised Modes (ELMs)

ELMs are repetitive instabilities which occur in the macro-scale in many machines [26, 27, 28, 29], and are associated with the steep pressure gradient of the H-mode profile. They are observed as explosive events during which the edge plasma confinement is temporarily degraded, leading to (1) crashes in the pedestal pressure and (2) fast energy and particle transport through the transport barrier into the SOL. Crucially, although only a small fraction of the plasma energy content, the ELM-related energy loss can happen fast enough such that the associated heat loads may pose significant erosion risks to the tokamak first wall and divertor target plates.

Despite the deleterious effects above, ELMs provide a necessary relaxation process of the H-mode edge transport barrier, expelling a proportion of an undesirable impurity population which would otherwise accumulate in the core degrading the fusion fuel and enhancing radiative energy loss.

Three main types of ELM are found. Type-I ELMs, or giant ELMs, are associated with the largest ELM energy and particle losses, and a repetition frequency which increases with heating power. Type-II ELMs and type-III ELMs are smaller events. ELM stability studies have shown that combining peeling and ballooning modes gives a region of stability in the so-called $s-\alpha$ diagram [30, 31], where α and s are quantities relating to the pressure gradient and current density respectively. Here, the quantity s is the magnetic shear, which is expressed as:

$$s = 2\left(1 - \frac{J_{LCFS}}{\langle J \rangle}\right),$$

where J_{LCFS} is the current density on the outermost flux surface, and $\langle J \rangle$ is the average plasma current density in the plasma. Similarly, α is given by:

$$\alpha = -\frac{2\mu_0 q^2}{\epsilon B_0^2}\frac{dP}{dr},$$

where r is the radial coordinate of the magnetic surface, B_0 the vacuum magnetic field at the axis. A typical diagram is shown below in figure 2.9. Different trajectories for each type of ELM (types I, II and III) in this parameter space are shown.

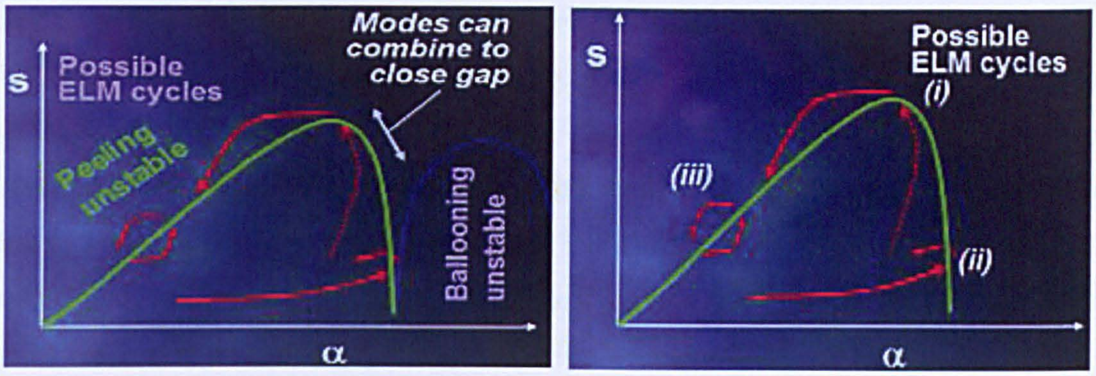

Figure 2.9: *Typical $s-\alpha$ diagram showing the stability boundaries of the edge pedestal, based on coupled peeling-ballooning MHD modes. Three distinct scenarios are indicated by (i), (ii) and (iii) and are related to ELM type.*

- ***Case (i)*** The high pressure and current density case is denoted by the letter (i). In this case, both peeling and ballooning mode stability criteria are exceeded and leads to a violent type-I ELM.
- ***Case (ii)*** In this case, the pressure gradient is sufficiently high to destabilise a ballooning mode while the peeling mode remains stable due to a low current density. The triggered ballooning mode may subsequently give rise to a small type-II ELM. Furthermore, the increased transport may drop the pressure gradient to below the critical value and stabilise the mode without giving rise to an ELM.
- ***Case (iii)*** If the pressure gradient is low and the current density is sufficiently high, the peeling mode alone could be triggered. These modes have an extremely small radial extent leading to small type-III ELMs.

The burst-like energy release due to the largest type-I ELMs is of no great concern in present day machines, but extrapolation to future devices (e.g. ITER where n_{ped} $=8 \times 10^{19}\text{m}^{-3}$, $T_{ped}=$ 3.5keV) shows that the energy released by ELMs (which for ITER would occur over ~ 500 μs) might easily exceed the heat load limits of divertors and first walls, and lead to damage or significant reduction of the lifetime of plasma facing components [29]. In the case of ITER, a crude calculation of the power balance exemplifies the heat load problem, and presents an important issue for the long term viability of fusion as a future energy source. Assuming a fusion gain $Q_{\text{DT}} \sim 10$, and that approximately 40 MW of heating power is provided (i.e. a total of 400 MW of thermonuclear power is achieved), it is expected that $P_\alpha = 80$ MW with the remaining 320 MW to the neutrons (since $Q_{\mathrm{DT}} = 5P_\alpha/P_H$). Assuming that 50% will be radiated away to the wall area ~ 800 m^2, leaves roughly 40 MW of power to the SOL. Assuming that 2/3 will also be lost in periods between ELMs (30 MW), this leaves ELMs with 15 MW. Moreover, inner-outer power deposition assymetries also imply that heat loads could easily exceed the steady state design limits currently set to 10 MW m^{-2}.

In light of the above, a detailed description of transport events that occur in the edge is paramount in order to establish the nature of the anomalous transport and consequences for design of vessel components. Investigations should include not only the ELM instability but also periods between ELMs. These, while not as short and violent as the ELMs, are equally important due to the sustained transport during these periods. First, the context of the work of this thesis is now outlined by closely inspecting some H-mode and L-mode edge profiles from the MAST tokamak.

2.5 H-mode and L-mode edge profiles

Figure 2.10 shows typical profiles of n_e and T_e obtained from the YAG laser Thomson Scattering (TS) system on MAST [32]. The data has been obtained from six L-mode shots and eight H-mode shots.

The profiles show four distinctive regions of the plasma edge during the L-mode and H-mode periods. For the H-mode, the innermost region (i.e. -4 cm $\leq \Delta r_{LCFS} \leq$ -2 cm) shows the outer-part of the H-mode pedestal – this being the region of high temperature and density that spreads over the whole core plasma and determines the plasma performance. Around the LCFS, as indicated by the solid vertical line, is the gradient region with a barrier width of ~ 1 cm, while the L-mode is characterised by a relatively broader profile. The steep gradient region evolves slightly further past its barrier width into the hot SOL (up to 1 cm from LCFS) with increased scatter particularly for the ELMing H-mode. This region of the SOL is often referred to as the inner SOL. Beyond this region is the cold SOL where $T_e \ll 20$ eV. Crucially, the main observation is that cross-field transport is highly intermittent with fluctuations of

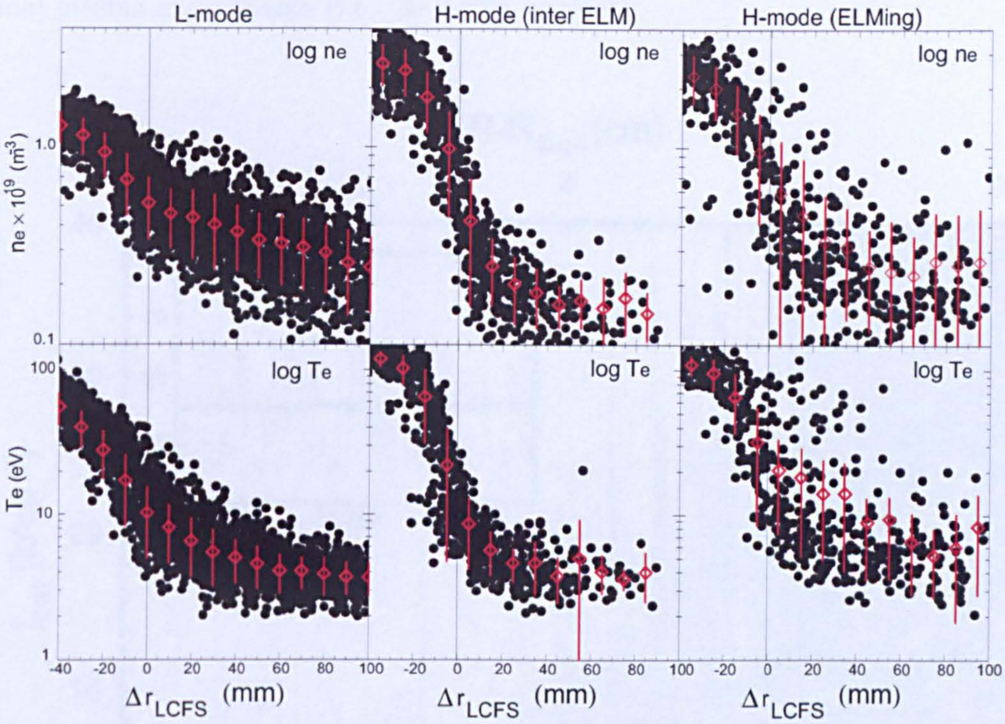

Figure 2.10: *Typical midplane profiles obtained from the edge Thomson Scattering system on MAST over six L-mode shots and eight H-mode shots. The position of the LCFS, indicated by the solid line, is taken from the EFIT reconstruction; in the case of the ElMing data, the reconstruction prior to the ELM event is taken. Averages shown in red are obtained by binning data to 10 mm.*

density and temperature observed as far out as 10 cm from the LCFS in both L-mode and H-mode periods. The profiles of n_e and T_e indicate that in addition to a diffusive background, spatially-localised and time-varying coherent events also contribute to this transport. In the next few subsections further evidence for the non-diffusive nature of the transport is presented from different tokamaks using a variety of diagnostics.

2.6 Langmuir probe fluctuations

Another commonly-used approach for detection of turbulent fluctuations is to view the raw signals from Langmuir probes [33, 34, 35, 36]. These are the most basic tool for plasma turbulence studies. They are relatively easy to design, and have excellent spatial resolution which is determined by the probe tip and the accuracy of its positioning within the plasma. However, one limitation is that they cannot withstand very high fluxes of particles and heat; their application is therefore limited to the edge region in toroidal plasma experiments (i.e. the LCFS at best).

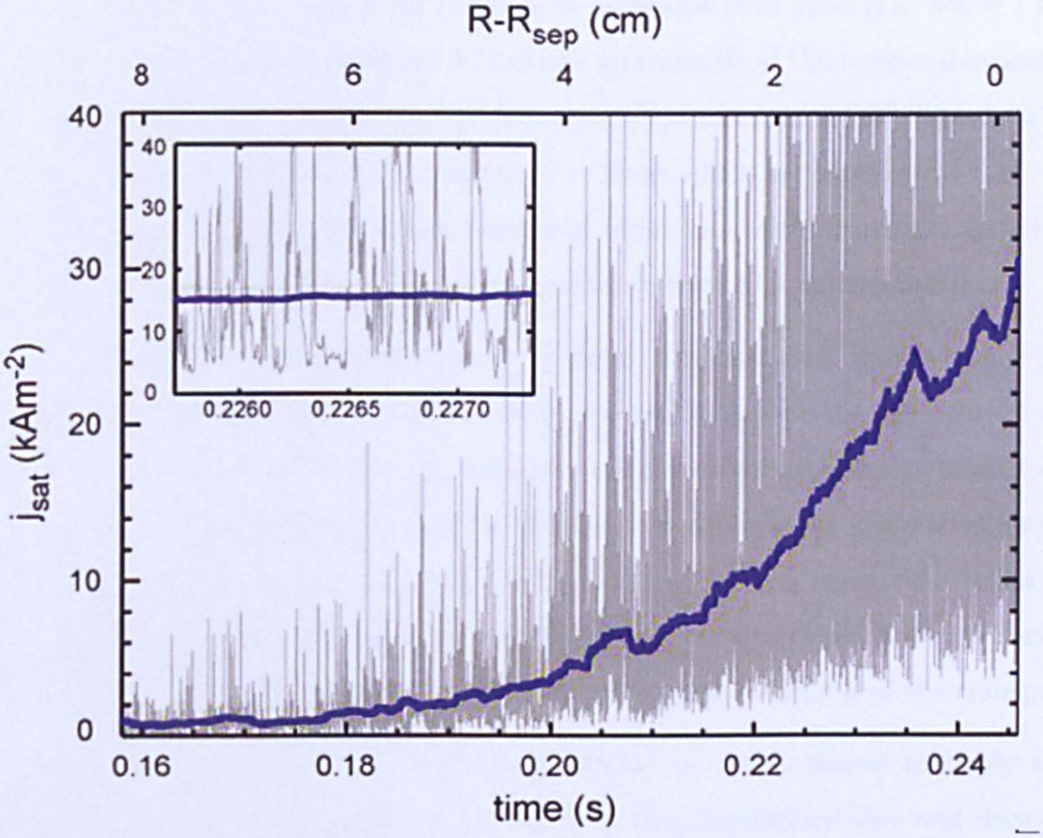

Figure 2.11: *Turbulent fluctuations shown on the raw signal of the ion saturation current density measured at the outboard midplane SOL using the MAST reciprocating Langmuir probe, as adapted from [38]. The time-averaged trace overlaid conceals the underlying turbulence intermittency.*

Historically, the traditional picture of a diffusive-like SOL was in fact ironically supported by Langmuir probe measurements which showed an apparently exponential decay in the plasma parameters across the SOL. This understanding was further supported across the community by simple interpretations of the SOL, as was shown in section 1.10, where n_e was shown to have simple exponential fall-offs. Now, a different view based on the fluctuation component is drawn from the same data. An example is shown in figure 2.11 where the ion saturation current density (J_{SAT}) from the MAST reciprocating Langmuir probe is plotted as functions of time (lower axis) and distance (top axis) from the LCFS during L-mode. It follows that typical averaging procedures of the data, as shown by the super-imposed blue line, do indeed show an exponential fall-off from beyond the LCFS. However it is also evident that applying an averaging procedure hides the overall large scatter in the underlying data which is highly fluctuating with a significant component dominant even close (i.e. below 1 cm) to the separatrix. The inset in figure 2.11 shows an example of the temporal evolution of the data obtained at a fixed distance Δr_{LCFS}= 2 cm from the LCFS. The data are composed of a series of peaks with a width of $\sim$ 20 μs which are separated by 40 – 60 μs. These peaks constitute the bursty behaviour of the cross-field transport, for which the amplitudes are much higher than the standard deviation of the fluctuations.

These observations, along with those from figure 2.10, not only questions the traditional picture of a simple diffusive-like SOL, but also questions the relevance of any mean-value based model of cross-field transport. The cross-field transport of heat and particles has been represented in many leading edge fluid codes by perpendicular diffusivities; clearly, it is ill-motivated to represent a signal with its mean value when the fluctuating part is comparable, if not larger than the mean value itself. A detailed study of these fluctuations is therefore essential for a proper understanding of the transport.

In this thesis, the use of the word "intermittent" is simply meant to imply that transport is generated in a sequence of randomly time-distributed rise and decay of burst-like events. Evidence for this is manifested in the experimental data of figures 2.10 and 2.11 which show that the fluxes at the plasma edge are not stationary, but rather, exhibit fluctuations and that the energy and particle losses take place in narrow randomly-distributed time intervals. A more rigorous statistical definition has been adopted in the community and will briefly be outlined in the following section.

2.6.1 Level of intermittency

In order to gain a better understanding of the properties of the underlying transport, various statistical methods have been applied to signals from edge diagnostics on both tokamaks [39, 40, 41, 42, 43] and stellerators [44]. In particular, the probability distribution function (PDF) of signals is often evaluated. PDFs are computed by dividing the analysed signals in pre-determined amplitude bins and counting the samples of the signals in each bin. The PDFs may subsequently be normalised to their maxima in order to make comparisons between them easier.

Figure 2.12 shows on a semi-logarithmic scale an example of five PDFs of J_{SAT} collected at different radial positions from the LCFS during L-mode. It can be seen that the PDF marked in red corresponding to the innermost radial position where $\Delta r_{LCFS} \leq 1$ cm is symmetric about the mean and can be approximated to a near Gaussian. As successive PDFs are calculated as a function of distance away from the LCFS, the signals become increasingly non-Gaussian with the emergence of high positive tails. This exponential decay, as indicated by the straight line in figure 2.12 is often interpreted to be a characteristic of distributions which are "intermittent", rather than Gaussian. The reproducibility of intermittent PDFs has been confirmed from an increasing number of precise fluctuation measurements in different machines. The significance of the stretched exponential tails in the PDFs is that the probability of large-amplitude events is anomalously large.

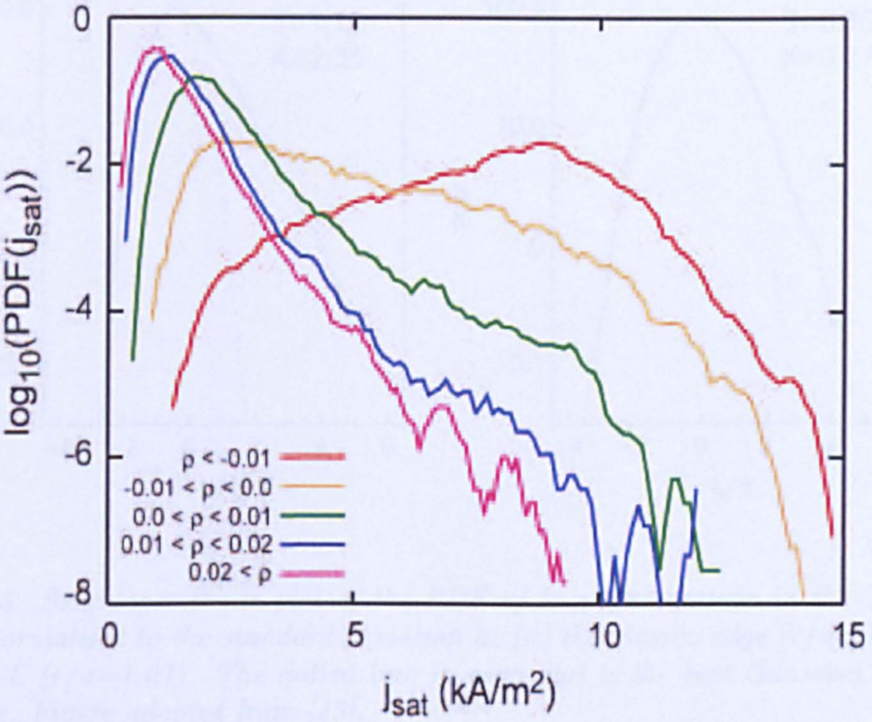

Figure 2.12: *Non-Gaussian PDFs of* J_{SAT} *values during L-mode at different radial positions in the MAST SOL, as adapted from [38]. The departure from Gaussianity is indicative of intermittent transport.*

So the question which naturally arises is not "whether the transport is intermittent", but rather "how intermittent is the transport?". The particular approach for determining the level of intermittency statistically relies on quantifying the degree of departure

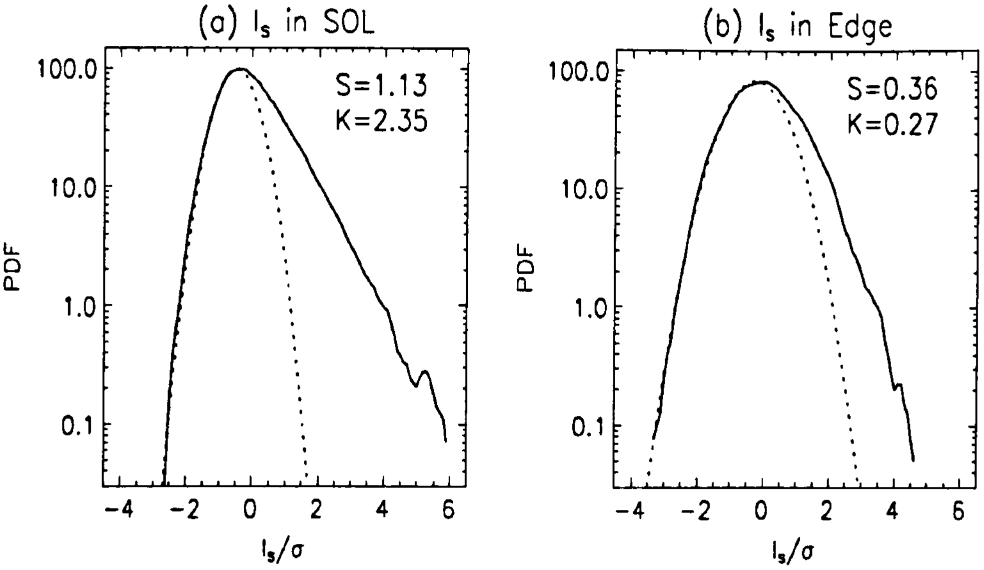

Figure 2.13: *Semi-logarithmic plot of the PDF of I_{SAT} fluctuations in the TEXTOR tokamak normalised to the standard deviation at (a) the plasma edge (r/a=0.95), and (b) the SOL (r/a=1.07). The dotted line in each plot is the best Gaussian fit to the PDF curve. Figure adapted from [45].*

of the observed distributions from the Gaussian PDF for which skewness (S) (measuring assymetry) and kurtosis (K) (measuring peakedness) characteristics are known; namely, $S = 0$ and $K = 3$ for a Gaussian distribution. For a signal I, skewness and flatness (F) parameters are defined as:

$$S = \frac{\langle (I - \langle I \rangle)^3 \rangle}{\langle (I - \langle I \rangle)^3 \rangle^{3/2}}, \tag{2.11}$$

and

$$F = \frac{\langle (I - \langle I \rangle)^4 \rangle}{\langle (I - \langle I \rangle)^2 \rangle^2}, \tag{2.12}$$

where $\langle ... \rangle$ is the mean, and F is *flatness factor* defined such that $K = F - 3$. The significance here is that (1) a distribution that is sufficiently deviated from a Gaussian will have higher values of skewness and kurtosis, and (2) a higher kurtosis value indicates that more of the variance is due to infrequent extreme deviations, as opposed to frequent modestly-sized deviations. An example (adapted from [45]) is shown in figure 2.13 where the PDFs of I_{SAT} values during L-mode are calculated at (a) the plasma edge (r/a=0.95), and (b) the SOL (r/a=1.07). The PDF in the SOL has a higher skewness and kurtosis than those calculated for the PDF at the edge.

Having shown that fluctuations in plasma quantities in the edge region contribute directly to cross-field transport (which was originally thought of as simply diffusive), it is useful to analyse the spatial structure of these fluctuations. A wealth of information in this topic was compiled during this thesis. As a prelude, some of the important results will be outlined therefore eluding to answers to some of the questions this thesis addressed.

2.7 Spatial Structure of intermittency

Assuming that the large scatter in TS profiles of figure 2.10 and intermittent events in Langmuir probe measurements (see figure 2.11) are correlated, forming the same transport event, it becomes useful to visualise these events as coherent density structures which exist near the plasma edge. The scatter in the 1D radial profiles afforded by the TS system suggests a radial motion, while the non-stationary peaks in I_{SAT} signals imply a toroidal motion at the midplane. Combining these two observations, a picture starts to form: the transport events can be thought of as spatially-localised structures in the toroidal direction that rotate with the spinning plasma and drift by some unknown mechanism outwards in the direction of the major radius. Indeed, the interpretation of I_{SAT} peaks as localised structures rotating with the plasma past fixed Langmuir probe heads was originally supported by observations drawn in [46] where it was shown by these authors that the separation between I_{SAT} peaks decreases as the toroidal velocity of the plasma increases.

The interpretation described above has now been widely accepted and constitutes a major advance in our understanding of anomalous cross-field transport. Studies have focused on the spatio-temporal evolution of the density structures from formation to decay. The evolution can generally be categorised into three distinct phases: a generation and growth phase, a saturation and detachment phase which is finally followed by a propagation and exhaust phase. Transport starts with a growth stage where it is assumed that an underlying instability in the micro-scale range leads to the formation of small perturbations in pedestal quantities which grow initially around the plasma pedestal region and remain connected to the plasma edge. This phase is then followed by a saturation phase where fully-formed coherent structures in the macro-scale can be seen at the periphery and detach from the main plasma by some magnetic reconnection process. Once detached, the structures are driven by some mechanism propagating into the SOL while draining energy until they decay.

In order to set the research of this thesis into context, examples of experimental evidence on the spatial structure and dynamics of intermittent transport gathered from different edge diagnostics will be outlined briefly. Thomson scattering, gas puff imaging, beam emission spectroscopy and infrared thermography have all been used to probe the cross-field transport. Despite numerous experimental investigations, most of the data are concentrated on the propagation and exhaust stage, while evidence for the generation, growth and detachment are far less frequent.

2.7.1 Thomson scattering (TS)

While the n_e and T_e profiles presented in figure 2.10 served to demonstrate the turbulent nature of the SOL fluctuations, the data does not capture the fast dynamics of these events. However, the multi-time point edge Nd-YAG TS system on MAST can be used to explore the fast dynamics since each laser can be fired independently of others such that their relative timings can be as little as 1 μs between them [47]. This was first performed in [48] where four independent electron density and temperature radial profiles were obtained during the rise time of a single ELM. An example is shown in figure 2.14.

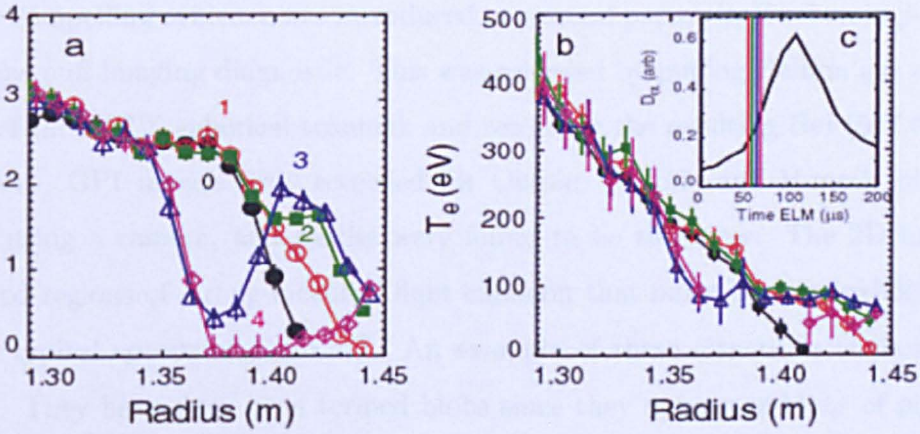

Figure 2.14: *Time evolution of the (a) edge density and (b) temperature profiles for a single ELM. (c) (inset) The target D_α signal indicating the time of the density profile relative to the ELM. Figure adapted from [49]*

Before the ELM, the typical steep H-mode gradient is observed (solid filled circle). The subsequent density profile (open red circles) shows the formation of an outboard tail. The corresponding electron temperature is ~ 80 eV, which is eight times hotter than the SOL (~ 2–10 eV) but not as hot as the pedestal (~ 150 eV). The next density profile (solid black squares) obtained 5 μs later shows the density perturbation having expanded radially by ~ 2 cm (corresponding to a radial expansion velocity of

4 km s^{-1}) while remaining connected to the mid-plane plasma edge. Further proof for this observation (i.e, that the density perturbation has not detached) comes from the associated electron temperature in this tail being still $\sim$ 80 eV – i.e no energy loss observed. The third density profile (open triangles) shows a sudden change: the density perturbation detaches from the mid-plane plasma leaving a depression (hole) in the profile. This detachment process occurs rapidly on sub $5\mu s$ timescales. Although the structure appears to be fully detached at the midplane, the associated electron temperature in this detached phase is still $\sim$ 80 eV. This implies that (1) the coherent structure is indeed an elongated structure that is still attached to the plasma elsewhere and (2) that the exhaust of energy only occurs once the plasma has fully detached. Further evidence for the existence of density structures outside the LCFS using the Thomson scattering diagnostic can also be found in [49, 50, 51, 52].

2.7.2 Gas Puff Imaging (GPI)

Further compelling evidence was introduced in seminal papers by Zweben in [53, 54] using the gas puff imaging diagnostic. This was achieved by puffing Helium gas at the periphery of the NSTX spherical tokamak and recording the resulting HeI (587.6 nm) line emission. GPI images were recorded for Ohmic, L-mode and H-mode plasma conditions using a camera, and results were found to be the same. The 2D images often showed regions of strong localised light emission that move both poloidally and radially at typical speeds of 1 km s^{-1}. An example of these structures is shown in figure 2.15. They have since been termed blobs since they appear as blobs of plasma which leave the edge.

The main advantage of this diagnostic method is that unlike the 1D profiles afforded by the Thomson scattering system or single point Langmuir probe measurements, a large number of spatial points can be sampled in two dimensions. This is done rapidly, simultaneously using discrete detectors or fast cameras. However, the main drawback is the complexity of the atomic physics of the line emission which depends non-linearly on the electron density and electron temperature. This means that an independent measurement of either n_e or T_e is required in order to directly estimate the actual density or temperature fluctuation level.

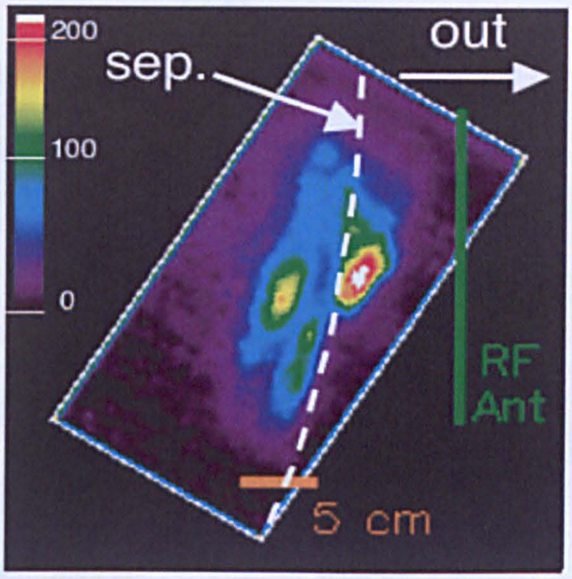

Figure 2.15: *Two dimensional structure of edge turbulence perpendicular to the magnetic field in the Alcator C-mod tokamak, as measured by the GPI diagnostic near the outer midplane separatrix. Shown is the single of the HeI (587.6 nm) light emission in NSTX viewed by the PSI camera with an exposure of 10 μs. The 160 × 80 pixel PSI camera is indicated by the white rectangle covers an area ≈ 32 cm × 16 cm in the poloidal vs radial plane. The gas manifold is located 3 cm radially outside the radial shadow of the RF antenna. The intensity scale is indicated by the color chart indicated at the top left, and the magnetic separatrix is shown by the white dashed line. Figure corresponds to Figure 2 as adapted from [54]*

2.7.3 Beam emission spectroscopy (BES)

The radiation due to the interaction of the neutral beam heating particles with plasma electrons and ions is used to derive local density and its fluctuations in the diagnostic method known as beam emission spectroscopy (BES) [55].

Shown in figure 2.16 are various frames from the BES diagnostic on the DIII-D tokamak [56] which reveals the ELM as a density structure appearing near the LCFS and moving upward in the poloidal and radial directions. The LCFS is indicated by the black solid line. As time progresses from the onset of the ELM marked at time t_0, a plasma ejection (marked with a white circle) produces a localised density perturbation near the separatrix. Its evolution is followed in subsequent frames at various time intervals from t_0, namely at t_0 +3, 7, 14, 16 μs in figures 2.16 (b, c, d, e) respectively. The density structure is seen to move radially at 8 km s^{-1}. Figure 2.16 corresponds to

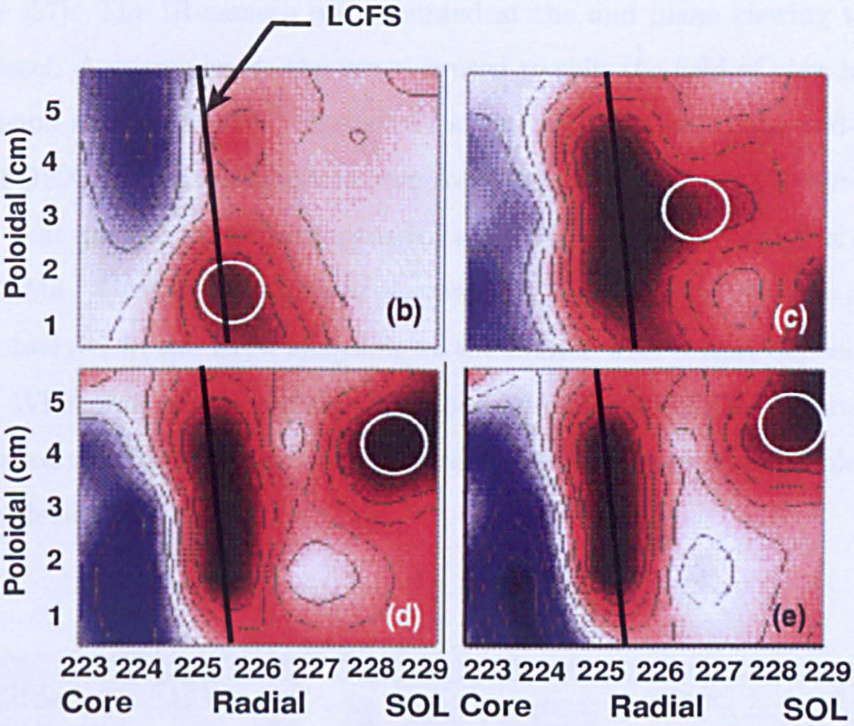

Figure 2.16: *Frames (b,c,d,e) from the BES DIII-D tokamak showing 2D density plots which are taken every 1 μs. The type-I ELM starts at* t_0 *and the frames are taken at key times thereafter to illustrate the propagation of density structures associated with the ELM. Radial and poloidal motions can clearly be seen.*

figure 7 as adapted from [56].

So far, experimental evidence presented in previous sections has demonstrated that intermittency in I_{SAT} signals, which were long ignored by averaging procedures, is in fact due to coherent blobby-like structures in pedestal parameters that exist in the plasma periphery and contribute directly to cross-field transport. Due to increasing concern that the density structures could reach the first wall due to their radial propagation, infrared thermography has been used in some machines in order to evaluate the resulting heat flux to plasma facing components. It is the purpose of the next section to describe briefly the thermographic measurements, but also shed more light on the spatial structure of the blobs - namely their distinct filamentary nature.

2.7.4 Infrared thermography (IR)

This was first performed on the ASDEX Upgrade tokamak where measurements using the high time resolution of heat deposition to non-divertor in-vessel components were made [57]. The IR-camera was mounted at the mid plane viewing tangentially into the vessel. A mirror inside the vessel is used to split the field of view between the ICRH antenna and the limiter. Figure 2.17 shows snaphots of (a) the mid-plane view into the ASDEX Upgrade tokamak as seen from the position of the IR camera, (b) the calculated heat flux during an early phase of an ELM, and (c) the heat flux recorded in between ELMs. A poloidally-localised narrow event on the scale of a few centimetres is clearly observed in the ELM snapshot at the limiter with a heat deposition of 4–8 MW m^{-2}. While still in the tolerable heat load range for an ITER-like tungsten wall, the heat deposition from localised blobby structures is a serious issue problem for next step fusion devices.

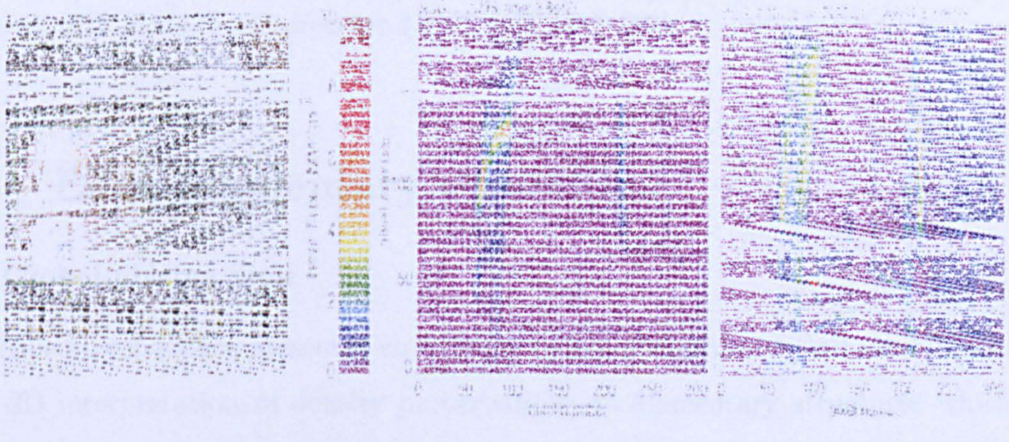

Figure 2.17: *Shown are: midplane view of the ASDEX Upgrade tokamak (far left), the calculated heat flux to in-vessel components of ASDEX-Upgrade during an early phase of an ELM (middle plot), and an inter-ELM phases (far right) [57].*

The experimental evidence presented thus far, whether 1D or 2D, has been centred on the mid-plane region of the plasma. However, similar to first-wall measurements, infrared thermography was used in the divertor region of tokamak plasmas in order to assess heat loads at the targets. Measurements revealed the existence of spatially localised heat depositions. An example is shown in figure 2.18 where heat flux measurements at the lower divertor of the MAST tokamak [58, 59] reveals several toroidal displaced stripes, in addition to the axisymmetric strike line. This characteristic spiral-like footprint was interpreted as a direct signature of the mid-plane density perturbations previously described. Spiral-like patterns were first observed at the target plates of the ASDEX Upgrade divertor - see [60] for details.

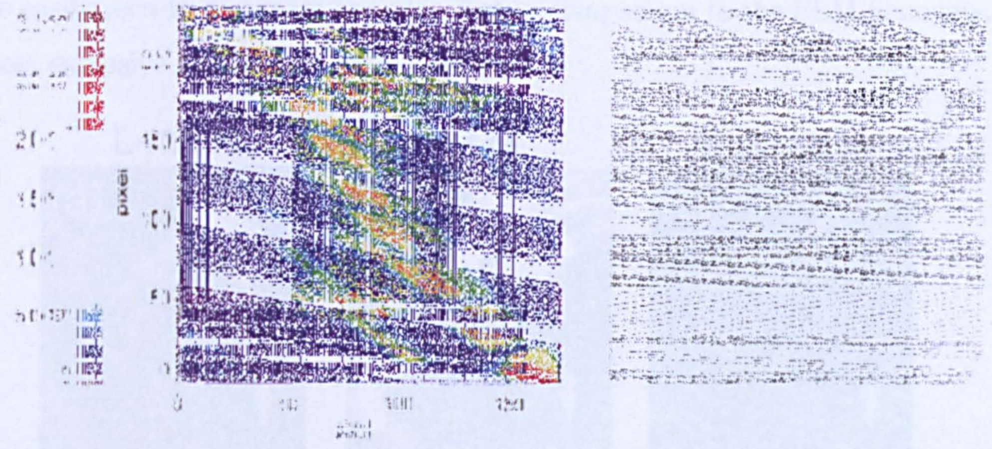

Figure 2.18: *Shown are (a) the calculated heat flux at the lower MAST divertor, and (b) view of the IR-camera image (for reference). Brighter spots in the form of spiral patterns with loads to the divertor 15–25 MW* m^{-2} *[59]*

2.8 Edge filamentary structures

Global plasma view

The collective evidence presented so far from different diagnostics and machines points to a 3D interpretation of density perturbations as filamentary structures which are localised in both toroidal/poloidal and radial directions but extend further distances in the parallel direction (i.e, along the magnetic field). However, perhaps the most compelling evidence for the blobby-like, or more adequately termed: filamentary nature of cross-field transport, is best shown by the fast camera diagnostic used in the MAST tokamak. Details of this camera will be presented in chapter 4 and only an example is shown here. The midplane-mounted camera captures in single wide-angle snapshots the entire plasma cross-section. The details of the edge plasma are clearly revealed mainly due to a large neutral density. Figure 2.19 shows the raw images of the MAST plasma during (a) L-mode and (b) H-mode phases. As can be seen, the structures in both L-mode and ELMing H-mode are clearly observed as elongated toroidally whilst being localised radially. The explosiveness of the ELM instability, and its manifestation in terms of localised structures is particularly well demonstrated: The pre-ELM LCFS (compare with figure 2.19(c)) is momentarily destroyed and plasma filaments appear to hit both the first wall and parts of the internal poloidal coil casing. L-mode filaments are also easily seen to dominate the edge, but in comparison to the ELM filaments, are much less explosive and appear more numerous.

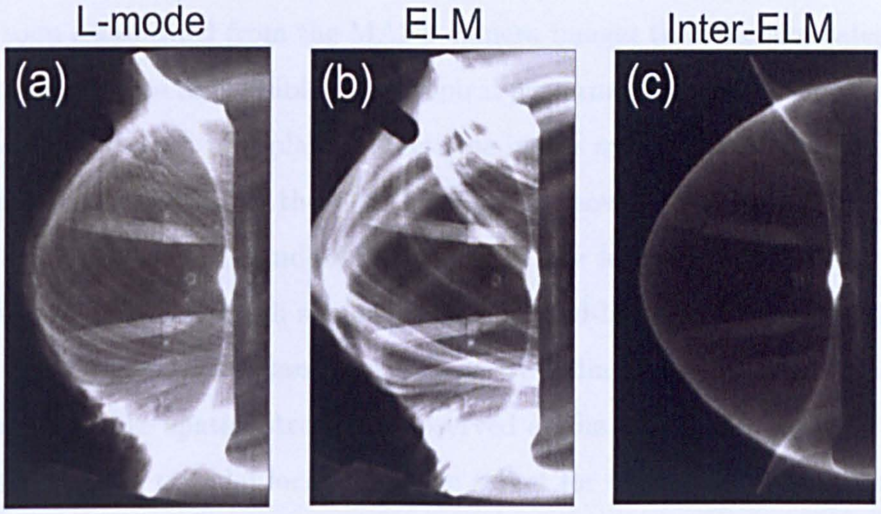

Figure 2.19: *Typical raw images of the fast camera on MAST showing images of the MAST plasma in (a) L-mode, (b) H-mode and (c) inter-ELM periods. Filamentary structures are seen in both confinement modes.*

A common feature of the L-mode and ELMing filaments is that they appear to be aligned with the local magnetic field. This property is not surprising since the concept of a filament is the manifestation of the ability of charged particles to travel along a magnetic field and a Larmor radius across it. This, with the well-recognised fact that transport timescales in the parallel direction are orders of magnitude faster than in the radial and perpendicular directions.

In stark contrast to both ELM and L-mode images, the inter-ELM figure shows a quiescent SOL and a sharp LCFS manifested in the narrow band of light intensity marking the clear reduction in cross-field transport. However, questions such as

- *"Is the cross-field transport during inter-ELM periods completely suppressed or simply reduced in magnitude?"*
- *"do filamentary structures in these periods contribute to transport?, and if so, what are their physical properties? are they similar to L-mode and ELM filaments? how do they differ?"*

are questions which this thesis will address and forms the direct contribution to this field.

Divertor view

It was soon established from the MAST camera images that the elongated filamentary perturbations are responsible for the spiral patterns observed at the targets (with visible and IR-cameras), and play a direct role in the energy loss in the SOL. An example of a divertor view using the MAST camera is shown in figure 2.20(c). Moreover, assuming that filaments are indeed aligned with the local magnetic field, Kirk and co-authors [49] showed through simulations using field-line tracing that small changes in radius of field-lines (i.e. filamentary structures) due to radial propagation would lead to the spiral-like spatial structures observed at the targets. Figure 2.20 (adapted from [49]) shows the toroidal location at the target for 6 field lines which start at the same toroidal location at the mid-plane but step in 2 cm intervals away from the LCFS (denoted by r_0). The radial extent of a field-aligned filament at the midplane translates into a toroidal extent at the target. It is only as a filament moves away from the edge that a spiral signature is produced. Figure 2.20(b) shows the predicted target pattern (using the field-line tracing method) resulting from a single filament expanding 12 cm [49] .

The foregoing discussion has provided the context into which the work presented in this thesis may be placed. While efforts have been dedicated to the study of fluctuations in ELM and L-mode phases, few efforts have concentrated on the H-mode period between ELMs. As a result, understanding of edge transport phenomena during these periods is still limited despite the diagnostic advances. In order to address previously raised questions concerning the nature of the transport during inter-ELM periods, and how it differs from L-mode and ELMing phases, it is necessary to present a brief summary of ELM and L-mode filament properties (such as size and propagation) that will be used in the discussion chapter. Note that results will simply be quoted without resorting to a detailed description of diagnostic or analysis method, whereas description of appropriate analysis methods that form original work undertaken in this thesis will be presented in the relevant chapters.

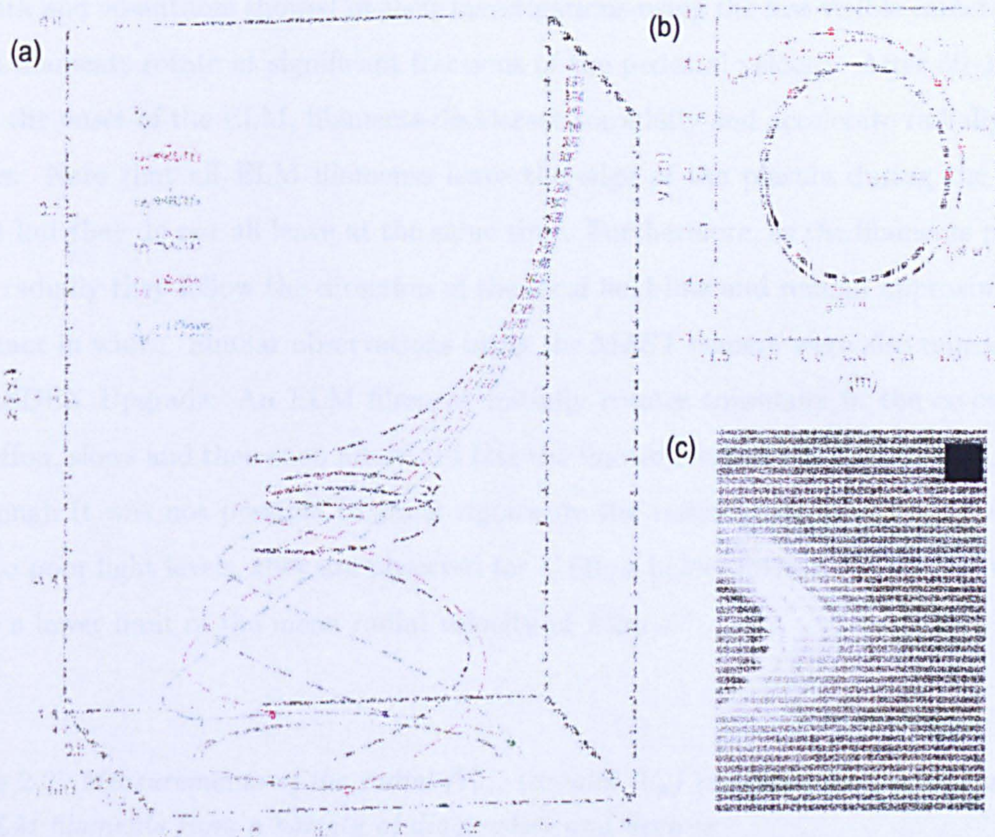

Figure 2.20: *Shown in (a) are six EFIT-calculated field-lines chosen at the same toroidal location as a function of distance from the LCFS, (b) the divertor target pattern prediction resulting from the radial propagation of a single filament with a 5° toroidal width to a distance of 12 cm, and (c) view of the MAST divertor using the fast camera.*

2.9 ELM filament characteristics

Radial and toroidal motion

Characterising the motion of ELM filaments in toroidal and radial directions has received much attention due to the potentially damaging heat loads associated with these filaments. Measurements of radial and toroidal velocities, denoted V_r and V_ϕ respectively, have been reported from a myriad of diagnostics, particularly fast visible imaging [49, 61, 62]. It follows naturally in this context that it is the toroidal component of velocity that influences the region of interaction of the filaments with the first wall, while the radial component, and energy content of the filament determine the magnitude of the interaction.

Kirk and co-authors showed in their investigations using the fast visible camera that ELM filaments rotate at significant fractions of the pedestal velocity. After 50–100 μs from the onset of the ELM, filaments decelerate toroidally and accelerate radially outwards. Note that all ELM filaments leave the edge of the plasma during the ELM event but they do not all leave at the same time. Furthermore, as the filaments propagate radially they follow the direction of the local field-line and remain approximately constant in width. Similar observations using the MAST camera were also reproduced on ASDEX Upgrade: An ELM filament initially rotates toroidally in the co-current direction, slows and then soon afterward hits the limiter located 12 cm from the LCFS. Although it was not possible to track rigorously the radial position of the filaments due to poor light levels, they are observed for $\sim 60\ \mu s$ before hitting the limiter, which gives a lower limit of the mean radial velocity of 2 km s^{-1}.

Table 2.2: *Measurements of the radial (V_r), toroidal (V_ϕ) velocities and mode numbers of ELM filaments from a variety of diagnostics and devices.*

Machine	Diagnostic	V_r (km s^{-1})	V_ϕ (km s^{-1})	Ref
DIII-D	BES	8	–	[56]
	Divertor tile currents	–	13.5	[56]
	CER	–	40	[63]
AUG	$t(probe_1) - t(probe_2)$	≥ 1	10–20	[64]
	TS	0.8	–	[65]
C-MOD	Visible	1–2	–	[66]
MAST	Visible	1–9	25	[67]
JET	$t(probe_{lim}) - t(D_\alpha)$	0.7	–	[68]

Measurements of V_r and V_ϕ from all devices are summarised in table 2.2. While there is general agreement, where data are available, that filaments rotate near to respective pedestal values, radial velocity measurements vary considerably in absolute magnitude as well as in qualitative behaviour (i.e. whether they accelerate or decelerate). Indeed, it was claimed in MAST [49] from analysis of the visible images that ELM filaments *accelerate* away from the edge while electric field measurements in DIII-D which indicate that filaments *decelerate* [56]. It was argued by Kirk in [69] that the discrepancies were largely attributed to the different analysis techniques used by different authors:

For instance, Kirk showed for the same data that the radial velocity calculated using the difference between the peak in the I_{SAT} and the start in the rise of the D_α light [70] is smaller than the velocity calculated using the time difference between two radially separated Langmuir probes [64].

ELM filament size

In addition to V_r and V_ϕ, properties such as size and the number of filaments per toroidal angle range (a pseudo toroidal mode number), have also been estimated. These results are summarised in Table 2.3 where the radial size of the filament is denoted as L_{rad}, and $L_\perp$ is defined as the size perpendicular to both the filament and the radial direction, i.e, its toroidal extent.

Table 2.3: *Measurements of the radial L_{rad} and perpendicular $L_\perp$ widths of ELM filaments, along with observed mode numbers from a variety of diagnostics and devices.*

Machine	Diagnostic	L_{rad}(cm)	$L_\perp$ (cm)	mode number	Ref
AUG	TS	1-2	6	8–20	[65]
	IR	–	2–6	10–20	[57]
	Visible	–	5–8	–	[70]
	RP mag	–	5–8	–	[64]
C-MOD	GPI	0.5-1	≥ 4.5	–	[66]
DIII-D	BES	1–2	2–5	–	[56]
	Visible	–	–	22	[71]
MAST	TS	4-6	–	–	[51]
	Visible	4-6	2–6	10–20	[67]
JET	TS	4-5	–	–	[72]
	IR outer limiter	–	10–20	11-16	[73]

Furthermore, estimates of V_ϕ and $L_\perp$ have also been obtained from the temporal width δt and separation Δt of the peaks in I_{SAT} signals of Langmuir probe arrays [46, 56, 70, 74]. See the inset in figure 2.11, section 2.6 for an example of I_{SAT} peaks (for the case of L-mode), and Table 2.4 which shows some of the data collected in [69].

Table 2.4: *Measurements of the temporal width (δt) and waiting time (Δt) of peaks observed in I_{SAT} traces during ELMs on a variety of devices. Table adapted from [69]. These measurements have been combined with toroidal velocity (V_ϕ) to estimate the perpendicular width $L_\perp$ and mode number of the filaments.*

Machine	δt (μs)	Δt (μs)	V_ϕ (km s^{-1})	$L_\perp$ (cm)	Mode number	Ref
AUG	50–80	100–200	10	8–13	10–20	[70]
DIII-D	50-100	150–250	13	8-16	10	[56]
MAST	15	60	10	7	10–20	[46]
NSTX	10	20-50	10	7	5-15	-
JET	100-150	300	80	10–20	10–20	[46]
JT-60U	10-25	-	30	4-10	10–20	[74]

2.10 L-mode filaments

Though the L-mode tokamak operating regime does not provide the level of confinement available in H-mode operation, it remains an important scenario for ITER and fusion power plants because any tokamak must operate in L-mode prior to a transition to H-mode, and L-mode operation avoids the high heat loads associated with ELMs. Results for L-mode filaments are less frequent than ELM results and most of the data has been carried on the MAST tokamak.

The dynamics of L-mode filaments on MAST show a complicated motion in both radial and toroidal directions. They are observed to gradually disintegrate into smaller structures and occasionally collide. Radial velocities have been found to be in the range 0.5–1.5 km s^{-1}, toroidal velocities in the range 1–7 km s^{-1} in the co-current direction. L-mode filaments are also more circular than ELM filaments where $L_\perp$ is in the range 7–9 cm while L_{rad} is in the range 5–10 cm.

Table 2.5: *Measurements of the radial L_{rad} and perpendicular widths $L_\perp$ of filaments, along with observed mode numbers from a variety of diagnostics and devices.*

Machine	Diagnostic	Type	L_{rad}(cm)	$L_\perp$ (cm)	mode number	Ref
C-MOD	GPI	L-mode	-	1	-	[75]
MAST	Visible	L-mode	5-10	7-9	20–50	[62]

2.11 Differences between ELM and L-mode filaments

In order to make a comparison with inter-ELM transport, the main difference between L-mode and ELM filaments is also briefly outlined. This is well demonstrated through their interaction with magnetic probes. Indeed, studies of magnetic signatures before ELMs have been performed for many years where authors usually focused on magnetic precursors [76, 77, 78]: these are magnetic oscillations at various frequencies that occur shortly before the onset of an ELM, and used mainly for ELM classification. Almost no studies on the magnetic signature during the ELM itself were made. However, interest in the magnetic signatures during ELMs has now been rekindled due to advances in current understanding regarding filamentary transport. This has been achieved in relatively few tokamaks, namely ASDEX Upgrade and MAST. In [52], the MAST reciprocating probe head was mounted with three coils to measure the radial, toroidal and vertical fields in both L-mode and H-mode phases. The magnetic coils were located 5 cm behind the Langmuir probe tips. Shown in figure 2.21 are the (a) D_α time traces (b) ion saturation current signals and (c) magnetic fluctuation signal dB/dt in the radial coil, for L-mode (dashed red) and ELM (solid black) filaments respectively. While the magnetic signatures of ELM filaments (which were cross-checked with visible images) were found to be well correlated with peaks in I_{SAT} signals; L-mode filaments showed no significant magnetic signatures.

In reference [52], simulations were performed in which a moving current-carrying wire was used to represent a filament. The induced field was calculated for the three coils. The best match with experimental data was found with an ELM filament current of $\sim$ 190 A where the filament was assumed to be aligned with the magnetic field and travelling mainly in the radial direction. Since magnetic signals decrease rapidly with distance, further investigations where the magnetic probe is reciprocated closer to the LCFS are required to verify with absolute certainty that L-mode filaments do not have a magnetic signature.

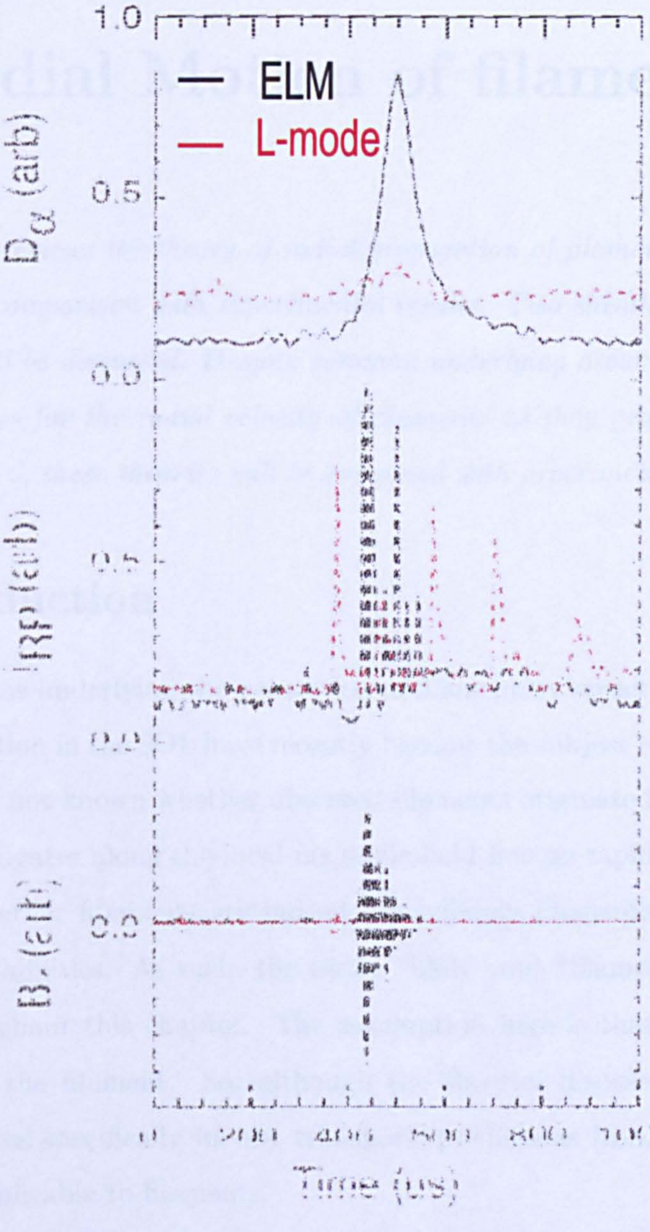

Figure 2.21: *Shown are (a) the target D_α, (b) mid-plane ion saturation current and (c) magnetic fluctuation signal as a function of time during a type-I ELM in MAST.*

Chapter 3

Radial Motion of filaments

This chapter reviews the theory of radial propagation of filamentary structures, in order to make a comparison with experimental results. Two sheath-limited and interchange models will be discussed. Despite common underlying assumptions, predictions from these theories for the radial velocity of filaments as they propagate in the SOL differ. In chapter 6, these theories will be compared with experimetnal results.

3.1 Introduction

The mechanisms underlying the generation of filamentary structures and their subsequent radial motion in the SOL have recently become the subject of substantial investigation. It is still not known whether observed filaments originate from a blobby-type structure that elongates along the local magnetic field line on rapid parallel transport timescales, or whether filaments are indeed immediately filamentary from the onset of underlying instabilities. As such, the terms "blob" and "filament" are used interchangeably throughout this chapter. The assumption here is that blobs are the 2D representation of the filament. So, although the theories discussed are strictly 2D models that address specifically blobby transport, predictions from these theories are assumed to be applicable to filaments.

The basic physics of filament/blob propagation was successfully identified by Krasheninnikov [79] to be the polarisation of the filament due to (1) the non-homogeneity of the magnetic field, and (2) curvature effects. Several leading candidate theories [79, 81, 82, 83, 84, 85, 86, 87, 88] have addressed the radial motion of filaments, with varying predictions for the radial velocity. Despite common underlying assumptions, their predictions for the radial velocity differ. This chapter provides a brief review of the most important theories.

3.2 Filament polarisation and E × B Drift

Charged particles in a magnetic field gyrate about magnetic field lines. Additional forces can cause the guiding centre of the particle motion to move perpendicular to the magnetic field. Denoting such a transverse force as $\mathbf{F}_\perp$, the drift velocity of a particle takes the expression:

$$\mathbf{V}_\perp = \frac{\mathbf{F}_\perp \times \mathbf{B}}{eB^2}, \tag{3.1}$$

where e is the species charge. It was first shown by Krashennenikov [79] in the context of filaments, which are none other than an ensemble of charged particles gyrating around a field line, that two such forces, namely the centrifugal force due to curvature and ∇B forces, lead to a vertical polarisation of a filament and its subsequent radial $\mathbf{E} \times \mathbf{B}$ drift.

Curvature of magnetic field

As the guiding centre of gyrating particle motion move along a curved magnetic field, it experiences a centrifugal force:

$$\mathbf{F}_c = \frac{mv_\parallel^2}{R_c^2}\mathbf{R}_c, \tag{3.2}$$

where $\mathbf{R_c}$ is the curvature radius of the magnetic field. This force is perpendicular to the magnetic field. Expressing $\nabla B/B = -\mathbf{R_c}/R_c^2$, the charge-dependent drift velocity is:

$$\mathbf{V}_c = \frac{mv_\parallel^2}{eB^3}\left(\mathbf{B} \times \nabla B\right). \tag{3.3}$$

Gradient of magnetic field

Another example of a transverse force is the gradient of the magnetic field strength. Indeed, in a tokamak, the radially-varying toroidal field, $B_\phi \propto 1/R$, leads to varying particle gyro-radii $\rho = mv_\perp/eB$. This causes an effective particle drift, the so-called ∇B-drift,

$$\mathbf{V}_{\nabla\mathbf{B}} = \frac{\rho v_\perp}{2B^2}\mathbf{B} \times \nabla B. \tag{3.4}$$

Due to $\nabla \cdot \mathbf{B} = 0$, drifts due to both curvature and non-homogeneity of the magnetic field occur simultaneously. The total drift velocity from both forces can thus be expressed as:

$$\mathbf{V}_c + \mathbf{V}_{\nabla B} = \frac{m}{eB^3}\left(\frac{1}{2}v_\perp^2 + v_\parallel^2\right)\mathbf{B} \times \nabla B. \tag{3.5}$$

Crucially, each drift is charge-dependent. Within the volume of a filament, the combined effect of both drifts leads to a charge separation within the volume of the filament as ions and electrons drift in opposite directions. This results in a polarisation current density ($\mathbf{j}_{\text{plr}}$) within the volume of the filament. This is illustrated in the cartoon picture in figure 3.1. For a filament of density n_{fil}, $\mathbf{j}_{\text{plr}}$ is given by:

$$\mathbf{j}_{\text{plr}} = \frac{n_{\text{fil}}m}{B^3}\left(\frac{1}{2}v_\perp^2 + v_\parallel^2\right)\mathbf{B} \times \nabla B, \tag{3.6}$$

and an associated polarising electric field $\mathbf{E}_{\text{plr}}$ propels the filament as a whole in the radial direction with a characteristic $\mathbf{E}_{\text{plr}} \times \mathbf{B}$ velocity. Note that $\mathbf{E}_{\text{plr}}$ is not the same as $\mathbf{E}_{\text{plr}}$ due to time-varying electric fields.

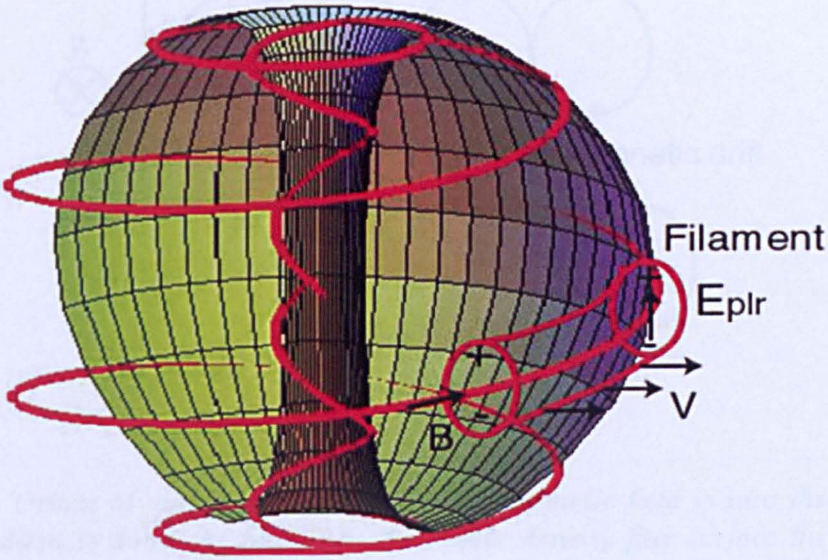

Figure 3.1: *The curvature and ∇B drifts drive a toroidal polarisation current I_{plr} with an associated electric field E_{plr} that leads to a radial motion in the direction of the major radius R.*

Usual quasi-neutrality cannot be directly re-established as transverse currents are hindered by the magnetic field: currents can only run force-free parallel to the magnetic field. In order to establish quasi-neutrality within the filament, i.e balance the polarisation current responsible for radial motion, two separate currents have been proposed. These are based on either:

1. Parallel currents: A force-free current running parallel to the magnetic field along the filament. The idea here is that parallel currents could be bridged at the end of the filaments, for example by interaction with divertor target plates. Several theories for filament propagation based on parallel currents have been proposed. They will be described in section 3.3.
2. Even though particle motion perpendicular to **B** is hindered, there could be a perpendicular toroidal current that is provided through drifts. One such drift is the diamagnetic drift. This is a mechanism that provides a perpendicular current and is based on a pressure gradient perpendicular to the magnetic field. In the case of filaments, the pressure gradient is the filaments' own pressure profile. The origin of diamagnetic current is illustrated in figure 3.2

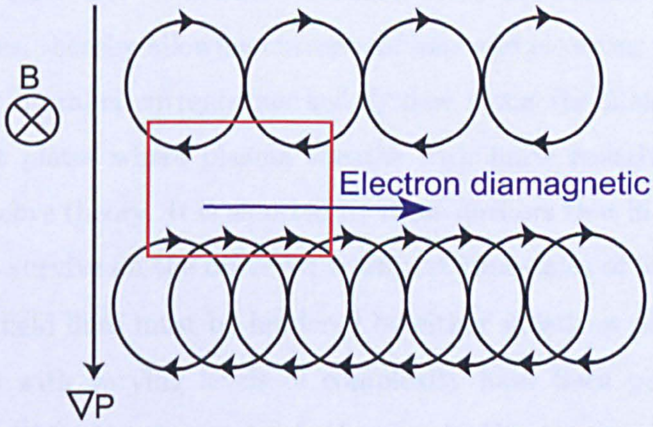

Figure 3.2: *Origin of diamagnetic current. The magnetic field is into the page and a density gradient is down the page. On the higher density flux surface there are more particles performing Larmor orbits than a lower density flux surface. The result is a net flow in the region between the flux surfaces (shown in the red box).*

For a filament density n_{fil}, the result is mainly toroidal drift velocity:

$$\mathbf{v}_{\mathrm{dia}} = \frac{\mathbf{B} \times \nabla P}{e n_{\mathrm{fil}} B^2}, \tag{3.7}$$

with an associated current density of the form:

$$\mathbf{j}_{\mathrm{dia}} = \frac{\mathbf{B} \times \nabla P}{B^2}. \tag{3.8}$$

In light of the above, the continuity equation can be written as [80]:

$$\nabla \cdot \mathbf{j} = \nabla \cdot \mathbf{j}_{\mathrm{plr}} + \nabla \cdot \mathbf{j}_{\parallel} + \nabla \cdot \mathbf{j}_{\mathrm{dia}} = 0, \tag{3.9}$$

and it states that the polarisation current I_{plr} (see equation 3.6) can be balanced by both the diamagnetic current I_{dia} (see equation 3.8) and the parallel current $I_{\parallel}$. In the next few sections, the different theories discussing the radial propagation of filaments based on either of the two hypothesis described above (i.e. parallel currents or diamagnetic current) will now be outlined in more detail.

3.3 Sheath-limited dissipative model

The first model considered is the so-called "sheath-limited dissipative" model which is based on the presumption of electrostatic sheaths at limiters and divertor plates. Authors in [79, 82, 83, 84, 88] consider the scenario that is illustrated in the cartoon schematic in Figure 3.3. A filament detaches from the plasma core and connects to the target plates, thereby allowing currents of ions and electrons to flow parallel to the magnetic field. Parallel currents marked $I_{\parallel}$ flow along the filament and are bridged over the target plates where plasma sheaths with finite resistivity form at the tiles according to Debye theory. It is asserted by these authors that in order for the induced electric field to survive on the observed transport timescales of 50–200 μs, the particle flow along the field lines must be hindered by either sheath or plasma resistivity.

Sheath models with varying levels of complexity have been proposed. First is the seminal work of Krashenennikov with the simple 1D sheath model. This was later extended to a 3D model of by D'Ippolito and Myra using modified Braginskii equations. Both these models do not take into account the edge region; rather, blobs/filaments are considered as steady state structures already formed. However, the work of Bisai and co-authors is also briefly outlined since their model equations treat the edge and SOL regions in a consolidated manner [89, 90].

3.3.1 Simple sheath model

With the assumption that curvature and ∇B are the underlying mechanisms for radial propagation (as described above in section 3.2), Krasheninnikov proposed that

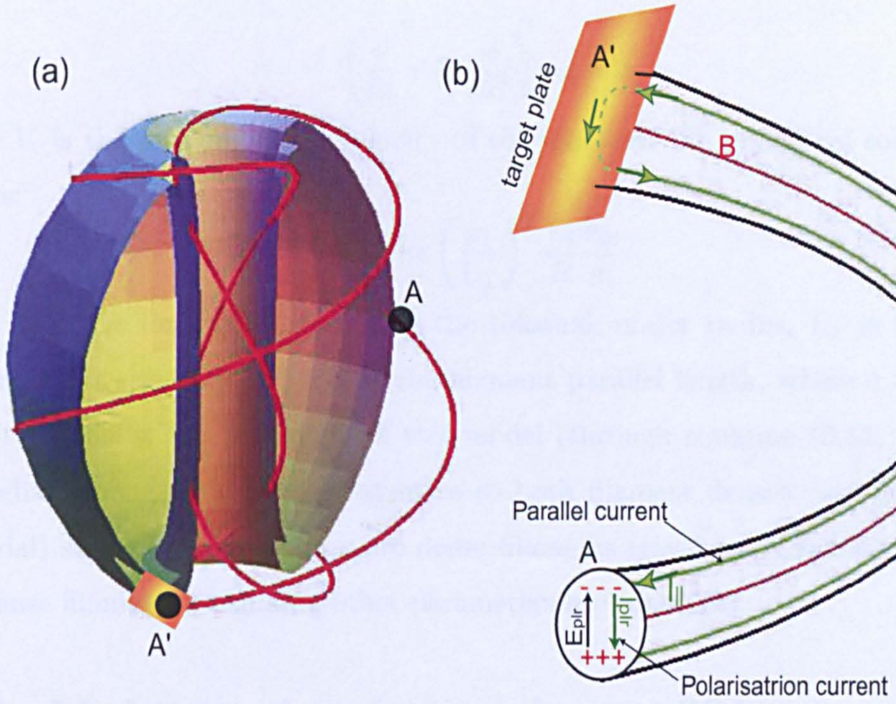

Figure 3.3: *As filament detaches from the plasma core and connects to the target plates, currents of ions and electrons flow parallel to the magnetic field. These currents are bridged over the target plates, where plasma sheaths with finite resistivity form at the tiles according to Debye theory.*

filamentary transport is damped in the SOL by the formation of resistive sheaths at the target plates. This sheath is the result of filaments touching the target plates while propagating radially outwards [79]. More specifically, Krasheninnikov's 1D model therefore included density variations along the filament in the parallel direction; namely, a density n_{fil} near the midplane and a density n_t near the target. For a small plasma resistivity, the electric potential (due to the polarisation) is constant along **B** and was found using the continuity equation for electric current (the quasi-neutrality condition):

$$\nabla \cdot \mathbf{j}_{\mathrm{plr}} + \mathbf{B} \cdot \nabla \left(\frac{j_{\parallel}}{B} \right) = 0 \tag{3.10}$$

where $\mathbf{j}_{\mathrm{plr}}$ is the polarisation current density. This current is the return current along **B** that neutralises charge flow. Integrating along the field lines, and using the sheath boundary condition:

$$j_{\parallel}|_{\mathrm{target}} = en_{\mathrm{t}} C_{\mathrm{s}} e\phi / T, \tag{3.11}$$

where n_t is the plasma density near the targets, $C_{\mathrm{s}} = \sqrt{T/M}$ is the plasma sound speed, M is the ion mass, a radial equation in [79] is derived from equation 3.10 such that:

$$\left(\frac{\partial}{\partial t}+V_r\frac{\partial}{\partial R}\right)n_{\text{fil}}=0, \tag{3.12}$$

where V_{r} is the uniform radial velocity of the filament. An analytical solution for V_{r} follows:

$$\frac{V_{\mathrm{r}}}{C_s}=\left(\frac{\rho_i}{\mathrm{L}_\perp}\right)^2\frac{L_{\|}}{R}\frac{n_{\text{fil}}}{n_{\mathrm{t}}} \tag{3.13}$$

where ρ_i is the ion gyro-radius, R is the tokamak major radius, $L_\perp$ is the filament perpendicular size and $L_{\|}\sim qR$ is the filament parallel length, where q is the safety factor. Crucially, the prediction of this model (through equation (3.13)) states that the radial propagation speed is sensitive to both filament density and perpendicular (toroidal) size, i.e, smaller and more dense filaments travel faster radially than larger less dense filaments (assuming other parameters are constant).

3.3.2 Model equations for the edge and SOL

More recently, the sheath model was extended in slab geometry using a two-dimensional, two-field fluid model of density $n(x,y,t)$ and potential $\phi(x,y,t)$ where x and y denote the radial and toroidal directions respectively [89, 90]. Unlike the simple sheath model, the electron continuity and current conservation equations were derived so as to include both the edge and SOL regions in a consolidated manner. Following the approach by authors in [89, 90], model equations take the form:

$$\frac{dn_e}{dt}+g\left(\frac{\partial n_e}{\partial y}-n_e\frac{\partial\phi}{\partial y}\right)-D_\perp\nabla_\perp^2 n_e=\langle\nabla_{\|}j_{\|}e\rangle_{\|}+S_n, \tag{3.14}$$

$$\frac{d\nabla_\perp^2\phi}{dt}+\frac{g}{n}\frac{\partial n}{\partial y}-\nu_\perp\nabla^4\phi=\langle n^{-1}\nabla_{\|}j_{\|}\rangle_{\|}. \tag{3.15}$$

Here $g\equiv\rho_s/R$ is a measure of the magnetic field curvature, and $\langle...\rangle_{\|}$ signifies an average along the field line. Parameters $D_\perp$ and $\nu_\perp$ are the normalised diffusion coefficient and viscosity respectively. The full details cannot be described here but the main qualitative points consist of the following:

- Parallel current $j_{\|}$ in the first term on the RHS of equations (3.14) and (3.15) is treated differently inside and outside the separatrix. Inside the separatrix where the magnetic field lines form nested flux surfaces, $j_{\|}$ has a finite parallel divergence and is determined by finite parallel resistivity $\eta=m_e\nu_e/n_e^2e^2$ where ν_e is the collision frequency of electron with the background. The turbulence in this region is characterised by radially elongated streamers. Outside the separatrix, the parallel current depends on the sheath physics rather than on the collision frequency with the background. Boundary conditions associated with the formation of a plasma sheath at the divertor plate are employed.

- In order to connect smoothly the edge and SOL regions, Bisai and co-authors have used spatially varying turn-on functions for the conductivity in the edge and sheath conductivities in the SOL [89].

Figure 3.4: *Dynamics of a blob marked by the "o" symbol. and ejection into the SOL. The formation of radial streamers and their subsequent detachment are observed.*

Numerical simulations using this model show that a substantial part of the radial particle transport in the SOL ($\sim 60\%$) is associated with blobs/filaments. An example is shown in figure 3.4 where radially-directed streamers are observed to form in the edge region that subsequently detach and propagate in the SOL. The trajectories of the blobby structures are complicated near the edge-to-SOL region. They are found to move radially, toroidally and spin about their axis. Because of the complicated trajectories, not all blobs are ejected at the transition region. They show that radial propagation only occurs beyond a critical distance while many blobs decay before reaching this distance.

3.3.3 Braginskii equations

Variants of the equations used by Bisai and co-authors were used earlier by D'Ippolito to elucidate the basic physics of blob propagation in the SOL. In [88], D'Ippolito and Myra extended the physical arguments of Krasheninnikov [79] by calculations using a three-field (density, temperature, potential) Braginskii fluid model. The Braginksii equations are a commonly-used fluid description of a plasma which describe the evolution of the first three moments of the Fokker-Plank equation [4]. The modified version used by D'Ippolito consists of the following density, temperature and vorticity equations:

$$\begin{aligned}
\frac{dn}{dt} + \nabla_{\parallel}(v_{\parallel} n) &= \xi n && (3.16)\\
\frac{dT_e}{dt} + \nabla_{\parallel}(v_{\parallel} T_e) &= \frac{2}{3n}\nabla_{\parallel}(\kappa_{\parallel}\nabla_{\parallel} T_e) - \xi E_i && (3.17)\\
\frac{c^2}{B^2} n m_i \frac{d}{dt}\nabla_{\perp}^2\phi &= \nabla_{\parallel} j_{\parallel} + \frac{2c}{B}\mathbf{b}\times\mathbf{k}.\nabla p && (3.18)
\end{aligned}$$

where $d/dt = \partial/\partial t + \mathbf{V_E}.\nabla$, $\mathbf{V_E} = (c/B)\mathbf{b}\times\nabla_{\perp}\phi$, $\mathbf{b} = \mathbf{B}/B$, $\mathbf{k} = \mathbf{b}\cdot\nabla b$ is the magnetic curvature, $v_{\parallel}$ is the parallel mass flow velocity, $n_e = n_i = n$, $\kappa_{\parallel}$ is the parallel heat conductivity, $\xi = n_0\langle\sigma v\rangle$ is the neutral particle ionisation rate (n_0 is the neutral density) and $\frac{3}{2}E_i$ is the total energy required per ionisation. Since ionisation in the far SOL can sustain the filaments longer against parallel loss of particles, a simple analytic model was used for the density decay time (τ_n) to the plates such that $\tau_n = 1/(\alpha - \xi)$ is determined by the balance between the loss rate due to particle flow to the plates, $\alpha = 2\rho_i/L_{\parallel}$, and the rate of particles that are resupplied by ionisation, ξ.

Unlike Bisai and co-authors, the edge region inside the separatrix was ignored and blobs were treated as steady state coherent structures propagating at constant radial velocity. In their investigation, the SOL was divided into 2 regions. The first region is located within one-exponential decay length from the separatrix and is determined by radial diffusion from the core and parallel loss to the sheaths. The second is the far SOL, distinguished purely by filamentary transport and neutral ionisation.

Assuming constant parameters along **B**, and integrating density, temperature and vorticity equations (3.16), (3.17) and (3.18) along the field lines with appropriate sheath boundary conditions leads to the result that density blobs/filaments with Gaussian profiles with a full width full maximum of $L_\perp$ propagate outwards with velocity:

$$\frac{V_r}{C_s} = \frac{\rho_i}{L_\perp}\frac{L_\parallel}{R}, \tag{3.19}$$

that is, smaller blobs move faster. Intuitively, smaller filaments move faster because a higher internal polarisation density results in a larger E_{plr}, and hence a greater $\mathbf{E}_{\text{plr}} \times \mathbf{B}$ velocity. The result is the same as that derived by Krashenninikov (see equation (3.13)) but without density variations.

Filament fragmentation

Because the filament radial velocity (and hence radial particle flux) is sensitive to the filament toroidal width $L_\perp$, D'Ippolito and Myra in [83] investigated mechanisms that influence this parameter. They showed through 2D simulations that secondary instabilities that are driven by the filament pressure profile can cause large filaments to bifurcate forming two smaller filaments, which in turn travel faster than the parent filaments. An example is shown in figure 3.5 where an initially circular blob distorts and splits into two smaller child filaments which are separated in the toroidal direction and elongated in the radial direction. Radial and toroidal directions are denoted as x and y respectively. Many more details were reported by D'Ippolito [88] and D'Ippolito and Myra [83]. These include for example:

- The temperature decays much more quickly than the density because parallel energy transport is much faster than the particle transport.
- An induced vorticity is also generated due to a radial potential in the filament. This subsequently leads to an azimuthal rotation of the filament about its axis.

3.3.4 BOUT simulation code

The BOUndary Turbulence (BOUT) code [91, 92] is a 2-fluid edge plasma simulation code. The equations solved are a reduced form of the Braginskii equations similar to those derived in ref [93] which reduce the 13 variables present in the Braginskii equations to 6: electron density n_e, electron and ion temperatures T_e, T_i, parallel ion velocity $V_{i\parallel}$, parallel current $j_\parallel$ and vorticity. The code was originally written at

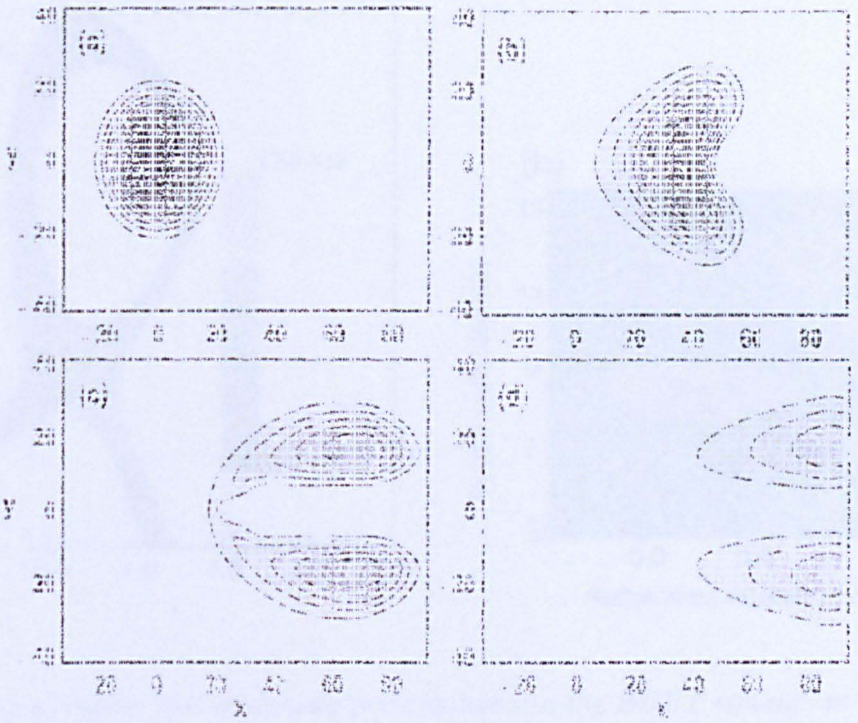

Figure 3.5: *Blob propagation showing bifurcation due to curvature driven interchange instability. Reproduced from [83]*

Lawrence Livermore National Laboratory (LLNL) with the purpose to model large aspect ratio plasmas; however, it has since been adapted and suitably modified by Ben Dudson to simulate small aspect ratio plasmas and particularly the spherical MAST plasma.

The BOUT code is used to model many plasma instabilities including drift waves, pressure-driven ballooning modes (ideal and resistive) and current-gradient driven modes. Furthermore, the simulation domain covers both the edge and SOL. The BOUT code is therefore well placed for simulations of filamentary transport. Initial BOUT results concerning the generation and propagation of L-mode filament-like structures at the plasma edge were recently presented by Dudson [62].

These simulations produce blob-like structures at the plasma edge. An example of this is shown in Figure 3.6 where density perturbations of $\sim 10^{18}$ m^{-3} are located at the outboard MAST mid-plane. A plot of density perturbations and electric potential at the outboard mid-plane as functions of radius and toroidal angle is also shown in Figure 3.6(b). This shows isolated plasma density structures (colours) moving across

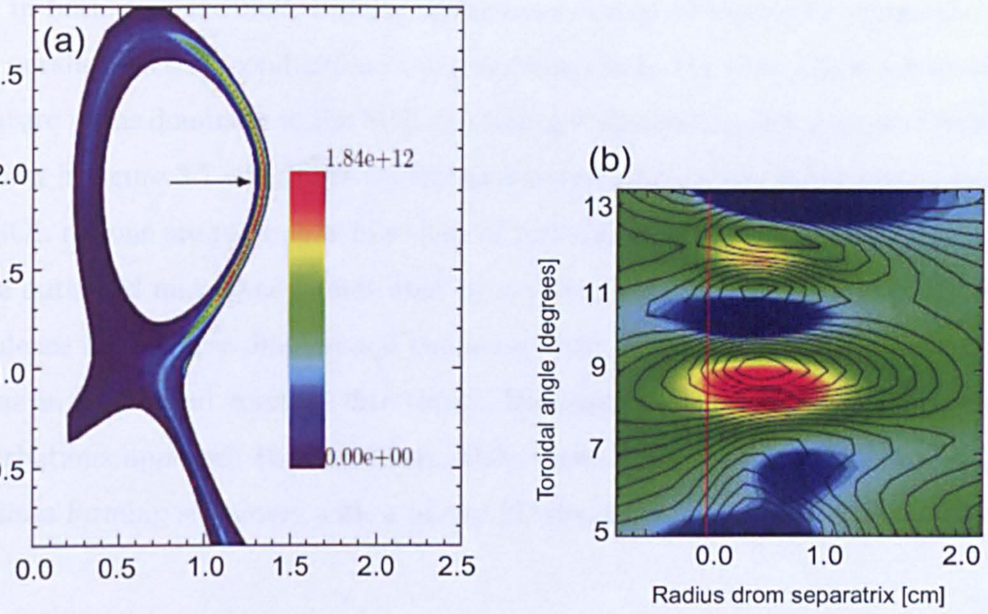

Figure 3.6: *(a) colour plot of density perturbations in the BOUT simulation domain of MAST plasma. (b) density (colours) and electric potential (contours) at the outboard midplane.*

the separatrix (marked with a vertical red line) into the SOL. A bipolar structure to the electric potential can also be seen, giving rise to a toroidal electric field across the density blob, and hence a radial $\mathbf{E} \times \mathbf{B}$ velocity. A phase shift can clearly be seen between the density and electric potential.

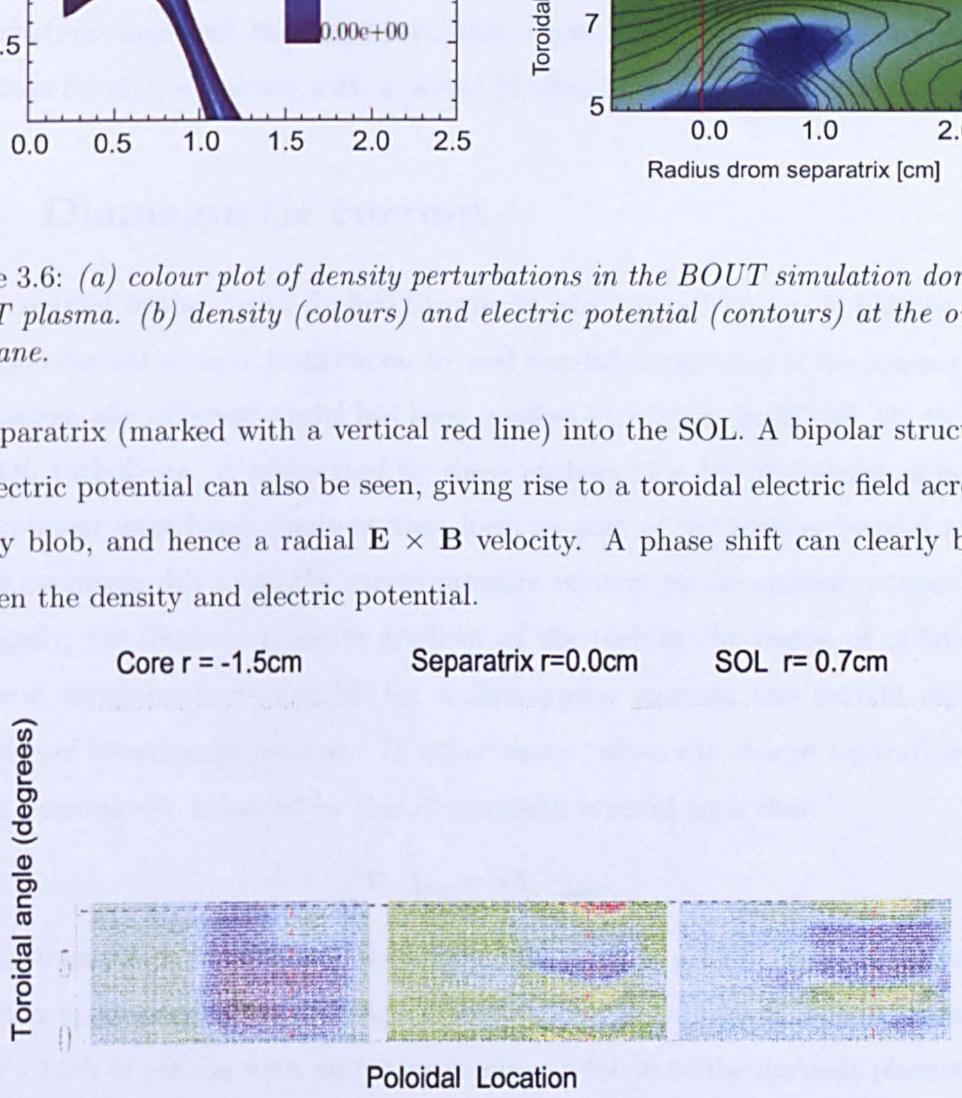

Figure 3.7: *Density (colours) and potential (contours) on flux surfaces for the core, separatrix and SOL. Field lines are horizontal dashed lines. The location of the outboard midplane is indicated by a vertical red dashed line.*

Analysis of the magnitude of the BOUT drive terms contributing most to the transport, in both core and SOL regions, indicates a change of behaviour across the LCFS [94]: parallel electron conduction is more important in the core, while advection and curvature terms dominate in the SOL. An example illustrating this change of behaviour is shown in figure 3.7 where the density and potential contours in the core, separatrix and SOL regions are plotted as functions of toroidal and poloidal angles. The location of the outboard mid plane is indicated by a vertical red dashed line. In the core, the turbulence has a three-dimensional character with variations along the field lines, as well as in radial and toroidal directions. However, as the density and temperature perturbations approach the separatrix, they become aligned with the local magnetic field lines forming streamers with a purely 2D dependence.

3.4 Diamagnetic current

In contrast to the sheath-limited theories in which parallel currents balance the polarisation current ensuing from curvature and non-inhomogeneity of the magnetic field, a fundamentally different model has been invoked by authors in [80, 95, 96] to explain the SOL turbulence: it is asserted by these authors that the turbulence is governed by non-linear interchange motions that form as part of the plasma inertial response due to curvature drive and the excess pressure relative to the ambient plasma. More specifically, the intrinsic pressure gradient of the blob in the region of unfavourable magnetic curvature is responsible for a diamagnetic current; this current represents the drive of interchange motions. In other words, when the charge separation in the blob is dynamically balanced by this diamagnetic current such that:

$$\nabla \cdot \mathbf{j}_{\mathrm{plr}} = -\nabla \cdot \mathbf{j}_{\mathrm{dia}}, \tag{3.20}$$

i.e. the term $\nabla \cdot \mathbf{j}_{\parallel} = 0$ in equation (3.9), the result is a large scale radial flow and advection in the form of interchange motions. The mechanism is illustrated in figure 3.8 for a blob of plasma with an excess pressure relative to the ambient plasma.

ESEL code

Accordingly, an electrostatic fluid model for the particle density, electric drift vorticity and electron temperature was derived and incorporated into a numerical ESEL code. This code is a simplified 2D model of the SOL in which blobs are advected through

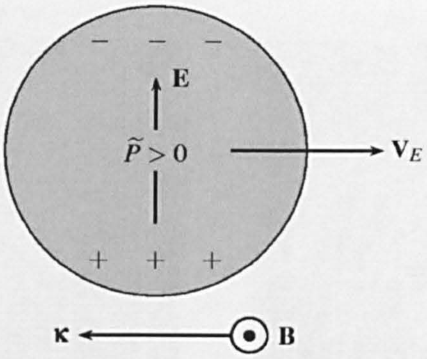

Figure 3.8: *Illustration of interchange mechanism leading to radial motion of a blob/filament structure with an excess pressure relative to the ambient plasma. The vertical polarisation current is balanced by the diamagnetic current leading to radial motion into the SOL.*

the curvature mechanism while an analytic model is used to determine loss of plasma along field lines to divertor targets. The dynamics of the parallel currents, the role of sheaths, and the presence of neutrals and impurities were neglected by the authors. However, despite the simplicity of the model, many features of the observed turbulence have been reproduced. Turbulence simulations of TCV midplane SOL plasma was successfully benchmarked against turbulence simulations. One example is shown in figure 3.9. The edge layer intermittently erupts blob-like structures into the SOL. The mushroom-like shape of the blob front is associated with a dipolar vorticity field and thus a large radial electric field.

Evolution of a filament

The evolution of a filament has been modelled by Garcia and co-authors by an advection-diffusion equation for the density:

$$\left(\frac{\partial n}{\partial t} + \frac{\hat{\mathbf{z}}}{B} \times \nabla\phi . \nabla n\right) = \chi \nabla_\perp^2 n. \tag{3.21}$$

The calculations start with a blob of circular-cross-section of the form:

$$n_{\text{fil}}(x, t = 0) = n_{fil,0} \exp\left[-\frac{1}{2}(x - x_0)^2\right]. \tag{3.22}$$

Diffusion with diffusivity D would spread the filament as:

$$n_{\text{fil}} = \frac{n_{fil,0}}{1 + 2Dt} \exp\left[\frac{(x - x_0)^2}{2(1 + 2Dt)}\right]. \tag{3.23}$$

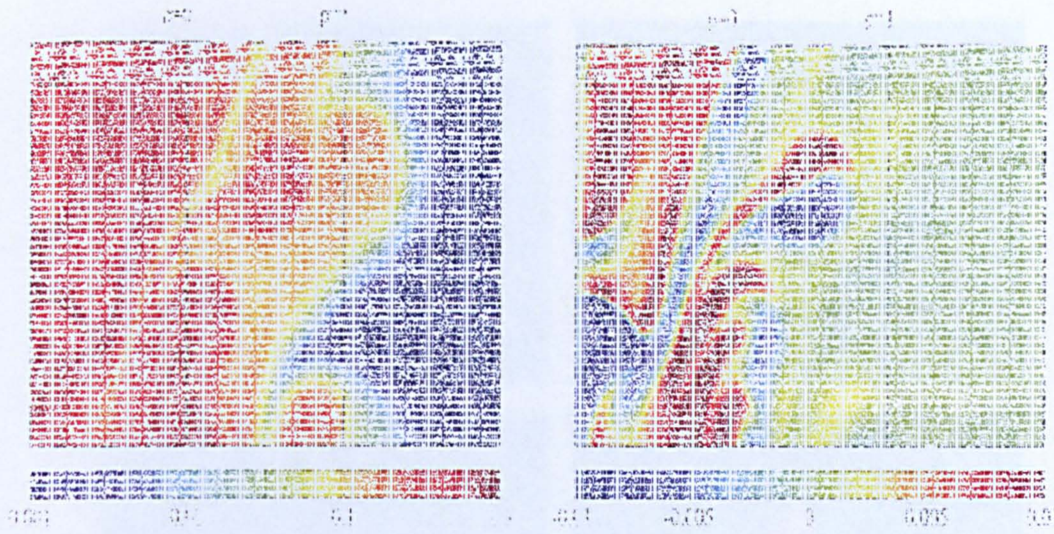

Figure 3.9: *Spatial structure of (a) the particle density and (b) the electric drift vorticity in the interchange simulation using the ESEL code. Exponential contour levelling is used for the particle density in order to reveal the structure across all regions.*

Figure 3.10 shows the filament evolution. Initially, the filament accelerates rapidly and travels a radial distance of 1–2 times its initial size. A steep front and a trailing wake can be seen. After the initial acceleration phase, the blob reaches a maximum constant velocity which is given by:

$$\frac{V_r}{C_s} \sim \left(\frac{2L_\perp}{R}\frac{\Delta\theta}{\Theta}\right)^{1/2}, \tag{3.24}$$

where $\Delta\theta$ is the relative change of a thermodynamic variable, (P, T or n), with respect to a background level. Taking the thermodynamic variable to be filament density, and the background level to be that of the immediate SOL (n_{SOL}), this scaling may be expressed in the reduced form as :

$$\frac{V_\mathrm{r}}{C_\mathrm{s}} \sim \left(\frac{2L_\perp}{R}\frac{n_\mathrm{fil}}{n_\mathrm{SOL}}\right)^{1/2}. \tag{3.25}$$

In the later stages, the filament/blob characteristics depend on parameters such as the Reynolds number ($R \equiv 1/\kappa\nu$) and Prandtl ($P_r \equiv \kappa/\nu$) numbers. Authors have shown that filaments undergo strong distortion and obtain a mushroom-shape cap in the toroidal direction as shown in figure 3.10. The filament may subsequently break into two sub-filaments with opposite vorticity, which might bring the filament to a halt.

Surprisingly, equation (3.25) predicts that larger filaments travel faster in the SOL

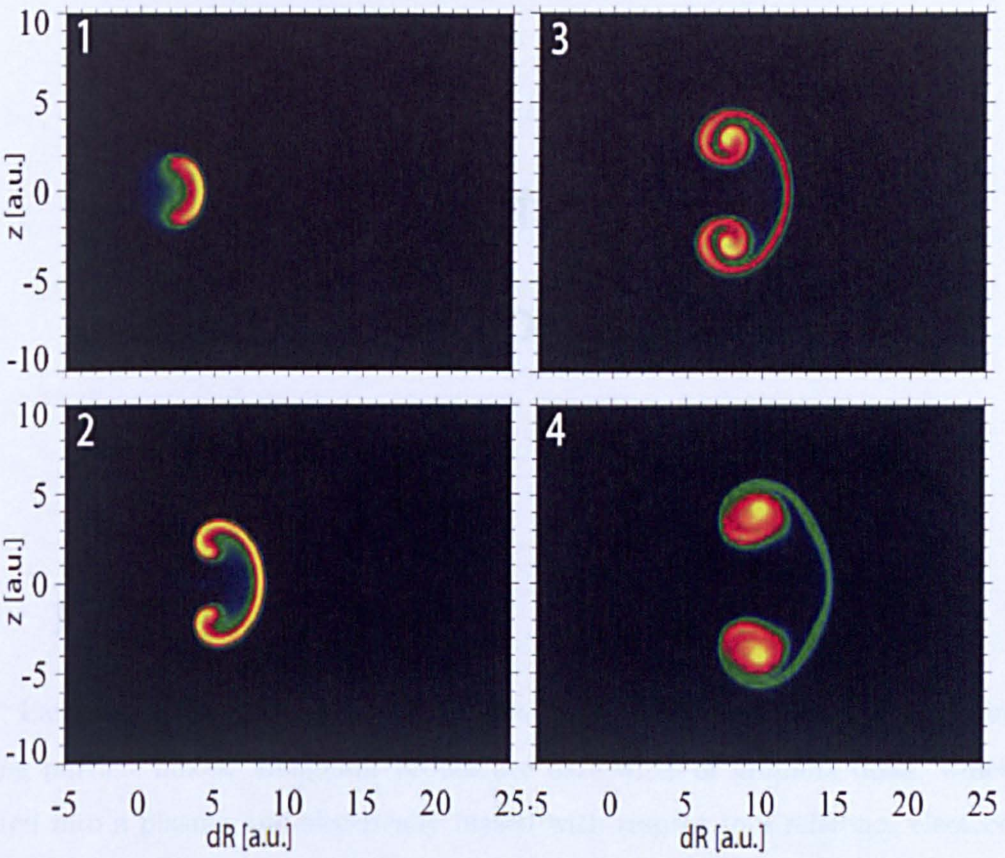

Figure 3.10: *Evolution of the filament shape according to [80]. The behavior has been shown to depend on the Reynolds and Prandtl numbers.*

than smaller filaments. This is in contrast to the prediction for the radial velocity in the sheath-limited models which show an inverse-proportionality of V_r with $L_\perp$ (see equation 3.13). This would be a cause for concern for first-wall structures in a tokamak since the faster-moving filaments would carry most of the particles.

Chapter 4

Introduction to data

4.1 Langmuir Probes

Langmuir probes are one of the oldest ways of diagnosing plasmas, by directly sensing particle fluxes. Langmuir probes are bare wires or graphite disks, which are inserted into a plasma and electrically biased with respect to a reference electrode to collect electron and/or positive ion currents. Because they make direct contact with the plasma, they are limited to investigating plasmas that the probe is able to withstand. This limits their access to the plasma edge. Because the measurement is made using particle flux to the probe, the reading is local and care must be taken to ensure that the probe is itself not perturbing the plasma to the point where the reading is no longer related to that of the unperturbed plasma.

Langmuir probes can be operated as single probes, measuring either the ion saturation current or the floating potential, as sweeping single or as triple probes to determine plasma parameters [97].

Floating potential

When a Langmuir probe comes into contact with a plasma, the electron flux to the surface of the probe is greater than the ion flux due to the higher thermal velocity of electrons. The surface collects a negative charge and the plasma, depleted of electrons acquires a positive charge which sets up an electric field. The field is localised to a small region close to the surface due to Debye shielding. The region is known as the sheath, and the electric field in this region acts to repel the slower electrons and accelerate the ions until the ion and electron fluxes reach equilibrium. The potential of the surface is referred to as the floating potential ϕ_f.

When an electrical bias is applied to the probes, the probe tip collects electron and ion currents. The usual practice is therefore to either apply a large constant bias, or to sweep the voltage around either side the floating potential and record the probe current-voltage I-V characteristic. A typical I-V characteristic of a Langmuir probe in a plasma is shown in figure 4.1.

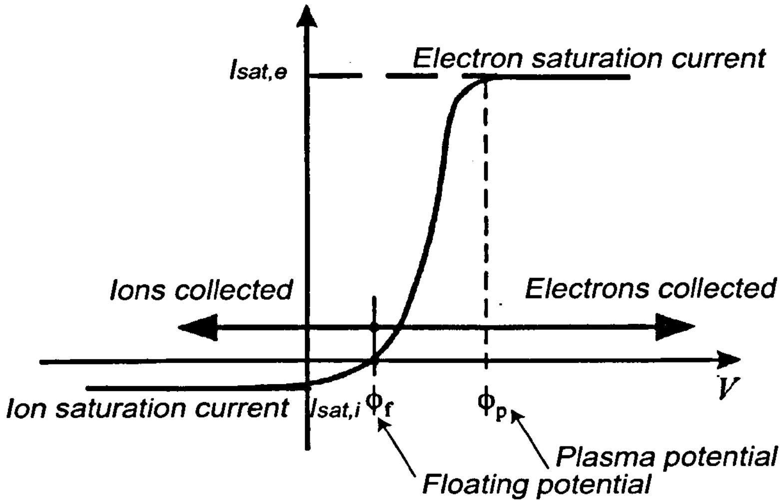

Figure 4.1: *Langmuir probe I-V characteristic.*

The potential at the probe corresponding to the zero current is the floating potential, ϕ_f. A Langmuir probe will draw an electron current, I_e, when biased to a voltage $V_B > \phi_f$. Similarly, an ion current is drawn I_i when the probe is biased to a voltage at $V_B < \phi_f$. An expression for the current I to a probe of fixed area A_p, biased to a voltage V, is [4]:

$$I = A_p\left(I_e + I_i\right) = A_p I_i\left[1 - \exp\left(\frac{V - \phi_f}{T_e}\right)\right]. \tag{4.1}$$

At sufficiently high negative bias, $I \longrightarrow A_p I_i$, and the current to the probe saturates at the level of the ion saturation current denoted $I_{\mathrm{SAT,i}}$:

$$I_{\mathrm{SAT,i}} = eA_p n_e C_s, \tag{4.2}$$

which corresponds to the probe becoming sufficiently negatively charged that all electrons are repelled and so the current is limited by the flux of ions entering the sheath at the ion sound speed given by:

$$C_s = \sqrt{\frac{k_B\left(T_e + Z\gamma_i T_i\right)}{m_i}}, \tag{4.3}$$

where T_e and T_i are the electron and ion temperatures respectively, m_i is the ion mass, Z is the ion charge state and γ_i is the adiabatic coefficient for the ions.

At sufficiently high positive bias voltage, the electron probe current saturates at the level of the electron saturation current:

$$I_{\mathrm{SAT,e}} = \frac{1}{4} e A_p n_e V_{th,e}, \tag{4.4}$$

where

$$V_{th,e} = \sqrt{\frac{8eT_e}{\pi m_e}}, \tag{4.5}$$

is the electron thermal velocity. The positive bias potential corresponding to the electron saturation current is referred to as the plasma potential. The electron temperature T_e can be determined from the slope of a semi-log plot of the $I-V$ characteristic.

Langmuir probe measurements are taken at two locations in MAST: by an array on the divertor target plates to measure incident plasma flux and by a reciprocating probe at the outer midplane. This second system is equipped with a circular array of 8 equally-spaced, flush-mounted Langmuir probes arranged in diametrically opposite pairs (see figure 4.2). These Langmuir probes are each biased to -200V, and measure the ion saturation current, I_{SAT}.

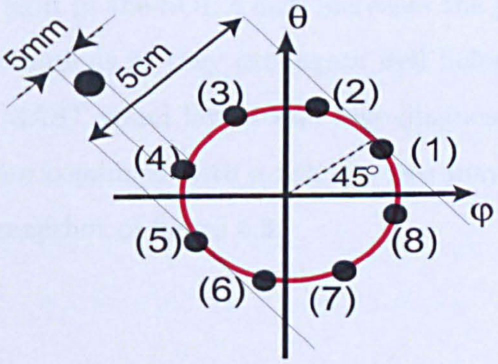

Figure 4.2: *Schematic (not to scale) showing the reciprocating probe configuration of Langmuir probes used in this thesis.*

4.2 The Photron camera

Fast Imaging in tokamaks

The first attempts of fast imaging in tokamaks dates back to the mid 1970s when high speed cine photographs of DITE [98], ALCATOR A [99] and the ATC [100] tokamaks were taken with film speeds running at 5000 frames per second (fps). At the time, the first commercial Charged Couple Devices (CCDs) were being designed offering a 100×100 pixel resolution at 2000 fps. Since the 1970s there has been a sustained effort to measure and understand plasma edge phenomena through imaging. CCD cameras today are routinely capable of 128×40 resolution at 100,000 fps, thereby offering a very powerful tool to visualise plasma turbulence at the edge.

Advantages of the MAST tokamak

Imaging diagnostics are currently used on several tokamaks including TFTR [101], ASDEX-Upgrade [102], JET [103], ALCATOR C-Mod [104, 105, 106] and NSTX [107, 108, 109, 110]. While successful in capturing the details of the edge turbulence, nearly all imaging diagnostics in these machines make use of localised gas puffing to increase light levels. Furthermore, these cameras are restricted to small sections of the plasma due to a small plasma-wall/limiter distance which does not typically exceed 12 cm. Both these disadvantages are alleviated naturally in the MAST machine which is well suited for imaging studies, particularly those of filamentary structures. Indeed, MAST benefits from both a large plasma-wall separation and a high neutral density. Owing to the large vessel volume/plasma volume ratio, the high neutral density results in significant levels of D_α light in the SOL which increases the probability of identifying the weakest of edge fluctuations as they propagate well before they hit the first wall. Furthermore, the open MAST vessel layout and easy diagnostic access (see figure 1.5) mean that cameras, when combined with a fish eye lens may view the entire plasma, as shown in the single snapshot of figure 4.3.

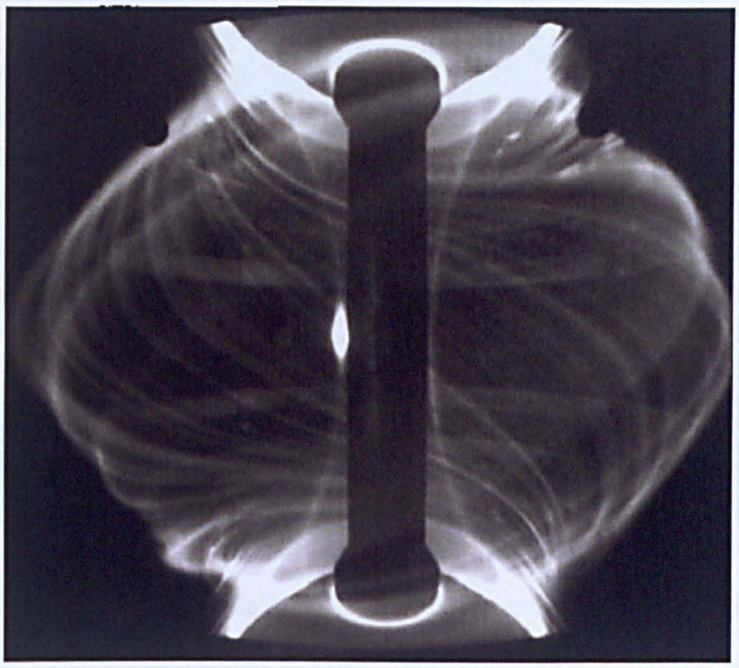

Figure 4.3: *Example of full view image in MAST using the Photron camera*

Description of the MAST camera

The Photron-APX RS camera, shown in figure 4.4, was installed on MAST in October 2005. It is a powerful visualisation tool which allows the capture of fast moving structures and subsequent slow motion observation, image processing and analysis. The Photron camera is used to capture a continuous set of images of the MAST plasma throughout an entire MAST shot. The unique wide angle view of the plasma and the gap between the LCFS and the first wall in MAST allows the radial propagation of any moving structures to be clearly tracked without interaction with vessel components.

The camera has no filters so that the light is dominated by D_α emission from the excitation of neutral gas by hot plasma electrons. The camera has a uniform (i.e. non rolling) electronic shuttering system making it possible to control the exposure time regardless of the selected frame rate. By using an exposure time that is shorter than the frame time, high-speed events may be captured as still images without any blurring.

The camera has a CMOS sensor, which, like a conventional CCD, consists of an array of 1024×1024 pixelated metal oxide semiconductors which accumulate the charge in

Figure 4.4: *The Photron-APX RS camera used in MAST*

each pixel proportional to the local illumination intensity. However, in contrast to the standard CCD technology where (after one integration time) the charge packet of each pixel is sequentially transferred to a common output structure for charge-to-voltage conversion, the conversion procedure in the CMOS detector takes place in each pixel. This difference in readout techniques allows cameras such as the Photron APX-RS the capability of reading out only a subsection of the sensor which in turn allows increased frame rates for smaller regions. At the full frame size, the camera can only record up to 10,000 fps, insufficient for following fast edge dynamics; however, smaller regions may be selected which then allow a higher frame-rate and tracking of individual features. For filament studies in this thesis, the preferred region of the plasma typically selected is the midplane view, shown by the white rectangular box in figure 4.5. This is because the midplane view avoids reflected light from poloidal field coils. This view also has the advantage that radial position (which changes the field-line pitch) has little effect on field-line shape across this narrow strip and so the toroidal velocity component can be distinguished from radial velocity.

Figure 4.5 shows the poloidal cross section of MAST with a typical equilibrium in a double null configuration. Shown on the figure are the locations of inboard and outboard targets, the midplane location of the reciprocating probe and the field of view of the camera when in fast mode. The bright spot on the midplane centre column is due to the gas feed used for fuelling the plasma.

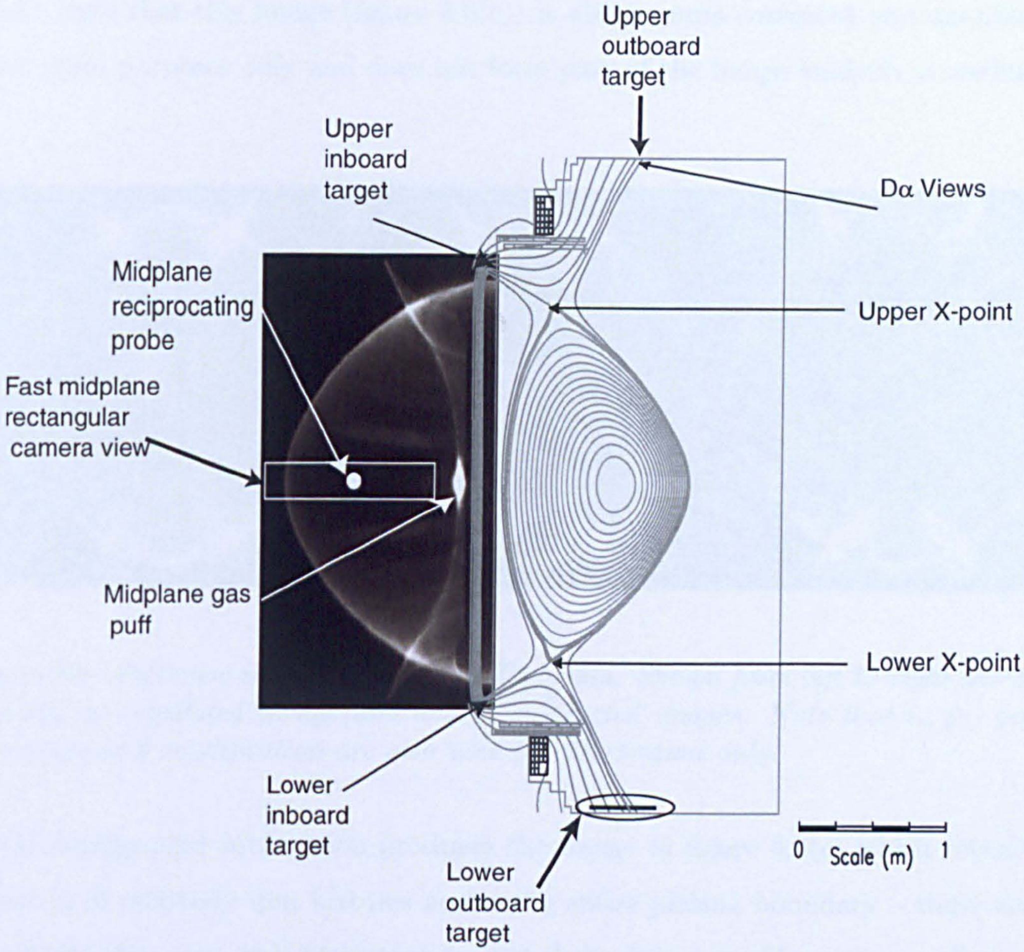

Figure 4.5: *Poloidal cross section of MAST with a typical equilibrium in a double null configuration. Shown on the figure are the midplane location of the reciprocating probe and the field of view of the camera when in fast mode. The bright spot on the midplane centre column is due to the gas feed used for fuelling the plasma.*

4.3 Background subtraction

In order to distinguish the D_α emission of the filaments from the overall slowly-varying background, an image-processing technique developed in [94] is used, whereby for each frame, a minimum light intensity (i.e. background) is calculated for each pixel over a variable number (6-21) of neighbouring frames, and subsequently subtracted from the original pixel. An example of this image processing is presented in figure 4.6: (a) a typical camera image during an inter-ELM period (resolution 512×462 at a speed of 3 kHz and 11 μs exposure time), (b) the minimum background calculated over 11 frames (the intensity is a significant fraction (typically up to 80%) of the original image), and (c) the result of subtracting the calculated minimum from the original image; note that this image (figure 4.6(c)) is also gamma-corrected and amplified for illustration purposes only and does not form part of the image analysis procedure.

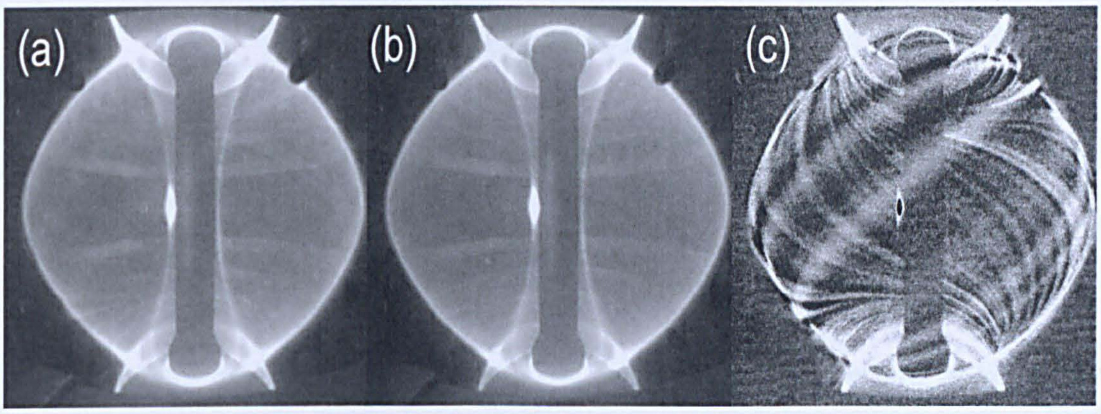

Figure 4.6: *Full view images of the MAST plasma. Shown from left to right are a) the original, b) calculated background and c) subtracted images. Note that in (c) gamma correction and amplification are also used for illustration only.*

The background subtraction produces the image in figure 4.6(c) which reveals the existence of relatively dim features across the entire plasma boundary – these are the inter-ELM filaments. It is important to note that while some filaments are observed in the raw images, the background subtraction method allows the less bright filaments to be more easily seen. Figure 4.6(c) indicates that in common to both ELM and L-mode images, and despite a seemingly quiescent SOL marking a reduction in the magnitude of cross-field transport, filamentary structures during H-mode inter-ELM periods also exist, and as will be shown in the next chapter, contribute directly to transport.

Tests, such as (1) varying the number of frames over which the minimum background is calculated, and (2) repeating this for a wide range of discharges and for different phases (L-mode and H-mode), have been performed to verify that the subtraction technique does not artificially generate these structures. Furthermore, a strong correlation (which will be shown in chatper 6) between Langmuir probe and image data for these structures provides further evidence for the robustness of the background subtraction technique. The background subtraction is valid for L-mode and inter-ELM phases but cannot be applied to the ELM.

Chapter 5

Analysis of camera images

This chapter describes the analysis of the camera images. Features in the images are located by manual tracking of projected field-lines from EFIT magnetic reconstructions onto the images. An automated method of field-line projection is used to calculate the mean image intensity along field-lines leading to intensity signals as a function of toroidal angle. Peak detection algorithms are then applied to these signals in order to determine properties such as pseudo mode numbers, sizes, toroidal and radial velocities of the filaments. Examples of radial and toroidal propagation are outlined and their dependence on plasma parameters is measured. Finally, properties of inter-ELM filaments are compared and contrasted with those of L-mode and ELM filaments.

5.1 Camera calibration

In order to extract any useful information from the 2D images, it is necessary to calibrate the camera so that the line of sight through each camera pixel on the CCD is known. From known 3D world (X, Y, Z) coordinates, it is possible to reconstruct the corresponding 2D (x, y) image coordinates in a simple camera model. Such a model depends on camera parameters, namely:

- Position of the camera denoted here as $X_{CAM}, Y_{CAM}, Z_{CAM}$. In figure 5.1, these are expressed in terms of the world plane distance from the centre of the camera lens along the optical axis, and is denoted l.

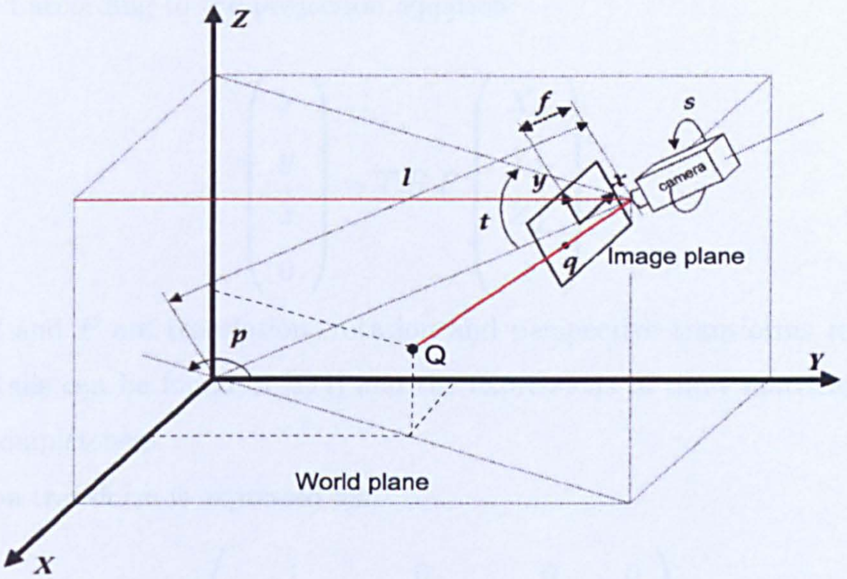

Figure 5.1: *Camera projection model*

- Focal length f of the camera which is the distance of the image plane from the centre of the camera lens along the optical axis of the camera.
- Tilt, pan and and swing angles denoted respectively t, p and s. The pan angle is the horizontal angle of the optical axis with respect to the Y axis. The tilt angle is defined as the vertical angle of the optical axis of the camera relative to the Y axis of the world coordinate system. The swing angle is the rotation angle of the camera along its optical axis.
- Distortion of the image due to fish-eye lens.

In the absence of distortion, this calibration is achieved using a similar method used to calibrate a road traffic camera for visual traffic surveillance [111]. Assuming that $Q(X_Q, Y_Q, Z_Q)$ is an arbitrary point in the 3D (X,Y,Z) world, and $q(x_q, y_q)$ is its corresponding image point in the (x,y) plane, a forward mapping function Φ:

$$\mathrm{q} = \Phi(\mathrm{Q}), \tag{5.1}$$

is calculated according to the projection equation:

$$\begin{pmatrix} x \\ y \\ z \\ 0 \end{pmatrix} = T.R.P \begin{pmatrix} X_Q \\ Y_Q \\ Z_Q \\ 1 \end{pmatrix}, \tag{5.2}$$

where T, R and P are translation, rotation and perspective transforms respectively. Further details can be found in [111] and the expressions of these matrices are given below for completeness.

The rotation transform is expressed as:

$$T = \begin{pmatrix} 1 & 0 & 0 & 0 \\ 0 & 1 & 0 & 0 \\ 0 & 0 & 1 & 0 \\ -X_{CAM} & -Y_{CAM} & -Z_{CAM} & 1 \end{pmatrix}, \tag{5.3}$$

The rotation transform is the product of three matrices, R_X, R_Y and R_Z – each representing rotation with respect to the X, Y and Z axis respectively.

$$R_Z = \begin{pmatrix} \cos p & -\sin p & 0 & 0 \\ \sin p & \cos p & 0 & 0 \\ 0 & 0 & 1 & 0 \\ 0 & 0 & 0 & 1 \end{pmatrix}, \tag{5.4}$$

$$R_X = \begin{pmatrix} 1 & 0 & 0 & 0 \\ 0 & \cos t & \sin t & 0 \\ 0 & \sin t & \cos t & 0 \\ 0 & 0 & 0 & 1 \end{pmatrix}, \tag{5.5}$$

$$R_Y = \begin{pmatrix} \cos s & 0 & -\sin s & 0 \\ 0 & 1 & 0 & 0 \\ 0 & \sin t & \cos t & 0 \\ 0 & 0 & 0 & 1 \end{pmatrix}. \tag{5.6}$$

Finally, in order to simulate perspective distortion, the projection equation as expressed in equation (5.2) includes:

$$P = \begin{pmatrix} 1 & 0 & 0 \\ 0 & 0 & 1/f \\ 0 & 1 & 0 \\ 0 & 0 & 0 \end{pmatrix}, \tag{5.7}$$

By substituting $X_{CAM} = l \sin p \cos t$, $Y_{CAM} = -l \cos p \cos t$, $Z_{CAM} = -l \sin t$ and rearranging equation (5.2), the x-coordinate x_q is given by:

$$x_q = \frac{f \begin{bmatrix} X_Q(\cos p \sin s + \sin p \sin t \sin s) \\ +Y_Q(\sin p \cos s - \cos p \sin t \sin s) \\ +Z_Q \cos t \sin s \end{bmatrix}}{-X_Q \sin p \cos t + Y_Q \cos p \cos t + Z_Q \sin t + l}, \tag{5.8}$$

and the y-coordinate y_q is expressed as:

$$y_q = \frac{f \begin{bmatrix} X_Q(-\cos p \sin s + \sin p \sin t \sin s) \\ +Y_Q(-\sin p \sin s - \cos p \sin t \sin s) \\ +Z_Q \cos t \cos s \end{bmatrix}}{-X_Q \sin p \cos t + Y_Q \cos p \cos t + Z_Q \sin t + l}. \tag{5.9}$$

The general expressions for the image coordinates given by equations (5.8) and (5.9) take simpler forms due to the MAST camera set-up: Mounted at the mid-plane and located approximately at 2.16 m in major radius, the MAST camera is fixed horizontally and views the entire plasma through a relay fish-eye lens of focal length 4.8 mm, with no tilting, panning or swing. The relevant projection equations thus become:

$$x_q = \frac{fY_Q}{l - X_Q}, \tag{5.10}$$

$$y_q = \frac{fZ_Q}{l - X_Q}. \tag{5.11}$$

These equations were adapted into an initial IDL code where refinement and calibration of the camera model was subsequently necessary to ensure accurate projection.

A series of systematic tests was conducted by projecting MAST vessel components such as the centre-column and poloidal field coils (whose 3D coordinates are known to better than a centimetre), and matching their locations in the images.

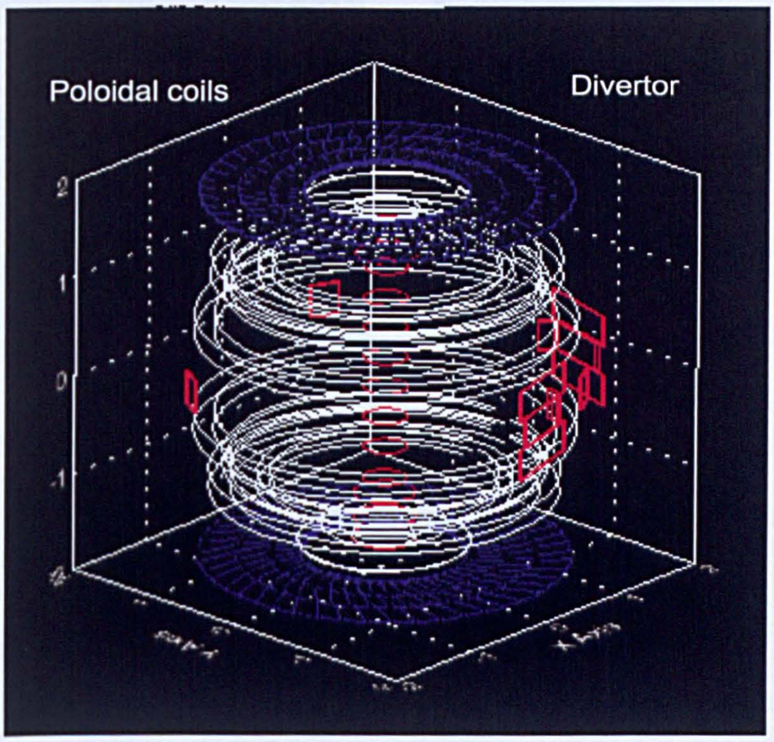

Figure 5.2: *The 3D coordinates of MAST components within vessel are known at an accuracy of ±1 cm. Shown is the 3D graphic representation of the MAST vessel including the P5 and P6 poloidal coils (in white), the center column (in red) and the divertor plates (in blue).*

Figure 5.2 shows a 3D rendering of the MAST vessel with the poloidal coils and the center column and the divertor plates marked by the white, red and blue lines respectively.

Full view images from the start and end of discharges, during breakdown and at disruptions respectively were used since the vessel is well-illuminated during these times without being obscured by the plasma. In order to verify accurate projection, the alignment of the camera was changed manually (in software) through a series of iterations, until a fit was found to all structures. Figure 5.3 shows an example of this calibration where in (a) vessel components are more easily seen during disruption and (b) P5, P6 poloidal coils and the center-column are projected by the white lines.

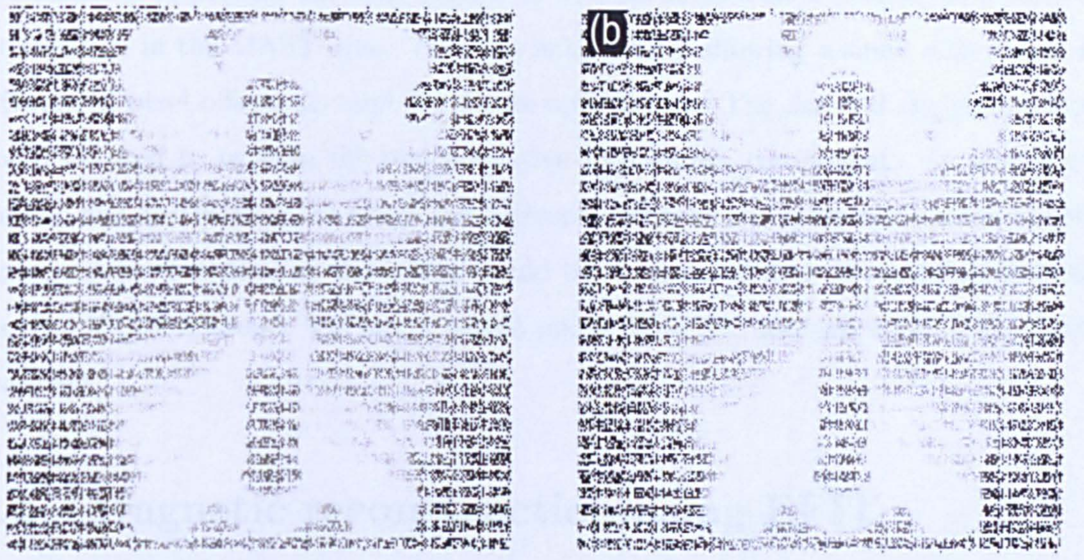

Figure 5.3: *Shown in (a) is the Photron image of the MAST vessel at disruption clearly indicating the location of certain vessel components used in the benchmarking of the projection, (b) the same image as (a) with projected P5, P6 poloidal coils and center-column, in white.*

Camera distortion

The camera is fitted with a fisheye lens with a barrel-type distortion, i.e. the distortion where the magnification decreases with distance from the optical axis. The distortion has the effect that straight lines become curved. Investigations into the effect of this distortion were carried out in the laboratory. The corrections were determined analytically by measurements of distorted images of straight lines forming a rectangular (x, y) grid: deviations in x and y coordinates of points tracing a line are measured on a rectangular grid. A line of best fit to the deviations then determines the analytical correction to projection equations. It was found during these investigations that this distortion was not significant.

Camera movement

The largest source of error in the projection was due to the movement of the relay lens which resulted in the movement of the optical axis. This occurred mainly during a MAST shot due to vessel movement especially at breakdowns and disruptions. Misalignments were also observed between MAST operating days where routine maintenance tasks on other diagnostics in the MAST experimental area surrounding the camera were identified to be the inevitable cause of camera movement. It was therefore essential to account for both sources of movement on a shot-to-shot basis without intervention in the MAST area. This was achieved by allowing a small adjustment in software of pixel offsets Δx and Δy of the optical axis. The Δx and Δy pixel offsets would be used to re-align the image relative to a known component. An automatic method was also introduced where the difference between the projected contours of the centre-column and that of the image would be determined and corrected throughout the shot if this difference was larger than 5 pixels; however, manual checks were always preferred.

5.2 Magnetic reconstruction using EFIT

Since the filaments appear to be field-aligned density structures, equilibrium magnetic field lines are used to track the filaments. This analysis procedure is now described in this section. Having calibrated the camera system and optimised the projection, magnetic reconstructions of equilibrium MAST discharges using the EFIT code [112, 113, 114, 115, 116] are used to calculate the 3D shape of magnetic field-lines at varying radii and toroidal angles. The 3D structures are then projected onto the 2D images to match the observed filaments. An example of this procedure is shown in figure 5.4 where a field line is projected at 20 cm from the last closed flux surface (LCFS) to match the observed filament which is shown more clearly in the background subtracted images (b) and (c).

This analysis procedure described above is done in the following steps:

- A magnetic equilibrium is calculated for the discharge at the required time t_0. This is achieved by calling the EFIT code and is done to within 200 μs of t_0. This results in a 2D cross-section (assuming toroidal symmetry) of poloidal and toroidal magnetic field strength and the location of the LCFS in major radius is also determined.
- Starting at the mid-plane $z = 0$ and radius of the LCFS, and for a given toroidal angle, the magnetic field is followed in both directions towards upper and lower targets. This gives the shape of a single field-line in 3D. Due to the toroidal symmetry of the total magnetic field, this field-line can then be rotated toroidally

to map out the flux-surface at the chosen radius.

- The 3D calculated field is then mapped onto 2D pixel locations using the projection method taking into account camera characteristics. To fit filaments in the toroidal direction, the toroidal angle is changed and the mapping re-calculated until the observed filament in the image is matched to the observed field-line.
- To fit filaments in the radial direction, the procedure described above is usually repeated for a range of field lines which are generated in 1 cm steps from the LCFS.

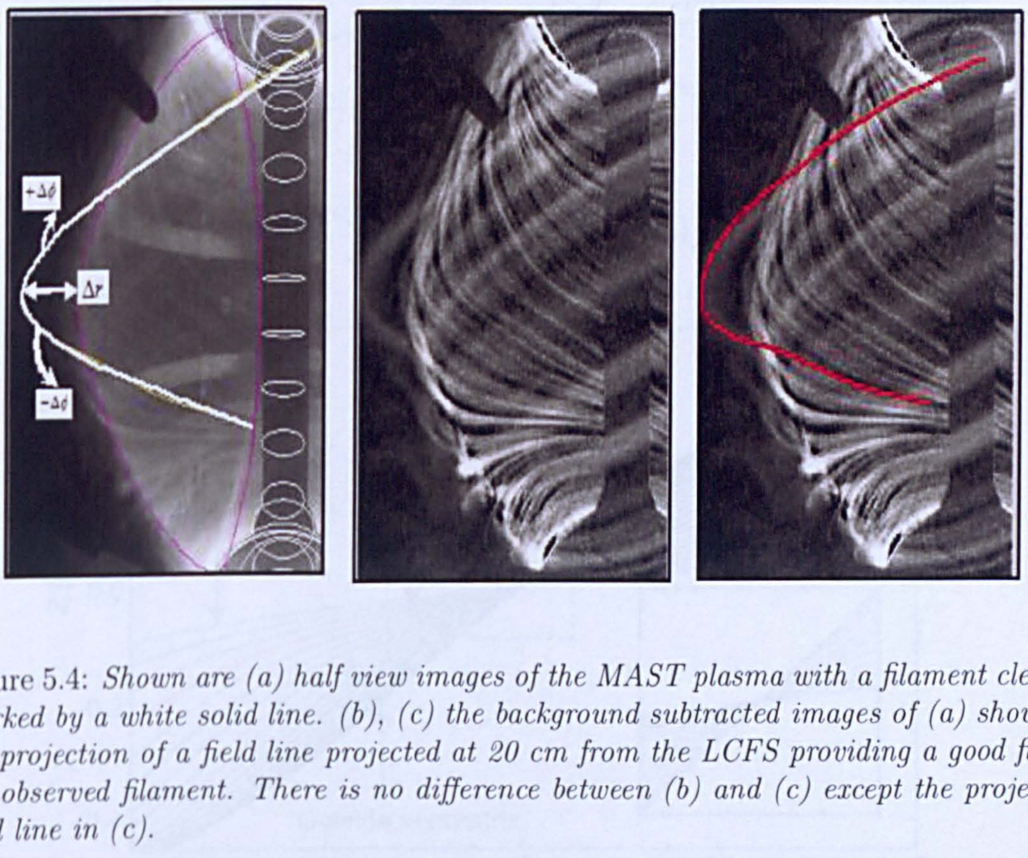

Figure 5.4: *Shown are (a) half view images of the MAST plasma with a filament clearly marked by a white solid line. (b), (c) the background subtracted images of (a) showing the projection of a field line projected at 20 cm from the LCFS providing a good fit to the observed filament. There is no difference between (b) and (c) except the projected field line in (c).*

Crucially, the tracking of filaments is made possible not only because of their field-aligned property, but because changes in radius of the field-lines from the LCFS in the MAST machine have an observable effect on the field-line pitch. This in turn is due to the spherical tokamak geometry. Shown in figure 5.5 are the 3D representations of field-lines at an arbitrarily-fixed toroidal angle projected in 1 cm steps from the LCFS. The twisting effect is better illustrated in the second plot figure 5.5(b) where the EFIT-generated field-lines are plotted in (ϕ, Z) space. This shows more clearly that as the filament is radially-propagating, and in order to follow the local magnetic field-lines, the filament becomes steeper as it moves outwards starting from a position

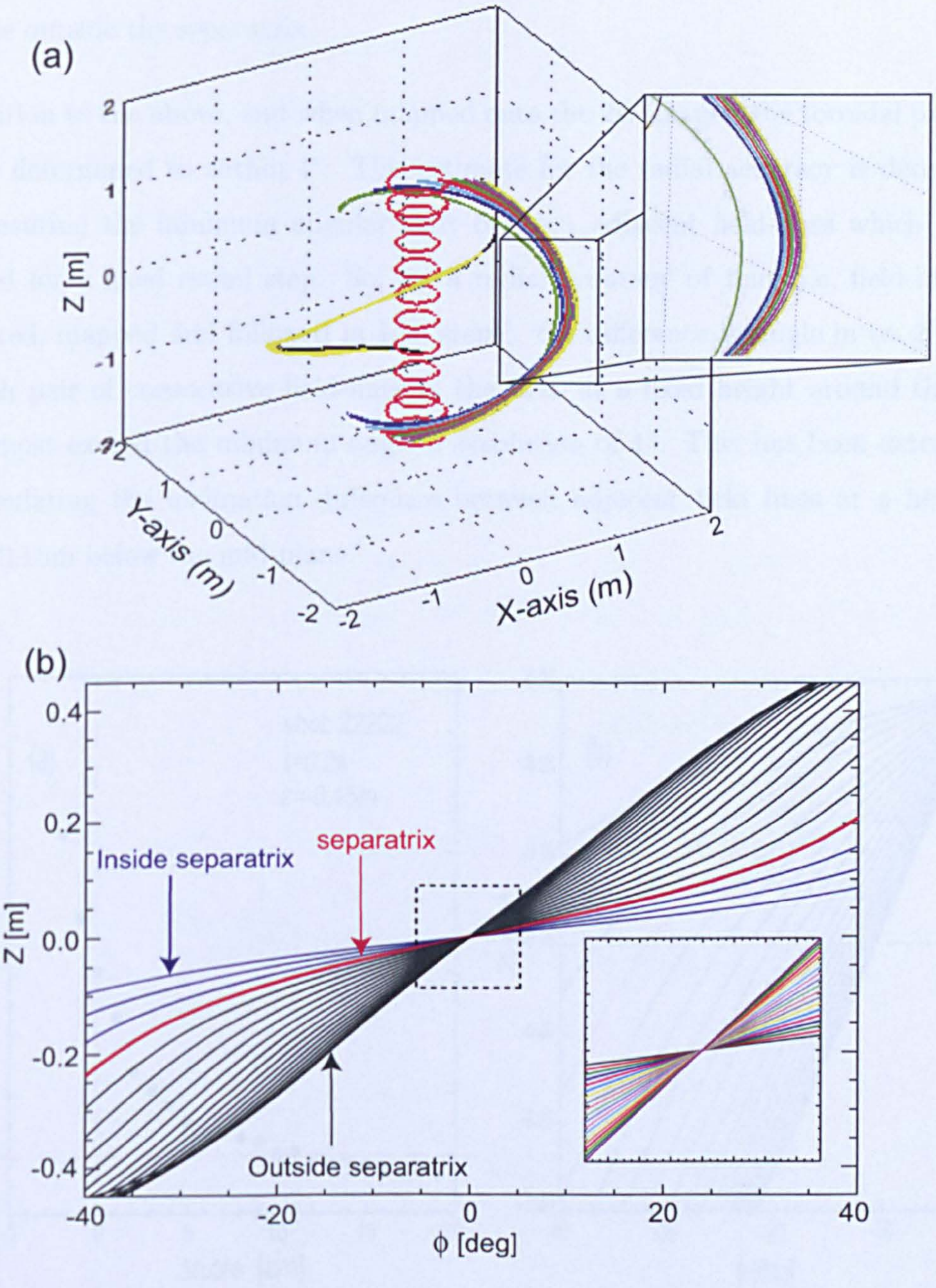

Figure 5.5: *Shown are (a) 3D representation of a field-line for a fixed toroidal angle in 1 cm steps from the LCFS. The filament in green is at the LCFS, (b) 2D representation of a field-line in* Z, ϕ *space from* $\Delta r_{LCFS} = -2$ *cm inside the separatrix (blue), at the separatrix (red) to a position* $\Delta r_{LCFS} = 15$ *cm outide the separatrix (black). A significant change of the pitch angle is observed outside the separatrix. The varying field-line pitch forces the filament to become steeper (i.e. more inclined) with distance in the SOL to follow the magnetic field lines.*

inside the separatrix $\Delta r_{LCFS} = -2$ cm, through the separatrix marked by the red line, to a position $\Delta r_{LCFS} = 15$ cm. The implication here is that there is significant change in the field-line pitch angle that a tracking of filaments during their radial motion is possible outside the separatrix.

In addition to the above, and when mapped onto the 2D images, the toroidal positions can be determined to within 1°. This estimate for the radial accuracy is determined by measuring the minimum angular shift between adjacent field-lines which can be resolved for a fixed radial step. So, for a radial accuracy of 1cm (i.e, field-lines are generated, mapped and followed in 1cm steps), the difference in angle in (ϕ, Z) space for each pair of consecutive field-lines in the SOL at a fixed height around the mid-plane must exceed the minimum angular resolution of 1°. This has been determined by calculating the inclination difference between adjacent field lines at a height of $Z = -0.15$m below the mid-plane.

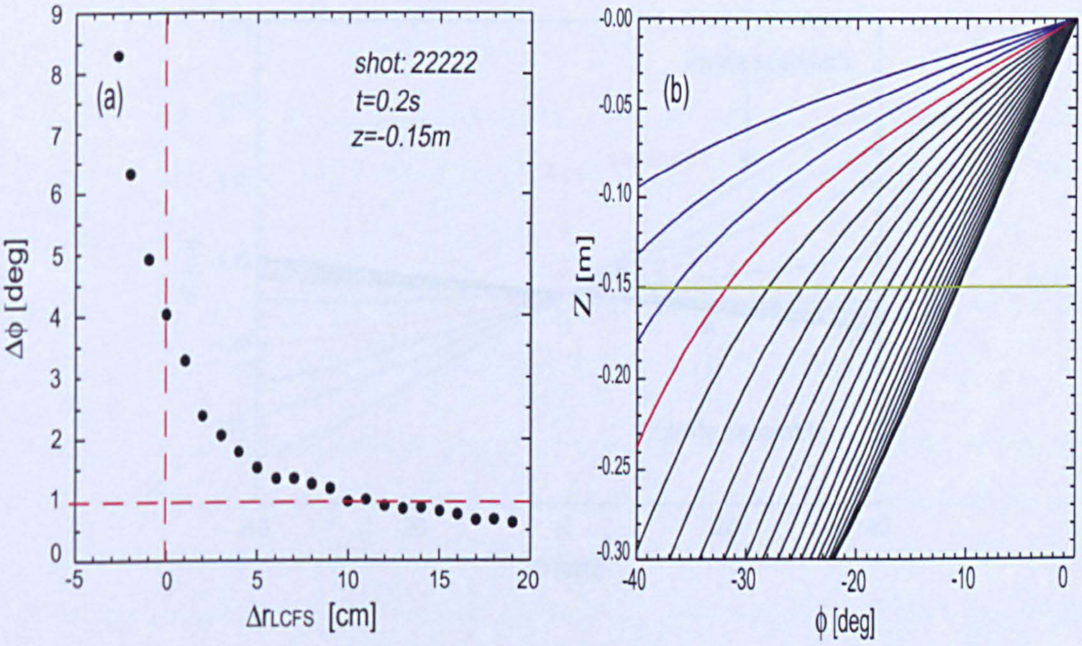

Figure 5.6: *Shown are (a) the measured pitch angle change at* $Z = -0.15$ m *below the mid-plane for each pair of consecutive field-lines as a function of* Δr_{LCFS}*, (b) shows the intersection of the* $Z = -0.15$ m *line with EFIT-calculated field-lines which have been generated in 1 cm steps*

Figure 5.6(a) shows the measured pitch angle change at $Z = -0.15$ m below the midplane for each pair of consecutive field-lines as a function of Δr_{LCFS} (the distance away from the LCFS). Figure 5.6(b) shows the intersection of the $Z = -0.15$ m line with the generated field-lines which have been generated in 1 cm steps.

As can be seen, a radial accuracy of 1 cm is maintained up to a distance of 15 cm where the minimum angle change is approximately 1°. Beyond this distance, the minimum angular separation falls to 0.5° but filaments in this thesis will not be tracked beyond this distance. However, it is important to note that in reality radial and toroidal motions are not entirely decoupled. As will be shown later, filaments are seen to propagate in toroidal and radial directions simultaneously.

Divertor views

It follows from figure 5.6 that the optimum choice of camera views for tracking field-lines are those near the mid-plane because of the significant changes of pitch angle as a function of SOL distance. This is in stark contrast to regions near the X-point region: Figure 5.7 shows the twisting of field-lines in 1 cm steps near the magnetic null point from $\Delta r_{LCFS} = -2$ cm inside the separatrix (blue), at the separatrix (red) to a position $\Delta r_{LCFS} = 10$ cm outside the separatrix (black). It can be seen that the distinction between field-lines is much less obvious near the X-point region, especially

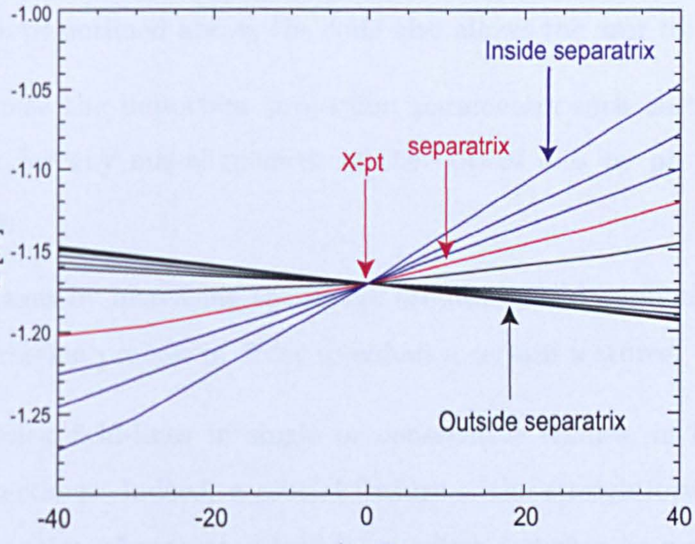

Figure 5.7: *Twisting of a filament near the X-point region as it propagates radially in 1cm steps from the LCFS outwards. The filament in red is at the LCFS. Distinction between filaments beyond 2 cm outside the LCFS is more difficult.*

after a distance of 2 cm.

5.2.1 Manual tracking of filaments

Since the analysis process involves several steps, ranging systematically from:

- loading the images according to the time and discharge,
- reconstruction of the magnetic equilibrium and field line generation using the EFIT code,
- projection of the 3D data (field lines and vessel components) onto the images,

all the while allowing for easy use and simple comparisons between consecutive frames from the same/or different discharges, a suite of analysis codes was developed to maximise efficiency of performing all these steps.

The DEFINER code was developed, and makes use of the IDL interactive widget facilities. A sample snapshot of the interactive widget can be seen in figure 5.8. In addition to the steps outlined above, the code also allows the user to:

- easily optimise the important projection parameters such as the focal length, and correct for any mis-alignement of the optical axis by projection of vessel components,
- enhance images by increasing the image brightness and applying the non-linear gamma correction process in order to enhance certain features,
- manually track field-lines in single or consecutive frames, in both radial and toroidal directions. Indeed, a crucial feature is the straightforward selection of the radial position of generated field-lines, which can then be easily changed and mapped when selected. The field-line for a given radius may also be rotated toroidally by moving the cursor on the sliding bar representing the full range of toroidal angle. The radial and toroidal positions of individual filaments can then be manually determined by choosing the best fit between the mapped field line and the observed filament.

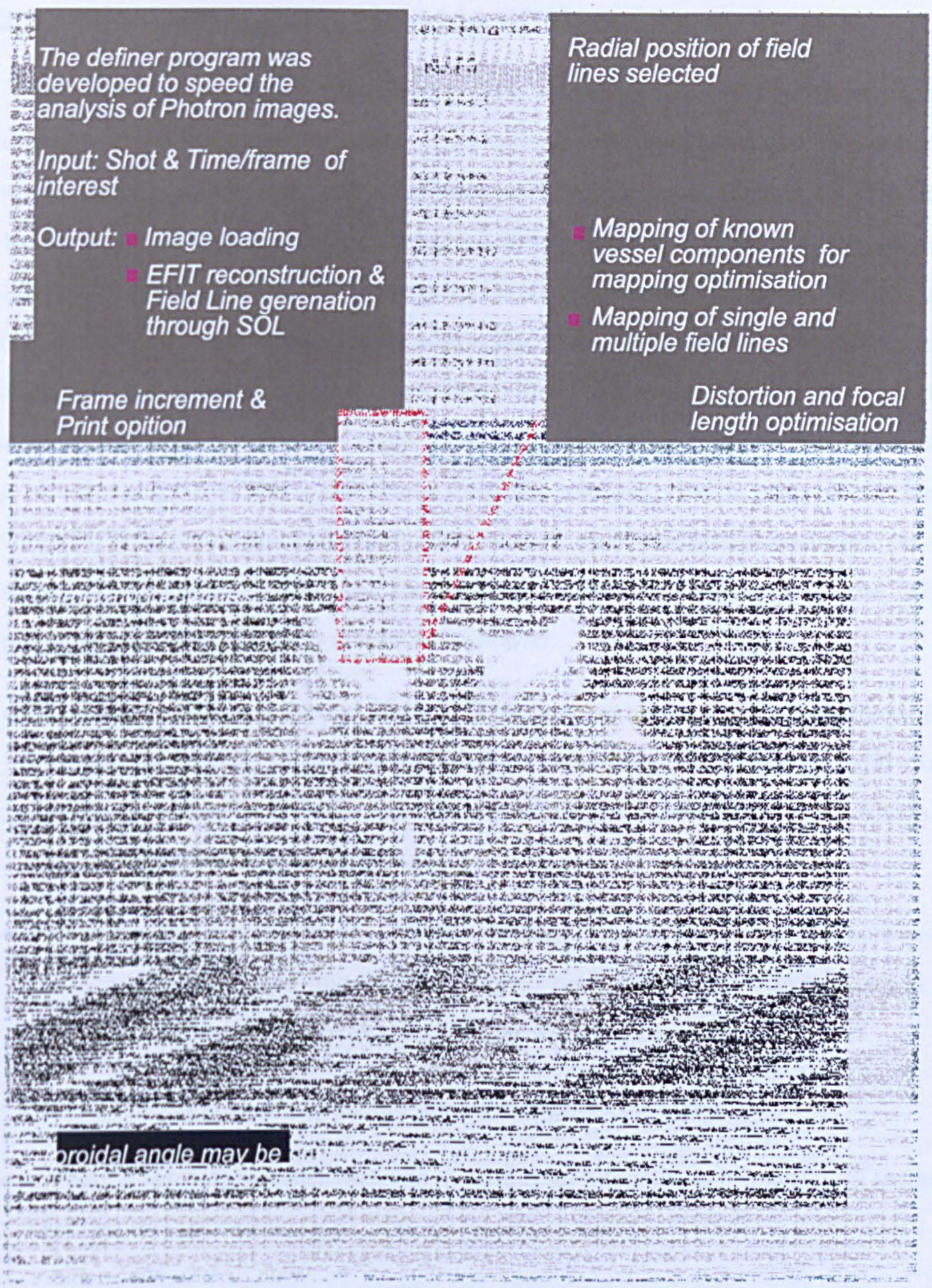

The definer program was developed to speed the analysis of Photron images.

Input: Shot & Time/frame of interest

Output:
- Image loading
- EFIT reconstruction & Field Line gerenation through SOL

Frame increment & Print opition

Radial position of field lines selected

- Mapping of known vessel components for mapping optimisation
- Mapping of single and multiple field lines

Distortion and focal length optimisation

oroidal angle may be

Figure 5.8: *The definer program: Due to axisymmetry of the magnetic field, mapped field-lines can be rotated toroidally at any given radius, or moved radially for a fixed toroidal angle. The radial and toroidal positions of individual filaments can then be determined manually by choosing the best fit between the mapped field line and the observed filament.*

5.2.2 Semi-automated tracking of filaments

When locating filaments and tracking their radial and toroidal motions, manual analysis has the advantage that unusual situations or spurious noise can be dealt with. However, manual analysis is time-consuming and limited to small samples. An automated mode of analysis is needed in addition to the manual tracking, to overcome the limitations of small samples, time constraints and subjective judgements. To this end, a semi-automated mode of analysis is also adopted in which a radial position is fixed *a priori* and the toroidal locations are determined. As will be shown, although this solution is not perfect since the radial position needs to be fixed, it has the advantage of removing subjective judgements from the analysis, and is particularly useful for inter-ELM filaments since measurements of their spatio-temporal evolution (as will be shown in section 5.4) show that the majority of filaments remain near the LCFS. More specifically, the following stages are followed:

- The radial position is fixed at the LCFS (or another chosen radius), and field-lines are mapped in 0.5° steps over a chosen toroidal range $\Delta\phi$. The toroidal range can be chosen so as to span the whole plasma in full view images, or a smaller range for smaller camera images.
- For each toroidal location, the intensity is calculated as the mean image intensity along a projected field-line at that angle. Each field-line is then ascribed an average intensity ($\bar{I}$) which is stored along with the field-line angle.

The toroidal locations of the filaments are subsequently obtained by:

- unfolding the total intensities so as to obtain an intensity as a function of toroidal angle trace $I(\phi)$, where

  $$I_\phi = \sum\nolimits_{i=0}^{i=\Delta\phi} \bar{I}(\Delta R_{LCFS}, i), \tag{5.12}$$

  corresponding to all mapped field-lines, and
- and applying suitable peak detection algorithms.

Averaging along the field line has the advantage of picking out peaks in intensity which are aligned with the field-lines, while reducing the amplitude of noise which will not be aligned with the projected field-lines. Note also that since the image intensity may vary significantly across the image, especially in the divertor region (where the light intensity dominates), the length of projected field-lines in the analysis method is cropped to a specific region of interest which is selected at the start. This has the effect of reducing the effect of ambient light in bright areas which would otherwise distort the results. Finally, note that the assumption of a fixed radial position introduces a further uncertainty of ~ 2° in toroidal angle for each 1 cm deviation in radial position. An example of this technique is illustrated in figure 5.9. Here, the radial position of field-lines is chosen to be the LCFS.

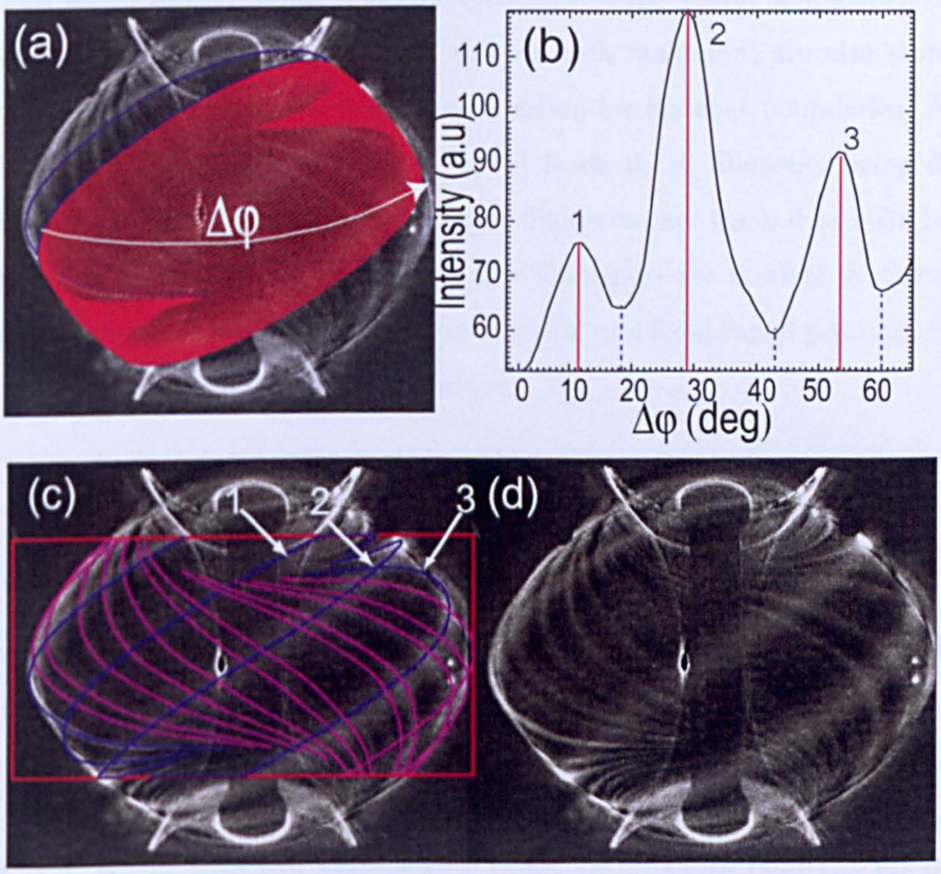

Figure 5.9: *(a): full view image with superposed field lines. (b): average intensity measured along each projected field line spanning the toroidal angle shown in (a). The maxima (marked by continuous red lines) correspond to filaments, and the minima (dashed blue lines). (c) the 3 detected filaments numbered 1–3 in (b) are shown along with other field-lines. (d) the background subtracted image shown for reference. Note the far left filament in (c) is not considered in toroidal range $\Delta\phi$. The filament labelled 1 is a low intensity filament.*

Shown is (a) the background-subtracted inter-ELM image with 130 projected field-lines on the near side of the plasma at 0.5° intervals covering a toroidal angle $\Delta\phi \equiv 65°$ as indicated by the white arrow, (b) the unfolded total intensity as a function of $\Delta\phi$ clearly showing the existence of three peaks with varying intensities within $\Delta\phi$, (c) is the result of this technique applied for the same inter-ELM frame to a full toroidal turn, (d) the background-subtracted image is shown for reference. The field-line averaging procedure is limited to the image intensity bounded by the red box.

As can be seen from the $I(\phi)$ trace, peaks (marked by solid red lines in 5.9(b)) and troughs (blue dashed lines) are found within $\Delta\phi$ and their positions recorded. When projecting the field-lines at the toroidal locations of the three maxima, the field-lines are indeed found to correspond with the locations of the visible filaments seen in the image. The minima which exist either side of each maximum are also stored since their locations can be used as a first approximation for filament boundaries. Applying this technique to the full toroidal turn in (c) leads to all filaments being detected. Filaments on the side nearer the camera (near filaments) are marked by solid blue lines while those on the far side of the plasma (far filaments) are marked by the magenta lines. As can be seen, despite the initial assumption of a fixed radial position, filaments are successfully localised using this technique.

5.2.3 Effect of far/near filaments on $I(\phi)$

Effect of far/near filaments on $I(\phi)$

Since the measured image intensity in the field-line fitting procedure is a combination of the intensity of the far (near) filaments for a given angle with a contribution from the near (far) filaments, a clarification of the effects of spurious contributions on the field-line fitting is now made. For this, it is important to note that near filaments are located at ~ 0.7 m, and will appear as a result to be wider than the far filaments located at ~ 3.5 m from the camera. As a result, although the total amount of light from near filaments is greater than from far filaments, the increased apparent breadth of the near filaments makes them appear faint relative to the far filaments which appear brighter. It is for this reason that, when fitting field-lines on the far side of the plasma, the contribution from the broad faint near filaments can be ignored since it is spread over many far filaments. An example of this is shown in figure 5.10 where the near filament indicated by the red double arrow in the rectangular box A spreads over many far filaments.

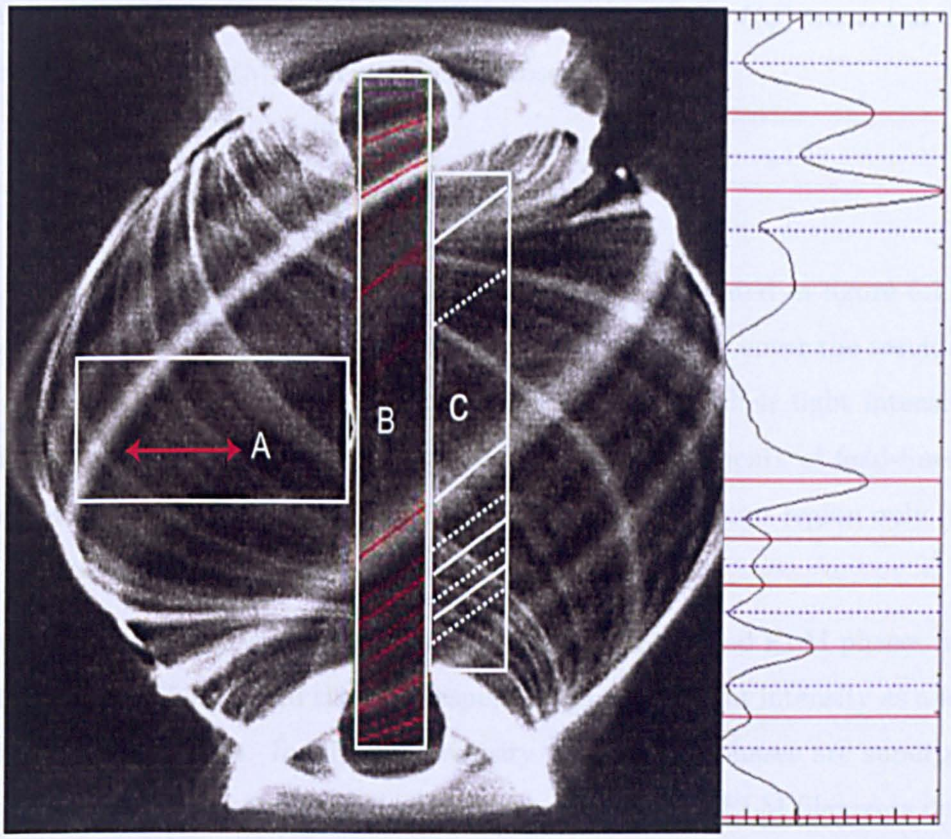

Figure 5.10: *(a): full view image of inter-ELM frame. In region A, the contribution of near filaments is spread over many far filaments. Region B has the advantage of no background light. A comparison of $I(\phi)$ traces obtained in regions B and C confirm that far filaments have no significant effect on the $I(\phi)$ signal. Example of $I(\phi)$ measured along centre-column is the vertical signal next to main image.*

Furthermore, the reverse situation is also true: although the filaments on the far side are generally brighter and "apparently" narrower, their contribution to the light intensity when fitting field-lines on the near side can also be ignored, due mainly to the difference in field-line pitches between near and far side filaments. More specifically, since it is the average intensity that is calculated for each near field line, this means the contribution of even the brightest of far filaments will only affect a small number of pixels along the near filament. In order to verify this, a comparison is made of the I_ϕ signals obtained from the analysis procedue is applied separately to two distinct regions: (1) the centre-column region where there is no contribution of background light (see region B in figure 5.10) and (2) an adjacent region (region C) where the image intensity is a combination of both near and far filaments. It was found from the comparison that no significant effect was found on the shape of the I_ϕ signals. Inclusion of the far filaments may result in a small distortion to the measured shape of the peak in the $I(\phi)$ trace, but does not significantly alter the location or number of observed peaks.

5.3 Light intensity comparison

Another example of semi-automated detection is presented in figure 5.11. Positions of filaments in L-mode, inter-ELM and ELM phases that cover the toroidal angle $\Delta\phi \sim 110°$ on the near side to the camera are found, and their light intensities are measured and compared. Note that light intensity measurements of field-lines, when mapping at half-degree steps, are restricted to the centre column region only (marked by the dashed white box in figure 5.11(a)).

Shown are (a,b,c) full view images of inter-ELM, L-mode and ELM phases from the same discharge (#15586), and their corresponding traces of light intensity as a function of scanned toroidal angle. In (d), the intensity traces of all phases are superposed in order to compare the fluctuations of each phase. Because the ELM filaments dominate the light emission, all intensities are normalised to the maximum peak ELM amplitude. Filaments of each type have been overlaid onto the images such that inter-ELM, L-mode and ELM filaments are marked by the blue (dotted), red (dashed) and green (solid) lines respectively.

The magnitudes of the relative light intensity fluctuations across the discharge vary considerably in the SOL, with maximum registered relative amplitudes of 14, 40 and 140 in arbitrary units for inter-ELM, L-mode and ELM regimes respectively.

A complementary piece of information can also be obtained: the number of filaments per fixed toroidal angle $\Delta\phi$, which is an indicative figure of the quasi toroidal mode number, is largest for the L-mode phase, followed by the inter-ELM, and lastly the ELM.

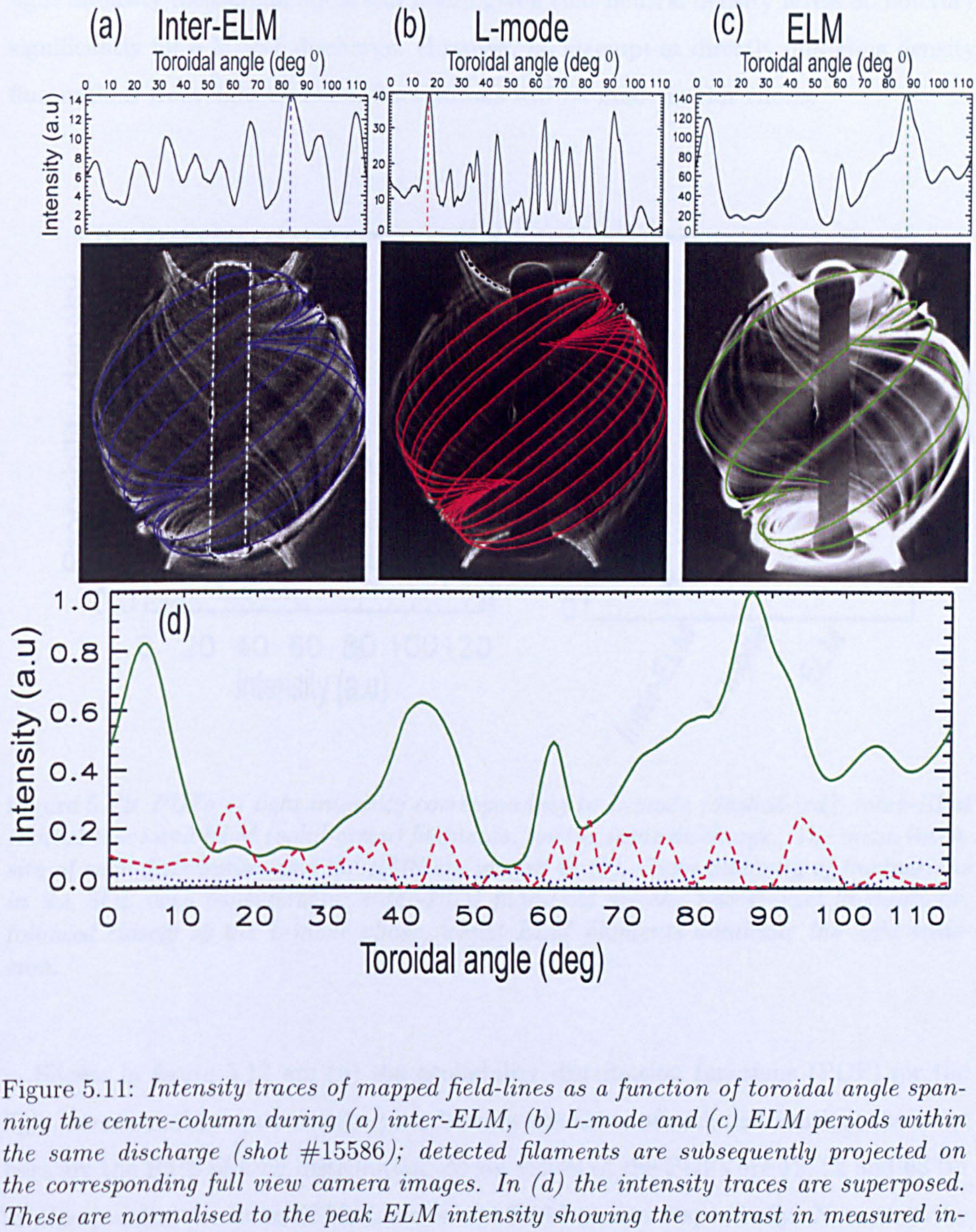

Figure 5.11: *Intensity traces of mapped field-lines as a function of toroidal angle spanning the centre-column during (a) inter-ELM, (b) L-mode and (c) ELM periods within the same discharge (shot #15586); detected filaments are subsequently projected on the corresponding full view camera images. In (d) the intensity traces are superposed. These are normalised to the peak ELM intensity showing the contrast in measured intensities across the three phases.*

A statistical analysis of the light intensity for each type of filament is obtained by repeating the procedure above for many frames within the same discharge. Though fluctuations in the D_α light intensity $I = n_0 n_e f(T_e)$ are due to fluctuations in either neutral density n_0, electron density n_e or electron temperature T_e, a comparison of light intensity measurements is still useful given that neutral density levels do not vary significantly for a MAST discharge. However, no attempt at directly unfolding density fluctuations from light emission fluctuations will be made in this thesis.

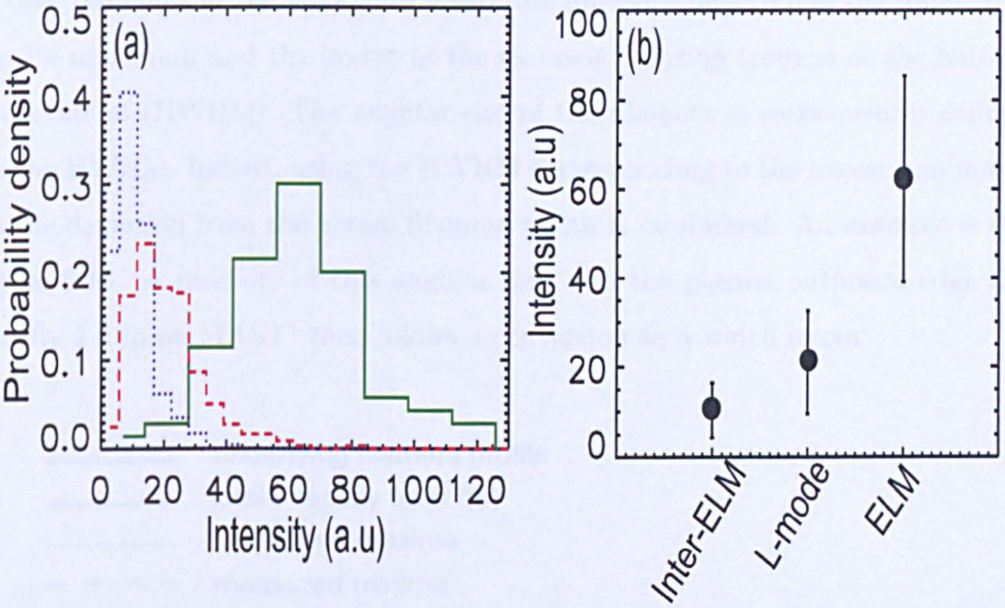

Figure 5.12: *PDFs of light intensity corresponding to L-mode (dashed-red), inter-ELM (dotted-blue) and ELM (solid-green) filaments, for the same discharge. The mean intensity of each distribution and the RMS are plotted in (b). Light intensity of fluctuations in the SOL vary considerably: inter-ELM filaments are the lowest-level fluctuations, followed closely by the L-mode phase, whilst ELM filaments dominate the light emission.*

Shown in figure 5.12 are (a) the probability distribution functions (PDF) for the light intensity, (b) a quantitative plot showing the mean of each distribution; the error bars are the RMS of each distribution. Mean values of the PDFs are 12, 22 and 63 (in arbitrary units) for inter-ELM, L-mode and ELM phases respectively. Note that the PDF intensities are not gamma-corrected or amplified. While the inter-ELM filaments are the weakest fluctuations in the MAST SOL, the light emission of L-mode filaments is twice that of the inter-ELM; and both these are much smaller than the stronger ELM disturbance.

5.4 Physical properties

Filament width measurement

As mentioned previously, estimates of the filament width (L_ϕ) have been obtained from the width of its corresponding peak in D_α emission. For any given peak, the method is to take the point in the $I(\phi)$ trace where the intensity falls to half the difference between its maximum and the lowest of the two neighbouring troughs as the half-width half maximum (HWHM). The angular size of the filament is subsequently defined as twice the HWHM. Indeed, using the HWHM corresponding to the lowest minimum ensures the deviation from the actual filament width is minimised. An example is shown in figure 5.13. A measure of this angular size, and the plasma outboard edge radius (typically 1.4 m on MAST) then allows a conversion to a width in cm.

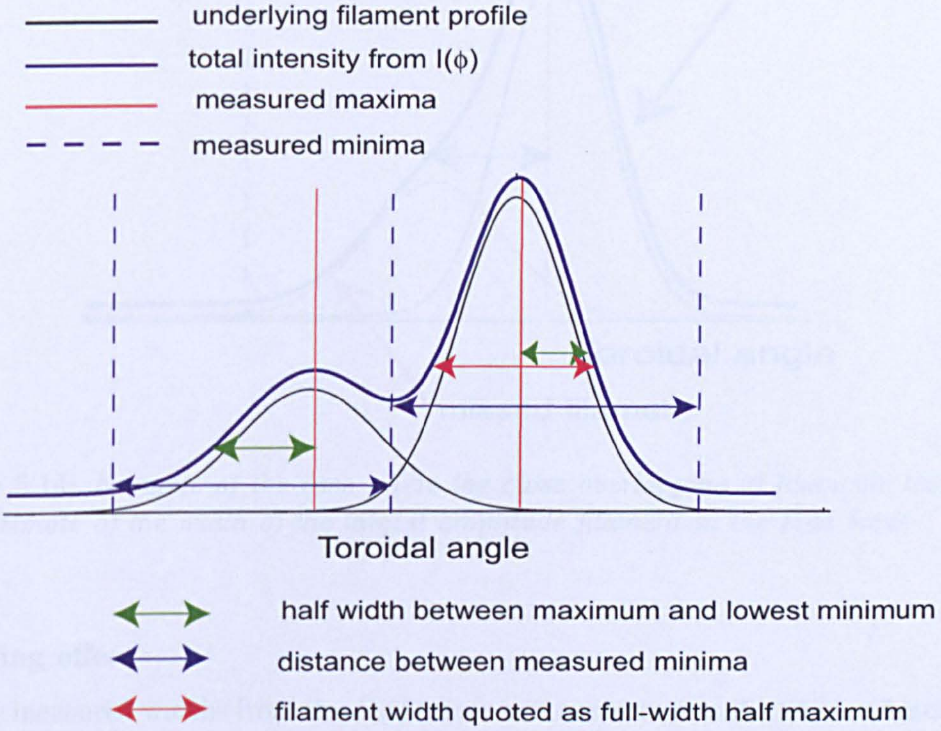

Figure 5.13: *Measurement of filament width: method is to take the point in the $I(\phi)$ trace where the intensity falls to half the difference between its maximum and the lowest of the two neighbouring troughs as the half-width half maximum HWHM (indicated by the green double arrows). Filament width is then quoted as Full Width Half Maximum.*

The measurements of filament widths using this method are a good first approximation when the filaments are regularly spaced; however, as will be shown later in section 5.5, separations between filaments are not constant and due to toroidal motion are constantly changing. Figure 5.14 shows one example where the close proximity of a small amplitude filament (see red curve in figure 5.14) to a neighbouring large amplitude filament (black curve) may lead to an over-estimation of the width of the large amplitude filament. Indeed, due to the close proximity of both filaments, the algorithm for peak detection in the $I(\phi)$ signal only picks out the larger filament, and records the large filament with an even larger width (see blue curve) because the minimum is displaced further from its true minimum.

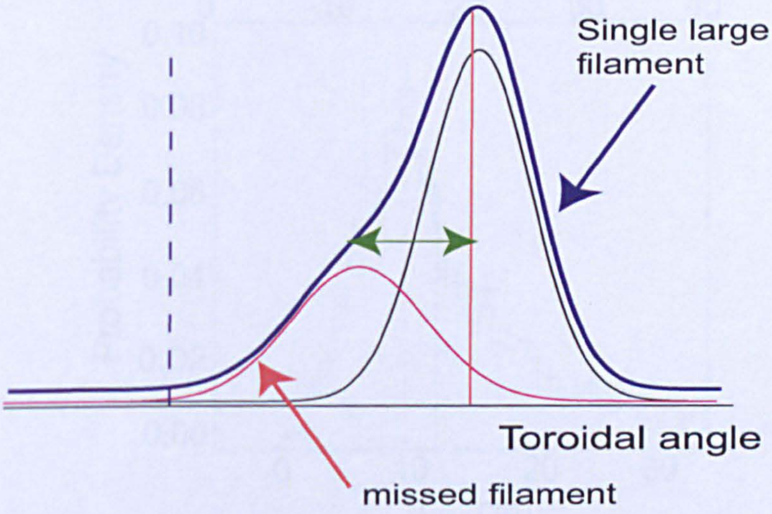

Figure 5.14: *Example of the case where the close overlapping of filaments leads to an overestimate of the width of the largest amplitude filament in the* $I(\phi)$ *trace.*

Blurring effect

The measured widths from the $I(\phi)$ traces are overestimates due to broadening which results from filament rotation over an integration time. This effect has been estimated in simulations where the D_α emission of a filament is prescribed as an initial Gaussian profile, and the Full Width Half Maximum (FWHM) corresponds to a pre-determined initial width. Assuming an average toroidal velocity of 9±2 km s^{-1} (as will be shown later), it was found that during a typical integration time of 10 μs, the final simulated filament width (which is the integrated sum of all Gaussian profiles) is broadened by

$L_\phi^{rot} \equiv$ 4–6 cm. Taking also into account the field line pitch, the perpendicular filament width ($L_\perp$) is given by:

$$L_\perp = \left(L_\phi - L_\phi^{rot}\right)\cos\alpha, \tag{5.13}$$

where α is the pitch angle, typically ~ 30° on MAST.

PDF of filament widths

Examination of 2000 filament widths in beam-heated MAST discharge #15622 (I_p ~ 0.73 MA; B_ϕ ~ - 0.51 T; $\bar{n}_e/n_{\rm GW}$ ~ 0.3 – 0.5; q_{95} ~ 5.5 – 6.5) reveals the PDF shown in figure 5.15. The PDF is non-gaussian with a peak value (most likely) ~ 10 cm, and a mean value $\bar{L}_\perp$ ~ 11.5 cm.

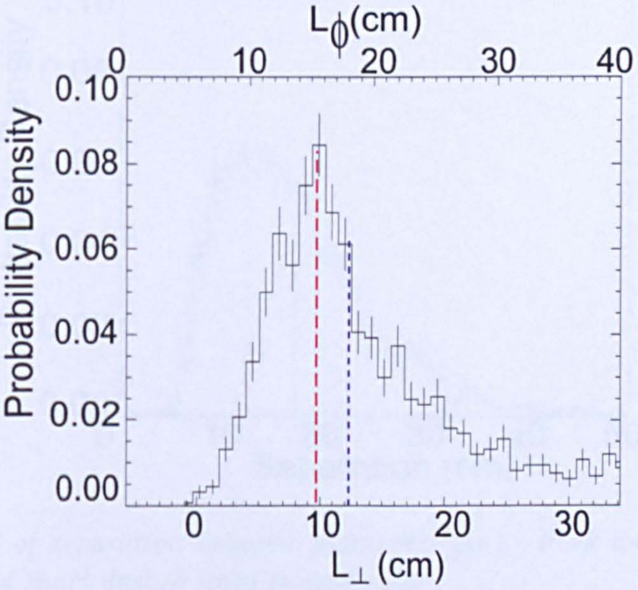

Figure 5.15: *Probability density function (PDF) of filament perpendicular widths ($L_\perp$); the top x-axis corresponds to the original measured widths (L_ϕ). Peak and mean values are marked by long and short dashed lines respectively.*

The long tail in the distribution is mainly due to the reasons outlined earlier: (a) the occurrence of closely-spaced and overlapping filaments whose separate widths have been measured as single filament widths, and/or (b) enhanced blurring resulting from filament rotation above 9 km s^{-1}. In order to test whether the occurrence of closely-spaced and overlapping filaments may lead to a non-gaussian PDF, artificial data was generated in Ref [94] so as to randomly change the filament separation. For this, a fixed number of Gaussians of a given width were added at random locations on a circular grid, and the intensity as a function of toroidal angle recorded. The effect of randomly changing the filament separations was to produce a spread of filament separations such that the underlying PDFs for filament separations and widths were indeed non-gaussian with long extended tails. Crucially, the peak in the distributions was recovered.

Filament separations

The separation (Δr) between filaments have also been measured: the PDF, shown in figure 5.16, has a peak value (most likely value) of $\Delta r \sim 15$ cm and a mean value $\Delta r \sim 18$ cm.

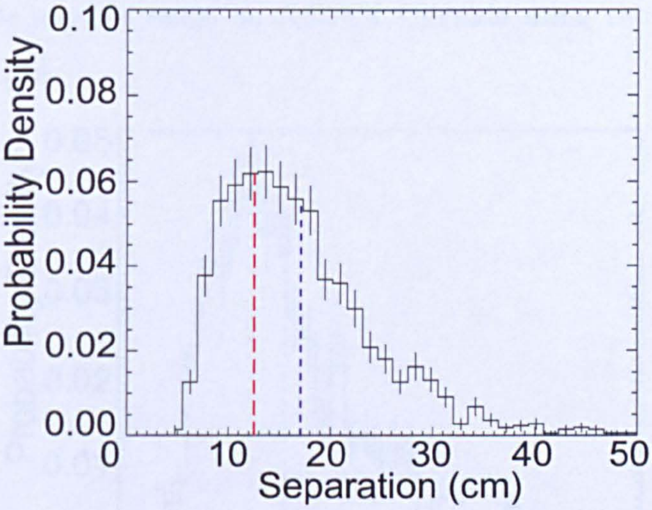

Figure 5.16: *PDF of separation between filaments* (Δr). *Peak and mean values are marked by long and short dashed lines respectively.*

Quasi Toroidal mode numbers

Although toroidal mode number n is strictly only defined for a regularly spaced structure with n peaks toroidally around the tokamak, some measure of quantifying the spacing and the number of filaments is still needed. For this reason, the terminology of a "quasi" toroidal mode number is used instead. One method to estimate the quasi toroidal number during the inter-ELM period, denoted herein as n_{ielm}, is to measure the filament separation and then to use the expression:

$$n_{\text{ielm}} = 2\pi R/\Delta r, \tag{5.14}$$

where R is the plasma radius. Using the peak separation of $\Delta r \sim 15$ cm (see figure

5.16), a peak quasi toroidal mode number $n_{\rm ielm} \sim 24$. The second method is to count directly the number of observed filaments which span the full toroidal circuit in the full view images. When smaller views are used, the method would then consist of counting the number of filaments over a toroidal domain, and then to define $n_{\rm ielm}$ = number × 360/toroidal domain. Using the second method when filaments are counted over the full toroidal domain, quasi mode numbers within the same discharge are found to vary significantly: they are found to be in the range 10–40 with a peak value of 20 and a mean, $\bar{n}_{\rm ielm} \sim 26$. This estimate is in agreement with the earlier estimate of $n_{\rm ielm} \sim 24$ from using the peak filament separation. Furthermore, the range of observed quasi mode numbers for the inter-ELM period is also in good agreement with the observed mode number range on ASDEX Upgrade using the vertical Thomson scattering system [50].

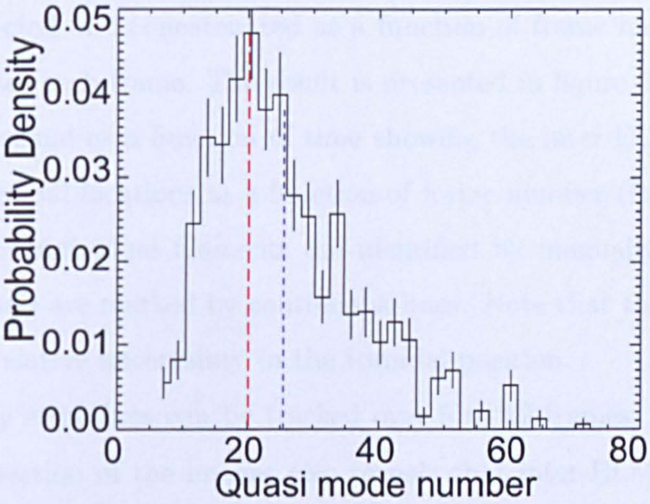

Figure 5.17: *Probability density function (PDF) of the number of filaments per toroidal circuit (quasi mode-number). Peak and mean values are marked by long and short dashed lines respectively.*

5.5 Toroidal propagation

A quantitative measurement of the spatiotemporal evolution of filaments during inter-ELM periods is made. In order to capture the fast dynamics, narrow views of the outboard midplane (see figure 5.18) are obtained at a frame rate of 100 kHz and an integration time of 7μs.

Figure 5.18: *An example of an analysed image with superposed field-lines marking the positions of far filaments.*

Filaments at the far side of the plasma are detected in consecutive frames for a fixed toroidal range $\Delta\phi$ spanning 90° for MAST discharge #16040 ($I_p \sim 0.63$ MA; $B_\phi \sim$ -0.48 T ; $\langle n_e^{ped} \rangle \sim 1.65 \times 10^{20}$ m^{-3}; $q_{95} \sim 7.2$). Figure 5.18 shows an example of an analysed raw mid-plane image (frame #3831) over which several field lines indicate the positions of the localised filaments. For each frame, toroidal positions of the far filaments in the toroidal range $\Delta\phi$ have been found from the $I(\phi)$ signals (of that frame) using the semi-automated analysis technique. These filament positions are subsequently collected and concatenated as a function of frame number (time). Note that 10 μs separates each frame. The result is presented in figure 5.19. Shown are (a) the midplane D_α signal as a function of time showing the inter-ELM period, (b) plot of the filament toroidal locations as a function of frame number (f=100kHz).
The trajectories of individual filaments are identified by manually joining intensity-correlated peaks and are marked by continuous lines. Note that the error bars are an indication of the relative uncertainty in the toroidal position.

The filamentary structures can be tracked over 5 to 12 frames, i.e, timescales $\tau \sim$ 50 – 120 μs. Inspection of the images also reveals that inter-ELM filaments for this MAST discharge show little sign of radial propagation (though as will be shown later, filaments do propagate radially outwards): they are found to remain in the immediate vicinity of the LCFS, i.e. $\Delta R_{LCFS} \leq 2$cm, while continuously rotating toroidally in the co-current direction. During their evolution, the filaments are found to rotate by a constant 2 – 5° every 10 μs which corresponds to a toroidal velocity in the range 5–12.5 km s^{-1}. As such, filaments rotate in the same direction as the pedestal, and at a significant fraction (up to 75 %) of the toroidal pedestal velocity measured by the charge exchange recombination spectroscopy system.

It is also found that whereas toroidal steps for any given filament are on average constant, the collective motions of the filaments is more complex: filaments are not

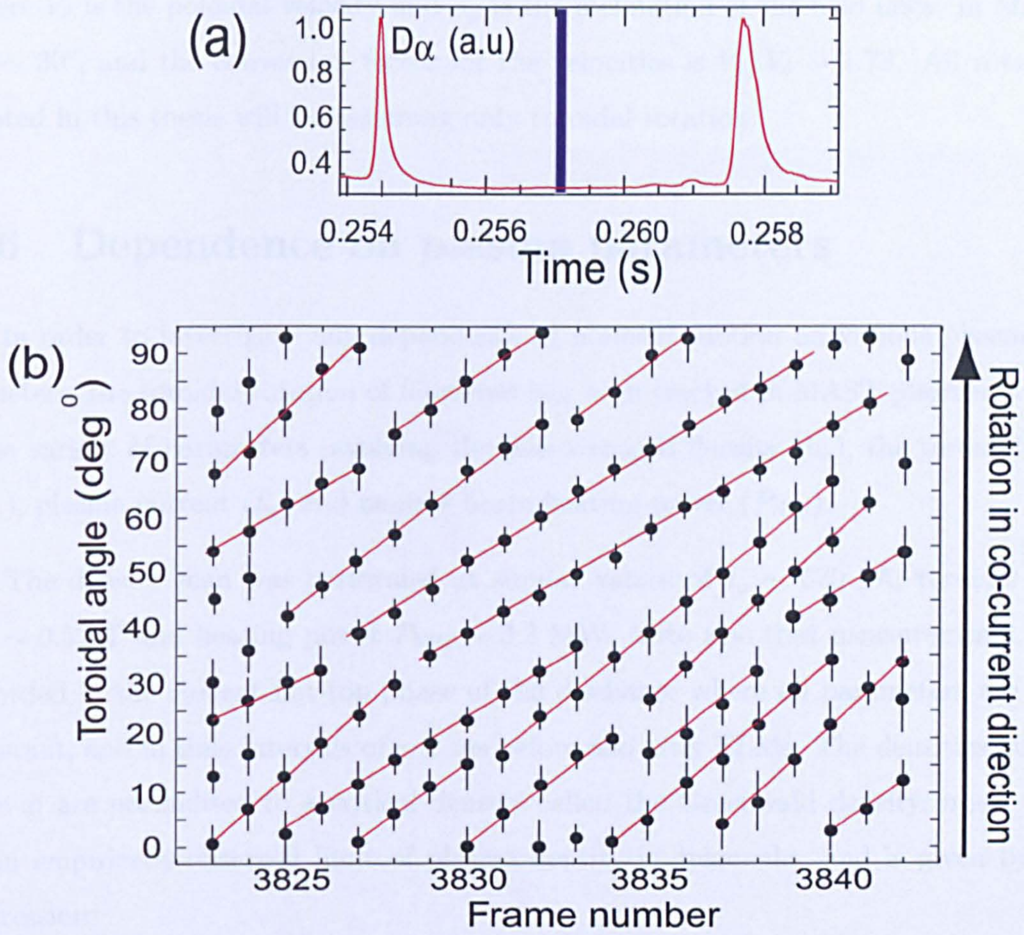

Figure 5.19: *(a) The D_α signal at the lower outboard target showing in blue the inter-ELM period, and (b) plot of the peak toroidal locations in the 0-90° range as a function of time. Trajectories of distinct filaments are marked by continuous lines.*

regularly spaced, and due to different toroidal velocities, their spacings are constantly changing. It is for this reason that inter-ELM quasi-mode numbers vary within the range 10–40 (see figure 5.17). It is important to note that due to the finite lifetime of these filaments, collisions between filaments are not observed.

Finally, a comment is made regarding poloidal motions of filaments. Due to toroidal geometry, it is impossible to distinguish between toroidal and poloidal motions, since geometrically, rotations in both directions are equivalent. This is known as the "Barber Pole" effect. As such, a poloidal motion can be described as a toroidal motion (and vice versa) such that:

$$V_\phi / V_\theta = \tan \alpha_p, \tag{5.15}$$

where V_θ is the poloidal velocity and α_p is the inclination of the field lines. In MAST, $\alpha_p \sim 30°$, and the conversion factor for the velocities is $V_\phi/V_\theta \sim 1.73$. All rotations quoted in this thesis will be assuming only toroidal rotation.

5.6 Dependence on plasma parameters

In order to investigate any dependence of filament motion on various plasma parameters, the toroidal rotation of filaments has been tracked in MAST plasmas with a wide variety of parameters involving the line-averaged density ($\bar{n}_e$), the toroidal field (B_ϕ), plasma current (I_p) and neutral beam heating power (P_{NBI}).

The density scan was performed at similar values of $I_p \sim 670$ kA, toroidal field $B_\phi \sim 0.52$ T and heating power $P_{\text{NBI}} \sim 3.2$ MW. Note also that measurements were recorded in the current flat-top phase of the discharge where all parameters are kept constant, and in time intervals of ~ 1 ms before and after ELMs. The densities quoted here-in are normalised to a critical density called the Greenwald density, n_{GW}. This is an empirically-observed limit of plasma density in tokamaks, and is given by the expression:

$$n_{\text{GW}}(10^{20}\text{m}^{-3}) = I_p/A\pi r^2, \tag{5.16}$$

where r is the minor radius measured in m and I_p is the plasma current measured in MA. As shown in Table 5.6, the low density discharges are characterised by a line-averaged plasma density normalised to the Greenwald density, such that $0.3 \leq \bar{n}_e/n_{\text{GW}} \leq 0.5$, whilst high densities are characterised by $0.55 \leq \bar{n}_e/n_{\text{GW}} \leq 0.8$. The threshold between high and low density intervals is simply the definition adopted in this analysis, and is not physically motivated.

Table 5.6: *A list of MAST discharges considered in the density scan showing the line-averaged plasma density normalised to the Greenwald density ($\bar{n}_e/n_{\text{GW}}$), parallel connection length ($L_\parallel$) and pedestal density (n_e^{ped})*

Dataset	Shot # range	$\bar{n}_e/n_{\text{GW}}$	$\langle L_\parallel\rangle$(m)	$\langle n_e^{ped}\rangle$ (10^{19} m^{-3})
Low density	18347–18353	0.3–0.5	7.20	2.1
High density	18354–18357	0.55–0.8	6.95	4.0

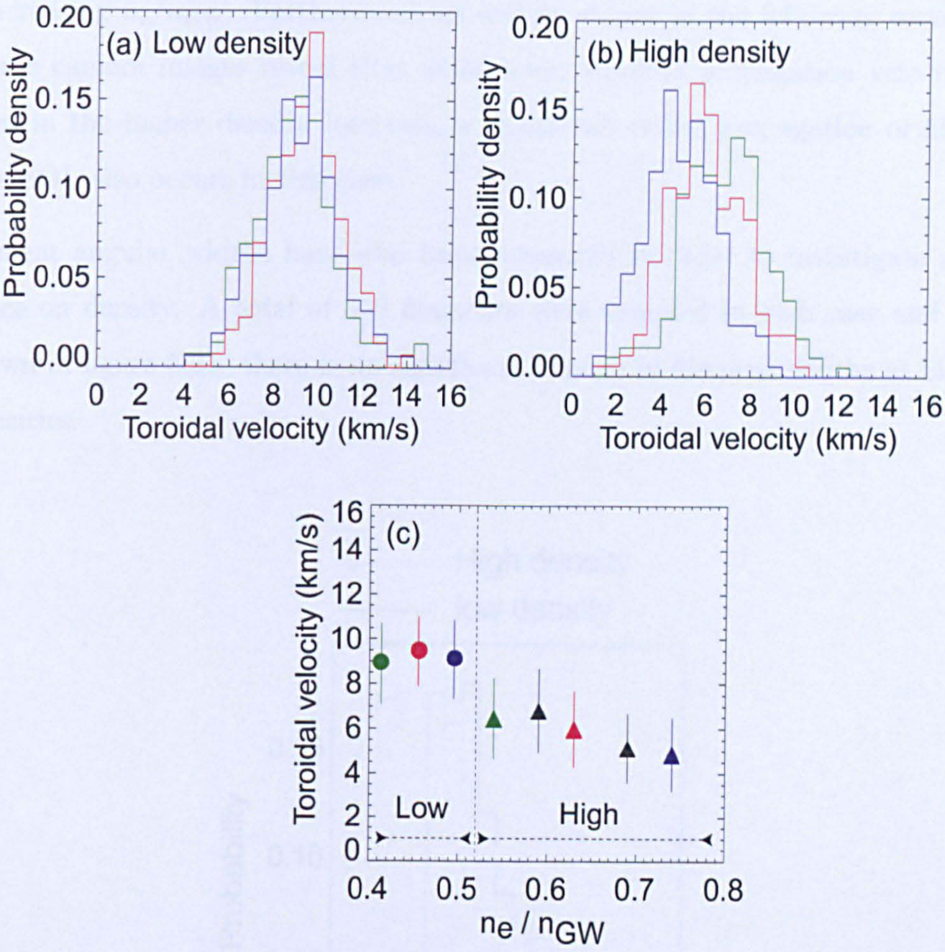

Figure 5.20: *PDFs of filament toroidal velocity in the case of plasmas at (a) low density* $0.3 \leq \bar{n}_e/n_{\mathrm{GW}} \leq 0.5$, *(b) higher density* $0.55 \leq \bar{n}_e/n_{\mathrm{GW}} \leq 0.8$; *(c) plot of the mean toroidal velocity as a function of* $\bar{n}_e/n_{\mathrm{GW}}$ *for all scans, where the color coded and represent the low and high density cases respectively. PDFs at low* $\bar{n}_e$ *show no significant changes with* $\bar{V}_\phi \sim 9 \pm 2$ *km* s^{-1}*; however, PDFs at high* $\bar{n}_e$ *show a systematic shift toward lower toroidal velocities (*$\bar{V}_\phi \sim 5 \pm 2$ *km* s^{-1}*) with increasing* $\bar{n}_e$.

Examination of 1000 filaments leads to the results presented in figure 5.20. Shown are (a) PDFs for the low density scan, (b) PDFs from the high density scan, and (c) plot of the mean toroidal velocity values for all scans with error bars $\pm 1\sigma$ as a function of $\bar{n}_e/n_{\mathrm{GW}}$. Whereas the PDFs in the low density discharges show little change with mean values of ~ 9 km s^{-1}, it is found that the PDFs in the high density intervals show a distinct shift toward lower toroidal velocities with increasing $\bar{n}_e/n_{\mathrm{GW}}$. The choice of cut-off does not change this overall trend. Regardless of the choice of cut off density, the main result here is that the observed toroidal velocity of inter-ELM filaments decreases with increasing $\bar{n}_e/n_{\mathrm{GW}}$. Furthermore, as will be shown in the following section, the mid-plane camera images reveal that while lower toroidal propagation velocities are recorded in the higher density intervals, a significant radial propagation of filaments into the SOL also occurs in this case.

Filament angular widths have also been measured in order to investigate any dependence on density. A total of 350 filaments were sampled in each case and results are shown in figure 5.21: there is no significant change in filament widths at high and low densities.

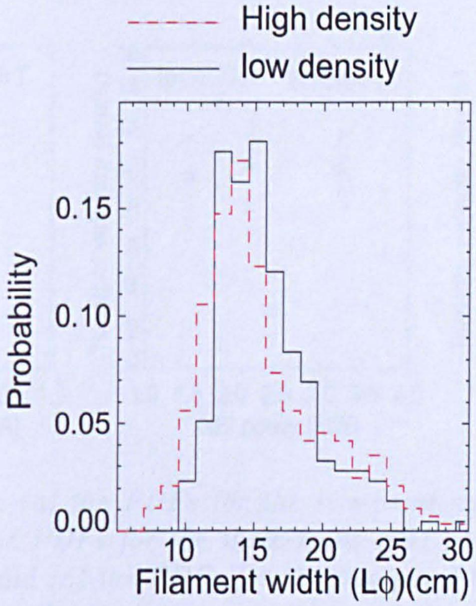

Figure 5.21: *PDFs for filament angular widths at high (solid) and low (dahsed) density plasmas. There is no significant change of filament width with density.*

Scans of toroidal velocity in I_p, B_ϕ and P_{NBI} have also been performed. Shown in figure 5.22 are (a) the PDFs for the two-point current scan, at $I_p = 630$ and 940 kA, (b) the PDFs for the three-point NBI power scan taken at $P_{\mathrm{NBI}} = 1.4$, 2.2 and 3.2 MW and (c) the PDFs for the two-point toroidal field scan $B_\phi = 0.42$ and 0.51 T; note the B_ϕ scans have been performed at high density. For each scan, the mean toroidal velocity ($\bar{V}_\phi$) of each distribution is plotted as a function of the scanning parameter. The error bars represent $\pm 1\sigma$. The PDFs in I_p and P_{NBI} parameters show no significant change in the measured toroidal velocities. A small change cannot be ruled out for the B_ϕ parameter but it is not significant.

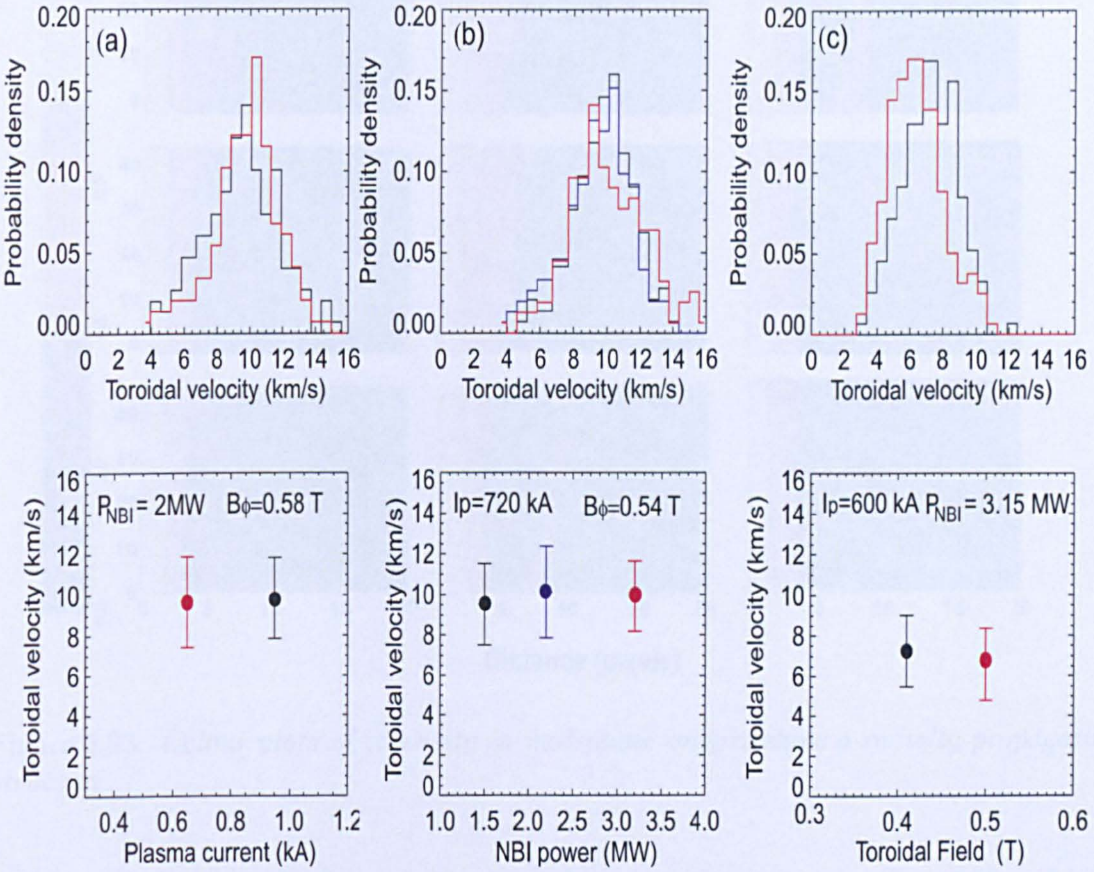

Figure 5.22: *Shown are (a) the PDFs for the two-point current scan at I_p values of 630 and 940 kA, (b) the PDFs for the three-point NBI power scan taken at $P_{\mathrm{NBI}} =$ 1.4, 2.2 and 3.2 MW and (c) the PDFs for the two-point toroidal field scan of $B_\phi =$ 0.4 and 0.5 T. Note that the B_ϕ scans are preformed at high density, whereas I_p and P_{NBI} were performed at low density. For each scan, the mean toroidal velocity, $\bar{V}_\phi$, of each distribution is plotted as a function of the scanning parameter. The error bars represent $\pm\sigma$. No significant change is observed in these scans.*

5.7 Radial propagation of inter-ELM filaments

Whilst it was shown in the previous section that filaments during inter-ELM periods usually remain close to the LCFS ($\Delta R_{LCFS} \leq 2$cm), with a dominantly toroidal rotation, it is found that they do occasionally propagate radially outwards; i.e. beyond the inner SOL region defined as $\Delta R_{LCFS} \geq 2$cm. The motion of such filaments is markedly different from the previous description of continuous toroidal rotation.

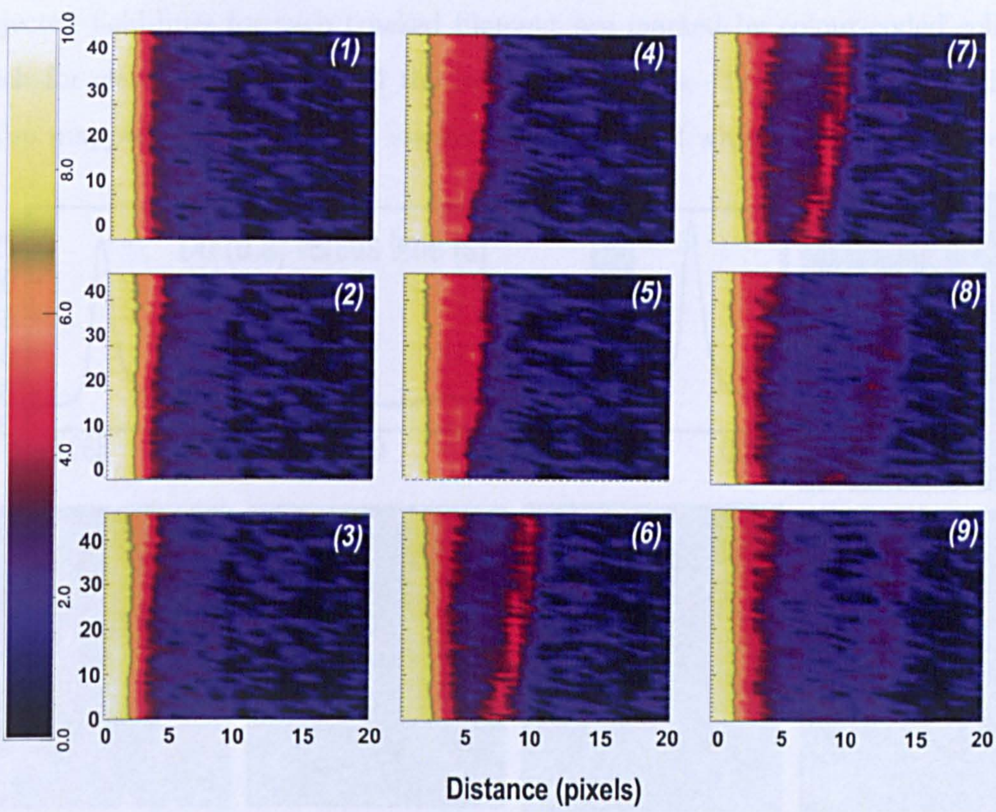

Figure 5.23: *Colour plots of intensity in mid-plane images show a radially-propagating structure.*

An example is shown in figure 5.23 where the mapped image intensity at the edge of a mid-plane image shows a radially propagating filament. Similar observations have been reported on NSTX [119]; however, as previously mentioned in section 2.7.2, their views were confined to the poloidal-radial plane due to the diagnostic set-up. This section presents new data concerning the radial propagation of inter-ELM filaments.

5.7.1 Tracking of radial motion

In order to gain more insight into the radial propagation on MAST, an example is shown in figure 5.24 where the motion of one protruding filament and its immediate neighbours are tracked using the manual tracking method described in section 5.2.1. For each frame, the radial distance of filaments from the LCFS (Δr_{LCFS}) and the toroidal steps ($\Delta\phi$) are simultaneously measured. Figure 5.24 shows in the top left corner the D_α time trace and a sequence (a-i) of images showing the temporal evolution of four filaments on the outboard mid-plane during the green-shaded time slice. The projected field-lines for each tracked filament are marked by colour-coded solid lines which for clarity extend beyond the image boundaries. The EFIT-calculated LCFS is also mapped onto the images marked by the dashed white and magenta line. The

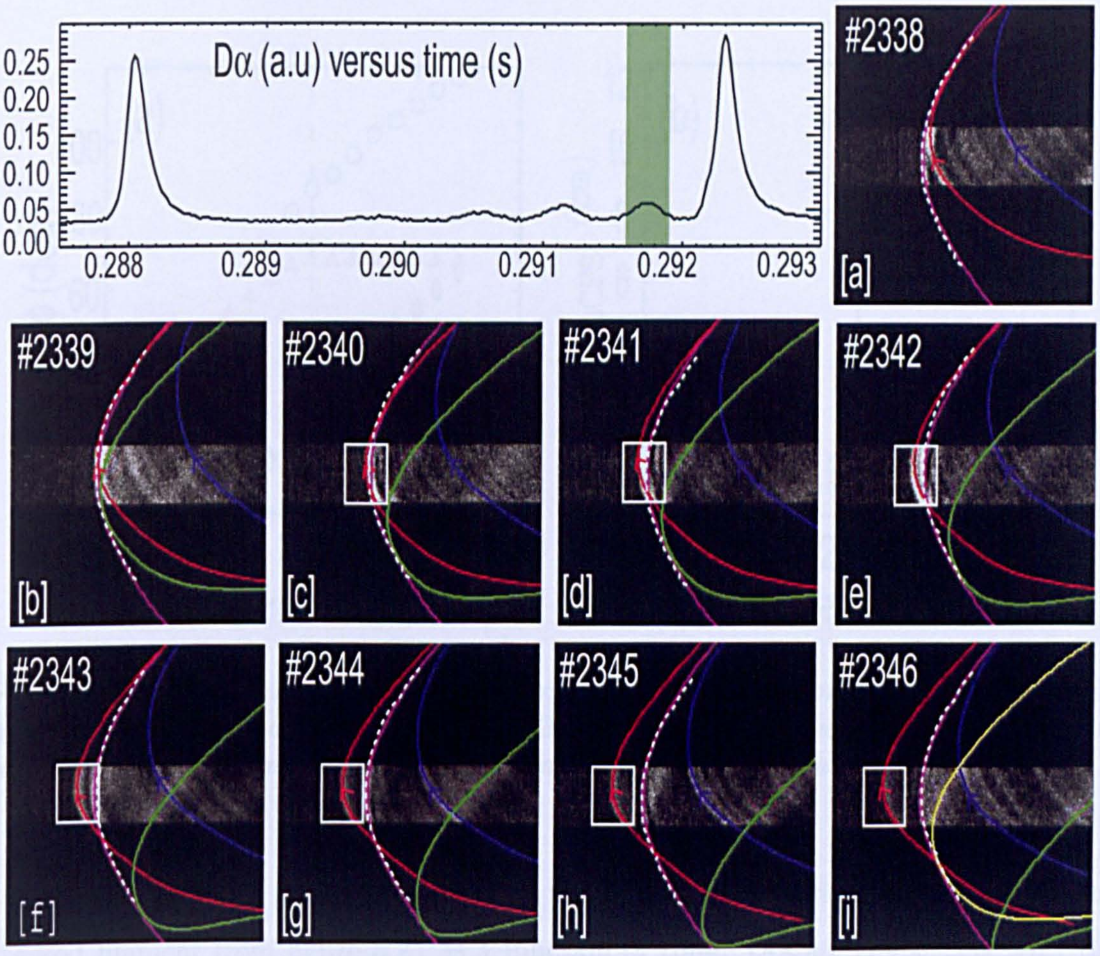

Figure 5.24: *Example of radial propagation of one filament during an inter-ELM period. Shown are (a) Time trace of the D_α signal showing the inter-ELM period, and a sequence of images from frames 2338 - 2346 showing the temporal evolution of one filament and its immediate neighbours during the period shaded in green. The filament marked by the red solid line rotates from frame 2338 to 2340 inclusive; the toroidal rotation then stops, and the radial expansion into the SOL starts from frame 2341.*

filament marked by the red field line initially rotates near the LCFS for the first 60 μs until frame 2340; soon after this, the toroidal rotation slows and as it does so, the filament accelerates radially outwards leaving the LCFS such that it is no longer attached to the plasma at the midplane. The start of the radial expansion is emphasised on the images by increased filament light emission due to increased interaction of filament plasma electrons with neutrals in the immediate SOL. The subsequent outward radial drift lasts for $\sim 60\mu$s, making the total lifetime roughly $\sim 120\ \mu$s. During this propagation, the radial excursions measure ~ 2 cm which corresponds to a constant radial expansion velocity of ~ 2 km s^{-1}.

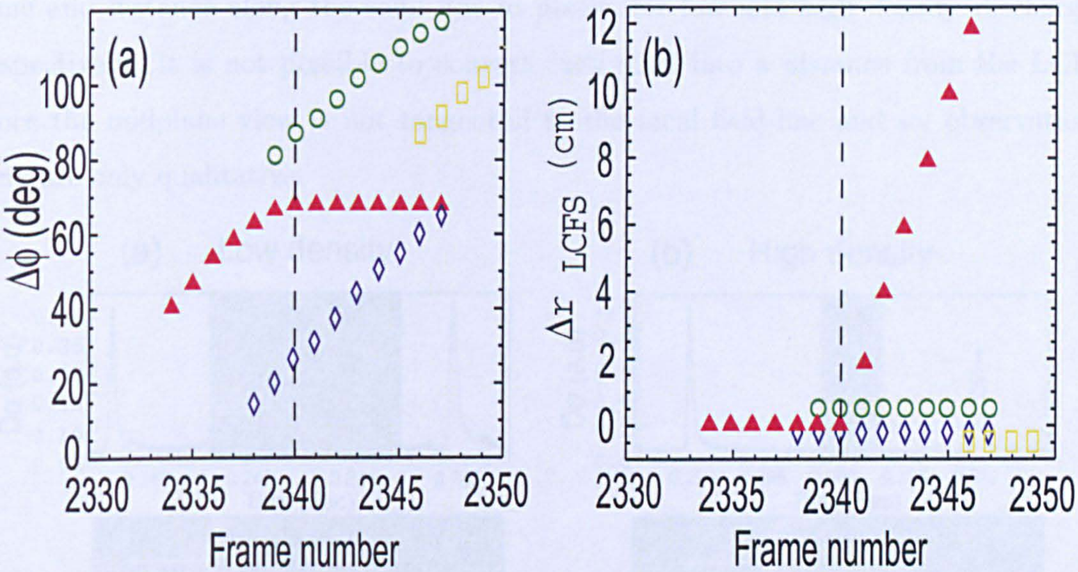

Figure 5.25: *Radial and toroidal excursions as a function of time for tracked filaments are shown in (a) and (b) respectively. During the radial expansion of the filament marked by the red triangle, neighbour filaments continue to rotate.*

Shown in figure 5.25 are measures of the toroidal and radial excursions of each tracked filament from figure 5.24 as a function of time. Despite co-existing with the radially-expanding red filaments, the yellow, green and blue filaments do not leave the edge of the plasma, but continue to rotate. This indicates that the radial motions of individual inter-ELM filaments are uncorrelated.

5.7.2 Dependence of radial motion on plasma density

Inspection of many images across a wide range of discharges with varying plasma conditions and parameters indicate that radial expansions during these periods are sporadic: the number of filaments which leave the boundary plasma and their relative penetration into the SOL varies considerably.

Similarly to toroidal rotation, the radial motion on inter-ELM filaments is found to depend strongly on plasma density $\bar{n}_e$. In order to show this, a solid line is drawn on two mid-plane images, as shown in figure 5.26. The images are snapshots from a high and low density discharge respectively, considered in section (see Table 5.6). The intensity along this line is then recorded as a function of time for each discharge for a period of 4 ms. Figure 5.26 (a,b) shows the colour intensity plots as a function of time and distance along the solid line in pixels, for low and high density discharges respectively. It is not possible to convert each pixel into a distance from the LCFS since the midplane view is not tangential to the local field-line and so, observations here are only qualitative.

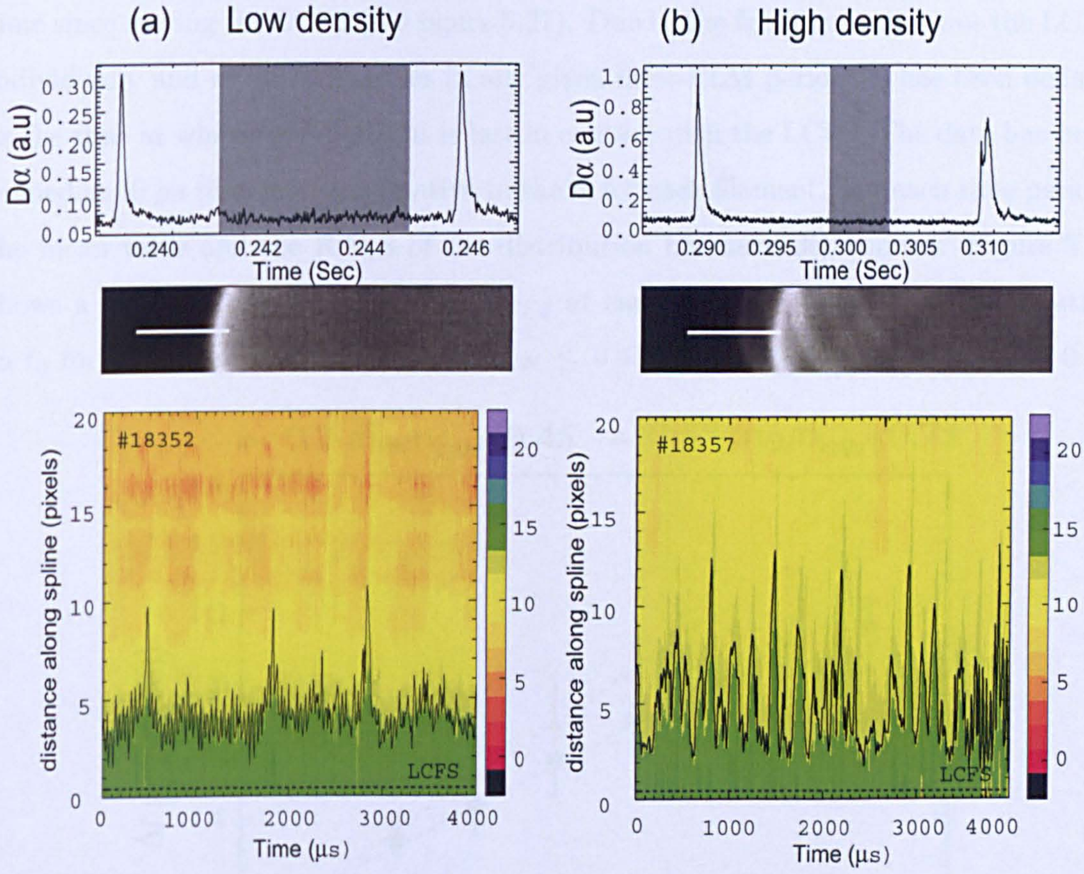
(a) Low density
(b) High density

Figure 5.26: *Colour plots of intensity along white solid line as a function of time (up to 4000 μs) and distance (in pixels) for (a) low and (b) high density discharges. The striking contrast in the radial transport between high and low* $\bar{n}_e$ *is immediately apparent. At high* $\bar{n}_e$*, there is an enhancement of the radial transport which is marked by a significant increase in the number of filaments leaving the edge.*

The colour intensity plots show a dramatic change with $\bar{n}_e$: at low $\bar{n}_e$, a total of 3 intermittent events are detected; these correspond to short-lived filaments which leave the LCFS and penetrate into the SOL. At higher $\bar{n}_e$, there is a significant increase in the number of intermittent events for the same time window, corresponding to an enhancement of the radial transport. There are approximately 5 times as many filaments leaving the edge of the plasma - compare a frequency of 6 kHz at high $\bar{n}_e$ with a minimum of 1 kHz at low $\bar{n}_e$ for these MAST discharges.

5.7.3 Radial propagation speeds

The radial position from the LCFS (Δr_{LCFS}) of individual inter-ELM filaments has been tracked as a function of time for high and low density discharges as a function of time since leaving the LCFS (see figure 5.27). Due to the fact filaments leave the LCFS individually and at different times in any given inter-ELM period, t_0 has been defined as the time at which each filament is last in contact with the LCFS. The data has been binned in 10 μs time intervals relative to the t_0 for each filament. For each time period, the mean value and the R.M.S of the distribution has been determined. Figure 5.27 shows a plot of the mean value of Δr_{LCFS} at each bin as a function of time relative to t_0 for filaments at low ($0.3 \leq \bar{n}_e/n_{\rm GW} \leq 0.45$) and high $0.55 \leq \bar{n}_e/n_{\rm GW} \leq 0.75$

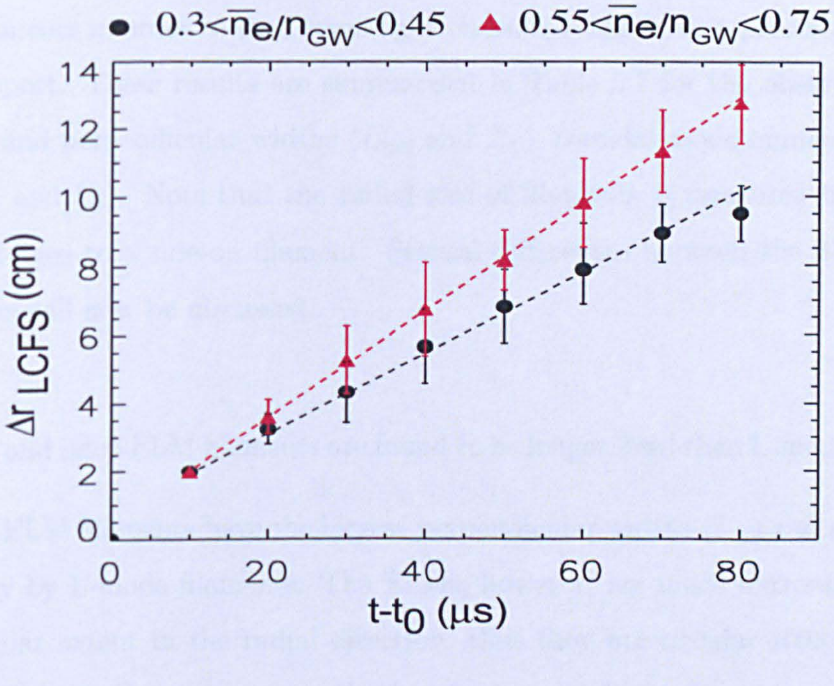

Figure 5.27: *The radial distance of filaments from the LCFS (Δr_{LCFS}) as a function of time relative to the point at which the filament left the LCFS (t_0) for inter-ELM filaments in a low density discharge* $0.3 \leq n_e/n_{\rm GW} \leq 0.45$ *and a high density discharge characterised by* $0.55 \leq n_e/n_{\rm GW} \leq 0.75$. *The dashed lines represent fits to the radial expansion assuming a constant velocity.*

densities.

Filaments at high and low densities have been tracked in their radial propagation for periods up to 80 μs and up to distances $\sim 10 - 12$ cm from the LCFS.

During this time, there is no evidence to suggest that, after an initial acceleration, filaments accelerate radially away from the edge: For both sets of data presented, linear fits corresponding to a constant radial velocity are good fits to the data.

Filaments in high density discharges expand away on average faster than filaments in low density discharges. Mean radial velocities are $\sim 1.65 \pm 0.15$ km s^{-1} and $\sim 1.2 \pm 0.1$ km s^{-1} respectively for high and low densities. These results will be discussed later.

5.8 Comparison with L-mode and ELM filaments

Having established some of the physical properties of inter-ELM filaments using the camera diagnostic alone, it is interesting to compare with L-mode [94] and ELM [48, 52] filaments in order to shed some light on underlying driving-processes for inter-ELM transport. These results are summarised in Table 5.7 for the observed lifetime (τ), radial and perpendicular widths (L_{rad} and $L_{\perp}$), toroidal mode number n and velocities (V_r and V_{ϕ}). Note that the radial size of filaments is measured by manually fitting field-lines to a side-on filament. Several differences between the filaments are apparent, as will now be discussed.

- ELM and inter-ELM filaments are found to be longer lived than L-mode filaments.
- Inter-ELM filaments have the largest perpendicular widths ($L_{\perp}$) and are followed closely by L-mode filaments. The ELMs, however, are much narrower and have a similar extent in the radial direction; thus they are circular structures. The inter-ELM filaments are more elliptical in shape and have a narrow radial extent relative to their perpendicular width, as shown in the schematic of figure 5.28. Both inter-ELM and ELM filaments have a similar radial extent, which is smaller than L-mode.

Table 5.7: *Measurements of the lifetime (τ), radial width (L_{rad}), perpendicular width ($L_\perp$) defined as direction perpendicular to both filament and L_{rad}, mode number (n) range, radial velocity (V_r), toroidal velocity (V_ϕ) and standard deviations of filaments during inter-ELM, L-mode and ELM phases. The range of mode numbers correspond to the number of filaments observed per toroidal circuit. Toroidal rotation velocities (V_ϕ) are measured from both camera and probe data (described later). Radial velocities (V_r) correspond to measurements from the camera data only.*

Phase	τ (μs)	$L_\perp$ (*cm*)	L_{rad} (*cm*)	n	V_r (kms^{-1})	V_ϕ (kms^{-1})
Inter-ELM	50–120	9–12	3–5	10–40	1–2	3–12.5
	(±10%)	(±10%)	(±10%)		(±5%)	(±5%)
L-mode	40–60	7–9	5–10	20–50	0.5–1.5	2–9
	(±10%)	(±10%)	(±10%)		(±5%)	(±5%)
ELM	100–180	2–6	4–6	10–20	1–9	10–30
	(±10%)	(±10%)	(±10%)		(±5%)	(±5%)

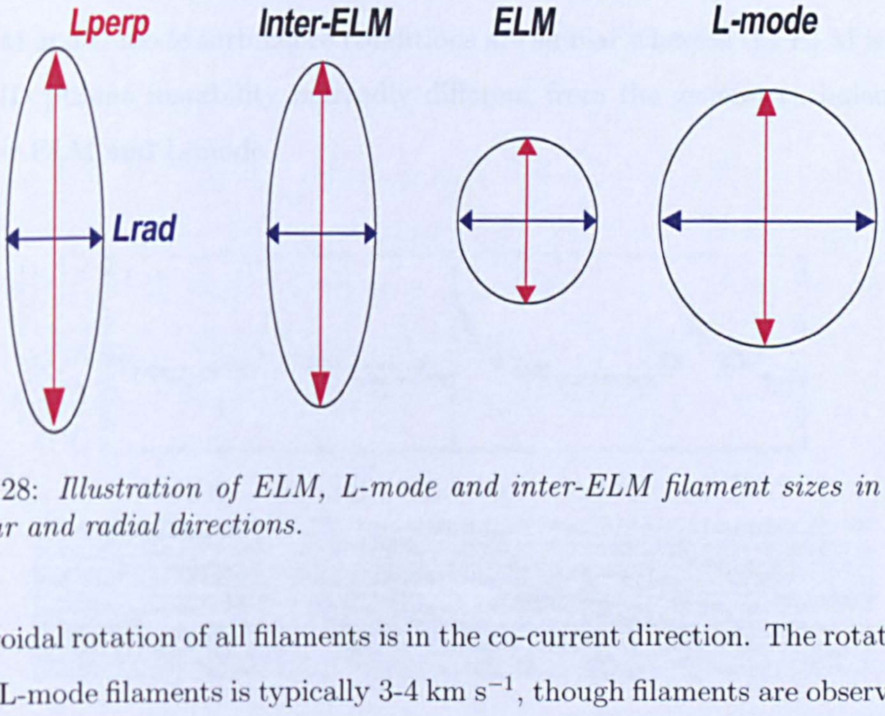

Figure 5.28: *Illustration of ELM, L-mode and inter-ELM filament sizes in both perpendicular and radial directions.*

- Toroidal rotation of all filaments is in the co-current direction. The rotation speed for L-mode filaments is typically 3-4 km s^{-1}, though filaments are observed with a wider spread as shown in table 5.7. In H-mode, the plasma edge rotates faster and indeed, ELM filaments are observed to rotate faster than those in L-mode. Inter-ELM filaments, however, do not rotate much faster than L-mode filaments with typical rotation velocities roughly 3 times that of L-mode filaments. A possible explanation for this is that inter-ELM and L-mode filaments originate in a similar region within the pedestal closer to the plasma edge where the bulk plasma rotation is slower, whereas the ELM filaments originate from deeper within the plasma where the bulk plasma rotation is faster. This would then indicate that the driving mechanisms for L-mode and inter-ELM are similar, while both being different to the underlying mechanism responsible for the ELM.

- For both inter-ELM and L-mode filaments, the toroidal rotation velocity was found to be constant for any given filament but to vary between filaments. This leads to constantly changing separations between filaments. This is in contrast to the ELM event where the spacings between filaments are constant. See figure 5.29 where it can be seen that filaments are regularly spaced with a well defined mode number. It is for these reasons that a significant spread in the range of quasi toroidal mode numbers for L-mode (see Table 2.5) and inter-ELM phases has been observed, whereas the spread in ELM toroidal mode numbers is less significant (see table 2.3) . Again, these observations would indicate that inter-ELM and L-mode turbulence conditions are similar whereas the ELM is a distinct MHD plasma instability markedly different from the general turbulent state of inter-ELM and L-mode.

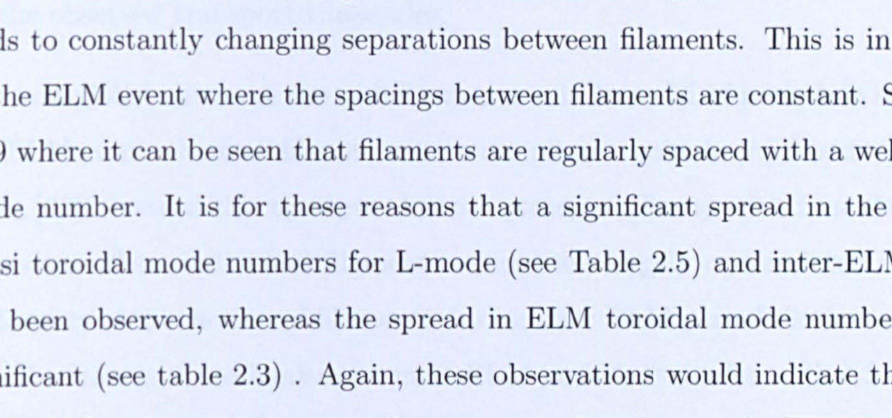

Figure 5.29: *(a) D_α signal at the midplane showing several small ELMs. (b) Midplane view of a small ELM on MAST. The mode structure shows a clear spacing between ELM filaments.*

- Although the edge turbulence is suppressed and the confinement improved, the transition to H-mode does not mean that filaments in inter-ELM periods do not leave the edge plasma. Indeed, the radial propagation of filaments in all regimes has been observed. Radial velocities for inter-ELM and L-mode filaments are similar in the range 0.5–2 km s^{-1}. ELM filaments, however, are observed to travel at much faster speeds which are in the range 2–9 km s^{-1}. A crucial difference is that the radial propagation for inter-ELM and L-mode is found to be constant (after an initial acceleration), whereas the ELM filaments accelerate explosively on the observed transport timescales.

- The non-global nature of the radial expansion in inter-ELM periods is also unlike the ELM event where all filaments leave the plasma boundary (-albeit at different times [69]); instead this transport bears a strong similarity with L-mode filament behaviour where individual filament motions are largely uncorrelated. The non-uniformity of the motion of filaments during inter-ELM periods is thus suggestive that the transport mechanism for inter-ELM periods is similar to that for L-mode periods, whereas a different transport mechanism is responsible for the ELM filaments.

- Measurements of toroidal velocities for L-mode and inter-ELM filaments are also similar despite the increase in the pedestal rotation velocity through the L-H transition - this may indicate that filaments do not necessarily rotate at the plasma rotation velocity. The differences in toroidal velocities between inter-ELM and ELM filaments may also indicate that both these types of filaments originate from different locations within the pedestal, and therefore would point to different drive mechanisms.

Transport during inter-ELM periods bears some similarity with L-mode filament behaviour. This is perhaps suggestive that the transport mechanism for inter-ELM preiods maybe similar to that of L-mode periods, whereas a different mechanism is responsible for the ELM instability.

- The non-global nature of the radial expansion is unlike the ELM event where all filaments leave the plasma boundary (-albeit at different times [?]); instead this transport bears a strong similarity with L-mode filament behaviour where individual filament motions are largely uncorrelated. The non-uniformity of the motion of filaments during inter-ELM periods is thus suggestive that the transport mechanism for inter-ELM periods is similar to that for L-mode periods, whereas a different transport mechanism is responsible for the ELM filaments.

Chapter 5

Langmuir Probes Results

A cross comparison with camera data reveals that small amplitude H-mode fluctuations in the ion satuation current (I_{SAT}*) signals correspond to inter-ELM filaments. These are found to exist immediately before and after an ELM. Physical properties such as width and toroidal motion of inter-ELM filaments are derived from probe data and found to agree with camera estimates. Density estimates are also obtained based on* I_{SAT} *values, and a comparison with L-mode and ELM filaments is presented. Furthermore, the exponential fall-offs of* I_{SAT} *are determined experimentally and confirmed through simulation of a simple model. Results are combined to test the sheath-limited and interchange theories of radial motion of propagating filaments.*

6.1 Intermittency of I_{SAT} trace

The outboard midplane reciprocating probe (RP) system on MAST is equipped with a circular array of 8 equally spaced, flush-mounted Langmuir probes arranged in diametrically opposite pairs (see figure 4.2). These probes are biased to -200V, and measure the ion saturation current, I_{SAT}. An example I_{SAT} time trace for beam-heated discharge # 18057 from Langmuir pin 2 is shown in figure 6.1: (a) is the target D_α trace as a function of time through the L-H transition, (b) is a plot of the distance of the reciprocating probe head from the EFIT-calculated LCFS as a function of time and (c) is the resulting time series of the I_{SAT} signal. In addition to the ELM peaks, the time series of the I_{SAT} signal reveals a number of intermittent peaks above the standard deviation in several periods separating the large ELM events. These peaks are found consistently across all probe pins, albeit with different amplitudes. Moreover, the frequency and amplitude of I_{SAT} fluctuations increase as the probe approaches the LCFS. This is particularly evident when the reciprocating probe is near the LCFS, as indicated in the shaded band region in figure 6.1.

6.2 Camera identification of I_{SAT} peaks

In order to determine if the peaks in the I_{SAT} traces during inter-ELM periods are due to filaments, midplane views using the fast camera are combined with the reciprocating probe measurements. Figure 6.2 (a) shows a magnified interval of the I_{SAT} time trace from figure 6.1(c). The peak highlighted by the shaded region lasts for $\sim 50\ \mu$s, is situated at the LCFS, and is shown in the magnified figure 6.2(b).
Also shown are the successive background-subtracted mid-plane images which span the duration of this I_{SAT} peak, obtained at 10 μs intervals. A sampling frequency of 300 kHz for the RP system implies that data is acquired every 3.33 μs; so the time resolution of 10 μs is sufficient for a diagnostic comparison with RP data.

The motion of the filament on the images is tracked and its physical boundaries, marked by the solid green lines, are located using the manual tracking method described in the previous chapter. The reciprocating probe position corresponds to the dark full circle on the midplane views. The filament makes first contact with the probe in frame 2, establishing a steep front in the I_{SAT} signal. In the following frames, the filament rotates past the probe, and the background I_{SAT} level is subsequently restored until the arrival of the next filament.

6.3 Contribution of filaments to I_{SAT} levels

The cross-comparison between Langmuir probes and fast camera images is proof that the small-amplitude peak (relative to ELMs) in H-mode periods corresponds to visible filaments passing the probe. While this is useful, it is not sufficient to assert with absolute certainty that the origin of most large-amplitude fluctuations in the I_{SAT} signals are due to inter-ELM filaments. It is important therefore to verify whether the

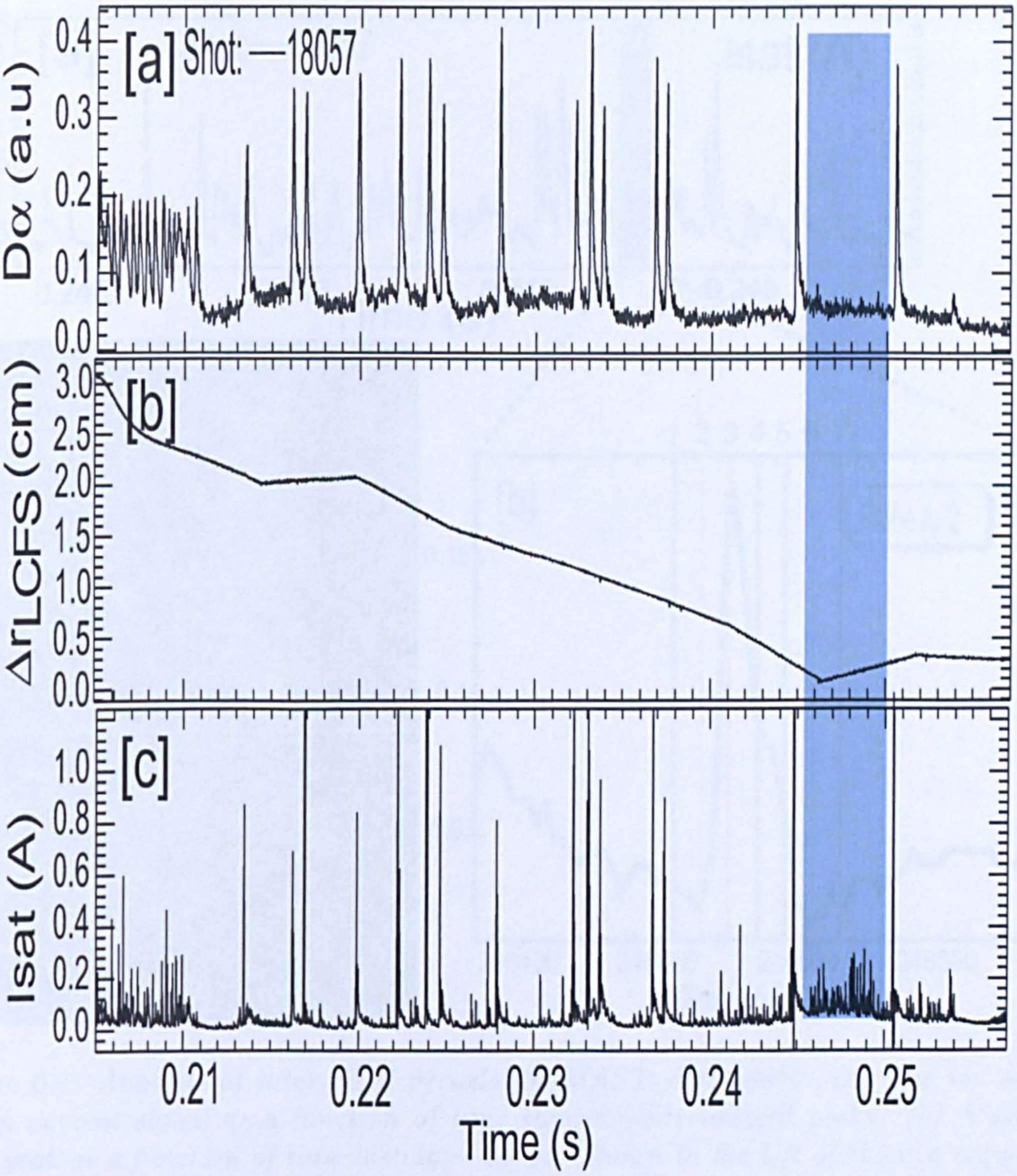

Figure 6.1: *Data from MAST shot #18057: (a) is the target* D_α *signal as a function of time showing the L-H transition and the appearance of several ELMs, (b) is the position of the reciprocating probe head relative to the EFIT-calculated LCFS as a function of time, and in (c) is the ion saturation current signal as a function of time showing the existence of a number of intermittent peaks in several inter-ELM periods. The amplitude of these peaks is above the standard deviation of the entire signal. Furthermore, the frequency and amplitude of intermittent fluctuations increase as the probe approaches the LCFS. The dark band corresponds to the inter-ELM period analysed in Figure 6.2.*

peaks in these signals can routinely be used to represent the filaments seen in the camera images, or whether these peaks are just the large fluctuations of a larger underlying continuous distribution of I_{SAT} signals. In order to check this, the probability density of all the I_{SAT} values recorded during an arbitrary inter-ELM period is calculated.

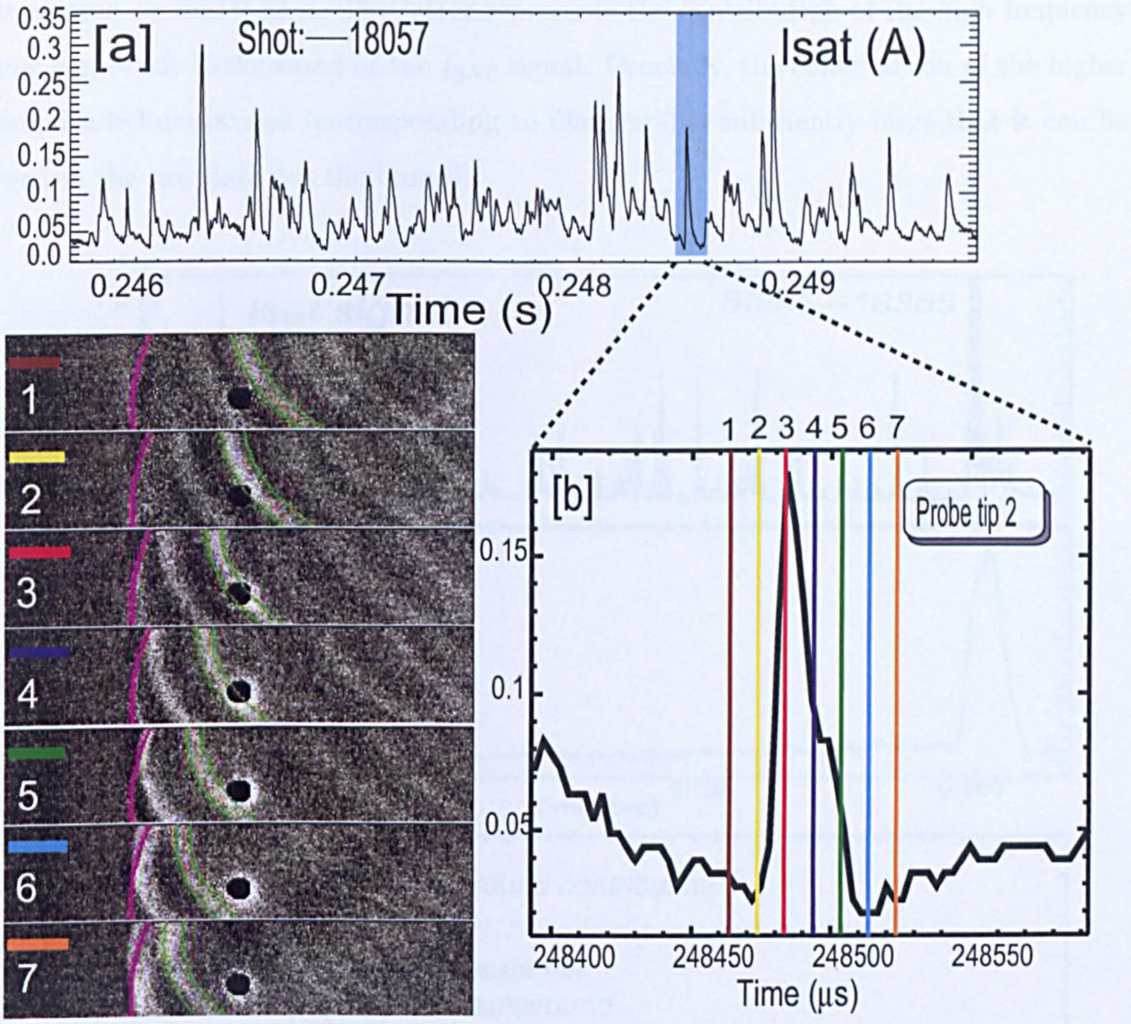

Figure 6.2: *Analysis of inter-ELM periods for MAST shot 18057: (a) The ion saturation current signal as a function of time showing intermittent peaks. (b) A single* I_{SAT} *peak as a function of time lasting* $\sim 50\ \mu s$. *Shown to the left of (b) is a sequence of mid-plane images showing the toroidal propagation of a single inter-ELM filament past the probe (seen as a dark circle). The filament boundaries are marked by the green lines. The filament makes first contact with the probe in frame 2, as shown establishing a steep front in the* I_{SAT} *trace. In subsequent frames, the filament rotates toroidally past the probe in the camera images, leaving a trailing wake in the* I_{SAT} *trace.*

The raw data are taken at the LCFS. Figure 6.3 shows (a) the I_{SAT} from pin 2 (b) the target D_α signal of an inter-ELM period lasting over 100 ms separating two large ELMs, and (c) the PDF of I_{SAT} values recorded for the duration of the inter-ELM period. The data reveals that the underlying distribution is not continuous. Rather, it consists of a main distribution with the emergence of a marked bump-on-tail. The main distribution has been fitted to a Gaussian, marked by the red dashed line, and is centred around 0.03 A. The latter represents the contribution of the high frequency low amplitude background of the I_{SAT} signal. Crucially, the contribution of the higher amplitude fluctuations (corresponding to filaments) is sufficiently large that it can be seen in the raw data (as the bump).

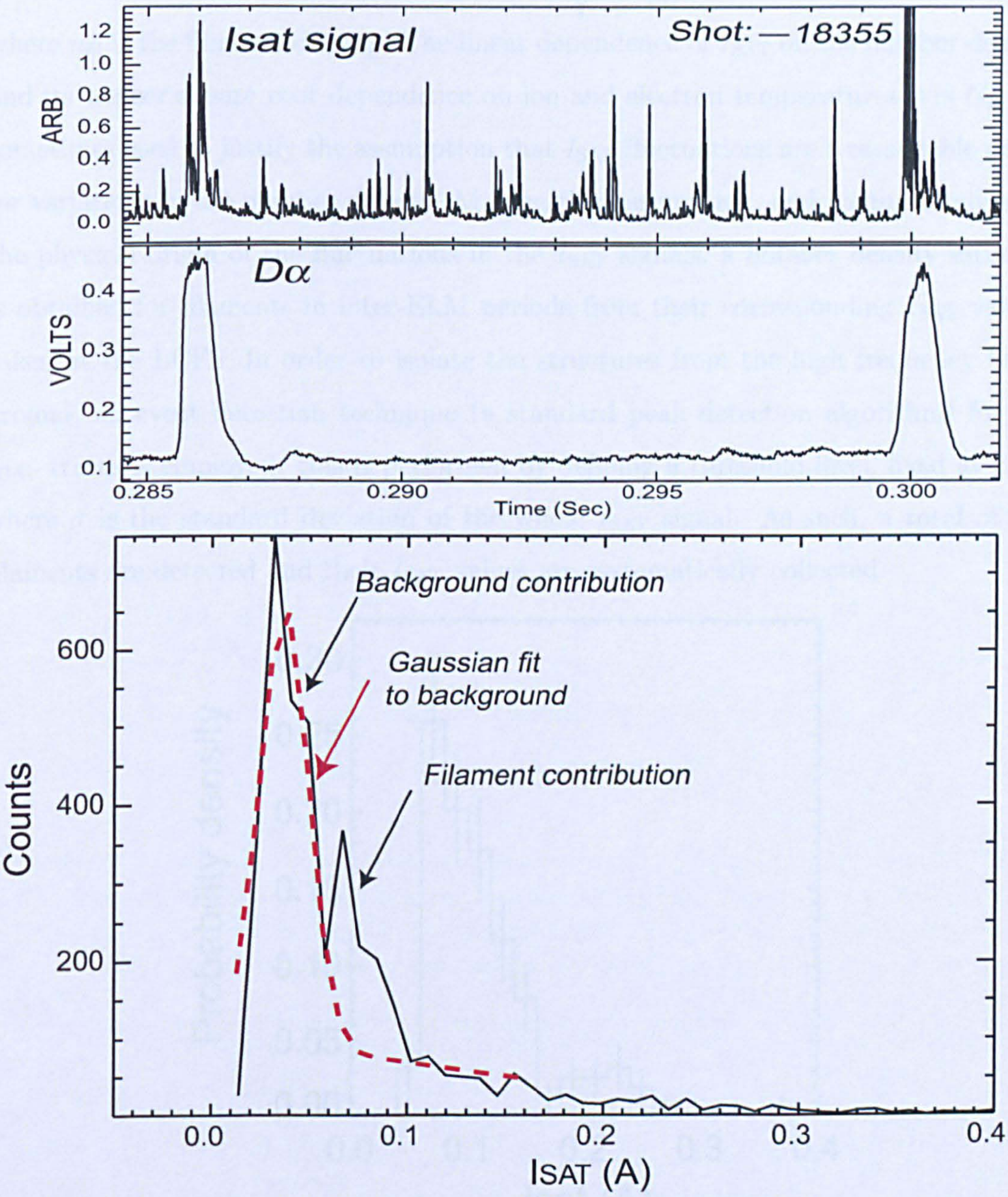

Figure 6.3: *(a) the* I_{SAT} *signal from pin 2 (b) the target* D_α *signal of an inter-ELM period lasting over 100 ms separating two large ELMs, and (c) the probability density of* I_{SAT} *values recorded for the duration of the inter-ELM period.*

6.4 Density of inter-ELM filaments

While the I_{SAT} signal is not the fundamental property of the plasma, it is related to the number density and the temperature through:

$$I_{\mathrm{SAT}} = en_{\mathrm{fil}}C_s \approx en_{\mathrm{fil}}\sqrt{\frac{k(T_i+T_e)}{m_i}}, \tag{6.1}$$

where n_{fil} is the filament density. The linear dependence of I_{SAT} on the number density and its weaker square root dependence on ion and electron temperatures (via C_s) are sometimes used to justify the assumption that I_{SAT} fluctuations are a reasonable proxy for variations in the number density. Making this assumption, and having established the physical origin of the fluctuations in the I_{SAT} signals, a number density estimate is obtained for filaments in inter-ELM periods from their corresponding I_{SAT} values, taken at the LCFS. In order to isolate the structures from the high frequency background, an event detection technique (a standard peak detection algorithm) for the I_{SAT} traces is employed: this is performed by defining a threshold level, fixed at 2.5σ, where σ is the standard deviation of the whole I_{SAT} signal. As such, a total of 233 filaments are detected and their I_{SAT} values are systematically collected.

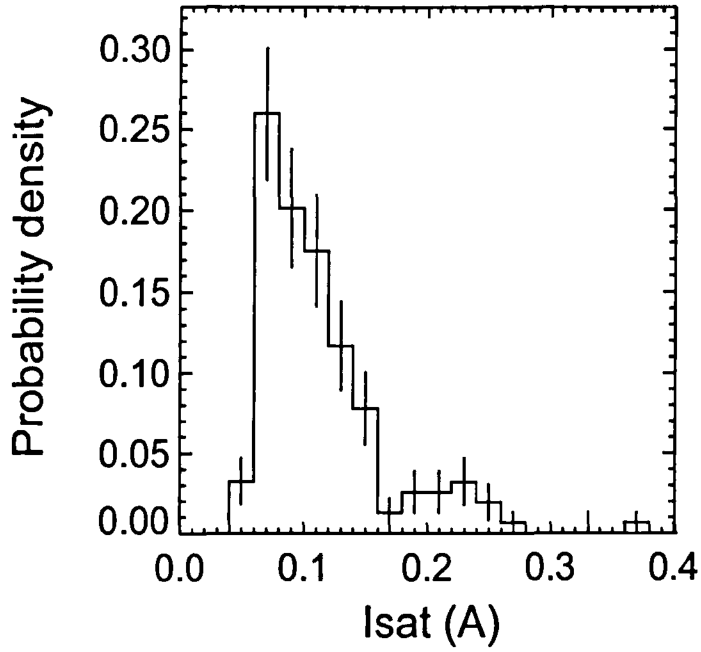

Figure 6.4: *PDF of I_{SAT} values corresponding to inter-ELM filaments; the mean value is 0.12 A.*

Figure 6.4 shows the resulting PDF. Inter-ELM $I_{\rm SAT}$ values are found to be in the range 0.04–0.25 A. A peak value of 0.08 A and mean value of 0.12 A are found.

The ion saturation current density $J_{\rm SAT}$ is given by the measured ion saturation current divided by the pin cross section:

$$J_{\rm SAT} = \frac{I_{\rm SAT}}{\pi r_{pin}^2} = \frac{I_{\rm SAT}}{78.5\rm mm^2}. \tag{6.2}$$

From a comparison based on 160 inter-ELM profiles obtained from the edge TS system, the edge electron temperature T_e during these periods is found to be in the range 10 - 25 eV at the LCFS [47, 51]. Assuming equal electron and ion temperatures for the probe collecting area, a range of ion sound speed values is found such that $C_s^{\rm min} \sim 32$ km s^{-1}, and $C_s^{\rm max} \sim 49$ km s^{-1}. Note that the background SOL temperature is estimated at 5 eV. A lower limit for inter-ELM filament number density is estimated such that $n_{\rm fil}^{\rm min} \equiv J_{\rm SAT}^{\rm min}/eC_s^{\rm max} = 6.5 \times 10^{16}$ m^{-3}. Similarly, a maximum value is such that $n_{\rm fil}^{\rm max} \equiv J_{\rm SAT}^{\rm max}/eC_s^{\rm min} = 6.7 \times 10^{17}\rm m^{-3}$. In conclusion, $n_{\rm fil} = f(I_{\rm SAT}, T_i) = 6.5 \times 10^{16} - 6.7 \times 10^{17}(\pm 20\%)$ m^{-3}.

A similar analysis has been performed for L-mode filaments: $I_{\rm SAT}$ values are found to be in the range 0.2–0.8 A. For measured temperatures in the range 10–40 eV, i.e., C_s values in the range 32–63.5 km s^{-1}, the density for L-mode filaments is found to be in the range 2.5×10^{17} - $2 \times 10^{18}\rm m^{-3}$. The density estimates of inter-ELM, L-mode and ELM filaments based on their $I_{\rm SAT}$ values are summarised in table 6.8.

Table 6.8: The estimated densities for L-mode, inter-ELM and ELM filaments based on the measured range of $I_{\rm SAT}$ values. A range of electron temperatures taken at the LCFS from the edge Thomson scattering system is also assumed in this calculation. The range of inferred densities correspond to the minimum and maximum of both $I_{\rm SAT}$ and T_e ranges.

	Ion saturation current $I_{\rm SAT}$[A]	Filament temperature $T_{\rm fil}$[eV]	Filament density $n_{\rm fil}[\rm m^{-3}]$
Inter-ELM	0.04-0.2	10-25	$6.5 \times 10^{16} - 6.5 \times 10^{17}$
L-mode	0.2-0.8	10-40	$2.5 \times 10^{17} - 2 \times 10^{18}$
ELM	0.5-3.5	50-80	$1 \times 10^{18} - 2 \times 10^{19}$

While the densities for filaments in the inter-ELM phase are lower than those in L-mode, both are much smaller than the density of ELM filaments. This observation is in qualitative agreement with the PDF of light intensity from imaging data presented in figure 5.12. The agreement is expected since both D_α light emission from the camera data and I_{SAT} are proportional to the number density.

It should be noted that filament density estimates, as described above, assume that filaments hit the reciprocating Langmuir probe pins flush, and rotate past with a purely toroidal rotation, i.e. move past the pin with no net radial motion. In this "ideal" scenario, the pin maps out the entire density distribution of the filament; the maximum value in the I_{SAT} peak would then correspond to the central area where the filament is most dense. However the radial motion of filaments complicates the situation. A small velocity component in the radial direction would mean that the Langmuir pin would not map the entire filament. Rather, it could make contact with the filament in either the dense (central) part or the less dense boundary region of the filament, depending on the finer details of each individual filament motion. The implication therefore is that I_{SAT} peaks corresponding to radially-propagating filaments would underestimate the peak values, and hence affect measurement of the number density. The error changes with the velocity ratio V_r/V_ϕ. Nevertheless, despite the complications of radial motion, this effect will not present significant deviations from the true values when measurements are taken at the LCFS. As such, the values can be treated as good first order approximations to real filament density.

6.5 Toroidal velocity

From the time shifts (Δt) of the I_{SAT} traces of probe tips, and a knowledge of the arc tip separations (Δs), toroidal rotation velocities of filamentary structures are given by:

$$V_\phi \sim \Delta s/\Delta t. \tag{6.3}$$

This calculation is based on two assumptions: firstly, that an inter-ELM filament remains as a coherent entity as it rotates past the probe, and secondly that the probe does not significantly slow down the filament as it rotates past. Both assumptions are reasonable since in figure 6.2, there is no evidence to suggest that filaments either disintegrate or that the toroidal velocity decreases. Furthermore, if the filament did slow, this would not be problematic for the determination of the peak since the position of the peak is established in the steep front (see figure 6.2(b)).

In order to determine V_ϕ using this approach, 250 peaks are located in the I_{SAT} time traces of diametrically opposing probe tips 1 and 5, and the time shift for each peak in both signals is subsequently measured. In this case, Δs is simply the diameter. Note the caveat of radial propagation as discussed in the previous section also applies to this calculation, and therefore measurements are taken at the LCFS to reduce this effect. Data are binned according to the maximum sampling frequency of 300 kHz. Shown in figure 6.5 is the probability density of the measured time shifts; these have been converted to toroidal velocity in the upper horizontal x-axis. Toroidal velocities are in the range of 3-12 km s^{-1} with a peak velocity of 9 km s^{-1}. These I_{SAT}-based estimates are in good agreement with estimates using the fast camera (see section 5.5).

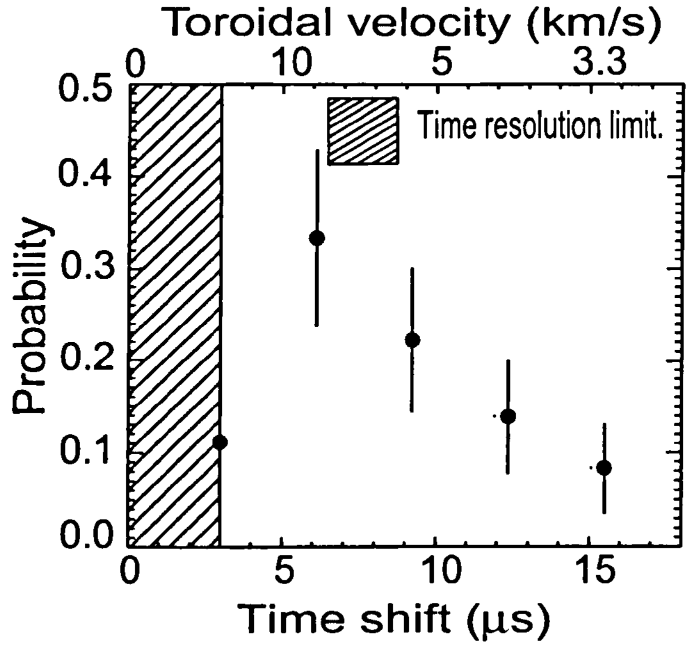

Figure 6.5: *PDF of toroidal velocity (top x-axis) as calculated from the time shifts (bottom x-axis) in I_{SAT} signals between diametrically opposing tips. The error bars represent the RMS of distributions for each bin. The shaded region corresponds to the limit of sampling frequency of the RP system (3.33 μs).*

6.6 Width estimates

With a knowledge of toroidal velocity, filament widths (L_ϕ) may be inferred from the time duration of corresponding I_{SAT} peaks, $\Delta\tau$, such that:

$$L_\phi \sim V_\phi \Delta\tau. \tag{6.4}$$

The method here is to take the time duration width between the maximum value of the I_{SAT} peak and the first minimum (to the left of the peak), since typically the I_{SAT} peaks are asymmetric as shown in figure 6.6. As can be seen, the I_{SAT} peak is characterised by a steep front and a slower trailing wake. Although the trailing wake is only slightly less steep than the front, an overestimate of the filament width would result if the whole I_{SAT} width was used (i.e., the distance between the blue dashed vertical lines in figure 6.6). Instead, the width of the filament is defined as twice the Half Width Full Maximum, as shown by the red line at the base of the I_{SAT} profile.

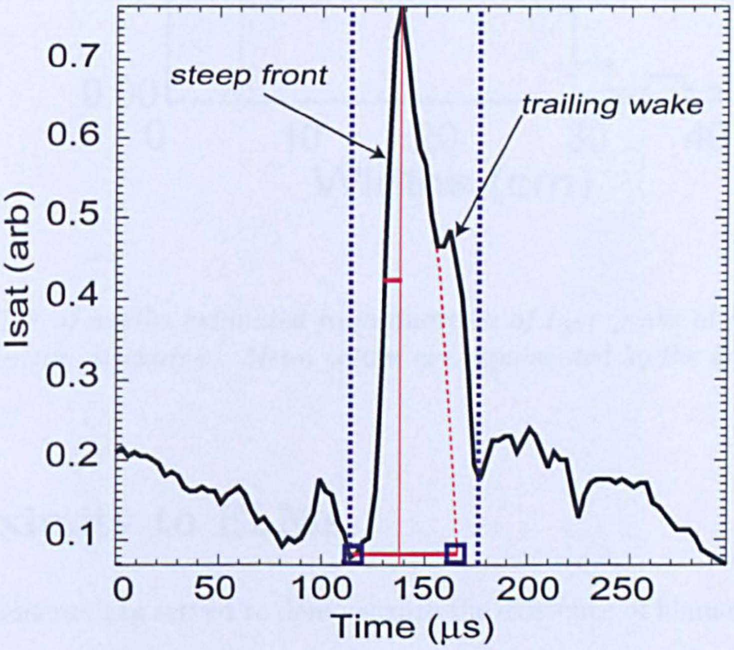

Figure 6.6: *Characteristic shape of* I_{SAT} *peak showing a steep front with a trailing wake.*

Measurements are taken at the LCFS. Although in general $V_\phi \sim 3$ – 12 km s^{-1}, close inspection of the toroidal excursions of the filaments in the camera images in the periods of interest showed that V_ϕ for the majority of filaments varies on a much smaller range of 8–10 km s^{-1} (see for example figure 5.22), and therefore a mean toroidal velocity is used $\langle V_\phi \rangle \sim 9$ km s^{-1} rather than calculating V_ϕ for each filament. Analysis of 250 filament peaks in a high and low density discharge leads to the PDF shown in figure 6.7. The peak width value for inter-ELM filaments is $L_\phi \sim 13$ cm, with mean ~ 16 cm. These are similar to the angular widths inferred from the camera data (see figure 5.15). We note that the filament widths inferred from probe data do not vary with density, again in agreement with fast camera data (see figure 5.21).

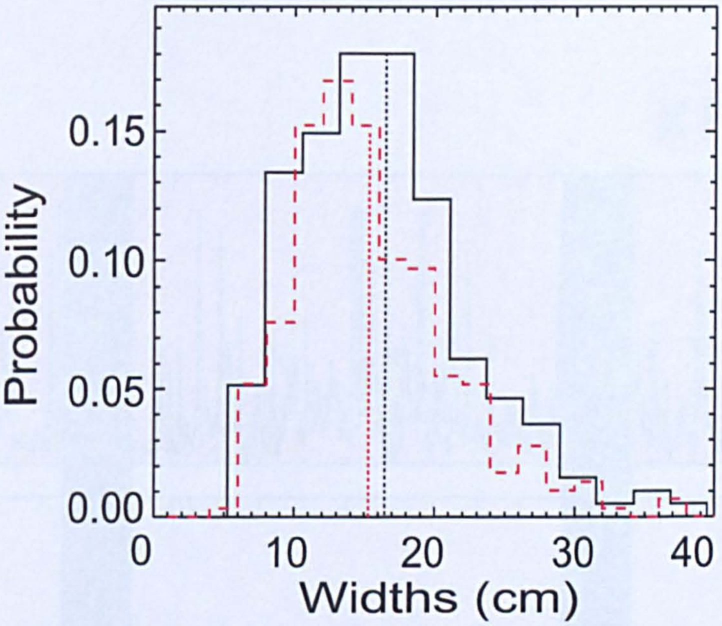

Figure 6.7: *PDF of widths estimated from duration of I_{SAT} peaks at high (solid) and low (dashed) density discharges. Mean values are represented by the dashed lines.*

6.7 Proximity to ELMs

While the camera data served to demonstrate the existence of filaments in the inter-ELM periods, it was not possible to analyse how soon these appear after the ELM, or how long they last till the ELM onset. Indeed, inter-ELM filaments could be seen till ~ 150 μs before the onset of the ELM; after this, an underlying ELM precursor mode dominated the image intensity to the extent that dim inter-ELM filaments can no longer be seen. These density fluctuations are observed in the line-integrated density as excursions from interferometer data, and details can be found in the Ref [51]. Furthermore, it was not possible to infer how soon filaments appear after the ELM event, due to an increase in overall light emission resulting from the explosive ejection of the (ELM) filaments. These disadvantages are overcome by analysing I_{SAT} signals which show with clarity the characteristic inter-ELM behaviour before and after the ELM. Figure 6.8 shows (a) an example I_{SAT} from Langmuir pin #2 where the fluctuations between two large type-I ELMs are magnified by a factor ~ 15, (b) the corresponding D_α signal and (c) the bias voltage of the pin with respect to the vessel (fixed at -200 V).

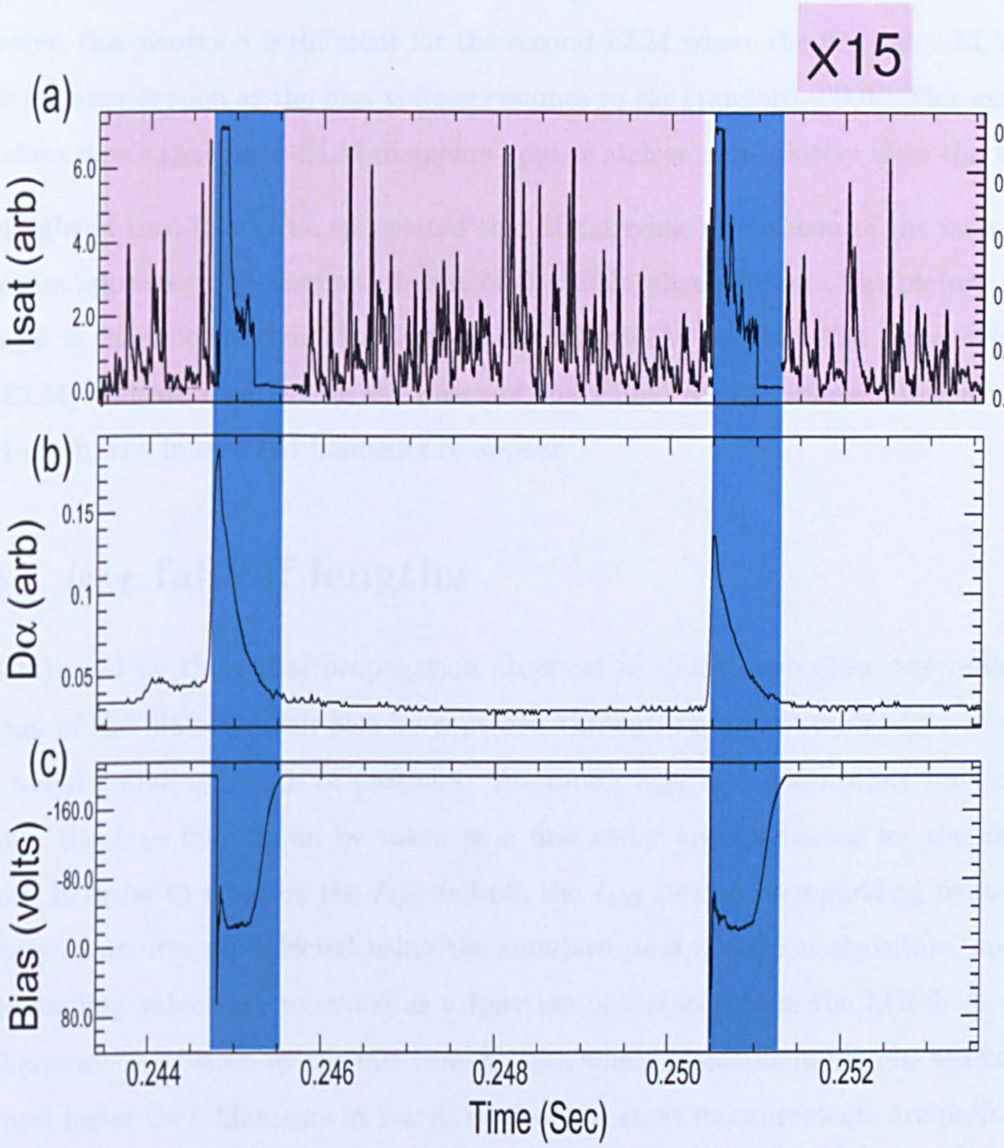

Figure 6.8: *(a) the* I_{SAT} *from pin 2 (b) the target* D_α *signal of an inter-ELM period lasting over 100 ms separating two large ELMs, and (c) the bias voltage on the pin.*

Two large type-I ELMs are shown in the blue shaded region. For both ELMs, I_{SAT} peaks can be seen immediately prior to the ELM crash indicating the existence of inter-ELM filaments until the ELM onset. Subsequent to this, a loss of voltage to the pin is observed because the power supplies cannot sustain the large currents seen during the ELMs. The implication is that a finite amount of time is required for the voltage to regain the fixed value of -200 V. Denoting τ_{REC} as the time duration between the ELM onset and that at which the power supplies recover to the pre-fixed value of -200 V, it can be seen that in the case of the first ELM in figure 6.8(a) that there exists a time delay $\sim$ 200 μs between τ_{REC} and the appearance of the first inter-ELM peak. However, this situation is different for the second ELM where the first inter-ELM filament appears as soon as the bias voltage resumes to the standard -200V. This example therefore shows that inter-ELM filaments appear almost immediately after the ELM.

In light of this, it may be speculated that the driving mechanism of the inter-ELM filaments appears to be distinct of that of the ELM phenomenon. The picture which emerges is that intermittent filaments in the inter-ELM periods exist independent of the ELM, and are dwarfed by the onset of the ELM. Almost immediately after the ELM crash, the inter-ELM filaments re-appear.

6.8 I_{SAT} fall-off lengths

Motivated by the radial propagation observed in the camera data, the radial expansion of the filaments can also be captured through Langmuir probe data in terms of a radial e-folding length of particles. Assuming I_{SAT} is a good proxy for number density, the I_{SAT} fall-off can be taken as a first order approximation for the density fall-off. In order to measure the I_{SAT} fall-off, the I_{SAT} peaks corresponding to the filamentary structures are selected using the standard peak detection algorithm, and the corresponding values are recorded as a function of distance from the LCFS, Δr_{LCFS}. Furthermore, motivated by the fast camera data where filaments in high $\bar{n}_e$ were found to travel faster than filaments in low $\bar{n}_e$ discharges, these measurements are performed at high ($0.55 \leq n_e/n_{\text{GW}} \leq 0.75$) and low ($0.3 \leq n_e/n_{\text{GW}} \leq 0.45$) density discharges (see table 5.1, section 5.6). Figure 6.9 shows on a log-linear scale the measured values of I_{SAT} as a function of Δr_{LCFS}. Data have been binned in 1cm intervals and the error bars are the RMS of the distributions at each bin. Exponential fits of the form $\exp(-x/\lambda)$ where λ is the e-folding length have been fitted to both sets of data from 1 – 6 cm from the LCFS and are shown by the dashed lines. The fits yield e-folding lengths of $\lambda \sim 41 \pm 3$ mm at high $\bar{n}_e$, and $\lambda \sim 28 \pm 3$ mm at low $\bar{n}_e$.

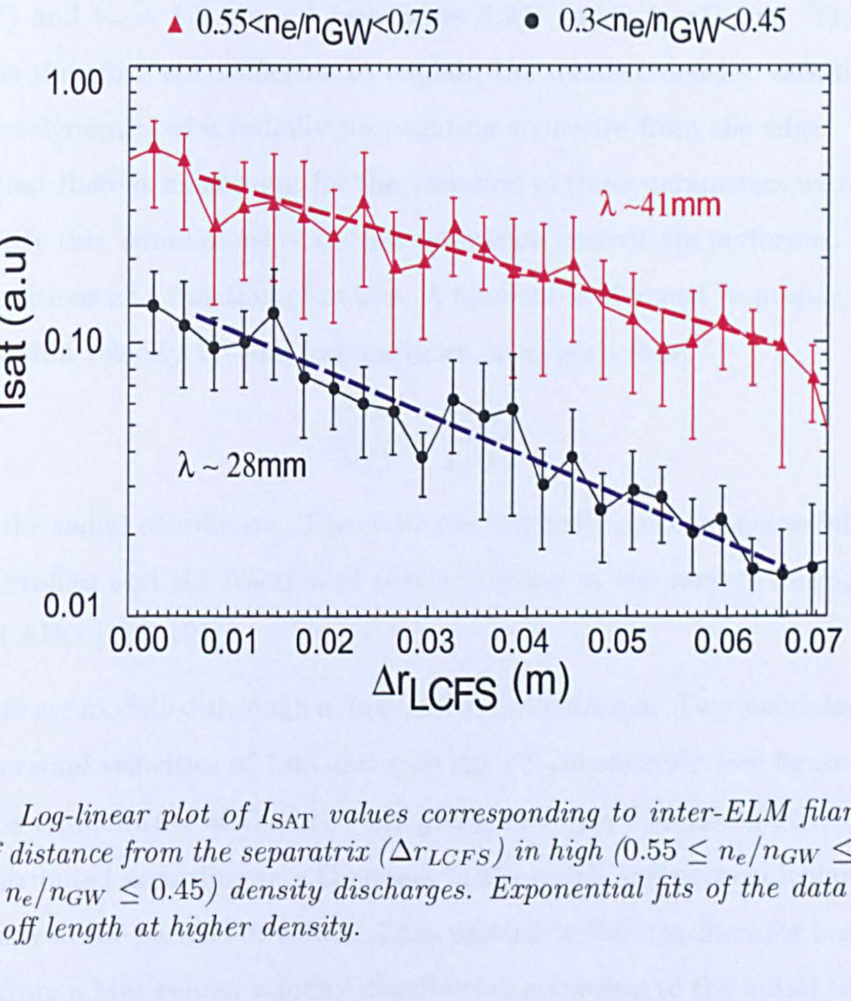

Figure 6.9: *Log-linear plot of* I_{SAT} *values corresponding to inter-ELM filaments as a function of distance from the separatrix* (Δr_{LCFS}) *in high* ($0.55 \le n_e/n_{GW} \le 0.75$) *and low* ($0.3 \le n_e/n_{GW} \le 0.45$) *density discharges. Exponential fits of the data indicate a higher fall-off length at higher density.*

A simple paradigm frequently used in the literature (see [118] are references therein) is one which assumes the radial extent of a radially-propagating filament to be directly related to the time required for all the particles within the filament to be lost through parallel transport. For the simple idealisation where a filament propagates radially with a velocity V_r, and loses particles on the ion parallel transport time scales $\tau_\parallel = L_\parallel / C_s$ (where $L_\parallel$ is the connection length and C_s is the ion sound speed), the I_{SAT} e-folding length, considered as a radial extent, is described in terms of $L_\parallel$, V_r and

C_s parameters through the relation:

$$\lambda = V_r \frac{L_{\|}}{C_s}. \tag{6.5}$$

While this paradigm may appear to be a reasonable first approximation, inserting typical values for the different parameters leads to values far from those observed experimentally. Indeed, taking for the inter-ELM, $L_{\|} \sim$ 7m, $C_s \sim$ 49 km s^{-1} (i.e. $T_e \sim$ 25eV) and V_r = 1.2 km s^{-1} (see figure 5.27) yields λ =17 cm. This "simple" paradigm is therefore not sufficient to explain the number density variations during the complex dynamics of a radially propagating structure from the edge. The reason for this is that there is no account for the variation of these parameters with radius. In order to verify this, simulations of the ion saturation current are performed taking into account variations as a function of radius. A filament is assumed to propagate radially outwards with a velocity V_r, and lose particles on $\tau_{\|}$ such that:

$$\frac{V_r(r)}{\lambda(r)} = \frac{C_s(r)}{L_{\|}(r)}, \tag{6.6}$$

where r is the radial coordinate. The code was originally used to successfully describe the target profiles and the fraction of power arriving at the targets during ELMs on MAST and AUG [120, 121].

Filaments are modelled through a flux-tube representation. Two simulated filaments with initial radial velocities of 1.65 and 1.20 km s^{-1} respectively (see figure 5.27), and an initial ion temperature of T_i=30 eV are populated with 1 million particles which are initially distributed according to a Gaussian in the radial and perpendicular directions and uniformly in the parallel direction. Each particle within the filament has a velocity as derived from a Maxwellian velocity distribution according to the initial temperature set above (i.e. T_i=30 eV). The method here is that for each time point in the simulation, the position of each particle is tracked along the relevant field-line until it arrives at the target, or intersects the wall. Naturally, as time increases, the total number of particles within the filament decreases. It is in this way that the total number of particles is used to represent the density variation within the filament (and therefore the corresponding I_{SAT} value). In addition to this, the velocity distribution is also re-calculated at each time point, and the resulting mean absolute velocity is used as a measure of the ion temperature T_i. This therefore includes the radial variation of C_s (through T_i). The result of the simulation is shown in 6.10. The radial distributions of I_{SAT} for high and low density cases are recovered (with e-folding lengths) in the simulations. More specifically, the simulated fall-off corresponding to the high density case (where $V_r \sim 1.65$ km s^{-1}) is $\lambda_{\mathrm{SIM}}^{\mathrm{HIGH}} \sim 40$ mm, while the fall-off length corresponding to the low density case (where $V_r \sim 1.2$ km s^{-1}) is $\lambda_{\mathrm{SIM}}^{\mathrm{LOW}} \sim 30$ mm. These are in good agreement with experimentally measured fall-off lengths of $\lambda_{\mathrm{EXP}}^{\mathrm{HIGH}} \sim 41$ mm at high and $\lambda_{\mathrm{EXP}}^{\mathrm{LOW}} \sim 28$ mm.

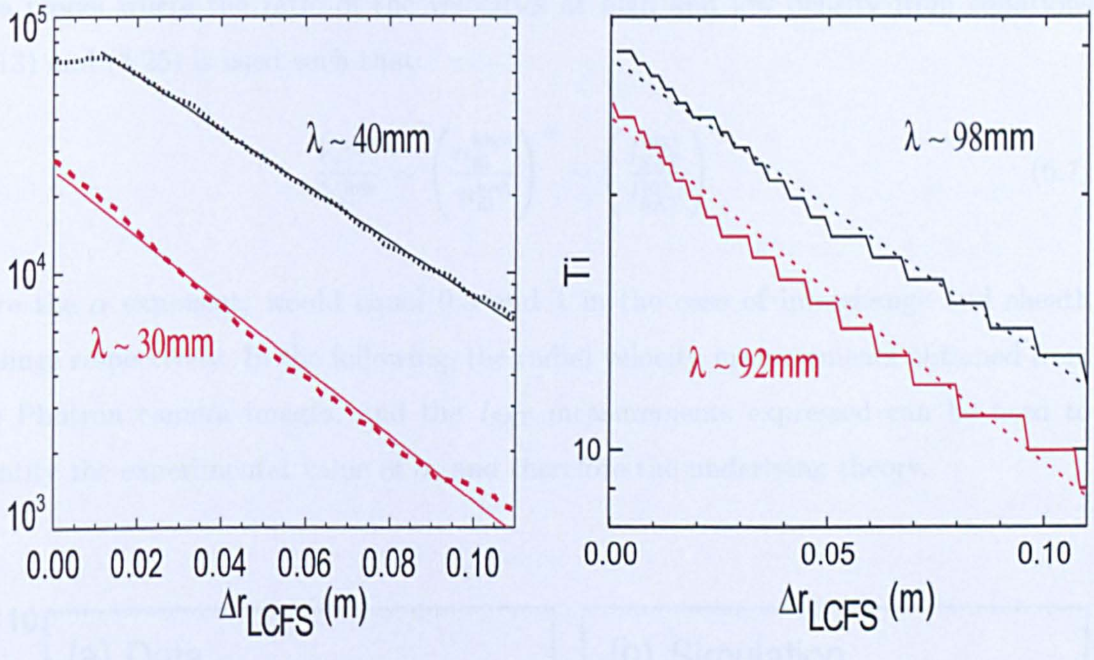

Figure 6.10: *The radial distributions of (a) ion saturation current, and (b) ion temperature at the mid-plane for two simulated filaments moving with constant radial velocities of 1.65 km s^{-1} (dotted), and 1.2 km s^{-1} (dashed) respectively.*

The result of the simulation therefore confirms that the model as shown in equation (6.5) is not sufficient in describing the complex dynamics of a filament in its radial motion, but rather, the radial dependence of parameters must be included. When this is the case, the physics of filament particle loss seems to be well captured in the paradigm.

6.9 Comparison of theories with experiment

Motivated by the discrepancy in the prediction for the radial velocities, experimental data is used to test the theories in the following subsection.

The quantities $L_\perp$, $L_\parallel$, C_s, n_t, n_{SOL} expressed in equations (3.13) and (3.25) from both sheath and interchange theories were found to be approximately the same for the high and low density discharges presented. This allows a comparison of the predictions in a model where the ratio of the velocities at high and low density from equations (3.13) and (3.25) is used such that:

$$\frac{V_r^{\mathrm{high}}}{V_r^{\mathrm{low}}} \sim \left(\frac{n_{\mathrm{fil}}^{\mathrm{high}}}{n_{\mathrm{fil}}^{\mathrm{low}}}\right)^{\alpha} \sim \left(\frac{I_{\mathrm{SAT}}^{\mathrm{high}}}{I_{\mathrm{SAT}}^{\mathrm{low}}}\right)^{\alpha}. \tag{6.7}$$

Here the α exponent, would equal 0.5 and 1 in the case of interchange and sheath scalings respectively. In the following, the radial velocity measurements obtained from the Photron camera images, and the I_{SAT} measurements expressed can be used to identify the experimental value of α, and therefore the underlying theory.

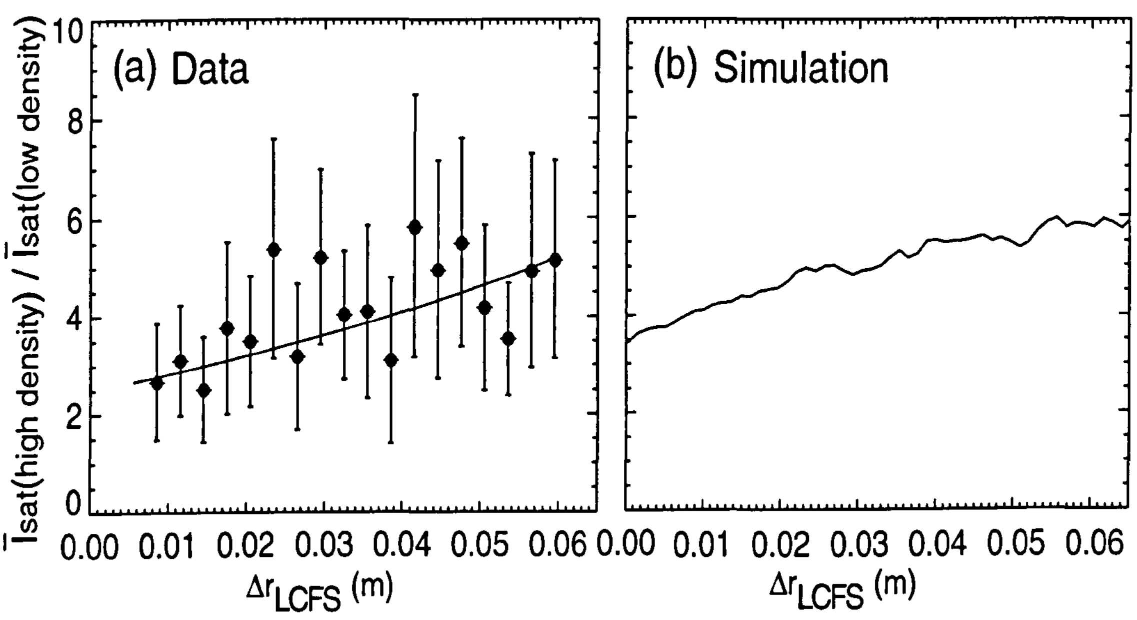

Figure 6.11: *Ratio of (a) experimentally measured and (b) simulated* I_{SAT} *values at high and low density, binned in 1 cm steps from the LCFS.*

Figure 6.11 (a) shows the ratio of the measured I_{SAT} values at high and low $\bar{n}_e$ binned as a function of distance from the LCFS, for $\Delta r_{LCFS} \geq 1$ cm. The immediate SOL has been avoided since filamentary transport dominates this region. The solid line is the exponential fit obtained by taking the ratio of $\exp(-x/\lambda_{\mathrm{EXP}}^{\mathrm{high}})/\exp(-x/\lambda_{\mathrm{EXP}}^{\mathrm{min}})$ where $\lambda_{\mathrm{EXP}}^{\mathrm{high}}$ and $\lambda_{\mathrm{EXP}}^{\mathrm{min}}$ are the experimental particle e-folding lengths at high and low $\bar{n}_e$ estimated in section 6.8. Furthermore, simulations of the ratio of I_{SAT} signals at high and low $\bar{n}_e$ also yield a similar trend, as shown in figure 6.11(b). The difficulty which arises when relating to the predicted velocity scalings is immediately apparent since the ratio of the I_{SAT} values is not constant as a function of distance from the LCFS.

Nevertheless, taking the radial velocity measurements drawn from section 5.7.2, namely, $V_r^{\mathrm{high}} = 1.6$ km s^{-1}, $V_r^{\mathrm{low}} = 1.2$ km s^{-1} at high and low densities respectively, and re-arranging equation (6.7), the α exponent is given by the expression:

$$\alpha \sim 0.29/\ln\left(\frac{I_{\mathrm{SAT}}^{\mathrm{high}}}{I_{\mathrm{SAT}}^{\mathrm{low}}}\right). \tag{6.8}$$

Figure 6.12 shows a plot of the α exponent as a function of distance. Experimental values of α decrease from 0.3 in the proximity of the LCFS to 0.2 approximately 6 cm from the edge, and are therefore factors of 4 and 2 smaller than sheath and interchange limits respectively. In fact, both experimental data and simulation confirm that the scaling of the α exponent varies as a function of distance in the SOL – a feature which is not captured in either model.

So far, predictions from both theories have been compared in a model where the filament density and related radial velocity are correlated, and $L_\perp$, $L_\parallel$, C_s, n_t, n_{SOL} are assumed to be constant to a first approximation. Because the conclusion drawn from the absolute value of α are very dedicated, the effect of the neglected parameters is now discussed. In other words, can the fluctuations in the background SOL density n_{SOL} for example account for the small deviations or even increase the values of the α exponent.

It was shown from both camera data (see section 5.21) and probe data (see section 6.7) that inter-ELM filament widths are similar at high and low n_e. The electron temperature profiles from Thomson scattering data are also similar, meaning the con-

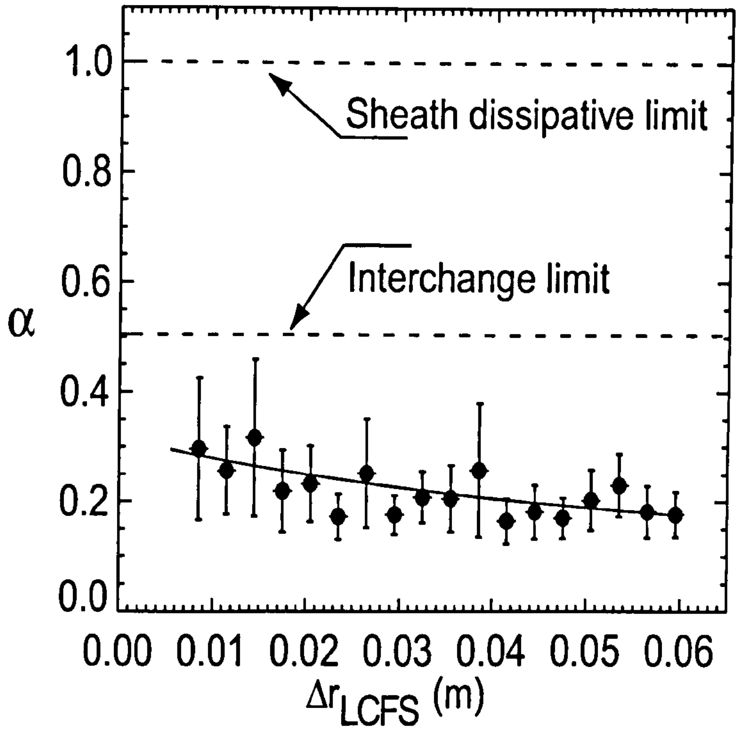

Figure 6.12: *Plot of the α exponent as a function of distance from the LCFS. The two dashed lines indicate the interchange and sheath dissipative limits. Experimental values of α are below both limits.*

tribution of the C_s term when taking the ratio also cancels out. The same applies for $L_{\parallel}$ since the magnetic geometry is the same for the set of high and low density discharges. The remaining quantities are n_{SOL} and n_t. Since they play equivalent roles in equations (3.13) and (3.25) (see chapter 3) only the n_{SOL} parameter is discussed.

In order to investigate the effect of n_{SOL} variation on the α exponent, changes in the background I_{SAT} signal in periods separating filaments are assumed to be proportional to a first approximation to changes in n_{SOL}. Figure 6.13 shows on a log-linear scale the I_{SAT} values recorded as a function of (Δr_{LCFS}) in high and low density discharges. Data have been binned in 1 cm intervals and the error bars are the R.M.S. of the distributions at each bin. Also shown in the bottom plot of figure 6.13 is the ratio of $n_{\mathrm{SOL}}^{\mathrm{low}}/n_{\mathrm{SOL}}^{\mathrm{high}}$ for $\Delta r_{LCFS} \geq 1$ cm, since this is the range over which results for the α parameter are drawn. Now, taking into account variations of n_{SOL}, the expression for α from equation (6.8) is given by:

$$\alpha \sim 0.29/\left[\ln\left(\frac{I_{\mathrm{SAT}}^{\mathrm{high}}}{I_{\mathrm{SAT}}^{\mathrm{low}}}\right) + \ln\beta\right], \tag{6.9}$$

where $\beta = n_{\rm SOL}^{\rm low}/n_{\rm SOL}^{\rm high}$.

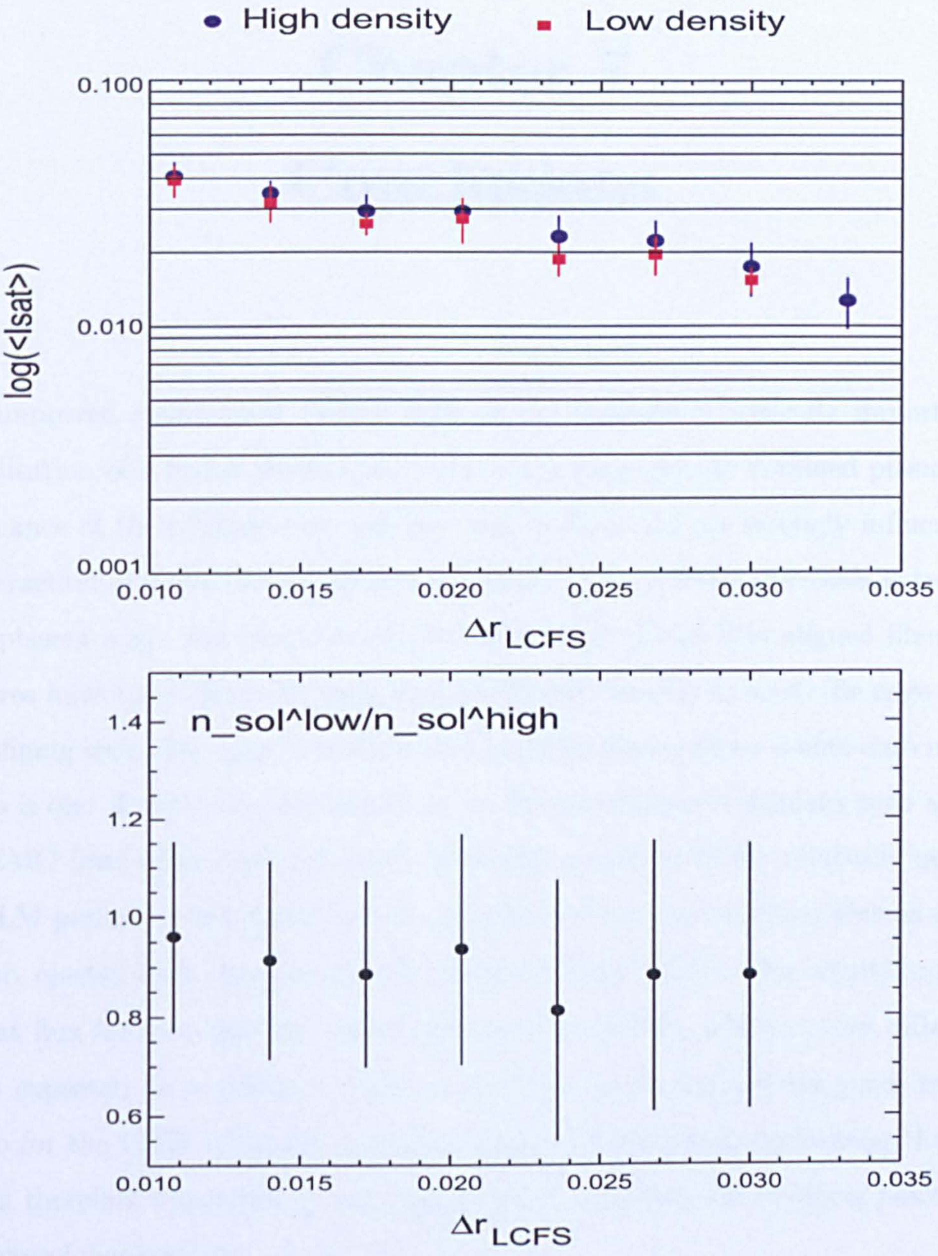

Figure 6.13: *Shown are (a) plot of* $I_{\rm SAT}$ *values as a function of distance from the LCFS, and (b) plot of the ratio* $n_{\rm SOL}^{\rm low}/n_{\rm SOL}^{\rm high}$ *for* $\Delta r_{LCFS} \geq 1$ *cm.*

According to equation (6.9), inserting the value of $n_{\rm SOL}^{\rm low}/n_{\rm SOL}^{\rm high} = 0.96$ would increase α from 0.26 to 0.27±25% at 1 cm from the LCFS. The effect of $n_{\rm SOL}$ variation on the α parameter is therefore negligible for the set of discharges described in this thesis.

Chapter 7

Conclusions

An improved confinement regime such as the H-mode is critically important for the realisation of a fusion power plant based on a magnetically confined plasma. The performance of the plasma core, stability and confinement are strongly influenced by the interaction of many diverse physics processes. Among these processes is transport at the plasma edge, and particularly during an ELM where field-aligned filamentary structures have been observed using high resolution cameras to leave the edge and hit the confining wall. The impact of the power loadings during these events onto material surfaces is one of the main constraints on the design of future tokamaks such as ITER and DEMO (and other fusion devices). However, transport in the relatively quiescent inter-ELM periods is also found to be a complicated process in which plasma is intermittently ejected from the core into the scrape-off layer (SOL). This results in particle and heat flux far from the last closed flux surface (LCFS), which is very different to what is expected for a diffusive process. So while the H-mode is the main reference scenario for the ITER tokamak, understanding the mechanisms underlying these processes is therefore important in calculating and controlling the resulting power loads on the vessel components.

In this thesis, experimental analysis of filamentary structures at the plasma edge in the Mega Amp Spherical Tokamak (MAST) during H-mode inter-ELM periods is presented using both a midplane-mounted ultra fast camera and reciprocating Langmuir probes (see chapter 4 for details of these diagnostics). A background subtraction code is applied to the camera images in order to distinguish the D_α light emission of filamentary structures from the overall slowly-varying background. Camera images recorded at a rate of 100 kHz during these periods have provided the first evidence which shows that similar to L-mode and ELM events, field-aligned filamentary structures also exist during inter-ELM periods. A comparison of their corresponding D_α light emission shows that inter-ELM filaments are the lowest amplitude fluctuations in the MAST SOL relative to L-mode and ELM filaments.

Using reconstructions of the magnetic equilibrium, field-lines are projected onto 2D images to track filaments in radial and toroidal directions. Projection codes which take into account the camera properties have been developed to perform these tasks. The tracking of filaments is done both manually and using semi-automated codes. Analysis of the spatio-temporal evolution of these filaments confirms that despite the reduction in turbulence levels seen in the H-mode, inter-ELM filaments exist on timescales ~ 50–120 μs, and during this time contribute directly to the cross-field transport: they are found to rotate in the vicinity of the LCFS with a mean toroidal velocity of 9 km s^{-1} in the co-current direction, and propagate radially outwards with a constant velocity in the range 1–2 km s^{-1}.

It was also found that whereas the toroidal steps are on average constant (i.e. no toroidal acceleration) for any given filament, the collective motions of the filaments is more complex: similar to L-mode and unlike ELM phases, filaments are not regularly spaced, and due to different toroidal velocities, their spacings are constantly changing.

Toroidal and radial excursions of filaments have also been tracked in order to determine any dependence of these motions on plasma parameters such as the plasma density $\bar{n}_e$, current I_p, heating power $P_{\rm NBI}$ and toroidal field B_ϕ. While no significant variation was observed with I_p, $P_{\rm NBI}$ and B_ϕ, the motion of these filaments was found to depend strongly on plasma density: with increasing $\bar{n}_e$, a marked decrease in the average toroidal rotation velocity has been observed, and an enhancement of radial transport clearly manifested by the departure of a higher number of filaments. Furthermore, filaments at higher densities ($0.55 \leq n_e/n_{\rm GW} \leq 0.75$) have been found to travel radially faster ($\bar{V}_r \sim 1.65$ km s^{-1}) than filaments at lower densities ($0.3 \leq n_e/n_{\rm GW} \leq 0.45$) ($\bar{V}_r \sim 1.2$ km s^{-1}). Similar observations from a number of machines have reported that increases in $\bar{n}_e$ are associated with a broadening of the particle density profile, higher fluctuation levels and stronger turbulence-driven radial transport [122, 123, 124, 125].

Experimental findings on the Alcator C-mod tokamak have also elucidated a possible link to the density limit in References [126, 127] which postulate that the density limit is simply the extreme case of many filaments leaving the edge. The observation of faster and more frequent filaments leaving the edge plasma at higher densities in MAST discharges is consistent with the conjecture made in [122] which suggests that filamentary structures may become electrically disconnected from the target sheaths at large collisionality, and thus experience less sheath dissipation, resulting in a substantial enhancement of the radial convective transport. The precise relationship of the filamentary transport in the SOL to the density limit remains to be checked in future dedicated experiments.

Semi-Automated methods are also applied to the inter-ELM camera images in order to determine physical properties of these filaments. A wide range of toroidal mode numbers is found (6–48) with a mean 24. Analysis of toroidal and radial widths indicate that inter-ELM filaments are elliptical in size with an average toroidal width of 16 cm and a radial width of 4 cm.

Camera images recorded at a rate of 100 kHz have been compared to data recorded simultaneously by the mid-plane reciprocating probe. The cross-comparison shows that intermittent fluctuations in ion saturation current (I_{SAT}) signals correspond to inter-ELM filaments passing the probe. Peak detection algorithms have been applied to I_{SAT} signals in order to isolate the peaks corresponding to filamentary structures from the high frequency background. The contribution of inter-ELM filaments can be seen in the PDF of the entire I_{SAT} signal as a bump-on-tail. The probability density of corresponding filament I_{SAT} values is in the range 0.05 – 0.25 A. Assuming that I_{SAT} is a good proxy for number density (with a weak square root dependence on temperature), a number density estimate for inter-ELM filaments is obtained based on these values. Density is found to be in the range $6.5\ \times 10^{16} - 6.7 \times 10^{17}$ m^{-3}. A similar analysis was repeated for L-mode and results compared with ELM data. While the densities for filaments in the inter-ELM phase are lower than those in L-mode, both are much smaller than the density of ELM filaments. This observation is in qualitative agreement with the PDF of light intensity from imaging data. The agreement is expected since both D_α light emission from the camera data and I_{SAT} are proportional to the number density.

Closer inspection of peaks in I_{SAT} signals indicates that these filaments appear immediately before and after the ELM. The existence of these filaments in the precursor stage of the ELM (lasting 150 μs till ELM onset) is suggestive that the driving mechanism of the inter-ELM filaments is independent of the ELM. Equally, the immediate appearance of filaments following the ELM crash also suggests that the critical gradient threshold for inter-ELM filaments, if any, is far lower than that of ELMs.

The I_{SAT} signals from single and and neighbouring probe tips have been used to verify the properties of filaments at the edge, finding toroidal widths, mode number and toroidal velocity - in good agreement with camera estimates.

The radial motion of inter-ELM filaments is also captured in Langmuir probe data through measurements of the radial fall-off of I_{SAT}, denoted λ_{SAT}. Exponential fits of the I_{SAT} values as a function of distance from the LCFS yield particle e-folding lengths of $\lambda_{\text{SAT}}^{\text{high}} \sim 41$ mm at high density discharges ($0.55 \leq n_e/n_{\text{GW}} \leq 0.75$ where n_e is the line-averaged electron density and n_{GW} is the Greenwald density), and $\lambda_{\text{SAT}}^{\text{low}} \sim 28$ mm at low density ($0.3 \leq n_e/n_{\text{GW}} \leq 0.45$). Similar trends are also obtained in simulations of a filament propagating radially with a velocity V_r and losing particles on ion parallel loss timescales $\tau_{\parallel}$, such that $\lambda \sim V_r\tau_{\parallel}$ where $\tau_{\parallel} \equiv L_{\parallel}/C_s$ ($L_{\parallel}$ is the connection length and C_s is the ion sound speed). Crucially, it is shown through simulation that this frequently used model is only valid, (i.e. that agreement with experimental data is only obtained) when the radial dependence of C_s and $L_{\parallel}$ parameters is included.

Radial velocity and I_{SAT} measurements reported in this thesis have been used to test predictions for the radial velocity made by the interchange and sheath-limited regime models. Taking the velocity scalings from each theory, predictions for the ratio of the velocity scalings at high and low density were instead used and expressed as $V_r^{\text{high}}/V_r^{\text{low}} \sim \left(I_{\text{SAT}}^{\text{high}}/I_{\text{SAT}}^{\text{low}}\right)^{\alpha}$ where $\alpha = 0.5$ and 1 for interchange and sheath-dissipative regimes respectively. Radial velocity and I_{SAT} measurements were subsequently used to determine the experimental values of the α exponent. The observed data were found to be at least a factor of 2 smaller than both models. In fact, the scaling observed was found to vary as a function of distance in the SOL – a feature which is not captured in either model. For a better comparison with experimental findings, a future model which takes into account interchange dynamics, parallel motions and the collisional resistivity in the SOL is required.

Finally, physical properties of inter-ELM filaments have been compared and contrasted with those of L-mode and ELM filaments. A common feature between all filaments is that they are field-aligned structures and contribute directly to transport. However, collective observations from data collected in this thesis and previously reported data regarding ELM and L-mode filaments (summarised in chapter 2), indicate that on the whole physical properties of inter-ELM filaments and their behaviour are more similar to L-mode than they are to ELM filaments. The original idea that inter-ELM filaments are mini-ELM events, or "failed" ELMs can be ruled out. Rather, inter-ELM filaments are distinct from ELMs. The understanding of the ELMs is the same: that these are repetitive plasma instabilities which are associated with a steep pressure gradient, marked by a strong magnetic signature and appear with a regular spacing of narrow filaments which accelerate explosively in the radial direction. This is in contrast to the inter-ELM and L-mode filaments whose motions indicate no acceleration in the radial direction, and spacings are constantly changing (due to individual filament motions) leading to complex dynamics with a considerable spread in toroidal mode numbers.

No noticeable magnetic signature has thus far been detected for inter-ELM filaments, suggesting therefore that these are electrostatic phenomena (although this remains to be checked in future experiments with an improved magnetic diagnostic).

The transition to H-mode means that the plasma edge rotates faster and inter-ELM filaments do indeed rotate faster than L-mode filaments. However, both L-mode and inter-ELM filaments are slow-rotating relative to the ELM. A possible explanation (as suggested in chapter 5) is that inter-ELM and L-mode filaments originate in a similar region within the pedestal closer to the plasma edge where the bulk plasma rotation is slower, whereas the ELM filaments originate from deeper within the plasma where the bulk plasma rotation is faster.

Finally, the fact that inter-ELM filaments persist all the way till the ELM despite the onset of a precursor mode 150 μs before the ELM crash is suggestive that the driving mechanism for inter-ELM filaments is different and independent of the ELM.

In light of the above observations, it may be speculated that the inter-ELM filaments are the "H-mode manifestation" of the L-mode filaments, i.e., L-mode filaments in the presence of a transport barrier. One possible interpretation is that L-mode and inter-ELM filaments are drift waves since all that is required is a density gradient which is universally inherent in each plasma. ELM filaments however are the manifestation of ballooning modes.

7.1 Future work

One important area of study would be to simulate inter-ELM filaments using a global 3D code. This is currently challenging, because the L-H transition is relatively poorly understood and self-consistent simulations of H-mode on transport time-scales have yet to be performed. This is partly because H-mode involves large gradients in temperature and density spanning a range from collisionless to collisional regimes which introduces a wide range of length and time-scales. Observations reported in this thesis can be used to test the simulation codes when these challenges are eventually overcome.

Statistical analysis of data from the reciprocating Langmuir probe in MAST could also form part of ongoing research. Recent work in references [40, 41] identifies two scaling regions for MAST L-mode data, and finds that the rescaled PDFs associated with these two scaling regions are different, with good fits to the Fréchet and Gumbel extreme value distributions respectively [40, 42]. It would be interesting to apply these statistical techniques to inter-ELM data to test the conjecture made in this thesis that L-mode and inter-ELM fluctuations are similar. Furthermore, it was recently shown in [128] that the statistical properties of turbulent I_{SAT} fluctuations in the ASDEX-Upgrade tokamak in H-mode are not modified when compared with L-mode; this statement echo's the observations made in this thesis, and has lead the authors in [128] to suggest that suppression or modification of turbulence is neither a necessary nor a sufficient condition to achieve H-mode in tokamaks. A comparison would therefore be worthwhile.

It was shown in Ref [52] that no magnetic signatures were observed in inter-ELM periods using the current reciprocating magnetic coil which is only capable of reaching the LCFS to within 2.5 cm. It would be particularly useful to check this at the LCFS since magnetic signatures are quickly attenuated with distance from the LCFS. This would require the design and implementation of a new magnetic probe head on MAST.

Finally, since it is possible that resonant magnetic perturbations (RMPs) will be applied to the edge in a future tokamak fusion device in an attempt to mitigate large ELMs, it would be interesting to determine the effect of these on the motion and properties of inter-ELM filaments in a new set of experiments using camera, Langmuir and magnetic probes.

REFERENCES

[1] Energy Information Administration (US DOE) http://www.eia.doe.gov

[2] http://www.ipcc.ch

[3] M. A. Gregory and M. Zeilik. "*Introductory Astronomy and Astrophysics*", Saunders Golden Sunburst Series, 4th edition, 2002.

[4] J. A. Wesson. "*Tokamaks*". Clarendon Press, Oxford, 4th edition, 2004.

[5] L. Spitzer. "*The physics of fully ionised gases*". Interscience publishers, New York, 90, 1956.

[6] https://lasers.llnl.gov/

[7] A. H. Boozer. "What is a stellarator?". *Phys. Plasmas*, **5**, 1647, (5) 1998.

[8] R. D. Hazeltine and J. D. Meiss. "*Plasma Confinement*". Dover Publications, Inc., New York, 2003.

[9] P. Helander and D. J. Sigmar. "*Collisional Transport in Magnetized Plasmas*". Cambridge University Press, Cambridge, 2002.

[10] Y-K. M. Peng and D. J. Strickler, "The spherical Tokamak". *Nuclear Fusion*, **26**, 769, 1986.

[11] F. Troyon, R. Gruber, H. Saurenmann, S. Semenzato and S. Succi. "MHD-Limits to Plasma Confinement". *Plasma Phys. Control. Fusion*, **26**, 209, 1984.

[12] https://www.ITER.org

[13] C. Llewellyn Smith "The fast track to fusion energy", *Proc. 20th Int. Conf. on Fusion Energy* (Vilamoura Portugal, 2004, (Vienna: IAEA) CD-ROM file FPM2 and http://www.nawem.iaea.org/napc/physics/fec/fec2004/talks/talkFPM.pdf

[14] D. Bohm, In A. Guthrie and R. K. Wakerling. "*The Characteristics of electrical discharges in Magnetic Fields*". volume 1 of *National Nuclear Energy Series*, page 77. McGraw-Hill Book Company, Inc., New York, 1949.

[15] P. A. Davidson. "*Turbulence*", Oxford University Press, 2004.

[16] A. Yoshizawa, S-I Itoh, K. Itoh, and N. Yokoi. "Turbulence theories and modelling of fluids and plasmas". *Plasma Phys. Control. Fusion*, **43**, R1R144, 2001.

[17] D. Biskamp. "*Magnetohydrodynamic Turbulence*", Cambridge University Press, 2003.

[18] Fifth Carolus Magnus Euro-Summer School: lecture notes. Bad Honnef, Germany, 2001.

[19] G. Husymans. "ELMs: MHD instabilities at the transport barrier". *Plasma Phys. Control. Fusion*, **47**:B165178, 2005.

[20] P. B. Snyder, H. R. Wilson, J. R. Ferron, L. L. Lao, A. W. Leonard, T. H Osborne, A. D. Turnbill, D. Mossessian, M. Murakami, X. Q. Xu. "Edge localised modes and the pedestal: A model based on coupled peeling–ballooning modes". *Phys. Plasmas* Vol. 9, No. 5, 2002.

[21] F. Chen. *"Introduction to plasma physics and controlled fusion"*. volume1. Plenum Press, 2nd edition, 1984.

[22] W. Horton. "Drift waves and transport". *Rev. Modern Physics,* **71**:, 35-773, April 1999.

[23] B. D. Scott. "The nonlinear drift wave instability and its role in tokamak edge turbulence". *New J. Physics*, **4**, 52.1-52.30, 2002.

[24] K. H. Burrell. "Physics of the L-mode to H-mode transition in tokamaks". *Plasma Phys. Control. Fusion*, Vol.34, No.13, 1859:1869, 1992.

[25] K. H. Burell. "Role of the electric field in the transition from L (low) mode to H (high) mode to VH (very high) mode in the DIII-D tokamak". *Phys. Plasmas*, **5**, 1994.

[26] A. Kirk, G. F. Counsell, H. R. Wilson, J-W Ahn, R. Akers, E. R. Arends, J. Dowling, R. Martin, H. Meyer, M. Hole, M. Price, P. B. Snyder, D. Taylor, M. J. Walsh, Y. Yang and the MAST team. "ELM characteristics in MAST". *Plasma Phys. Control. Fusion*, **46**, 551–572, 2004.

[27] W. Suttrop, K. Buchl, H. J. de Blank, J. Schweinzer, H. Zohm and the ASDEX Upgrade Team, NBI group and ICRH group. "Characteristics of edge localised modes in ASDEX-Upgrade". *Plasma Phys. Control. Fusion*, **38** 1407-1410, 1996.

[28] N. Oyama, N. Asakura, A.V. Chankin, T. Oikawa, M. Sugihara, H. Takenaga, K. Itami, Y. Miura, Y. Kamada, K. Shinohara and the JT-60 Team."Fast dynamics of type-I ELMs and transport of the ELM pulse in JT-60U". *Nucl. Fusion*, **44**, 582, 2004.

[29] A. Loarte, G. Saibene, R. Sartori, M. Becoulet, L. Horton, T. Eich, A. Herrmann, M. Laux, G. Matthews, S. Jachmich, N. Asakura, A. Chankin, A. Leonard, G. Porter, G. Federici,M. Shimada, M. Sugihara, G. Janeschitz. "ELM energy and particle losses and their extrapolation to burning plasma experiments". *Journal of Nuclear Materials*, **313-316**, 962966, 2003.

[30] P. B. Snyder, H. R. Wilson, T. H. Osborne and A. W. Leonard. "Characterization of peelingballooning stability limits on the pedestal". *Plasma Phys. Control. Fusion*, **46**, A131-A141, 2004.

[31] H. Wilson, S. Cowley, A. Kirk and P. Snyder. "Magnetohydrodynamic stability of the H-mode transport barrier as a model for edge-localised modes: an overview". *Plasma Phys. Control. Fusion*, **48** (5a), A71-A84, 2006.

[32] R. Scannell, M. J. Walsh, P. G. Carolan, A.C Darke, M.R Dunstan, D. Hare, R. B. Huxford and S.L Prunty. *Rev. Sci. Instr.*, 77:10E510, 2006.

[33] S. J. Zweben and R. W. Gould. **25** 171, 1985.

[34] M. Endler. "Turbulent SOL transport in stellarators and tokamaks". *J. of Nucl. Mat.*, **266-269**, 84, 1999.

[35] A. J. Wootton, B. A. Carreras, H. Matsumoto, K. McGuire. "Fluctuations and anomalous transport in tokamaks". *Phys. Fluids* B, **2**, 2879, 1990.

[36] E. Sanchez, C. Hildalgo, D. Lopez-Bruna, I. Garcia-Cortes, R. Balbin, M. A. Pedrosa, B. Van Milligen, C. Riccardi, G. Chiodini, J. Bleuel, M. Endler, B. A. Carreras, D. E. Newman. "Statistical characterization of fluctuation wave forms

in the boundary region of fusion and nonfusion plasmas". *Phys. Plasmas*, **7**, 1408, 2000.

[37] U. Frisch. "*Turbulence*". Cambridge University Press, Cambridge, 2005.

[38] G. F. Counsell, N. Ben Ayed, R. O. Dendy, B. D. dudson, B. Hnat, A. Kirk, S. Lisgo, T. D. Rognlien, R. Scannell, S. Tallents, M. V. Umansky, and X. Q. Xu. "Analysis of L-mode turbulence in the MAST boundary plasma". In *21st fusion Energy Conference*, Chengdu, China, IAEA, 2006.

[39] M. Agostini, S. J. Zweben, R. Cavazzana, P. Scarin, G. Serianni, R. J. Maqueda, D. P. Stotler. "Study of statistical properties of edge turbulence in the National Spherical Torus Experiment with gas puff imaging diagnostic". *Phys. Plasmas*, **14**, 102305, 2007.

[40] B. Hnat, B. D. Dudson, R. O. Dendy, G. F. Counsell and A. Kirk. "Characterisation of edge turbulence in L-mode plasmas in the Mega Amp Spherical Tokamak". In 33^{rd} EPS *Conference on Plasma Physics*, Rome, Italy, 2006.

[41] B. Hnat, B. D. Dudson, R. O. Dendy, G. F. Counsell, A. Kirk, and the MAST team. "Statistical properties of L-mode edge plasma turbulence for three different magnetic configurations in the Mega Amp Spherical Tokamak". In 34^{th} EPS *Conference on Plasma Physics*, Warsaw, Poland, July 2007.

[42] B. Hnat, B.D. Dudson, R.O. Dendy, G.F. Counsell, A. Kirk and the MAST team. "Characterisation of edge turbulence in relation to edge magnetic field configuration in Ohmic L-mode plasmas in the Mega Amp Spherical Tokamak". *Nuclear Fusion*, **48**, 085009, 2008.

[43] B. D. Dudson, R. O. Dendy, A. Kirk, H. Meyer, and G. F. Counsell. "Comparison of L and H-mode plasma edge fluctuations in MAST". *Plasma Phys. Control. Fusion*, **47**:885-901, 2005.

[44] J. M. Dewhurst, B. Hnat, N. Ohno, R. O. Dendy, S. Masuzaki, T. Morisaki and A. Komori. "Statistical properties of edge plasma turbulence in the Large Helical Device", *Plasma Phys. Control. Fusion*, **50**, 095013, 2008.

[45] Y. H. Xu, S. Jachmich, R. R. Weynants and the TEXTOR Team. "On the Properties of turbulence intermittency in the boundary of the TEXTOR Tokamak". *Plasma Phys. Contr. Fusion*, **47**:1841-1855, 2005.

[46] A. Kirk, H. R. Wilson, R. Akers, N. J. Conway, G. F. Counsell, S. C. Cowley, J. Dowling, B. Dudson, A. Field, F. Lott, B. Lloyd, R. Martin, H. Meyer, M. Price, D. Taylor, M. Walsh and the MAST team. "Structure of ELMs in MAST and the implications for energy deposition". *Plasma Phys. Control. Fusion*, **47** 315-333, 2005.

[47] R. Scannell, M. J. Walsh, P. G. Carolan, N. J. Conway, A. C. Darke, M. R. Dunstan, D. Hare and S. L. Prunty. "Enhanced edge Thomson scattering on MAST". *Rev. Sci. Instrum.*, **77**, 10E510, 2006.

[48] A. Kirk, H. R. Wilson, G. F. Counsell, R. Akers, E. Arends, S. C. Cowley, J. Dowling, B. Lloyd, M. Price, M. Walsh, and MAST Team. "Spatial and Temporal Structure of Edge-Localised Modes". *Phys. Rev Lett*, **92**(24):021, 2004.

[49] A. Kirk, G. F. Counsell, G. Cunningham, J. Dowling, M. Dunstan, H. Meyer, M. Price, S. Saarelma, R. Scannell, M. Walsh, H. R. Wilson, and the MAST Team. "Evolution of the Pedestal on MAST and the Implications for ELM Power Loadings". *Plasma Phys. Contr. Fusion*, **49**, (8), 1259-1275, 2007.

[50] B. Kurzan, L. D. Horton, H. Murmann, J. Neuhauser, W. Suttrop and the ASDEX UPgrade Team. "Thomson scattering Analysis of Large Scale Fluctuations in the ASDEX Upgrade edge". *Plasma Phys. Contr. Fusion*, **49**, 825-844, 2007.

[51] R. Scannell, A. Kirk, N. Ben Ayed, P. G. Carolan, G. Cunningham, J. McCone, S. L. Prunty, M. J. Walsh. "Experimental Investigation into ELM Filament Formation on MAST". *Plasma Phys. Contr. Fusion*, **49**, 1431-1446, 2007.

[52] A. Kirk, N. Ben Ayed, G. F. Counsell, B. Dudson, T. Eich, A. Herrmann, B. Koch, R. Martin, A. Meakins, S. Saarelma, R. Scannell, S. Tallents, M. Walsh, H. R. Wilson and the MAST team. "Filament Structures at the plasma edge on MAST". *Plasma Phys. Contr. Fusion*, **48**:B433–B441, 2006.

[53] S. J. Zweben and R. W. Gould."Structure of edge plasma turbulence in the CALTECH tokamak". *Nulcear fusion*, **25**,(2), 171-183, 1985.

[54] S. J. Zweben, R. J. Maqueda, D. P. Stotler, A. Keesee, J. Boedo, C. E. Bush, S. M. Kaye, B. LeBlanc, J. L. Lawrence, V. J. Matrocola, R. Maingi, N. Nishino, G. Renda, D. W. Swain and J. B. Wilgen. "High-speed imaging of edge turbulence in NSTX". *Nulcear fusion*, **44**:134-153, 2004.

[55] R.J. Fonck, P.A. Duperrex, S. F. Paul. "Plasma fluctuation measurements in tokamaks using beam-plasma interactions". *Rev. Sci. Instr.*, **61**, 3487, 1990.

[56] J. A. Boedo, D. K. Rudakov, E. Hollmann, D. S. Gray, K. H. Burrell, R. A. Moyer, G. R. McKee, R. Fonck, P. C. Stangeby, T. E. Evans, P. B. Snyder, A. W. Leonard, M. A. Mahdavi, M. J. Schaffer, W. P. West, M. E. Fenstermacher, M. Groth, A. S. Allen, C. Lasnier, G. D. Porter, N. S. Wolf, R. J. Colchin, L. Zeng, G. Wang, J. G. Watkins, T. Takahasi, and DIII-D Team. "Edge-localised mode dynamics and transport in the scrape-off layer of the DIII-D tokamak". *Phys. Plasmas*, **12**, 072516, 2005.

[57] A. Hermann, T. Eich, V. Rohde, C. J. Fuchs, J. Neuhauser and Asdex Upgrade team. "Power deposition outside the divertor in ASDEX Upgrade". *Plasma Phys. Control. Fusion*, **46**:971-979, 2007.

[58] F. Lott, A. Kirk, G.F. Counsell, J. Dowling,D. Taylor, T. Eich, A. Herrmann. "Thermographic power accounting in MAST". *Journal of Nuclear Materials*, **337-339**, 786–790, 2005.

[59] B. Lloyd, N. Ben Ayed, A. Kirk, B. Dudson, et al. and the MAST Team. "Overview of Physics results from MAST". *Nuclear Fusion*, **47**(S):658-667, 2007.

[60] T. Eich, A. Hermann, J. Neuhauser, R. Dux, J. C. Fuchs, S. Gunter, L. D. Horton, A. Kallenbach, P. T. Lang, C. F. Maggi, M. Maraschek, V. Rohde, W. Shneider and the Asdex Upgrade Team. "Type-I ELM substructure on the divertor Target Plates in Asdex Upgrade". *Plasma Phys. Control. Fusion*, **47**(6):815-842, 2005.

[61] A. Kirk, B. Koch, R. Scannell, H. R. Wilson, G. Counsell, J. Dowling, A. Hermann, R. Martin, M. Walsh, and the MAST team. "Evolution of Filament

Structures during Edge-Localized Modes in the MAST Tokamak". *Phys. Rev. Lett*, **96**, 185001, 2006.

[62] B. Dudson, N. Ben Ayed, A. Kirk, H. R. Wilson, G. Counsell, X. Xu, M. Umansky, P. B. Snyder, B. Lloyd and the MAST team. "Experiments and simulation of edge turbulence and filaments in MAST". *Plasma Phys. Control. Fusion*, **50** 124012, 2008.

[63] M. R. Wade, K. H. Burrell, A. W. Leonard, T. H. Osborne, and P. B. Snyder. "Edge-Localized-ModeInduced Transport of Impurity Density, Energy, and Momentum". *Phys. Rev. Lett*, **95**, 225001, 2005.

[64] A. Schmid, A Herrmann, H. W. Mller, and the ASDEX Upgrade Team. "Experimental observation of the radial propagation of ELM induced filaments on ASDEX Upgrade". *Plasma Phys. Control. Fusion*, **50**, 4, 045007, 2008.

[65] B. Kurzan, H. D. Murmann, and J. Neuhauser. "Fine Structure of Type-I Edge-Localized Modes in the Steep Gradient Region". *Phys. Rev. Lett*, **95**, 145001, 2005.

[66] J. L. Terry, I. Cziegler, A. E. Hubbard, J. A. Snipes, J. W. Hughes , M. J. Greenwald, B. LaBombard, Y. Lin, P. Phillips, S. Wukitch. "The dynamics and structure of edge-localized-modes in Alcator C-Mod". *Journal of Nuclear Materials*, **363365**, 994999, 2007.

[67] A. Kirk, G. F. Counsell, E. Arends, H. Meyer, D. Taylor, M. Valovic, M. Walsh, H. Wilson, and the MAST Team. "H-mode pedestal characteristics on MAST". *Plasma Phys. Control. Fusion*, **46** A187-94, 2004.

[68] W. Fundamenski, W. Sailer and JET EFDA contributors. "Radial propagation of Type-I ELMs on JET". *Plasma Phys. Control. Fusion*, **46** 233-259, 2004.

[69] A. Kirk, N. Asakura, J. A. Boedo, M. Beurskens, G. F. Counsell, T. Eich, W. Fundamenski, A. Herrmann, Y. Kamada, A. W. Leonard, S. Lisgo, A. Loarte, N. Oyama, R. A. Pitts, A. Schmid, and H. R. Wilson for the Pedestal and Edge Physics ITPA Topical Group. "Comparison of the spatial and temporal structure of type-I ELMs". *J. of Physics - conference series*, **123**, 012011, 2008.

[70] A. Kirk, T. Eich, A. Herrmann, H. W. Muller, L. D. Horton, G. F. Counsell, M. Price, V. Rohde, V. Bobkov, B. Kurzan, J. Neuhauser, H. Wilson and the ASDEX Upgrade and MAST Teams. "The spatial structure of type-I ELMs at the mid-plane in ASDEX Upgrade and a comparison with data from MAST". *Plasma Phys. Control. Fusion*, **47** 995-1013, 2005.

[71] M. Fenstermacher. Proc of 20th IAEA Fusion Energy Conf. (Villamora), IAEA-CN-116 /EX2-5Rb, 2004.

[72] M. Beurskens, *Private communication.*

[73] P. Andrew, *et al*, Proc. 34th EPS conf. on Plasma Physics and Controlled Fusion I1-005, 2004.

[74] N. Asakura. "ELM Propagation and Fluctuations Characteristics in H- and L-mode SOL Plasmas on JT-60U". Proc of 21st IAEA Fusion Energy Conf., (Chengdu) IAEA-CN-149/EX9-2, 2006.

[75] O. Grulke, J. L. Terry, B. LaBombard and S. J. Zweben. "Radially propagating fluctuation structures in the Scrape-off-Layer of Alcator C-Mod". *Physics of Plasmas*, **13**, 012306, 2006.

[76] T. Bolzonella, H. Zohm, M. Maraschek, E. Martines, S. Saarelma, S. Gunter and the ASDEX Upgrade Team. "High frequency MHD activity related to type-I ELMs in ASDEX Upgrade". *Plasma Phys. Control. Fusion*, **46**(5A), A143-A149, 2004.

[77] H. Reimerdes, A. Pochelon and W Suttrop. "Toroidally asymmetric ELM precursors in TCV". *Nucl. Fusion*, **38**(3), 319-323, 1998.

[78] S. Fielding, J. D. Ashall, P. Carolan, A. Colton, D. Gates, J. Hugill, A. W. Morris, M. Valovic, and the COMPASS and ECRH Teams. "The H-mode in Compass-D". *Plasma Phys. Control. Fusion*, **438**(8), 1091-1102, 1996.

[79] S. I. Krasheninnikov. "On scrape-off later transport". *Phys. Lett. A*, **283**, 368–370, 2001.

[80] O. E. Garcia, N. H. Bian and W. Fundamenski. "Radial interchange motions of plasma filaments". *Phys. Plasmas*, **13**, 082309, 2006.

[81] N. H. Bian , S. Benkadda, J-V Paulsen and O. E. Garcia. "Blobs and front propagation in the scrape-off layer of magnetic confinement devices". *Phys. Plasmas*, **10** 671, 2003.

[82] G. Q. Yu and S. I. Krasheninnikov. "Dynamics of blobs in scrape-off layer/shadow regions of tokamaks and linear devices ". *Phys. Plasmas*, **10**, 4413–4418, 2003.

[83] D. A. D'Ippolito and J. R. Myra. "Blob stability and transport in the scrape-off layer". *Phys. Plasmas*, **10**, 4029–4039, 2003.

[84] D. A. D'Ippolito., J. R.Myra, S. I. Krasheninnikov, G. Q. Yu, and A. Yu. Pigarov. "Blob Transport in the Tokamak Scrape-off-Layer". *Contrib. Plasma Phys.*, **44**, No. 1-3, 205-206, 2004.

[85] Y. Sarazin and Ph. Ghendrih. "Intermittent particle transport in two-dimensional edge turbulence". *Phys. Plasmas*, **5**, Number 12, 4214, 1998.

[86] Y. Sarazin,Ph. Ghendrih, G. Attuel, C. Clment, X. Garbet, V. Grandgirard, M. Ottaviani, S. Benkadda, P. Beyer, N. Bian and C. Figarella. "Theoretical understanding of turbulent transport in the SOL". *J. Nucl. Mater.*, **313-316**, 796-803, 2003.

[87] V. Rozhansky and A. Kirk. "Possible mechanism for filament motion in the SOL of a tokamak". *Plasma Phys. Control. Fusion*, **50**, 025008, 2008.

[88] D. A. D'Ipplito, J. R. Myra, S. I. Krasheninnikov. "Cross-field blob transport in tokamak scrape-off-layer plasmas". *Phys. Plasmas*, **9**, 222-233, 2002.

[89] N. Bisai, A. Das, S. Deshpande, R. Jha, P. Kaw, A. Sen, and R. Singh. "Edge and scrape-off layer tokamak plasma turbulence simulation using two-field fluid model". *Phys. Plasmas*, **12**, 072520, 2005.

[90] N. Bisai, A. Das, S. Deshpande, R. Jha, P. Kaw, A. Sen, and R. Singh. "Formation of a density blob and its dynamics in the edge and the scrape-off layer of a tokamak plasma". *Phys. Plasmas*, **12**, 102515, 2005.

[91] X. Q. Xu, W. M. Nevins, R. H. Cohen, J. R. Myra, and P. B. Snyder. "Dynamical simulations of boundary plasma turbulence in divertor geometry". *New J. Physics*, 4:53.153.15, 2002.

[92] M. V. Umansky, X. Q. Xu, B. Dudson, and L. L. LoDestro. "BOUT Code Manual". LLNL, June 2006. Available from www.mfescience.org/bout/.

[93] A. N. Simakov and P. J. Catto. "Drift-ordered fluid equations for field-aligned modes in low-β collisional plasma with equilibrium pressure pedestals". *Physics of Plasmas*, **10**(12), 47444757, December 2003.

[94] B. Dudson. "Edge turbulence in the Mega-Amp Spherical Tokamak", PhD Thesis University of Oxford, 2008.

[95] O. E. Garcia, N. H. Bian, V. Naulin, A. H. Nielsen and J. Juul Rasmussen. "Mechanism and scaling for convection of isolated structures in nonuniformly magnetized plasmas". *Phys. Plasmas*, **12**, 090701, 2005.

[96] O. E. Garcia, J. Horacek, R. A. Pitts, A. H. Nielsen, W. Fundamenski, J. P. Graves, V. Naulin and J. Juul Rasmussen. "Interchange turbulence in the TCV scrape-off layer ". *Plasma Phys. Control. Fusion*, **48**, L1-L10, 2005.

[97] R. L. Merlino. "Understanding Langmuir probe current-voltage characteristics", *American Journal of Physics*, **75**, 1078, 2007.

[98] D. H. J. Goodall and J. A. Wesson. "Cine observations of MHD instabilities in a Tokamak". *Plasma Phys. Control. Fusion*, **26**(6) 789-797, 1984.

[99] R. S. Granetz, I. H. Hutchinson and D. O. Overske. *Nuclear Fusion*, **19**, 1587, 1979.

[100] R. A. Jacobsen. "High speed photographic studies of the equilibrium and stability of the ATC Tokamak". *Plasma Physics* **17**, 547-554, 1975.

[101] R. J. Maqueda and G. A. Wurden. "Fast imaging of visible phenomena in TFTR". *Nuclear Fusion*, **39**. 629636, 1999.

[102] G. Kocsis, S. Klvin, and G. Veres, P. Cierpka, P. T. Lang, J. Neuhauser, C. Wittman, and ASDEX Upgrade Team. "A fast framing camera system for observation of acceleration and ablation of cryogenic hydrogen pellet in ASDEX Upgrade plasmas". *Rev. Sci. Inst.*, **75**, 4754–4762, 2004.

[103] J. A. Alonso, P. Andrew, A. Neto, J. L. de Pablos, E. de la Cal, H. Fernandes, J. Gafert, P. Heesterman, C. Hidalgo, G. Kocsis, A. Manzanares, A. Murari, G. Petravich, L. Rios, C. Silva and P.D. Thomas and JET EFDA contributors. "Fast visible camera installation and operation in JET". In 34th EPS Conference on Plasma Phys. Warsaw, ECA Vol.31F, P-2.124, 2007.

[104] S. J. Zweben, D. P. Stotler, J. L. Terry, B. LaBombard, M. Greenwald, M. Muterspaugh, C. S. Pitcher, K. Hallatschek, R. J. Maqueda, B. Rogers, J. L. Lowrance, V. J. Matrocola, and G. F. Renda. "Edge turbulence imaging in the Alcator C-Mod tokamak". *Phys. Plasmas*, **9**(5), 19811989, 2002.

[105] J. L. Terry, N. P. Basse, I. Cziegler, M. Greenwald, O. Grulke, B. LaBombard, S. J. Zweben, E. M. Edlund, J. W. Hughes, L. Lin, Y. Lin, M. Porkolab, M. Sampsell, B. Veto, and S. J. Wukitch. "Transport phenomena in the edge of Alcator C-Mod plasmas". *Nuclear Fusion*, **45**, 13211327, 2005.

[106] O. Grulke, J. L. Terry, B. LaBombard, and S. J. Zweben. "Radially propagating fluctuation structures in the scrape-off layer of Alcator C-Mod." *Phys. Plasmas*, **13**, 2006.

[107] G. McKee, R. Ashley, R. Durst, R. Fonck, M. Jakubowski, K. Tritz, K. Burrell, C. Green-field, and J. Robinson. "The beam emission spectroscopy diagnostic on the DIII-D tokamak". *Review of Scientific Instruments*, **70**(1):913916, 1999.

[108] R. J. Maqueda, G. A. Wurden, S. Zweben, L. Roquemore, H. Kugel, D. Johnson, S. Kaye, S. Sabbagh, and R. Maingi. "Edge turbulence measurements in NSTX by gas puff imaging". *Rev. of Sci. Instr.*, **72**, 931934, 2001.

[109] S. J. Zweben, R. J. Maqueda, D. P. Stotler, A. Keesee, J. Boedo, C. E. Bush, S. M. Kaye, B LeBlanc, J. L. Lowrance, V. J. Matrocola, R. Maingi, N. Nishino, G.

Renda, D. W. Swain, and J. B. Wilgen. "High-speed imaging of edge turbulence in NSTX". *Nuclear Fusion*, **44**, 134153, 2004.

[110] J. R. Myra, D. A. DIppolito, D. P. Stotler, S. J. Zweben, B. P. LeBlanc, J. E. Menard, R. J. Maqueda, and J. Boedo. "Blob birth and transport in the tokamak edge plasma: analysis of imaging data". Submitted to POP, June 2006.

[111] G. S.K. Fung, N. H. C. Yung, and G. K. H. Pang. "Camera calibration from road lane markings". *Opt.Eng.*, **42**(10):29672977, 2003.

[112] EFIT equilibrium code at culham. http://fusion.org.uk/EFIT/.

[113] L. L. Lao, H. St. John, R. D. Stambaugh, A. G. Kellman, and W.Pfeiffer. "Reconstruction of current profile parameters and plasma shapes in tokamaks". *Nuclear Fusion*, **25**, 161122, 1985.

[114] L. L. Lao. "MHD equilibrium reconstruction in the DIII-D tokamak". Fusion Science and technology, **48**, 968, 2005.

[115] D. P. OBrien, L. L. Lao, E. R. Solano, M. Garribba, T. S. Taylor, J. G. Cordey, and J. J. Ellis. "Equilibrium analysis of iron core tokamaks using a full domain method". *Nuclear Fusion*, **32**, 1351, 1992.

[116] W. Zwingmann. "Equilibrium analysis of steady state tokamak discharges" *Nuclear Fusion*, **43**, 842, 2003.

[117] R. D. Hazeltine and J. D. Meis. *Plasma Confinement.* Dover publications, 2003.

[118] W. Fundamenski, R. A. Pitts, and JET contributors. "ELM-wall interaction on JET and ITER". *J. Nucl. Mat.*, **363-365**, 319-324, 2007.

[119] J. A Alonso, S. J. Zweben, P Caravalho, J. L. de Pablos, E. de la Cal, C. Hidalgo, T. Klinger, B. Ph van Milligen, R. J. Maquada, M. A. Pedrosa, C. Silva, M. Spoloare, H. Thomsen and the TJ-II team. "Impact of different confinement regimes on the two-dimensional structure of edge turbulence". *Plasma Phys. Control. Fusion*, **48**, B465-B473, 2006.

[120] A. Kirk, A. Herrmann, N. Ben Ayed, T. Eich, H. W. Muller, G. F. Counsell, S. Lisgo, M. Price, A. Schmid, S. Tallents, and H. Wilson "Comparison of the filament behaviour observed during type-I ELMs in ASDEX Upgrade and MAST". *J. of Physics - conference series*, **123**, 012012, 2008.

[121] A. Kirk, S. Lisgo, E. Nardon, T. Eich, A. Herrmann, A. Kallenbach, A. Louarte "Physics of ELM power fluxes to plasma facing components and implications for ITER". *Journal of Nuclear Materials*, **390-391**, 727-732, 2009.

[122] O. E. Garcia, J. Horacek, R. A. Pitts, A. H. Nielsen, J. Maden, V. Naulin and J. Juul Rasmussen. "Collisionality dependent transport in TCV SOL plasmas ". *Plasma Phys. Control. Fusion*, **49**, B47-B57, 2007.

[123] B. LaBombard, J. W. Hughes, D. Mossessian, M. Greenwald, B. Lipschultz, J. L. Terry and the Alcator C-Mod Team. "Evidence for electromagnetic fluid drift turbulence controlling the edge plasma state in the Alcator C-Mod tokamak". *Nucl. Fusion*, **45**, 1658-1675, 2005.

[124] O. E. Garcia, J. Horacek, R.A. Pitts, A.H. Nielsen, W. Fundamenski, V. Naulin, and J. Juul Rasmussen. "Fluctuations and transport in the TCV scrape-off layer". *Nucl. Fusion*, **47** 667-676, 2007.

[125] B. Kurzan *Proc. 35th EPS Conf. on Controlled Fusion and Plasma Physics* (Crete,Greece) ECA vol. **32** P-2.001, 2008.

[126] B. LaBombard, R. L. Boivin, M. Greenwald, J. Hughes, B. Lipschultz, D. Mossessian, C. S. Pitcher, J. L. Terry and S. J. Zweben "Particle transport in the scrape-off layer and its relationship to discharge density limit in Alcator C-Mod". *Phys. Plasmas*, **8**, 2107, 2001.

[127] M. Greenwald. "Density limits in toroidal plasmas". *Plasma Phys. Control. Fusion*, **44**, R27, 2002.

[128] G. Y. Antar, M. Tsalas, E. Wolfrum, V. Rohde and the ASDEX Upgrade Team. "Turbulence during H- and L-mode plasmas in the scrape-off layer of the ASDEX Upgrade tokamak". *Plasma Phys. Control. Fusion*, **50**, 095012, 2008.